Neutron Scattering Studies of Low-Dimensional Quantum Spin Systems

Stefan Paul Gosuly

A dissertation submitted in partial fulfilment
of the requirements for the degree of

Doctor of Philosophy
of
University College London

Department of Physics and Astronomy
University College London

September 2016

I, Stefan Paul Gosuly, confirm that the work presented in this thesis is my own. Where information has been derived from other sources, I confirm that this has been indicated in the work.

Abstract

This thesis describes how neutron scattering is used to reveal aspects of the physics of three experimental realizations of model systems with localized quantum spins and low-dimensional magnetic character of exchange interactions.

The first studied system is $(5CAP)_2CuCl_4$ (CAPCC), a realization of the famous S=1/2 square-lattice Heisenberg antiferromagnet. High-resolution time-of-flight inelastic neutron scattering is used to measure the excitation spectrum in applied magnetic field. A fit of the magnon dispersion predicted by linear spin-wave theory, to the dispersion measured in the field-polarised state, gives the parametrization of the low-energy effective Hamiltonian in terms of exchange couplings. These results establish that CAPCC is a quasi-2D square-lattice quantum Heisenberg antiferromagnet with a leading nearest neighbour Heisenberg exchange $J = 0.100(2)$ meV, but with significant inter-planar coupling $J' = 0.032(2)$ meV. The excitation spectrum measured in a magnetic field $B = 0.85 \times B_s$, just below the saturation field, provides experimental evidence that supports the theoretical prediction of field-induced magnon decays in CAPCC.

The second investigated system is Y_2BaNiO_5, an excellent realization of the S=1 Heisenberg antiferromagnetic chain. Very high-resolution inelastic neutron spin-echo is used to extend the magnon lifetime study by measuring the temperature dependence of the lifetime of triplet excitations and blue shift of the gap energy. The results are compared with theoretical predictions based on the non-linear sigma model, which fails to describe the measured lifetimes and blue shift over the whole range of measured temperatures. The residual measured lifetime as $T \to 0$ is attributed to chain-breaking defects and a mean chain length of 148 Ni-Ni sites is extracted. The possible limitation of the neutron spin-echo technique is highlighted when the excitation lineshape is asymmetric and the curvature of the dispersion surface probed by the resolution ellipsoid is large.

The third studied system is Cs_2CoCl_4, an effective S=1/2 XXZ antiferromagnetic spin chain. In a first part, time-of-flight magnetic neutron diffraction is used to extract the quantum correlations along the chain and an entanglement witness quantity that is theoretically predicted to signal an entanglement transition. In a second part, a triple-axis neutron technique is used to investigate the magnetic field evolution of the magnetic ordering in Cs_2CoCl_4, when a magnetic field is applied along the chain direction. Spin-wave excitations measured in the field-polarised state provide the parameters of the low-energy spin Hamiltonian which are responsible for the observed complex ordering.

Acknowledgements

A physics PhD involves a tremendous amount of individual work but the success of it is nevertheless a collaborative effort between the student and people who either continuously or at various points provide invaluable input. I take the opportunity to express my gratitude to the people who have one way or another contributed to this thesis.

I start by thanking Toby G. Perring and Desmond F. McMorrow for their supervision and guidance as well as for giving me the opportunity to carry out this work alongside them. Toby has been my main supervisor with whom I have worked most closely during my years at ISIS. I thank him for his attitude towards experimental science and all the guidance he has provided during my baby steps in neutron scattering. I have benefited enormously from all the scientific and non-scientific discussions we had. Des has been my UCL supervisor and I thank him for introducing me to the CAPCC project and for the valuable advice I received during my visits to London.

High-quality samples are crucial for successful neutron scattering experiments and so I thank Gøran Nilsen for growing the CAPCC single crystal and Daniel Biner and Karl Krämer for the Cs_2CoCl_4 single crystals. The sample mounts I designed on paper for the Cs_2CoCl_4 experiments have been transformed to reality by John Crawford and Tom Charleston at ISIS. I thank them for their efforts. Thanks to Matthias Gutmann on SXD who has helped me during the preliminary alignment of two Cs_2CoCl_4 crystals. Thanks to Martin Ruminy and Simon Ward for their help during the alignment of a Cs_2CoCl_4 crystal on Morpheus at SINQ. I also want to thank Richard Down, Dave Bunce and Jeff Keeping at ISIS and Markus Zolliker at SINQ for their involvement in the sample mounting.

During the experiments I performed at ISIS, FRM-II and SINQ, I received a great deal of help from the instrument scientists. A big thanks to Pascal Manuel on WISH for all his help with the Cs_2CoCl_4 experiments. Thanks to Rob Bewley on LET for the help during and after the CAPCC experiment. Special thanks to Thomas Keller at TRISP who apart from providing support during and after my experiments at FRM-II, has also had the patience of explaining in detail how the NRSE technique works. I also thank Thomas for making my short stays in Munich as enjoyable as possible by taking me to a wonderful organ concert and for drinks. During the experiment at RITA-II I have received a lot of support from Christof Niedermeyer for which I thank him.

A very special thanks to Martin Mourigal, Niels Christensen and Henrik Rønnow for their close involvement in the CAPCC project. I have had the pleasure of performing my first inelastic neutron scattering experiment together with Niels and Henrik on LET and I thank them for the tips and tricks they shared with me. I thank Martin and Niels for their enthusiasm, interest in the outcome of the experiment and the numerous skype conversations we had. I am grateful to Martin's involvement

and his continued theoretical support which has greatly contributed to the overall outcome of the CAPCC project.

I thank Jorge Quintanilla and Luigi Amico for discussions on the theoretical aspects of the entanglement project and for their initial enthusiasm during the experiments.

A shout out to some of my fellow PhD students Bruno Tomasello, Gianluca Messina and Mattia Mena. Thanks for all the good time spent together. Also thanks to Diego Alba Venero and Jordi Jacas Biendicho for the drinks in Oxford and making my time at ISIS enjoyable. During my stay at ISIS I received help at various stages and I thank everyone for all their help.

Outside of science I thank Ciprian Plostinar and Catalin Condurache for the morale boost during the afternoon coffees at RAL and to Alex Bugnar for the evenings in Oxford and for recommending two eye-opening books.

A very special thanks to Lucian Pascut for all his help and involvement in convincing me to apply for a PhD position in Des' group at UCL. I am grateful to Viorel Pop who allowed me to work in his magnetism group previous to starting my PhD and also for putting me in contact with Lucian.

A general thanks to everyone with who I have ever interacted during my PhD and who I did not name.

Last but not least, I am deeply grateful to my family who has encouraged and supported me during all this time. I know how hard it was for all but what doesn't kill us makes us stronger. Fulvia, Carmen, Ofelia, Mara, Horia, I thank you for the unconditional love. A special thanks goes to the second Carmen for all the love, support and putting up with me during the least pleasant moments.

This thesis is dedicated to the memory of my grandmother. Thank you for everything you did for me.

When you have eliminated the impossible, whatever remains, however improbable, must be the truth.

(Sherlock Holmes)

Contents

List of Figures

List of Tables

Chapter 1

Introduction

Magnetism is a fundamentally important aspect of solid state physics which originates in the exchange interaction due to Coulomb repulsion between electrons and the consideration of the Pauli exclusion principle. In systems with a large number of interacting electrons, interesting electronic and magnetic phenomena often arise. Examples include metal-insulator transitions, heavy fermion phenomena, superconductivity, multiferroicity, giant and colossal magnetoresistance, structural distortions, to name a few. These complex, many-body effects can only be understood in terms of collective behaviour that arises from interactions between a large number of electrons.

The quantum collective behaviour of magnetic systems is increasingly becoming important because the low-temperature properties of many new magnetic materials are potentially useful in future devices and because nanotechnology has emerged as a new discipline where the understanding and accurate control of magnetic phenomena is crucial in view of creating applications in a variety of fields such as nanoscale functional materials, nanoelectronics, nanometrology, information processing, medicine and biology.

The focus of this thesis is on low-dimensional, low-spin systems with localized magnetic moments, which provide an ideal context, both theoretically and experimentally, in which to explore many-body quantum effects. A large variety of model systems with the most diverse ground and excited states can be obtained by considering spins of different magnitude localized on a lattice of given geometry (cubic, triangular, square, kagome, honeycomb, etc.) which have three, two or one dimensional nature of magnetic interactions and are characterised by different types of exchange interactions such as Ising, XY or Heisenberg. Examples of interesting ground states

include the quantum spin liquid ground state in herbertsmithite [1] and the ground state of copper formate tetradeuterate (CFTD) which is understood as a superposition of classical Néel and resonating valence bond states due to the presence of quantum correlations [2]. In terms of excitations, examples include the excitations of the half-integer spin Heisenberg antiferromagnetic chain which are unbound pairs of one-dimensional spinons that propagate independently through the lattice and give rise to an interesting low-energy continuum [3, 4], and two-dimensional spinon excitations that were recently shown to exist in CFTD [5]. Spin-ice materials such as $Dy_2Ti_2O_7$ and $Ho_2Ti_2O_7$ have a highly degenerate ground state due to magnetic frustration. The excitations from this ground state arise from the fractionalisation of the electron spin degrees of freedom which behave as individual sources of magnetic field - magnetic monopoles that travel through the lattice [6, 7].

In this thesis we use neutron scattering as an experimental probe to investigate the magnetic properties of three real systems which are good realisations of low-dimensional model quantum magnets. Neutron scattering is often used for the study of quantum spin systems because it directly measures the dynamic spin-spin correlations or equivalently the imaginary part of the generalised magnetic susceptibility, as will be shown in Chapter 2.

- The first system we study is the layered organic magnet $(5CAP)_2CuCl_4$ (CAPCC) which has been proposed to be a good realisation of the quasi-2D square lattice quantum Heisenberg antiferromagnet with low nearest-neighbour exchange interaction that allows experimental investigations in all interesting applied magnetic field regimes. Various theoretical predictions [8–11] have been made of the evolution of the excitation spectrum with applied field including wave vector dependent magnon decay. High-resolution time-of-flight neutron spectroscopy is used to fully characterise the low energy effective Hamiltonian for the first time. These results establish that CAPCC is indeed a quasi-2D square lattice quantum Heisenberg antiferromagnet with a leading nearest neighbour Heisenberg exchange $J = 0.100(2)$ meV, but with significant interplanar coupling of $J' = 0.032(2)$ meV. The excitation spectrum measured in a field regime just below full saturation provides qualitative evidence for field induced magnon decay which results from magnon-magnon interactions. The data is compared against theoretical predictions based on linear spin-wave theory which ignores interaction between magnons and 1/S spin-wave theory which explicitly considers interactions. It is clearly shown that linear spin-wave

theory fails to give a good description of the excitations, whereas the 1/S spin-wave theory describes much better the measured spectrum, thus proving that magnon-magnon interactions have to be included in order to correctly account for the low energy excitation spectrum of CAPCC.

- The second system we study is Y_2BaNiO_5, an excellent realisation of the famous S=1 Heisenberg antiferromagnetic chain, also known as the Haldane chain. For this model, theoretical predictions established that despite lack of classical long-range magnetic order, the ground state is quantum coherent due to finite string order [12], with the degree of coherence which is reflected in the lifetime of the triplet excited states. High-resolution inelastic neutron spin-echo (NSE) was used to measure the temperature dependence of the lifetime of triplet excitations and gap energy in Y_2BaNiO_5. Comparison of the data to predictions based on the non-linear sigma model shows that theory fails to give a good description for temperatures smaller than the gap energy. From the limiting case of zero temperature, it is shown that static defects in the sample are most likely to be responsible for the observed finite lifetimes. As a result of this study, we highlight the possible limitation of the NSE technique when the excitation lineshape is asymmetric and the depolarisation correction due to the curvature of the dispersion is large.

- The third investigated material is Cs_2CoCl_4, a good realisation of the quasi-1D S=1/2 XXZ antiferromagnetic chain. In a first part we present results from neutron diffuse magnetic scattering and show that there are limitations of the experiment and the material which prevent the unambiguous identification of the theoretically predicted entanglement transition. Motivated by brief measurements of the magnetic ordering and the discovery of incommensurate magnetic order, we present, in a second part, results from a dedicated neutron triple-axis study, which shows that the applied magnetic field dependency of the magnetic ordering of Cs_2CoCl_4 is very complex and is driven by competing frustrated inter-chain interactions when the field is applied along the chain direction. As a function of field, the magnetic ordering changes from antiferromagnetic commensurate to incommensurate and the system goes through a quantum phase transition towards the high-field quantum paramagnetic state. From excitations measured at a field above saturation, we determine the parameters of the magnetic Hamiltonian which are responsible for the observed

ordering and show that inter-chain couplings are in the range of $5\% - 15\%$ of the main intra-chain exchange interaction J.

The experiments presented in this thesis were performed with the aim of investigating the influence of quantum fluctuations and quasi-particle interactions on the magnetic properties of model systems. In one dimension quasi-particles cannot avoid each other as they travel through the lattice and interactions between them have to be explicitly considered as in the case of the triplet excitations of the S=1 Haldane chain which we study in Chapter 4. In two dimensions, the magnon-magnon interactions can give rise to deviations of the excitation spectrum from conventional spin-wave theory predictions which include a dispersion renormalisation, magnon damping and presence of multi-magnon continuum, which we investigate in Chapter 3. The search for experimental evidence for a phase transition driven by entanglement between spins and the types of magnetic ordering for a S=1/2 XXZ antiferromagnetic chain model in an applied magnetic field are presented in Chapter 5.

1.1 Low-Dimensional Quantum Magnetism

The term quantum magnetism may seem like a tautology to purists, as it is well-known that magnetism is fundamentally a quantum effect, as shown by the Bohr-van Leeuwen theorem [13]. Here, by quantum, we mean the low limit (S=1/2) of the spin quantum number, for the various models we discuss. The low dimensionality of the magnetic exchange (dominant exchange coupling in one or two dimensions) leads to an enhancement of quantum fluctuations and as we will see, the consideration of the quantum limit and low dimensionality has serious implications for the nature of the magnetic ground state and excitations.

Quantum magnetism is a very active and rich field of research in modern solid state physics due to several reasons. Firstly, it provides an ideal ground for investigations of many-body physics through a large variety of relatively simple models that can be constructed out of interacting quantum objects placed in certain spatial geometries. Many of the models have excellent experimental realisations that allow detailed comparison between theory and experiment. Secondly, quantum magnetism allows for investigations of phenomena that arise as a consequence of quantum fluctuations such as disordered ground states and the corresponding excitations, both

highly non-classical. Examples include algebraic spin liquids, valence bond solids, resonating valence bond liquids and nematic phases. Thirdly, quantum correlations determined by entanglement in the ground state are ideally studied in quantum spin models due to their tunable Hamiltonians.

1.2 Order and Excitations

Depending on the lattice topology and dimensionality of the magnetic interactions, systems may or may not display magnetic long range order in the ground state. The origin of the exchange interaction which is responsible for long range order, lies in the symmetry properties of the spin degree of freedom. The total wave function for fermionic identical particles has to be antisymmetric with respect to the exchange of any two particles. The total wave function has a spatial part and a spin part. When the spatial part is symmetric/antisymmetric, the spin part has to be antisymmetric/symmetric, respectively. The interaction between two spins can be parametrised using $\mathbf{S_i} \cdot \mathbf{S_j}$ with strength J, as shown for example in the book by Blundell [14]. The Hamiltonian of the system can be generalised for many spins in the form of an effective low energy spin-Hamiltonian that describes the strength of the exchange and it represents the well-known Heisenberg Hamiltonian [14, 15].

When quantum fluctuations play a significant role, as for quantum magnets, the true ground state is very different from its classical analogue. The simplest case that illustrates this is a dimer system of two spins S=1/2 that are coupled by an antiferromagnetic exchange J, with the Hamiltonian $\mathcal{H} = \mathrm{J}\mathbf{S}_1 \cdot \mathbf{S}_2$.

In the classical case, the spins are considered as unit vectors and the ground state is one in which the spins point in opposite directions $|\uparrow\downarrow\rangle$, with a ground state energy of $\mathrm{E_{gs}} = -\mathrm{JS}^2 = -\mathrm{J}/4$. Quantum mechanically, the spins are quantum objects which have components that do not commute and a quantization axis is chosen in order to characterize the direction of the spin. Conventionally this axis is taken as the z-axis and the spin is projected onto the z-axis. The eigenvalue of the z-component, measured in units of $\hbar$, can be either $+1/2$ (spin-up) $|\uparrow>$ or $-1/2$ (spin-down) $|\downarrow>$. The possible states of the system are described in terms of product states of individual spins, with four possibilities $|\uparrow\uparrow>$, $|\downarrow\downarrow>$, $|\uparrow\downarrow>$ and $|\downarrow\uparrow>$. The ground state, with energy $\mathrm{E_{gs}} = -\mathrm{JS(S+1)} = -3\mathrm{J}/4$, is the singlet state $\frac{1}{\sqrt{2}}(|\uparrow\downarrow> - |\downarrow\uparrow>)$, where the spins are coupled anti-parallel and the total spin is $\mathrm{S} = 0$. The remaining three states $|\uparrow\uparrow>$, $|\downarrow\downarrow>$ and $\frac{1}{\sqrt{2}}(|\uparrow\downarrow> + |\downarrow\uparrow>)$ are degenerate in energy, $\mathrm{E_{ex}} = \mathrm{J}/4$,

and form the excited triplet state with total spin $S = 1$.

We note that there are several important differences between the classical and quantum system. Firstly, the classical ground state is not even an eigenstate of the Hamiltonian and it has a considerably higher energy than that of the actual ground state. Secondly, in infinite classical systems, choosing a direction for the spins breaks rotational symmetry so the lowest lying excitations at the ferromagnetic ordering wave vector $q = 0$ have zero energy and are known as Goldstone excitations. This practically means that it costs a vanishingly small energy to create a long-wavelength magnetic excitation. In contrast, the quantum ground state does not break rotational symmetry, so the excitations are gapped. Thirdly, in the classical case, the magnitude of the spin is $S_c = S$, whereas in the quantum case it is $S_q = \sqrt{S(S+1)}$. A useful estimate of deviation from the classical case is the ratio of the spin expectation values $S_q^2/S_c^2 = 1 + 1/S$. It indicates that the fluctuations about the classical values are largest for the quantum limit $S = 1/2$ and that for large spin values the quantum behaviour approaches the classical one.

To determine the magnetic ground state angular momentum quantum numbers for an atom, one usually uses Hund's rules. For multi-electron atoms where the spin-orbit coupling is weak, it is assumed that the orbital angular momenta of individual electrons add to form a resultant orbital angular momentum $\mathbf{L}$. Likewise, the individual spin angular momenta are presumed to couple to produce a resultant spin angular momentum $\mathbf{S}$ and so $\mathbf{J} = \mathbf{L} + \mathbf{S}$. Hund's rules say that electrons in a given shell will occupy orbitals in such a way that the ground state has the maximum value for total S (allowed by the exclusion principle), then the maximum value for L, consistent with S, and that J is determined differently if the shell is less or more than half-filled.

Table 1.1: Magnetic moments of isolated ions of Cu^{2+}, Ni^{2+} and Co^{2+}. Taken from [15].

Ion	Config.	$^{2S+1}L_J$	$\mu_{\text{eff}}(J)[\mu_B]$	$\mu_{\text{eff}}(S)[\mu_B]$	Exp. moment $[\mu_B]$
Cu^{2+}	$3d^9$	$^2D_{5/2}$	3.55	1.73	1.9
Ni^{2+}	$3d^8$	$^3F_4$	5.59	2.83	3.2
Co^{2+}	$3d^7$	$^4F_{9/2}$	6.63	3.87	4.8

In the case of transition metal ions with open 3d shells, when put together in a solid, the energy associated with the crystal field created by the surrounding

environment is much larger that the energy of the spin-orbit coupling. Because of this and of the interaction between electrons, the electrons do not have well-defined orbits any more. As a result, the contribution of the orbital angular momentum to the magnetic moment becomes negligibly small and the elements from the 3d series have quenched orbital moment and the magnetic moment is mainly determined by the electron spin. An exception to this is the case of Co^{2+} where the orbital contribution is important. See Table 1.1 for experimental data on 3d ions relevant to the work in this thesis.

Determining the nature of the excited states of a system is as important as describing and understanding the ground state, because all thermodynamical properties such as magnetisation, susceptibility, specific heat, resistivity, and the response to weak external fields, are determined by the dynamic correlations that characterise the excitations. Excitations are collective fluctuations above the ground state and in magnetically ordered systems, they can be viewed classically as precessions of individual spins about the mean spin direction. These fluctuations are called spin-waves and propagate through the system having a wave-like character with a well-defined wave vector q and frequency ω. Their energy is quantised and they are formally considered as quasi-particles known as magnons. For example, in an isotropic spin ferromagnet at non-zero temperatures, the magnetic order is broken by spin-waves. An example of a derivation of the dispersion relation for classical magnons in a 1D ferromagnet with lattice spacing a and nearest-neighbour interaction J can be found in [16] with the result

$$\hbar\omega = 4\mathrm{JS}(1 - \cos(\mathrm{qa})) \tag{1.1}$$

For a simple 1D antiferromagnet, the magnon dispersion relation is given by

$$\hbar\omega = 4\mathrm{JS}\sin(\mathrm{qa}) \tag{1.2}$$

In the ferromagnetic case, at long wavelengths $\mathrm{qa} << 1$, so $1 - \cos(\mathrm{qa}) \approx \frac{1}{2}(\mathrm{qa})^2$ and

$$\hbar\omega \approx 2\mathrm{JSa}^2\mathrm{q}^2 \tag{1.3}$$

where the spin-stiffness constant is given by $\rho_\mathrm{s} = 2\mathrm{JSa}^2$ and represents a measure of the change in the ground state energy of a spin system as a result of introducing a slow in plane twist of the spins.

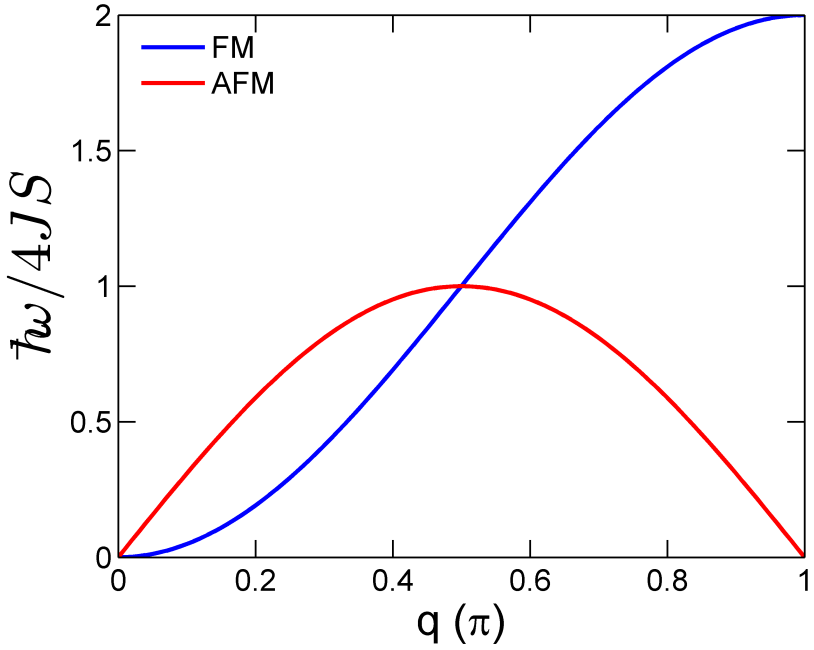

Figure 1.1: Comparison between ferromagnetic and antiferromagnetic dispersions for a one-dimensional chain of spins S with nearest neighbour exchange J.

If we compare the ferromagnetic dispersion with the antiferromagnetic dispersion (see Fig. 1.1) we observe that for ferromagnets close to the ferromagnetic wave vector $q = 0$ the dispersion is quadratic in q, whereas for antiferromagnets close to the ordering wave vector $q = \pi$, the dispersion is linear in q. We will see in Chapter 4 that the curvature of the dispersion close to the antiferromagnetic wave vector gives the spin-wave velocity.

Dispersion relations are traditionally measured across the entire Brillouin zone using inelastic neutron scattering, which determines the dynamical structure factor that completely characterises the momentum and energy dependence of the low-lying magnetic excitations. Quite recently, dispersion relations have also been successfully measured across the entire Brillouin zone using the novel technique of resonant inelastic X-Ray scattering (RIXS) [17–19]. From measurements of the dispersion relation, the exchange interaction strength between pairs of spins is very accurately determined when fitted to theoretical models. In Chapters 3 and 5 we measure the dispersion relations of magnetic excitations in $(5CAP)_2CuCl_4$ and Cs_2CoCl_4 and extract the exchange constants by fitting data to predictions given by conventional or linear spin-wave theory.

1.3 Quantum Phase Transitions

Phase transitions play an important role in understanding the behaviour of condensed matter systems. They describe the transition between different phases of a system, most often between an ordered and a disordered phase, where the properties change qualitatively. A prime example is the metal to superconductor transition that results upon lowering temperature. Another familiar example is the phase transition from a ferromagnet to a paramagnet upon crossing a critical temperature. Depending on the temperature at which the transition takes place, two classes of transitions are identified. Classical phase transitions which occur at $T \neq 0$ and quantum phase transitions which occur at $T = 0$. The former are controlled by thermal fluctuations and the control parameter is the temperature, whereas for the latter, the transitions are controlled by quantum fluctuations and are driven by either hydrostatic pressure, applied magnetic field or doping. Classical phase transitions have been extensively studied and are well-understood, whereas scientific interest for quantum phase transitions as arisen only in the past 20 years or so. Experimental and theoretical investigations have revealed that quantum phase transitions play a crucial role in many interesting and still disputed phenomena in condensed matter. Examples include rare-earth magnetic insulators, heavy-fermion systems, high-temperature superconductors and two-dimensional electron gases.

At finite temperatures, thermal fluctuations can drive a system from an ordered phase, with a finite order parameter, to a disordered phase where the order parameter vanishes. The analogue case happens at zero temperature where quantum fluctuations and the variation of a control parameter, drive the system through a similar phase transition. The point where the order parameter is on one side finite and on the other zero, is called a quantum critical point (QCP). At the QCP the correlation length and correlation time diverge and the system is characterized by scale invariance, meaning that fluctuations occur at all length and time scales. Even though the quantum phase transition occurs at exactly $T = 0$, the critical behaviour extends to a region above the transition point, at low, finite temperature. In this region quantum fluctuations dominate over thermal fluctuations and novel physics such as non-Fermi liquid behaviour and unconventional power laws is expected. At higher temperatures, the system is disordered and classical. Around the classical phase transition line (solid black line in Fig. 1.2 b)), the system is characterized by thermal fluctuations. This region becomes narrower with decreasing energies and

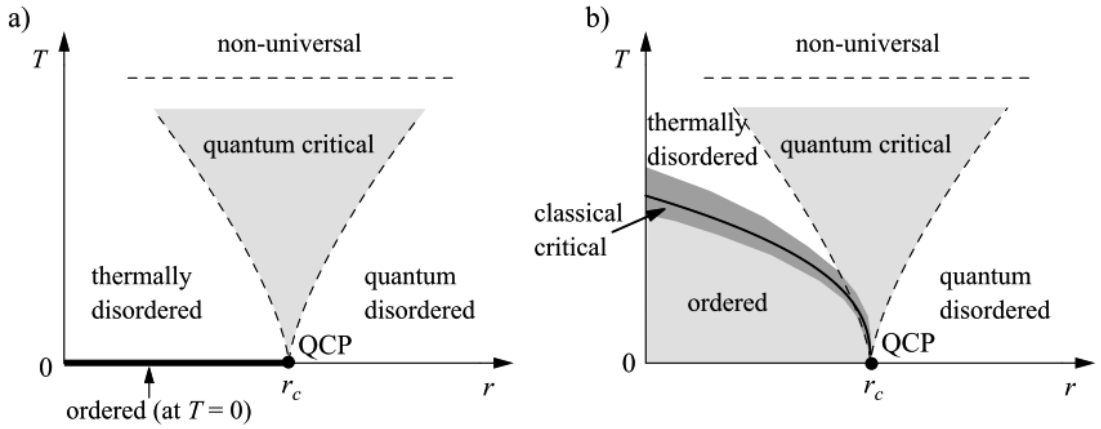

Figure 1.2: Phase diagrams that illustrate the concept of a quantum phase transition. On the horizontal axis, a control parameter is continuously varied in order to drive the phase transition. On the vertical axis, the temperature is varied. a) Order present only at T=0. b) Order exists in a finite region above T=0. The solid line marks the transition line between the ordered and thermally disordered phases. In a region close to this line, the behaviour of the system is classical critical with thermal fluctuations driving the transition. The dashed lines delimit a region (grey) where quantum critical behaviour is expected at T > 0, due to the presence of the quantum critical point at T = 0. Taken from [20]

.

converges towards the quantum critical point. An illustration of these concepts is presented in the schematic phase diagrams in Fig. 1.2.

An interesting aspect is that a fairly recent quantum information theory description of phase transitions, has revealed previously unpredicted features in the phase diagram of model spin systems. Such a novel feature is the quantum entanglement phase transition [21, 22] predicted for a large variety of spin models, where upon crossing the critical point, the type of entanglement present in the system qualitatively changes. This is relevant to the quasi-1D spin-1/2 XXZ antiferromagnetic chain - Cs_2CoCl_4 as an entanglement transition is predicted to occur near a quantum critical point [23].

Chapter 2

Neutron Scattering Technique

2.1 Introduction

Neutron scattering is a widely used experimental technique in condensed matter research because it very well suited for obtaining information about the structure and dynamics of studied systems. To understand why it is a powerful tool one has to consider some of the fundamental properties of the neutron. Firstly, its mass determines the associated de Broglie wavelength to be of the order of inter-atomic spacings in solids. The energy of a thermal neutron ($T \approx 293$ K) is $E = k_B T = h^2/2m_n\lambda^2$ and is approximately $E = 25$ meV which corresponds to $\lambda = 1.8$ Å. Interference effects offer information about the structure of the scattering system. Secondly, the charge neutrality of the neutron makes it penetrate deep into the target and because there is no Coulomb barrier to overcome, it interacts directly, via the very short-ranged strong force, with the nucleus. Thirdly, the kinetic energy of slow neutrons is of the same order of magnitude as that of many elementary excitations in solids. The analysis of the scattered neutron energy provides information about the excited states. Very importantly, the neutron possesses a magnetic moment, hence it interacts magnetically with the unpaired electrons in atoms. Elastic scattering from this interaction gives information about the spin structure whereas inelastic scattering provides information about the magnetic excitations through the spin-spin correlations characteristic to the system.

2.2 Scattering Theory

All the experiments presented in this thesis used neutron scattering to study properties of real systems which are good realisations of model quantum magnets. The aim of this section is to outline the essential features required to appreciate experimental results. Full theoretical details can be found in the excellent textbooks by Lovesey and Squires [24, 25].

In order to have a common language for presenting results from a variety of scattering experiments, there are a few useful relationships between wavelength, wave vector, velocity, energy and temperature for thermal neutrons

$$\begin{aligned} \lambda &= 6.283\frac{1}{\mathrm{k}} = 3.956\frac{1}{\mathrm{v}} = 9.045\frac{1}{\sqrt{\mathrm{E}}} = 30.81\frac{1}{\sqrt{\mathrm{T}}} \\ \mathrm{E} &= 0.08617\mathrm{T} = 5.227\mathrm{v}^2 = 81.81\frac{1}{\lambda^2} = 2.072\mathrm{k}^2 \end{aligned} \tag{2.1}$$

where λ is in Å, k is in Å^{-1}, v is in km/s, E in meV and T in K. The equivalence between different units for energy is useful when quoting results. It is known that 1 meV = 11.6 K = 8.64 T (g = 2) = 0.2418 THz = 8.065 cm^{-1} = 1.602×10^{-22} J.

2.2.1 Scattering Cross Section

In a neutron scattering process the neutron momentum and total energy are conserved quantities. For a neutron of mass $\mathrm{m_n}$ and wave vector $\mathrm{k_i}$ incident on a sample, the wave vector transfer is defined as

$$\mathbf{Q} = \mathbf{k}_\mathrm{i} - \mathbf{k}_\mathrm{f} \tag{2.2}$$

where $\mathbf{k}_\mathrm{f}$ is the wave vector of the outgoing neutron and $\hbar\mathbf{Q}$ is the momentum transferred to the sample. This is in fact the momentum conservation law. The process of scattering through a 2θ angle is schematically illustrated in Fig. 2.1.

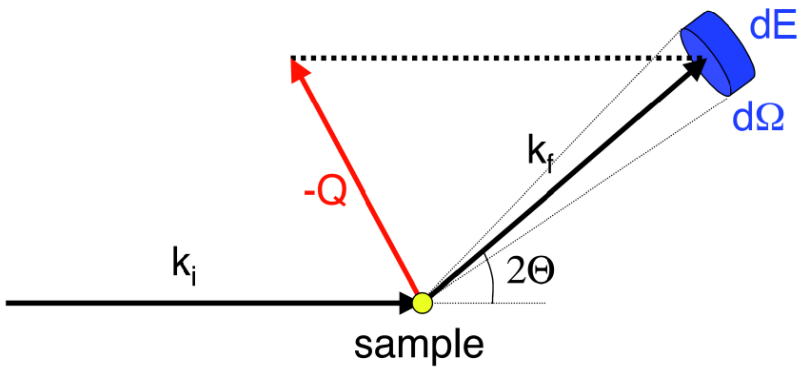

Figure 2.1: Schematic neutron scattering geometry with incident neutron and outgoing neutron wave vectors, solid angle spanned by a detector element dΩ and energy interval dE. Taken from [26].

In an elastic scattering process, where the neutron does not transfer any energy to the sample and where $\mathbf{k}_i = \mathbf{k}_f = k$, the wave vector transfer is $|\mathbf{Q}| = 2k \sin\theta$. In the case of an inelastic scattering process, momentum and energy are being transferred to/from the sample. Conservation of energy is then written as

$$E = \hbar\omega = \frac{\hbar^2}{2m_n} \cdot (\mathbf{k}_i^2 - \mathbf{k}_f^2) \tag{2.3}$$

The energy transferred to the sample is used to excite phonon or magnon modes which can thus be measured using inelastic neutron scattering. The outgoing neutron is being detected with the help of detector arrays. The spatial position of each detector is usually described by two degrees of freedom, the scattering angle 2θ and an out-of-plane angle ϕ, using a polar coordinate system. The physical quantity that is being measured in a scattering experiment is the scattering cross-section. Depending on the nature of scattering, several types of cross-sections can be defined. The inelastic cross-section which is also known as the partial differential cross-section reads

$$\frac{d^2\sigma}{d\Omega dE_f} = \frac{\mathcal{N} \text{ in the direction } (2\theta, \phi) \text{ with final energy between } E_f \text{ and } E_f + dE_f}{\Phi d\Omega dE_f} \tag{2.4}$$

where $\mathcal{N}$ represents the number of neutrons scattered per second into the solid angle $d\Omega$, Φ is the incident neutron flux and dE_f is the allowed variation in final energy. If one is not interested in the final energy of the neutrons but only takes into consideration $\mathcal{N}$ in the direction (2θ, ϕ), then Eq. 2.4 can be integrated with

respect to E_f and result in the so-called differential cross-section

$$\frac{d\sigma}{d\Omega} = \frac{\mathcal{N} \text{ in the direction } (2\theta, \phi)}{\Phi d\Omega} \tag{2.5}$$

If one is only interested in the number of neutrons that have been scattered per second in all directions, then a further integration of equation 2.4 with respect to $d\Omega$ gives the total scattering cross-section

$$\sigma_{tot} = \frac{\text{total number of neutrons scattered per second}}{\Phi} \tag{2.6}$$

The aim is to find useful expressions for the cross-sections in terms of material dependent quantities that allow direct comparison to theoretical models. Depending on the type of interaction potential between the neutron and the sample, one can have nuclear interaction, where the neutron interacts via the strong force with the nuclei in the sample, and magnetic interaction, where the magnetic moment of the neutron plays a key role and couples to the unpaired electron spins in the sample. Nuclear scattering allows the determination of the crystal structure and study of the lattice excitations, whereas magnetic scattering allows the determination of the magnetic structure and low-energy magnetic excitations. In the following, a general formula for the cross-section will be derived and then particularised to magnetic scattering. The focus is on magnetic scattering because this type of interaction is relevant to all experiments presented in this thesis.

2.2.2 General Result for the Cross Section

For a scattering process where the incoming neutron changes the state of the target system from $|\lambda_i\rangle$ to $|\lambda_f\rangle$, with corresponding energies E_{λ_i} and E_{λ_f}, the differential cross-section is

$$\left(\frac{d\sigma}{d\Omega}\right)_{\lambda_i \to \lambda_f} = \frac{1}{\Phi d\Omega} \sum_{\mathbf{k_f}} W_{\mathbf{k_i}, \lambda_i \to \mathbf{k_f}, \lambda_f} \tag{2.7}$$

where $W_{\mathbf{k_i}, \lambda_i \to \mathbf{k_f}, \lambda_f}$ represents the number of transitions per second from the state $|\mathbf{k_i}, \lambda_i\rangle$ to $|\mathbf{k_f}, \lambda_f\rangle$, Φ is the incident flux and $d\Omega$ is the small solid angle subtended by a detector element. To get an expression for W one can use Fermi's Golden Rule because the interaction of the neutron with the scattering system can be considered very weak and to a good approximation, higher order scattering events can be neglected

$$W_{\mathbf{k_i},\lambda_i\to\mathbf{k_f},\lambda_f} = \frac{2\pi}{\hbar}\cdot\rho_{\mathbf{k_f}}|\langle\mathbf{k_f}\lambda_f|V|\mathbf{k_i}\lambda_i\rangle|^2 \tag{2.8}$$

where $\rho_{\mathbf{k_f}}$ is the number of momentum states in $d\Omega$ per unit energy range for neutrons in the state $\mathbf{k_f}$. Because in most cases the source of neutrons and the detector are far away from the sample, we can make use of the Born approximation for scattering processes which considers both the incoming neutron wave function and the outgoing neutron wave function as plane waves. This leads to a general expression for the cross-section that is written

$$\left(\frac{d^2\sigma}{d\Omega dE_f}\right)_{\lambda_i\to\lambda_f} = \frac{k_f}{k_i}\left(\frac{m_n}{2\pi\hbar^2}\right)|\langle\mathbf{k_f}\lambda_f|V|\mathbf{k_i}\lambda_i\rangle|^2\delta\left(E_{\lambda_i}-E_{\lambda_f}+E_i-E_f\right) \tag{2.9}$$

where the square of the matrix element depends on the type of interaction potential considered and the delta function represents the law of conservation of energy.

2.2.3 Magnetic Scattering

The neutron is an uncharged particle with $S = 1/2$. The spin degree of freedom gives rise to a magnetic moment and leads to interaction with matter not only via the strong force but also via magnetic dipole-dipole forces. The magnetic moment of the neutron couples to the spins of unpaired electrons. If the spins in materials are arranged in a periodic way, this interaction can lead to Bragg magnetic scattering with the formation of Bragg peaks and to excitation of the spin system. Magnetic neutron scattering can be described by suitably choosing a potential term in Eq. 2.9. One starts by deriving an expression for the magnetic potential denoted V_M. The associated magnetic moment of the neutron reads

$$\boldsymbol{\mu}_n = -\gamma\mu_N\boldsymbol{\sigma} \tag{2.10}$$

where μ_N is the unit of measure for nuclear magnetic moments known as the nuclear magneton, $\gamma = 1.913$ is the gyromagnetic ratio (ratio between the magnetic moment and angular momentum of a particle) and $\boldsymbol{\sigma}$ is the Pauli spin operator for the neutron. The interaction potential is

$$V_M = -\boldsymbol{\mu}_n\cdot(\boldsymbol{B_L}(\mathbf{r})+\boldsymbol{B_S}(\mathbf{r})) \tag{2.11}$$

and is the potential of the neutron in the field created by the orbital $\boldsymbol{B_L}$ and spin $\boldsymbol{B_S}$ contributions of the electrons. The steps that lead to the exact form of $\mathrm{V_M}$ are presented in Chapter 7 of the book by Squires [25]. This flux density can then be related to the magnetisation of the system and gives

$$\mathrm{V_M}(\mathbf{Q}) = -\boldsymbol{\mu}_\mathrm{n} \cdot \mathbf{B}(\mathbf{Q}) = -\mu_0 \boldsymbol{\mu}_\mathrm{n} \mathbf{M}_\perp \tag{2.12}$$

where $\mathbf{B}(\mathbf{Q})$ is the Fourier transform of the real space $\mathbf{B}(\mathbf{r})$ and $\mathbf{M}_\perp$ is the component of magnetisation perpendicular to $\mathbf{Q}$

$$\mathbf{M}_\perp = \hat{\mathbf{Q}} \times \left(\mathbf{M} \times \hat{\mathbf{Q}} \right) \tag{2.13}$$

where $\hat{\mathbf{Q}}$ is the unit vector in the direction of the scattering vector $\mathbf{Q}$.

The next objective is to derive useful expressions for the interaction differential cross-sections and start by considering expressions for $\mathbf{M}_\perp$. Using the dipole approximation, the magnetisation can be calculated in the case of 3d transition metals and 4f rare-earths [24]. For 3d ions, the d-type electrons participating in the interaction, form an open shell that directly interacts with the crystal fields. The crystal field interaction is stronger than the spin-orbit interaction and leads to orbital quenching in compounds with 3d ions. The spin-orbit interaction can induce a small component of $\mathbf{L}$ in the direction of $\mathbf{S}$. In this case $\mathbf{L}$ is replaced by $(\mathrm{g}-2)\mathbf{S}$ and the magnetisation can be written as

$$\mathbf{M}(\mathbf{Q}) = -\mathrm{g}\mu_\mathrm{B}\mathrm{f}(\mathbf{Q})\mathbf{S} = \mathrm{f}(\mathbf{Q})\boldsymbol{\mu} \tag{2.14}$$

where $\mathrm{g} = 2$ for electrons, $\boldsymbol{\mu} = -\mathrm{g}\mu_\mathrm{B}\mathbf{S}$ is the magnetic moment of the unpaired electrons, and $\mathrm{f}(\mathbf{Q})$ is the magnetic form factor. The form factor can be calculated from tables [27, 28]. 4f ions have finite orbital and spin angular momenta and J is a good quantum number. By adopting an L-S type coupling, the magnetisation can be written

$$\mathbf{M}(\mathbf{Q}) = -\mathrm{g_J}\mu_\mathrm{B}\mathrm{f}(\mathbf{Q})\mathbf{J} = \mathrm{f}(\mathbf{Q})\boldsymbol{\mu} \tag{2.15}$$

where $\mathrm{g_J}$ is the Landé splitting factor, $\boldsymbol{\mu} = -\mathrm{g_J}\mu_\mathrm{B}\mathbf{J}$ and the magnetic form factor is calculated differently from the 3d ions case [27, 28]. The magnetic form factor is the Fourier transform of the normalised spin density $\mathcal{S}(\mathbf{r})$ of the magnetic ion and can be written as

$$\mathrm{f}(\mathbf{Q}) = \int \mathcal{S}(\mathbf{r}) \exp(\mathrm{i}\mathbf{Q}\mathbf{r}) \mathrm{d}\mathbf{r} \tag{2.16}$$

In practice the magnetic form factor is responsible for the rapid decrease of the magnetic scattering intensity with increasing wave vector transfer. For an ion like Cu^{2+} the scattering intensity is reduced to 50% of its $Q = 0$ value within $Q = 4$ $\mathrm{\AA}^{-1}$.

The actual derivation of the form factors is rather complicated [29] and for many purposes it can be approximated analytically in terms of spherical Bessel functions. If $s = \sin(\theta)/\lambda = Q/4\pi$, where θ is the angle between the incident neutron wave vector and the atomic scattering plane, λ is the wave length of the incident neutron and s is in units of $\mathrm{\AA}^{-1}$, then the form factors can be written as

$$\langle \mathrm{j}_0(\mathrm{s}) \rangle = \mathrm{A} \exp(-\mathrm{as}^2) + \mathrm{B} \exp(-\mathrm{bs}^2) + \mathrm{C} \exp(-\mathrm{cs}^2) + \mathrm{D} \tag{2.17}$$

and

$$\langle \mathrm{j}_2(\mathrm{s}) \rangle = \mathrm{s}^2 \left(\mathrm{A} \exp(-\mathrm{as}^2) + \mathrm{B} \exp(-\mathrm{bs}^2) + \mathrm{C} \exp(-\mathrm{cs}^2) + \mathrm{D} \right) \tag{2.18}$$

with the magnetic form factor

$$\mathrm{f}(\mathbf{Q}) = \langle \mathrm{j}_0 \rangle + \langle \mathrm{j}_2 \rangle \frac{\mathrm{J}(\mathrm{J}+1) - \mathrm{S}(\mathrm{S}+1) + \mathrm{L}(\mathrm{L}+1)}{3\mathrm{J}(\mathrm{J}+1) + \mathrm{S}(\mathrm{S}+1) - \mathrm{L}(\mathrm{L}+1)} \tag{2.19}$$

Depending on the type of magnetic atom present in the system, one of the two forms (see Eq. 2.14 and 2.15) for the magnetisation can be used in the matrix elements which enter the cross-section.

Elastic Scattering

In ordered crystals, when the scattering vector $\mathbf{Q}$ is equal to a reciprocal magnetic lattice vector $\boldsymbol{\tau}_\mathrm{M}$, magnetic Bragg scattering occurs. The scattering cross-section from such processes is given, in the dipole approximation, by

$$\begin{aligned} \left(\frac{\mathrm{d}^2\sigma}{\mathrm{d}\Omega \mathrm{d}\mathrm{E}_\mathrm{f}} \right)^{\mathrm{el}}_{\mathrm{mag}} &= \frac{\mathrm{N}_\mathrm{m}(2\pi)^3}{\mathrm{V}_{\mathrm{m0}}} \left(\frac{\gamma \mathrm{r}_0}{2} \right)^2 \sum_{\alpha\beta} \left\langle \left(\delta_{\alpha,\beta} - \hat{\mathrm{Q}}_\alpha \hat{\mathrm{Q}}_\beta \right) \mathrm{F}^\alpha(\mathbf{Q}) \mathrm{F}^{\beta\star}(\mathbf{Q}) \right\rangle \\ &\quad \times \delta(\mathbf{Q} - \boldsymbol{\tau}_\mathrm{M}) \delta(\hbar\omega) \end{aligned} \tag{2.20}$$

where N_m is the number of magnetic unit cells, V_{m0} is the volume of the magnetic

unit cell, γ is the gyromagnetic ratio, $r_0 = 2.8 \times 10^{-15}$ m is the classical electron radius, $\boldsymbol{\tau}_M$ is a reciprocal magnetic lattice vector, α, β can be any of the x, y, z cartesian components, $\langle \dots \rangle$ represents a thermal average and the magnetic structure factor is given as

$$F^{\alpha}(\mathbf{Q}) = \sum_{j} \mu_j^{\alpha} f_j(\mathbf{Q}) \exp(i\mathbf{Q}\mathbf{r}_j) \exp(-W_j(Q,T)) \tag{2.21}$$

where the sum runs over all j atoms in the unit cell, with μ_j^{α} being the α component of the magnetic moment of the j^{th} atom and $f_j(\mathbf{Q})$ is the magnetic form factor corresponding to atom j. W_j is the Debye-Waller factor corresponding to atom j which describes the attenuation due to thermal motion. The $\sum_{\alpha,\beta}\left(\delta_{\alpha,\beta} - \hat{Q}_{\alpha}\hat{Q}_{\beta}\right)$ part in the cross-section indicates that in the case of magnetic scattering only components of the magnetisation which are perpendicular to the scattering vector $\mathbf{Q}$ give rise to scattering intensity.

Inelastic Scattering

For inelastic scattering processes, the cross-section for unpolarised neutrons reads

$$\left(\frac{d^2\sigma}{d\Omega dE_f}\right)_{mag}^{inel} = \frac{k_f}{k_i}\left(\frac{\gamma r_0}{2}\right)^2 f^2(\mathbf{Q}) e^{-2W(Q,T)} S(\mathbf{Q},\omega) \tag{2.22}$$

where $S(\mathbf{Q},\omega)$ is the response function or scattering function and has the form

$$S(\mathbf{Q},\omega) = \sum_{\alpha,\beta}\left(\delta_{\alpha,\beta} - \hat{Q}_{\alpha}\hat{Q}_{\beta}\right) \cdot S^{\alpha\beta}(\mathbf{Q},\omega) \tag{2.23}$$

Here $S^{\alpha\beta}(\mathbf{Q},\omega)$ are the space and time Fourier transforms of the spin-spin correlation function

$$S^{\alpha\beta}(\mathbf{Q},\omega) = \frac{1}{2\pi\hbar}\int_{-\infty}^{+\infty} \sum_{j,j'} e^{i\mathbf{Q}(\mathbf{r}_j - \mathbf{r}_{j'})} e^{i\omega t} \left\langle S_{j'}^{\alpha}(0) S_j^{\beta}(t)\right\rangle dt \tag{2.24}$$

where $S_j^{\beta}(t)$ are the beta components of the spin at site j and time t and $\langle \dots \rangle$ denotes a thermal average over the initial states of the system.

An important property of the response function is that it is directly connected with the imaginary part of the generalised susceptibility through the fluctuation-dissipation theorem [30]

$$S(\mathbf{Q},\omega) = (n(\omega)+1)\chi''(\mathbf{Q},\omega) = \frac{\chi''(\mathbf{Q},\omega)}{1-\exp(-\hbar\omega/k_B T)} \tag{2.25}$$

where $n(\omega) = 1/(\exp(\hbar\omega/k_B T) - 1)$ is the Bose occupation factor. The complex generalized susceptibility $\chi(\mathbf{Q},\omega)$ describes the response of a system, initially in thermal equilibrium, to a perturbation which is space and time dependent. It has a real reactive part χ' and an imaginary absorptive part χ''. The fluctuation-dissipation theorem, which assumes a linear response to an external perturbation, shows the intimate connection between fluctuations in the magnetic system described by the correlation function and the response of the system to external perturbations as described by the imaginary part of χ. A dissipative response to small perturbations is equivalent to the response to fluctuations. This result is very important because the generalised susceptibility can usually be calculated from first principles and can be directly compared with the measured scattering function.

2.3 Neutron Sources

The primary goal of neutron sources is to deliver a high intensity beam of neutrons which are useful for scattering experiments. There are two conventional ways of producing neutrons for research, nuclear fission and spallation based processes. In Europe, nuclear reactors, which include the high flux reactor at the Institut Laue-Langevin, Grenoble, France and the FRM-II reactor in Garching, Germany are based on the process of nuclear fission of ^{235}U for producing neutrons. Spallation sources such as the ISIS neutron source at the Rutherford Appleton Laboratory, United Kingdom and the SINQ spallation source at the Paul Scherrer Institute, Villigen, Switzerland, are based on proton accelerators and generate neutrons by smashing high energy protons into heavy elements (e.g. tungsten, tantalum, mercury) known as targets. The resulting neutrons from both processes are highly energetic, in the range of MeV, and are not of any real use for scattering experiments. They are slowed down by inelastic collisions with the atoms inside a moderator material. At a reactor, thermal neutrons are generated at a steady rate by using a moderator kept at T = 293 K and they emerge with a Maxwellian velocity distribution. At a spallation source, the thermal neutrons are generated in finite time pulses and are slowed-down by moderation. Different neutron energy distributions can be obtained using different types of moderators kept at different temperatures.

All the experiments presented in this thesis were performed at the neutron sources mentioned in the previous paragraph. In Chapter 3, the spontaneous magnon decay in $(5CAP)_2CuCl_4$ was investigated using the time-of-flight inelastic cold neutron spectrometer LET at the ISIS neutron source. The lifetime and blue-shift of the gap energy in the S=1 Haldane chain Y_2BaNiO_5 presented in Chapter 4 was studied using the neutron resonant spin-echo triple-axis spectrometer TRISP at the FRM-II reactor. For the study of the entanglement transition, magnetic ordering and high-field excitations in Cs_2CoCl_4 in Chapter 5 we used the cold diffractometer WISH at the ISIS neutron source and the triple-axis spectrometer RITA-II at SINQ.

2.4 Neutron Scattering Instruments

An experimental arrangement for neutron scattering is most often very complex, with a multitude of components that make up the measuring instrument with each component that has a very precise role in the whole process. A few examples include beam tubes and guides used to transport the neutron beam, monochromator crystals and chopper systems used to precisely define the properties of the incident beam such as wavelength and pulse length, spin-flippers and guide fields used for polarized neutrons and detectors used to detect neutrons in the scattered beam.

A traditional way of classifying neutron scattering instruments is in terms of elastic and inelastic scattering. For elastic scattering, the energy of the scattered neutron is the same as the energy of the incident neutron. The instruments that perform elastic scattering are called diffractometers. They are used to probe the static properties of materials, such as crystal and magnetic structure and ordering. For inelastic scattering, where the energy dependence of the outgoing neutrons is necessary, the instruments are called spectrometers and they include time-of-flight, triple-axis, backscattering and spin-echo machines. They are used to probe the dynamical properties of materials which include excitations of the crystal and magnetic structure and also dynamics of molecules. In the following subsections we will briefly describe the particular categories of instruments that were used for collecting data presented in this thesis.

The Time-of-Flight Spectrometer

The time-of-flight (TOF) method makes use of the accurate measurement of the time it takes a neutron to travel a fixed distance in space. Spectrometers that use the

TOF method are divided into two categories: direct geometry and indirect geometry instruments. For direct geometry, the incident neutron energy is kept fixed and the outgoing neutron energy is analysed. For indirect geometry, the incident energy is varied and the outgoing neutron energy is kept fixed. In the following we only describe direct geometry instruments.

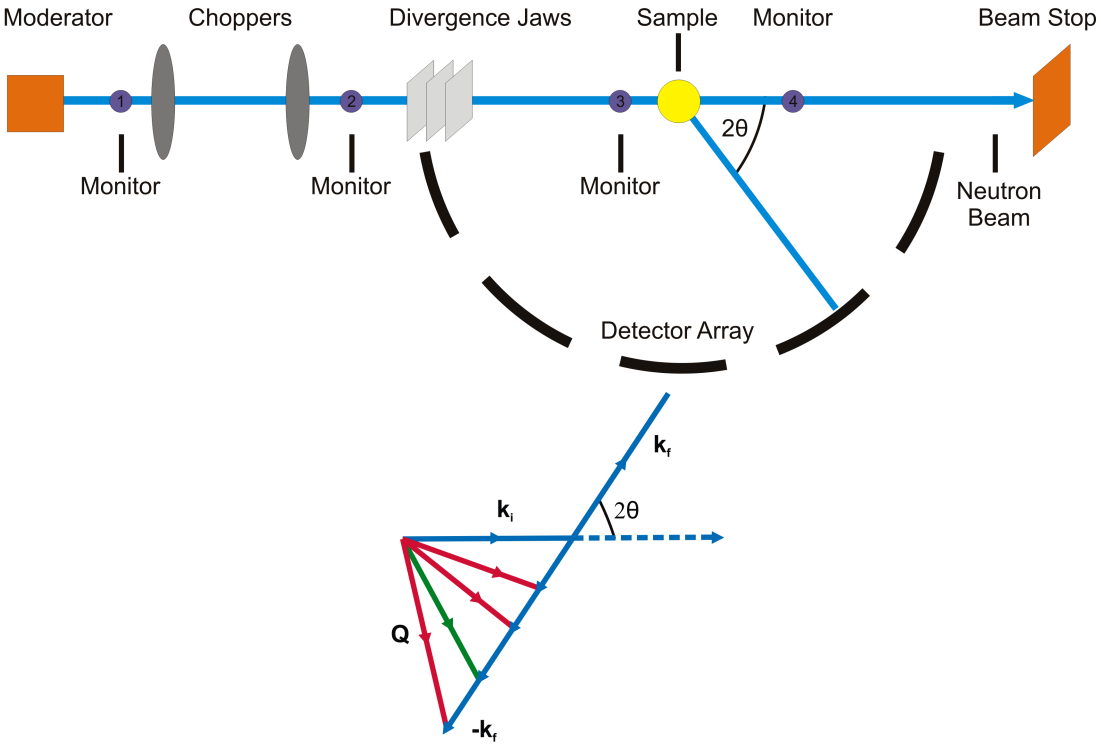

Figure 2.2: Top: Direct geometry schematic time-of-flight spectrometer with main components shown. The neutrons travel along the blue lines for a given scattering process. Bottom: The scattering triangle showing elastic and inelastic processes for a detector positioned at 2θ with respect to the incident beam. For a set of different k_f's, different Q vectors are measured in the same detector but at different times of flight.

Time-of-flight spectrometers are divided into the primary spectrometer (instrument components before the sample) and secondary spectrometer (instrument components after the sample). In the primary spectrometer, the polychromatic incident neutron beam which comes from the moderator is monochromatised which fixes the incident neutron energy to E_i. At LET, the monochromatisation is performed with a double-disk chopper. Pulse removal choppers are used to prevent high energy neutrons from the spallation process to reach the sample position. These choppers run at the frequency of the proton source which is 10 Hz. Frame overlap choppers

are used to prevent slow neutrons and fast neutrons from a later pulse to reach the detectors at the same time and give spurious features in the data. A schematic presentation of a general TOF spectrometer with its various elements is given in the top part of Fig. 2.2.

The incident energy of the incoming neutrons is

$$E_i = \frac{\hbar^2 k_i^2}{2m_n} \tag{2.26}$$

The time needed by these neutrons to travel the distance between the monochromating chopper and the sample L_{ms} is given by

$$t_{ms} = \frac{L_{ms}}{v_i} \tag{2.27}$$

where v_i is the incident neutron velocity. Also the momentum k_i of the neutron is related to t_{ms} by

$$t_{ms} = \frac{m_n L_{ms}}{\hbar k_i} \tag{2.28}$$

The overall time t_{tot} it takes the neutron to travel from the monochromating chopper to the detector is being measured and so the time it takes the scattered neutrons to travel from the sample to the detector is

$$t_{sd} = t_{tot} - t_{ms} \tag{2.29}$$

The momentum of the scattered neutron is thus

$$k_f = \frac{m_n L_{sd}}{\hbar t_{sd}} \tag{2.30}$$

and the final energy is

$$E_f = \frac{\hbar^2 k_f^2}{2m_n} \tag{2.31}$$

with the energy transfer

$$\hbar\omega = E_i - E_f \tag{2.32}$$

The wave vector transfer Q varies with energy transfer (for fixed E_i) according to

$$\frac{\hbar^2 Q^2}{2m_n} = 2E_i - \hbar\omega - 2\cos(2\theta)\sqrt{E_i(E_i - \hbar\omega)} \tag{2.33}$$

and gives the parabolic dependency given in Fig. 2.3. It shows the typical detector coverage in the $(\mathbf{Q}, \omega)$ space of the instrument.

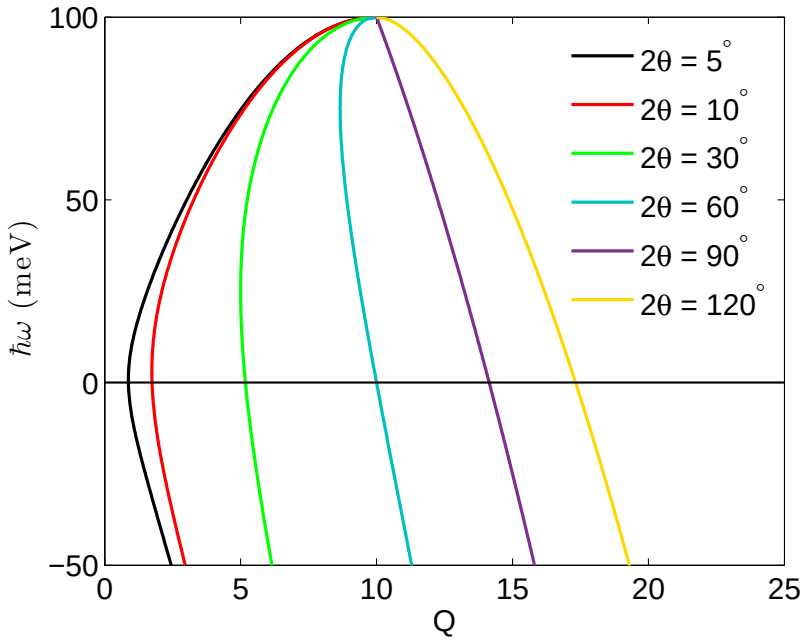

Figure 2.3: Energy transfer and momentum transfer measured with a direct geometry spectrometer at fixed detector positions at $2\theta = 5°$, $10°$, $30°$, $60°$, $90°$ and $120°$. The incident neutron energy is fixed at 100 meV.

The neutron TOF technique can be implemented in practice because in the thermal energy range neutrons have typical velocities of a few km/s and by travelling for a few meters their flight time can be determined quite accurately with the help of modern advanced electronics.

LET is equipped with large area detectors which allow a large portion of the sample $(\mathbf{Q}, \omega)$ space to be measured in one go. The detectors are pixelated in the horizontal and vertical directions. At the time when we performed the experiment on CAPCC, LET had ^{3}He detectors covering scattering angles from $-10°$ to $+50°$ in the horizontal scattering plane and $\pm 30°$ in the vertical direction. Most recently LET has had its detector bank completed and now covers horizontal scattering angles from $-40°$ to $+140°$ thus making it ideal for the measurement of excitations in the full Brillouin zone.

LET allows for the measurement of three independent degrees of freedom, two spatial ones due to the horizontal and vertical coverage of the detectors, and time-of-flight. As the scattering function $S(\mathbf{Q}(h,k,l),\omega)$ is a four dimensional quantity with three components of wave vector transfer and energy transfer, this means that for a given sample orientation and incident energy, two of the components of wave vector transfer are intrinsically coupled between them and they are also coupled to energy transfer. This is the case for the data presented in Chapter 3 where due to the particular choice of sample orientation, the h-component of wave vector transfer and the energy transfer depend implicitly on the k-component of wave vector transfer. To decouple these variables one would need to perform a series of measurements with different sample orientations and combine them. This measuring strategy is employed for experiments where the full four dimensional datasets of $S(\mathbf{Q},\omega)$ are required and is called a Horace scan.

The energy resolution at LET depends on the energy linewidths defined by the moderator and the monochromating chopper. The resolution is set by a particular choice of frequency and phase of the monochromating chopper. The faster it rotates, the better the energy resolution but less neutrons get to pass through it. There is a trade-off between the energy resolution and the intensity of the neutron beam at the sample position so during an experiment a compromise is always made, which is dependent on the aim of the experiment.

The Triple-Axis Spectrometer

Data presented in the second half of Chapter 5 was collected on the triple-axis spectrometer RITA-II (see Fig. 2.4) at the Paul Scherrer Institute in Switzerland. RITA-II is a versatile neutron scattering instrument used to probe excitations in solids. Its increased flexibility comes from the fact that one is able to configure the instrument to focus on measuring at specific points in $(\mathbf{Q},\omega)$ space. This is achieved with the help of three degrees of freedom (axes) which allow for independent rotations of the monochromator, sample and analyser, around a vertical axis. The monochromator crystal uses Bragg scattering to select incident neutrons of a certain wavelength from the broad distribution that comes from the moderator, with reflections from pyrolitic graphite (PG) and Si being most used in practice. For intensity considerations, the monochromator crystals are not perfect but are manufactured with a finite mosaic of a few tens of arcminutes which allows a finite range of neutron wavelengths to pass through. The analyser is very similar to the

monochromator and has the role of selecting a given wavelength from the scattered neutron beam. Both the monochromator and analyser are made up of several small plates mounted on benders which can be rotated around a horizontal and vertical axis to give a horizontal and/or vertical focusing of the neutron beam depending on the requirements of the experiments. Higher order scattering is suppressed by energy selective filters such as cooled Be or BeO. The scattered neutrons are detected using a position sensitive area ^{3}He detector positioned after the analyser.

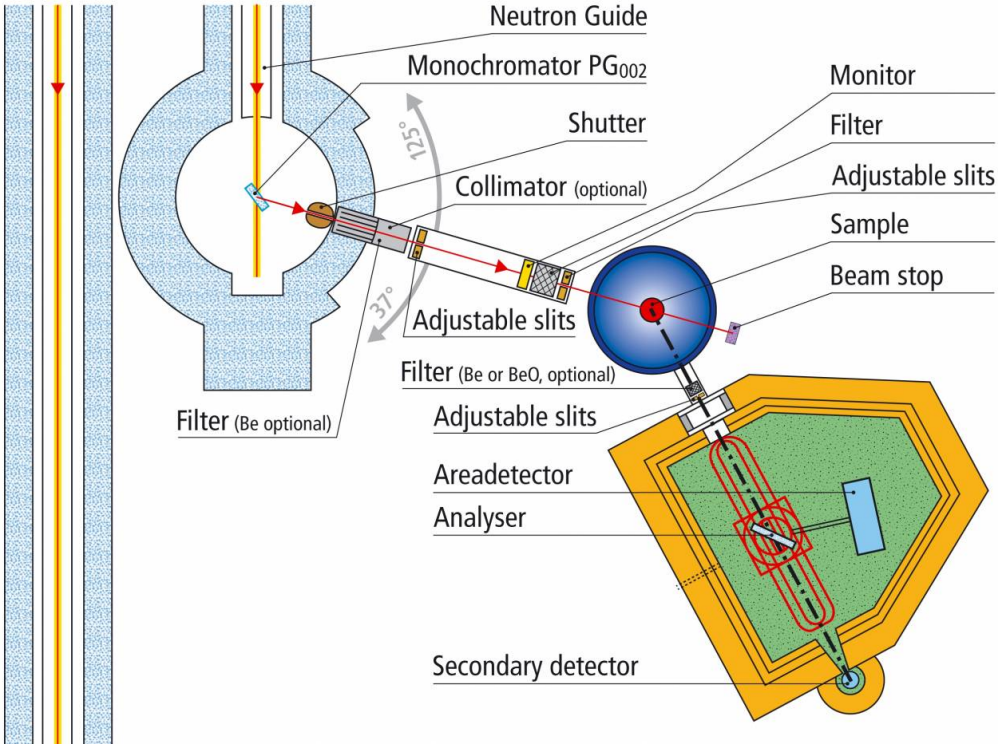

Figure 2.4: Schematic representation of the RITA-II triple-axis spectrometer at the Paul Scherrer Institute. Taken from the PSI website.

The finite beam divergence and mosaicity of the monochromating and analyser crystals, together with sample imperfections, lead to uncertainties in the neutron wavevector which in turn lead to the measurement of a finite volume in $(\mathbf{Q}, \omega)$ space which is centred on the nominally chosen $(\mathbf{Q}_0,\omega_0)$. The effective volume measured is described by the resolution function of the TAS [31–33]

$$\mathrm{R}(\mathbf{Q} - \mathbf{Q_0}, \omega - \omega_0) = \mathrm{R}_0 \exp(-\frac{1}{2}\Delta\nu \mathrm{M} \Delta\nu) \tag{2.34}$$

where $\Delta\nu$ is a four-vector that depends on the difference from the nominal setting

and M is a 4×4 matrix that depends on k_i, k_f, $2\theta_s$ as well as sample imperfections. The measured intensity is then a convolution of the sample scattering function and the resolution function

$$I(\mathbf{Q_0}, \omega_0) = \int d\omega d\mathbf{Q} R(\mathbf{Q} - \mathbf{Q_0}, \omega - \omega_0) S(\mathbf{Q}, \omega) \tag{2.35}$$

The resolution volume determines the energy and Q resolutions and also the scattered intensity at the detector. The smaller the volume, the better the resolution but the worst the intensity.

The NRSE-TAS Spectrometer

Neutron Spin-Echo (NSE) is a polarised neutron inelastic scattering technique which has the highest attainable energy resolution, usually in the μeV range, thus outperforming a standard triple-axis instrument, with typical resolution in the meV range, by about two orders of magnitude. It is very well suited for studies of excitation lineshapes, mode doublets with small energy separation and high resolution Larmor diffraction. Originally, the idea of spin-echo came from F. Mezei [34,35] who showed that the velocity of the neutron can be encoded in the Larmor precession angle of its spin, around an applied static magnetic field. The energy transfer is determined by measuring the difference in the velocity of the neutron before and after the sample. A typical layout of a spin-echo spectrometer is similar to a triple-axis, with the difference that between the monochromator and sample and between the sample and analyser, there are constant magnetic field precession regions known as the encoding and decoding arms. As a neutron passes through the first region, its spin precesses about the field direction and the number of revolutions is encoded in the precession phase angle. For fixed length regions, the accumulated phase depends only on the neutron velocity and the strength of the field. For the case of elastic scattering, where the velocity change is zero, the precession angle in the second field region is the same as in the first region and the so-called echo is measured. A totally polarised neutron beam with a fairly wide velocity distribution before the first arm, will become totally depolarized at the exit of the arm. This happens due to the fact that the precession angle is different for different velocity neutrons. After scattering at the sample, spins are flipped by π (either by a flipper or by the sample itself) and enter the second arm. If elastic scattering occurs at the sample and neglect other depolarising effects, then, at the exit of the second region, the beam regains

its initial polarisation and the echo signal is measured. If the scattering is inelastic, then there will be a change in the velocity of neutrons and thus at the exit of the second arm, the beam will not recover full polarisation. The final polarisation, which is the mean of the cosine of the difference in phase in the first and second arms, is measured at the analyser. The outgoing beam mean polarisation is proportional to the intermediate scattering function of the system $I(\mathbf{Q}, t) = \int S(\mathbf{Q}, \omega) e^{-i\omega t} d\omega$ which is the time-Fourier transform of $S(\mathbf{Q}, \omega)$.

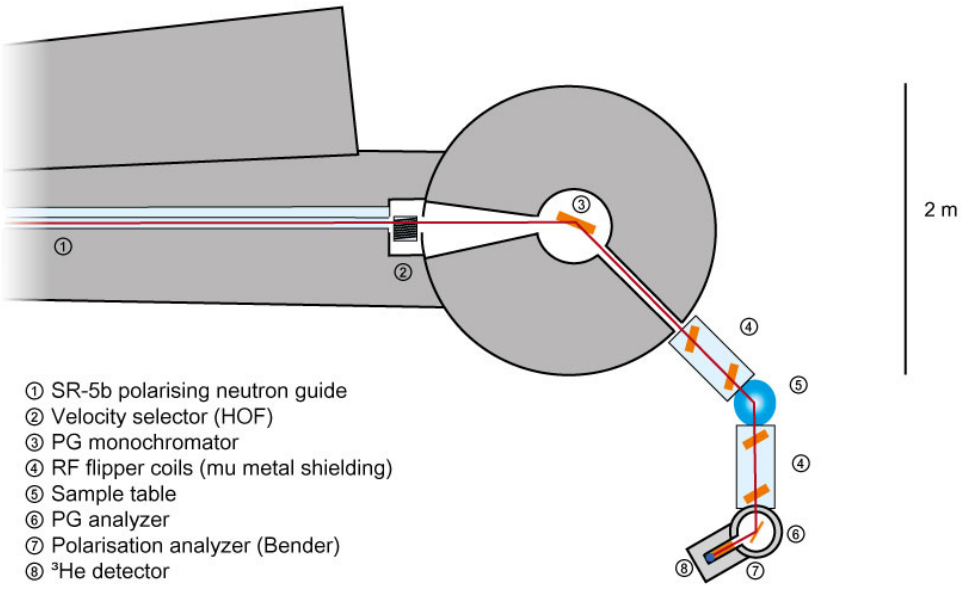

Figure 2.5: Schematic representation of the NRSE-TAS spectrometer TRISP at the FRM-II reactor at the Heinz Maier-Leibnitz Zentrum. Taken from the FRM-II website.

TRISP at the FRM-II uses the Neutron Resonant Spin-Echo (NRSE) [36] variation of NSE that consists of replacing the static coils in the two spectrometer arms by radio-frequency RF coils. It provides two times better energy resolution over the same arm lengths. Each spectrometer arm consists of either 2 or 4 RF coils and a region of zero field between them. Each arm is enclosed in mu-metal shielding to screen against external sources of beam depolarisation. The schematic representation of TRISP is given in Fig. 2.5.

For NRSE the energy resolution is decoupled from the Q resolution. This allows for a broad wavelength distribution of incident neutrons in cases where high Q resolution is not crucial. Typical distributions are in the range $\Delta\lambda/\lambda = 10\% - 20\%$.

The energy resolution, in the μeV range, depends on the spectrometer arm length and strength of the applied magnetic field. The more revolutions the neutron spin makes around the magnetic field, the more sensitive the phase is to small changes in the neutron velocity or energy transfer.

The Single Crystal TOF Diffractometer

WISH is a cold neutron powder and single-crystal diffractometer used for determining the nuclear and magnetic structures by measuring the intensity of elastically scattered neutrons. This instrument is similar to the TOF spectrometer which was presented earlier, with the major difference that the incident neutrons have a wide spectral distribution and that the energy of the scattered neutrons is not analysed, as one is only interested in elastic scattering events at the sample. The incident neutron pulse is cleaned from unwanted fast neutrons and other high-energy particles which result from the spallation process by a system of choppers. An elliptical guide is used to transport and focus the beam towards the sample position. The beam focusing is additionally controlled by a set of divergence jaws and a beam snout placed just before the sample. Scattered neutrons are detected with the help of ^{3}He position sensitive pixelated area detectors which surround the sample and cover almost 360° in the horizontal scattering plane and ±13° vertically.

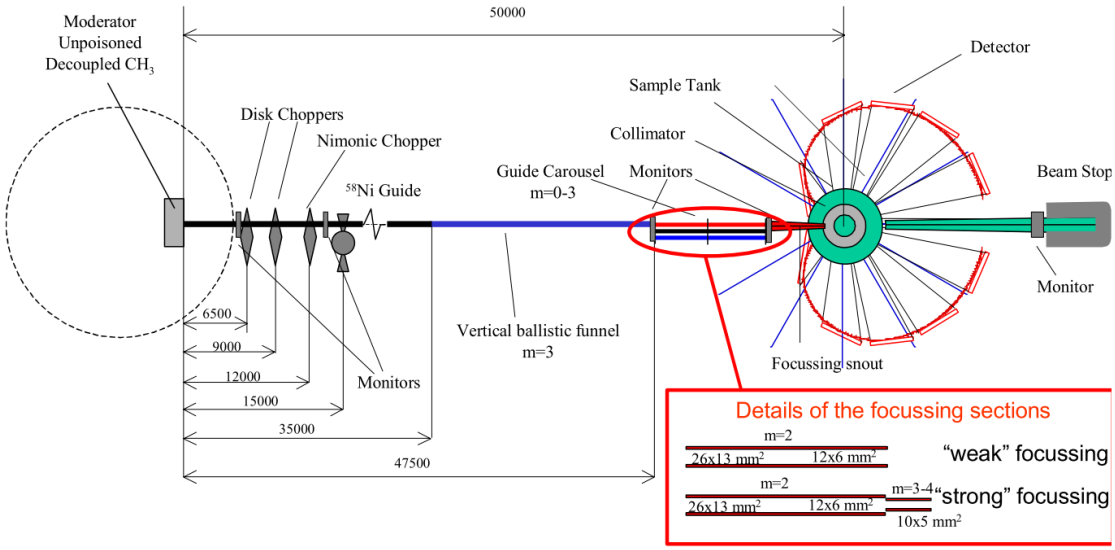

Figure 2.6: Schematic representation of the WISH diffractometer at ISIS at the Rutherford Appleton Laboratory. Taken from WISH Science Case.

The wavelength of a neutron can be calculated if one knows the time it takes for it to travel along a path of known length. The de Broglie relation gives

$$\lambda = \frac{\mathrm{h}}{\mathrm{m_n v}} \tag{2.36}$$

where the velocity of the neutron is $\mathrm{v} = \mathrm{L/t}$, with L being the flight path of the neutron and t the time-of-flight. The wavelength is given by

$$\lambda = \frac{\mathrm{h}}{\mathrm{m_n}} \frac{\mathrm{t}}{\mathrm{L}} \tag{2.37}$$

and this relates to the d-spacing via Bragg's law

$$\mathrm{d} = \frac{\mathrm{h}}{2\mathrm{m_n}} \frac{1}{\sin(\theta)} \frac{\mathrm{t}}{\mathrm{L}} \tag{2.38}$$

where θ is the angle between the incident neutron momentum and the family of crystallographic planes which are separated by distance d. This equation shows that one can scan the d-spacing by keeping θ fixed (the sample orientation) and varying the incident neutron wavelength λ, which is exactly what is done in the case of TOF diffraction.

Chapter 3

Evidence for Field-Induced Magnon Decay in $(5CAP)_2CuCl_4$

In this chapter we study the effects of magnon-magnon interactions on the excitation spectrum of the quasi-2D square lattice quantum Heisenberg antiferromagnet using high-resolution time-of-flight neutron spectroscopy. We start with a general presentation of the Heisenberg antiferromagnet focusing on the two-dimensional case. We review the properties of the two-dimensional Heisenberg antiferromagnet in its quantum limit S=1/2 and on a square lattice and make a distinction between the model in zero and finite magnetic field. In section 3.2, we introduce the concept of spontaneous magnon decay on the square lattice and discuss the implications of a finite inter-layer coupling on the possibility of experimentally observing decays. Next, we present currently known properties of $(5CAP)_2CuCl_4$. In section 3.4, we describe the experimental LET neutron scattering setup and in section 3.5, we show spin-wave data collected in the polarised phase, at B = 7 T, from which we extract the parameters of the magnetic Hamiltonian of $(5CAP)_2CuCl_4$. In section 3.6, we show and discuss the results of data collected in the intermediate-field (B = 3.35 T $= 0.85B_s$) canted phase with the aim of investigating the theoretically predicted decay dynamics. We end with the conclusions and outlook, suggesting a possible definitive experiment meant to allow for a fully quantitative investigation of spontaneous magnon decay in the case of $(5CAP)_2CuCl_4$.

3.1 Introduction

The Heisenberg model of magnetism is the traditional model used to describe magnetic interactions. Its Hamiltonian is written as

$$\hat{\mathcal{H}} = \sum_{<i,j>} J_{ij} \mathbf{S}_i \cdot \mathbf{S}_j \tag{3.1}$$

where the interaction between the spins J_{ij} is isotropic in spin space and the summation is taken over pairs of spins, each interaction being counted once. If the exchange interaction is ferromagnetic then $J_{ij} < 0$ and if it is antiferromagnetic then $J_{ij} > 0$. The following discussion is based on the simplified version of the model, where only nearest neighbours are allowed to interact via the isotropic exchange $J_{ij} = J$. Viewed from a classical point of view when spins are considered as unit vectors, the ground state of the ferromagnetic model is reached when all spins point along a given direction and parallel to each other, whereas for the antiferromagnetic model, the spins point along the same direction but adjacent spins are anti-parallel. These states are known as the fully polarised and Néel states respectively. If the vector character of spins is replaced by quantum mechanical operators, then one ends up with the quantum model and quite different conclusions result. The Hamiltonian reads

$$\hat{\mathcal{H}} = J \sum_{<i,j>} \frac{1}{2}(\mathbf{S}_i^+ \mathbf{S}_j^- + \mathbf{S}_i^- \mathbf{S}_j^+) + \mathbf{S}_i^z \mathbf{S}_j^z \tag{3.2}$$

where the spin operator components have been written in terms of the ladder operators ($\mathbf{S}^+$ and $\mathbf{S}^-$) and the interaction is taken only between nearest neighbours. The analysis of the ground state shows that for ferromagnetic interactions the state $|0\rangle = |\ldots\uparrow\uparrow\uparrow\ldots\rangle$ is an eigenstate of the Hamiltonian and is in fact the ground state. It coincides with the classical fully polarised state. For the antiferromagnet though, the analogue of the classical Néel state $|\text{Néel}\rangle = |\ldots\uparrow\downarrow\uparrow\downarrow\ldots\rangle$ is not the true ground state. This is due to the fact that the application of the $\frac{1}{2}(\mathbf{S}_i^+\mathbf{S}_j^- + \mathbf{S}_i^-\mathbf{S}_j^+)$ operator on $|\text{Néel}\rangle$ gives rise to finite overlap between the Néel state $|\text{Néel}\rangle$ and states with one spin reversed $|\ \ldots\uparrow\downarrow\downarrow\uparrow\ldots\rangle$ with respect to the Néel state. The induced transitions between the two states means that the Néel state is not an eigenstate of the Hamiltonian and in addition they lead to fluctuations in the components of spin which has the effect of changing the values of physical observables such as the ground state energy, staggered magnetisation, perpendicular susceptibility with

respect to their values in the classical Néel state.

One important aspect in the study of the Heisenberg antiferromagnet is the consideration of quantum fluctuations [37]. A measure of their strength is given by the spin modulus in the classical and quantum cases. Classically, $|\mathbf{S^2}| = S^2$ whereas quantum mechanically, the expectation value $\langle \mathbf{S^2} \rangle = S(S+1)$. The ratio $S(S+1)/S^2 = 1 + 1/S$ suggests that quantum fluctuations become more important as the quantum $S = 1/2$ limit is approached. Their relative strength also increases with decreasing the number of nearest neighbours [38]. For example, it is well known [39] that in the case of the $S = 1/2$ Heisenberg antiferromagnetic chain there is no long range magnetic order in the ground state even at zero temperature, due to the fact that quantum fluctuations are strong enough to overcome any ordering tendencies. In contrast, the three-dimensional $S = 1/2$ Heisenberg antiferromagnet, orders at finite temperature [40,41]. If one assumes that there is a continuous evolution from one-dimension to three-dimensions by gradually turning on inter-chain and inter-planar couplings, two-dimensions can be considered the crucial place where order starts to develop. The case of the two-dimensional $S = 1/2$ quantum Heisenberg antiferromagnet is then important to study as it is placed at the transition between order in 3D and disorder in 1D.

In the extended review of Manousakis [42], the properties of the S=1/2 square lattice Heisenberg antiferromagnet are discussed in the context of high-Tc superconductors based on square lattices of S=1/2 copper ions. At zero temperature, the influence of zero-point fluctuations is to disorder the system and renormalise the value of the relevant physical observables away from their value in the corresponding classical system. For example, the sublattice mean spin is reduced to about 60% of its classical value [42]. The model lacks an exact solution but there is strong analytical and numerical evidence [42] that at zero temperature the effect of the zero-point fluctuations is not strong enough to destroy the long-range magnetic order, despite the low dimensionality and low spin value. There is proof [42] that the ground state is a singlet with $S^z_{tot} = 0$ which implies that states such as the resonating valence bond [43] could describe the ground state. The resonating valence bond was introduced by Anderson in 1973 to explain the ground state of the triangular lattice Heisenberg antiferromagnet and has come into focus again in an attempt to gain insight into the physics of high-Tc superconductors. At finite temperature the long range order of the S=1/2 square lattice Heisenberg antiferromagnet is destroyed by thermal fluctuations [44] and the correlation length, for $k_B T << J$, has

a $\xi(T) = C\exp(\alpha J/k_B T)$ temperature dependence. The excitations are bosons and at low T and for $\lambda < \xi$, they are well-defined spin-waves. In zero-field there is no energy gap from the ground state to the first excited state but as a magnetic field is being applied, a gap starts to develop in the excitation spectrum and the system moves towards saturation.

The spin dynamics of the S=1/2 square lattice Heisenberg antiferromagnet have been studied in detail by several theoretical methods which include analytic approaches (spin-wave theory [37,45–50], Schwinger boson mean-field theory [51], series expansion [52, 53]), and numerics (quantum Monte Carlo [54, 55], renormalisation group [56]). Spin-wave theory has been successful in predicting the low energy excitation spectrum with first results from Anderson (semi-classical) and Kubo (based on Holstein-Primakof formalism) [37, 45] that were proven to be equivalent when conventional or linear spin-wave theory was considered. The resulting one-magnon spin-wave dispersion is given as

$$\omega_{\mathbf{q}} = 4JS\sqrt{1-\gamma_{\mathbf{q}}^2} \tag{3.3}$$

where the exchange coupling is given by J and the lattice sums are given as

$$\gamma_{\mathbf{q}} = \frac{1}{z}\sum_{\boldsymbol{\delta}} \exp(i\mathbf{q}\boldsymbol{\delta}) \tag{3.4}$$

with δ being the vectors connecting interacting neighbours and z the number of neighbours. This dispersion is plotted in Fig. 3.1 (black line) together with the square lattice Brillouin zone. The dispersion has the expected linear behaviour close to the magnetic zone centre M (π, π) point and no dispersion along the magnetic zone boundary (from $(\pi, 0)$ to $(0, \pi)$).

The expansion to first order in the 1/S parameter by Oguchi [47] predicts uniform positive rescaling of the dispersion $\omega_{\mathbf{q}}^1 = Z_c^1 \times \omega_{\mathbf{q}}$ with $Z_c^1 = 1.158$. As the 1/S approximation takes into account interactions between excitations (zeroth order approximation assumes ideal non-interacting excitations), the almost 16% rescaling of the dispersion shows that contribution from spin-wave interactions is non-negligible an has to be taken into consideration when extracting exchange parameters from experimental data. The second order $1/S^2$ corrections were computed by Igarashi [48] and they result in a positive almost uniform correction to the harmonic dispersion with $Z_c^2 = 1.18$. The $1/S^2$ dispersion is gapless and has Goldstone modes at the Γ (0,0) point and the M (π, π) point. Notable deviations from a uniform rescaling

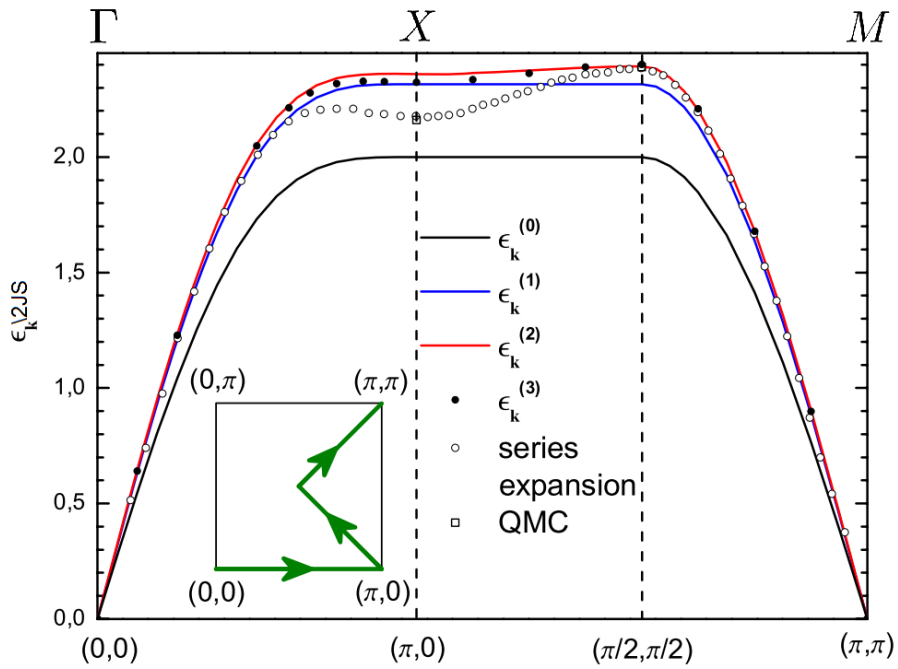

Figure 3.1: Spin-wave theory predictions for the single-magnon dispersion of the S=1/2 Heisenberg antiferromagnet on a square lattice along a high-symmetry path of the Brillouin zone. $\epsilon_{\mathbf{k}}^{(i)}$ represents the dispersion calculated within the ith order in the 1/S expansion so that $i = 0$ corresponds to the classical or linear spin-wave result. For the $1/S^2$ approximation, along the $(\pi/2, \pi/2) - (\pi, \pi)$ line, the dispersion is uniformly renormalised by $Z_c = 1.18$ with respect to the linear approximation. Along the magnetic zone boundary $(\pi, 0) - (\pi/2, \pi/2)$, there is a small dispersion evidenced by an energy dip at $(\pi, 0)$. The linear approximation predicts no dispersion along the zone boundary. The Brillouin zone of the square lattice is plotted in the inset together with the convention for notation of high-symmetry points. The Γ point corresponds to $(0, 0)$, M to (π, π), X to $(\pi, 0)$ and the middle of the Γ-M line corresponds to the $(\pi/2, \pi/2)$ point. Results of series expansion around the Ising limit and quantum Monte Carlo are also shown [57] and [55], respectively. Taken from [58].

of the dispersion are along the magnetic zone boundary where the energy of the X $(\pi, 0)$ point is $\approx 1\%$ smaller than that of the $(\pi/2, \pi/2)$ point. Syromyatnikov [58] obtained a magnetic zone-boundary dispersion of $\approx 3.2\%$ by expanding spin operators up to the $1/S^3$ order. His results show that the spin-wave expansion converges slowly for the $(\pi, 0)$ point while it is well behaved for the $(\pi/2, \pi/2)$ point. The effect of magnon-magnon interactions is strongest for short-wavelength excitations close to $(\pi, 0)$.

Canali et al. [49,50] approached the problem by using the Dyson-Maleev formal-

ism to second order in 1/S and found generally consistent results with Igarashi [48]. They studied the dispersion across the whole Brillouin zone and found a small 3% dispersion along the magnetic zone boundary which connects the $(\pi/2, \pi/2)$ and $(\pi, 0)$ points. The series expansion from the Ising limit of Singh [52] gives values for the spin stiffness constant (ρ_s) and perpendicular susceptibility ($\chi_\perp$). Using the hydrodynamic relation, the spin-wave velocity is computed as $c^2 = \rho_s/\chi_\perp$, which results in $Z_c^{se} = 1.18$, in excellent agreement with the results of Igarashi [48] and Canali et al. [49,50]. In addition, Singh [52] found a 7% dispersion along the antiferromagnetic zone boundary which is approximately twice the value obtained from the Dyson-Maleev treatment. Quantum Monte Carlo has also been used by Syljuasen and Ronnøw [59] and by Sandvik and Singh [55] to study the excitation spectrum of the two-dimensional S = 1/2 square lattice Heisenberg antiferromagnet. Syljuasen and Ronnøw [59] calculated the energies of the single magnon modes at $(\pi, 0)$ and $(\pi/2, \pi/2)$ for lattices up to 32×32 spins. By taking the thermodynamic limit, they ended up with the T = 0 result which predicts a 6% lower energy at $(\pi, 0)$ compared to $(\pi/2, \pi/2)$. An important point which became clear from their study is that the dispersion along the magnetic zone boundary is a many particle effect as it was not observable for lattices up to 8×8. Their result is in good agreement with the series expansion investigation of Singh and Gelfand [53]. Sandvik and Singh [55] have used quantum Monte Carlo and numerical analytic continuation to study the high-energy spin excitations and found a 10% dispersion between the two zone boundary points. A nice comparison between different parameters computed using several theoretical approaches can be found in Table 1 of the PhD thesis of Dr. Niels Christensen [60].

Experiments on a few realizations of the S=1/2 square lattice Heisenberg antiferromagnet [61–65] have all identified the same general features in the excitation spectrum. These include an almost uniform renormalisation of the single-magnon energies and a dispersion along the magnetic zone boundary. Christensen et al. [2] have measured the spin excitation spectrum of copper formate tetradeuterate (CFTD) and confirmed that the single magnon energies at $(\pi, 0)$ are about 7% lower than at $(\pi/2, \pi/2)$. They were able to extract the intensities of the modes and found a surprising 40% drop in intensity at $(\pi, 0)$ as compared to $(\pi/2, \pi/2)$, which is a severe deviation from the predictions of linear spin-wave theory [37,45]. This intensity anomaly is qualitatively explained by a variational theory that mixes Néel wave functions with resonating valence bond wavefunctions [66,67] and goes hand in hand with the consideration that the ground state is described as a combination of a classical

Néel state on top of which quantum fluctuations are added in the form of resonating valence bond states [2,68]. Using polarised neutron scattering Christensen et al. [2] were also able to identify multi-magnon continuum scattering for the first time. All spectral weight corresponding to the continuum at the (π, π) point was contained in the longitudinal channel and was attributed to classical two-magnon processes. In contrast, the high energy continuum measured at the $(\pi, 0)$ and $(\pi/2, \pi/2)$ points is not well described by the classical two-magnon spin-wave theory which assumes scattering due to classical non-interacting pairs of magnons. A better description of the continuum is given by the quantum Monte Carlo prediction of Sandvik and Singh [55] but it does not give a physical insight of why the classical two-magnon theory fails. Huberman et al. [69] performed a neutron scattering experiment on the classical S=5/2 square lattice Heisenberg antiferromagnet Rb_2MnF_4 and found a weak $\approx 1\%$ dispersion along the magnetic zone boundary which was not attributed to quantum corrections to the Néel-type ground state but was suggested to be due to finite next nearest neighbour interactions. They also measured a weak continuum at the zone boundary which was attributed to scattering by pairs of non-interacting spin-waves. These features suggest that the anomalies identified in the excitation spectrum of the S=1/2 square lattice Heisenberg antiferromagnet are related to the strength of quantum fluctuations in the ground state.

Until recently it was thought that the excitations of the S=1/2 square lattice Heisenberg antiferromagnet are well-defined magnons [42]. In 2010, Headings et al. [70] suggested that the anomalous lineshape they observed in La_2CuO_4 could be due to the decay of the one-magnon excitations into pairs of high energy fractional spinon excitations. In a recent Nature Physics publication, Dalla Piazza et al. [5] have shown that the observed isotropic scattering continuum at the $(\pi, 0)$ zone boundary point in CFTD can be attributed to fractionalisation of magnons into pairs of independently propagating spinon excitations which are the analogue of what is observed in the quantum Heisenberg antiferromagnetic chain [4, 71, 72]. In the quantum Heisenberg antiferromagnetic chain the magnetic excitations are deconfined fractional S=1/2 spinon excitations that lead to a highly non-classical neutron scattering spectrum dominated entirely by a continuum which is attributed to scattering from an even number of spinons. It is well known that the excitations from a resonating valence bond state are fermionic excitations and so this recent discovery of Dalla Piazza et al. [5] comes to support the original work of Anderson [73] who proposed the resonating valence bond state to play a major role in the

physics of high-Tc cuprate superconductors.

The S=1/2 square lattice Heisenberg antiferromagnetic model in zero field is a fundamental model in magnetism which is fairly well understood. In contrast, the same model in a magnetic field has attracted attention only in the past ≈15 years due to a breakthrough in synthesis of novel materials [74–77] which are good realisations of the model and have small exchange constants that allow experimental investigations in all interesting field regimes. Several theoretical investigations [8–10] have all revealed anomalous spin dynamics of the S=1/2 square lattice Heisenberg antiferromagnet for a magnetic field region close to saturation. They predict an instability of the one-magnon excitations with respect to decay into two-magnon excitations for magnons with certain momenta. This spontaneous decay [8] occurs as a direct consequence of the canted antiferromagnetic spin structure which is induced by the application of a magnetic field perpendicular to the two-dimensional planes. In the following section we give more details about the origin of this instability for the pure two-dimensional case and for a finite inter-layer coupling and then present specific neutron scattering predictions arising from this effect.

3.2 Magnon Decay on the Square Lattice

The spin dynamics of the Heisenberg antiferromagnet on a square lattice have been studied extensively. Theoretical predictions describe quite well the measured excitation spectra for several different materials [2, 62–65, 78] which are good realisations of the model. In most of the Brillouin zone, the low energy excitations are well-defined magnons described accurately by classical spin-wave theory with quantum corrections. Deviations from spin-wave theory, which are due to strong influence of quantum fluctuations, include a dispersion along the magnetic zone boundary (MZB), a multi-magnon longitudinally polarised continuum observed at the zone centre point (π, π) (CFTD [2]) and an isotropic continuum at the $(\pi, 0)$ point which is attributed [5] to high energy pairs of spinons.

The fairly recent synthesis of novel compounds [74, 76, 77, 79] that can be experimentally investigated in high-field regimes close to saturation has presented as an opportunity to study the effects of an applied magnetic field on the spin dynamics of the Heisenberg antiferromagnet on a square lattice. This scenario was first considered by Zhitomirsky and Chernyshev [8] using an analytical approach and, subsequently, by Syljuåsen [9] using Quantum Monte Carlo and Lüscher and

Lauchli [10] using exact diagonalisation. The spin-wave theory approach predicts that in the case of a non-collinear arrangement of spins, a cubic interaction term (see Eq. 3.6) in the Hamiltonian which is absent in zero field [11] due to symmetry considerations, generates instabilities of the one-magnon states towards decay into two-magnon continuum for fields close to the saturation field. The spin-wave prediction is confirmed by numerical studies [9,10]. The Hamiltonian for the case of an applied field reads

$$\mathcal{H} = \mathrm{J} \sum_{<\mathrm{i,j}>} \mathbf{S}_\mathrm{i}\mathbf{S}_\mathrm{j} - \mathrm{g}\mu_\mathrm{B}\mathrm{B} \sum_\mathrm{i} \mathrm{S}_\mathrm{i}^\mathrm{z} \tag{3.5}$$

where J is the antiferromagnetic exchange and the sum is restricted to nearest neighbours only. The magnetic field is applied along the z-direction, perpendicular to the 2D planes.

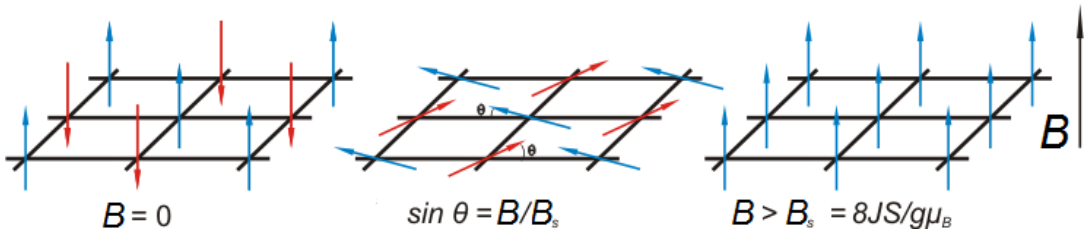

Figure 3.2: Classical field evolution of the ground state. At H = 0 spins are arranged in a Néel-type state and as the field is turned on, a spin-flop phase develops with spins canting out of the plane. By further increasing the field, spins gradually move towards the field direction and for $\mathrm{B} > \mathrm{B_s}$ they are all aligned parallel to the field.

In order to understand the origin of the decay effects, we first need to understand the evolution of the magnetic ordering. In zero field, the spin structure can be considered as classical Néel with spins aligned anti-parallel along the direction perpendicular to the 2D planes. As a magnetic field is applied perpendicular to the 2D planes, a spin-flop transition takes place, with the spins pointing perpendicular to the field, in the plane. As B is increased, spins cant towards the field direction and make an angle $\theta = \sin^{-1}(\mathrm{B}/\mathrm{B_s})$ (canting angle) with the 2D plane. By further increasing the field, the system gradually moves towards saturation ($\mathrm{g}\mu_\mathrm{B}\mathrm{B_s} = 8\mathrm{JS}$) and at $\mathrm{B_s}$, the spins have a parallel arrangement with the direction of the field (see Fig. 3.2 for an illustration of this spin structure evolution). Zhitomirsky and Nikuni [80] have studied the evolution of the spins in the canted phase and concluded that this classical picture remains valid and that the effect of quantum fluctuations

is to renormalise the value of the canting angle. In the canted phase, the spin-wave expansion and subsequent bosonisation of the spin Hamiltonian lead to the form

$$\mathcal{H} = \mathcal{H}_0 + \mathcal{H}_1 + \mathcal{H}_2 + \mathcal{H}_3 + \mathcal{H}_4 + \cdots \tag{3.6}$$

where the first term is the classical ground state energy who's minimization determines the canting angle as $\theta = \sin^{-1}(\mathrm{B}/\mathrm{B_s})$ and the second term which is linear in the creation and annihilation operators arises due to the canted spin structure and vanishes for this particular choice of the canting angle [11,81]. The third term $\mathcal{H}_2$ is the harmonic term which does not take into account interactions between magnons and its diagonalisation gives the classical dispersion. The cubic term $\mathcal{H}_3$ introduces to lowest order magnon-magnon interactions and physically corresponds to decay and recombination processes involving three magnons. The quartic term $\mathcal{H}_4$, which is present in zero field as well, involves magnon-magnon interactions with decay and recombination of four magnons. Terms larger than four in the bosonic operators are not included due to the fact that they do not affect the conclusions of the analysis that takes into account terms up to the quartic term inclusive. The explicit form of all these terms can be found in Ref. [81].

The prediction for the spin dynamics in the spin-flop phase is that for a field regime just below $\mathrm{B_s}$, more specifically for $\mathrm{B}^\star < \mathrm{B} < \mathrm{B_s}$ ($\mathrm{B}^\star = 0.76\mathrm{B_s}$), single-magnon states overlap with two-magnon states in a region of momentum space know as the decay region [81]. The coupling of transverse and longitudinal fluctuations which introduces cubic anharmonicities in the Hamiltonian, leads to instabilities of the single-magnon excitations towards decay into the two-magnon continuum. By computing the dynamical structure factors and the lifetimes of magnons in this field region, Mourigal et al. [82] showed that for S=1 and S=5/2, the magnons acquire a finite lifetime and they become damped in most of the Brillouin zone of the 2D square lattice. Such a behaviour was observed by Masuda et al. [83] who performed inelastic neutron scattering on the S=5/2 square lattice antiferromagnet $Ba_2MnGe_2O_7$. An even more dramatic effect is expected for the S=1/2 case [8, 11] where quantum fluctuations are strongest. A very detailed presentation of these concepts is given in the papers [82,84,85] and in the extended recent review of Zhitomirsky and Chernyshev [11].

Accurate predictions for the dynamical structure factor in the case of S=1/2 are given in Refs. [8–10, 86]. In the canted phase, the spectral weight distributes into

two distinct transverse magnon branches. One branch corresponds to fluctuations in the plane (perpendicular to the field) and the other one, which is shifted in momentum space by the antiferromagnetic ordering wave vector (π, π), corresponds to fluctuations along the field direction (out-of-plane). The relative intensity of the two modes changes as a function of the strength of the applied magnetic field. As the saturation field is approached, the in-plane mode dominates and the out-of-plane mode gradually disappears, an indication of suppression of the longitudinal fluctuations. For the pure 2D case, these modes are degenerate along the magnetic zone boundary. At the Γ point which corresponds to a uniform spin precession mode, the lineshape of the excitations remains well-defined [11, 81], indicative of classical spin-waves which are not affected by decays. At the M point which corresponds to a sound mode, the damping is predicted to be negligible. As the $(\pi/2, \pi/2)$ point is approached, there are dramatic changes to the lineshape. The one-magnon excitations lose coherence and become overdamped, almost indistinguishable from the higher energy two-magnon continuum. In contrast, the excitations at the $(\pi, 0)$ point, remain better defined [8, 9, 11, 81].

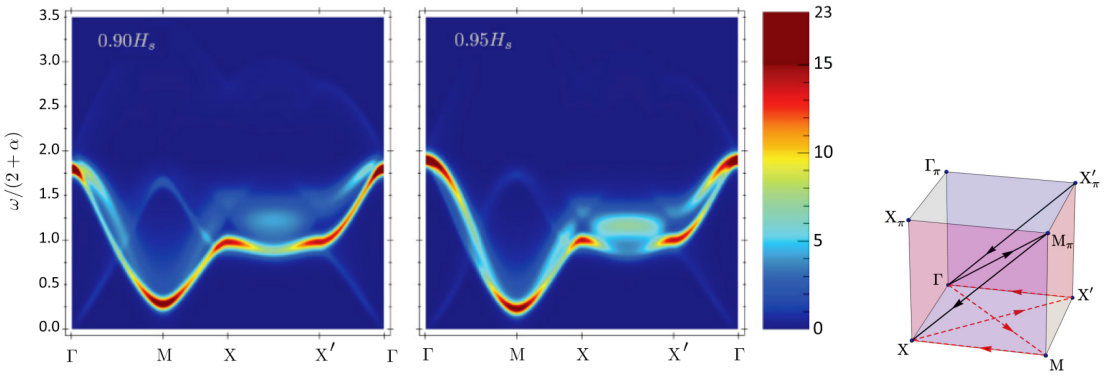

Figure 3.3: Calculated full dynamical structure factor for the S=1/2 quasi-2D square lattice Heisenberg antiferromagnet at $B = 0.9B_s$ (left colour plot) and $B = 0.95B_s$ (right colour plot) along a given reciprocal space path. Energy convolution was performed in ω with a Gaussian with standard deviation $\sigma = 0.1J$. The convention of labelling high symmetry points is given on the right side where we show 1/8 of the full 3D Brillouin zone. Taken from [87].

The case of a finite inter-layer coupling has been studied by Fuhrman et al. [87]. The order is described by the (π, π, π) wave vector and the Brillouin zone has a 3D character (see Fig. 3.3). Fuhrman et al. [87] compute the dynamical structure factor for the quasi-2D S=1/2 square lattice Heisenberg antiferromagnet

with moderate inter-layer coupling $\alpha = J'/J = 0.2$. As we show in section 3.5, this is relevant to $(5CAP)_2CuCl_4$, where the interlayer exchange has been measured to be $J'/J \approx 0.3$. The main conclusion of Fuhrman et al. [87] is that in the case of finite inter-layer coupling, although the strength of decays is reduced as compared to the corresponding pure 2D model, effects of intrinsic magnon decays remain sizeable up to $J'/J = 0.4$. In the case $J'/J = 0.2$, the dynamical structure factor shows completely unexpected features which are not predicted by classical spin-wave theory. Double peak features are identified along certain high-symmetry directions for a given strength of the applied field (see the $\Gamma - M$ and $X' - \Gamma$ lines in Fig. 3.3). For a fixed k_z plane, along the $X' - X$ line, the spectrum suffers strong modifications as in the 2D case. As one approaches the middle of the $X' - X$ line $(\pi/2, \pi/2, 0)$, there is a spectacular transfer of spectral weight from the one-magnon peak to the two-magnon continuum. For example, for $B = 0.9B_s$ the one-magnon mode is still well-defined but weak in intensity, whereas for $B = 0.95B_s$ the one-magnon mode disappears completely, with almost all the weight being transferred to the two-magnon channel.

In conclusion, the observation of broad, overdamped one-magnon modes around the $(\pi/2, \pi/2, 0)$ point as compared to better defined modes around $(\pi, 0, 0)$ should be considered a strong indication of the presence of intrinsic magnon decay. We will see in section 3.6 that the quality of the neutron data, together with the presence of continuum scattering and almost degenerate modes along the magnetic zone boundary makes the identification of magnon decay in $(5CAP)_2CuCl_4$ quite challenging.

3.3 Sample Properties

High magnetic field neutron scattering investigations of spontaneous decay dynamics require materials with good 2D character (low J'/J) and relatively low in-plane exchange couplings. The maximum currently attainable continuous magnetic fields for neutron instruments are in the range $B = 14 - 17$ T, which corresponds to $J = 0.4 - 0.5$ meV by taking $B = 8JS/g\mu_B$, $S = 1/2$ and $g = 2$. The parent compounds of the superconducting cuprates such as La_2CuO_4, $Sr_2CuO_2Cl_2$ have $J \approx 130$ meV. CFTD has $J \approx 6$ meV, $Cu(pz)_2(ClO_4)_2$ has $J \approx 1.5$ meV and $K_2V_3O_8$ has $J \approx 1.1$ meV. These values make them all unsuitable for high field studies. The new family of metal-organic systems described in Refs. [74–77] are known to have good 2D character and also exchange couplings in the desired energy

range.

$(5CAP)_2CuCl_4$ (CAPCC) is a fairly novel synthesized metal-organic compound with small nearest neighbour exchange coupling J = 0.1 meV [74]. It is part of the family of magnetic insulators where the magnetism is determined by Cu^{2+} ions. In this oxidation state, Cu^{2+} has an unpaired electron in its 3d shell. In a crystal environment, due to the quenching of orbital angular momentum, the magnetism is solely determined by its spin (S=1/2) angular momentum. In CAPCC, copper ions are positioned on successive two-dimensional layers and due to the finite inter-layer coupling $J' \approx 0.3 \times J$, CAPCC is considered a good realisation of the S=1/2 quasi-2D S=1/2 square lattice Heisenberg antiferromagnet that offers the possibility of experimental investigations of the predicted spontaneous magnon decay process.

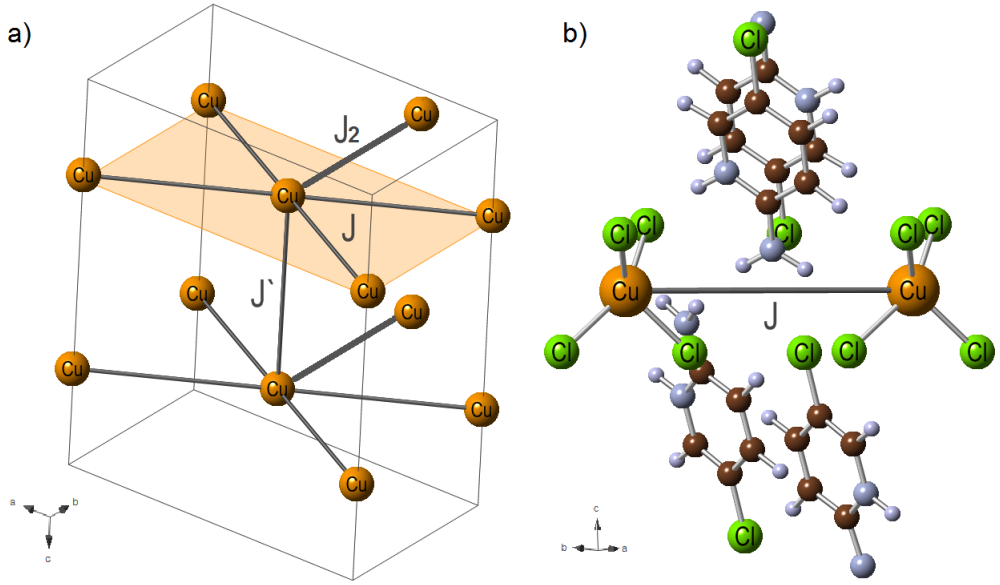

Figure 3.4: $(5CAP)_2CuCl_4$ crystal structure where we show in a) one paramagnetic unit cell with the nearest neighbour Cu atoms in the ab plane (light orange) coupled by J and atoms out of plane coupled by J′. Next nearest neighbours in the plane are coupled by J_2. In b) we show a plane perpendicular to the ab plane where the $CuCl_4^{2-}$ anions are separated by organic 5CAP molecules along the c-direction.

CAPCC crystallises in the monoclinic C2/c space-group. Its lattice parameters at 145 K are: a = 12.85 Å, b = 8.37 Å, c = 15.71 Å, $\alpha = \gamma = 90°$ and $\beta = 94.37°$ [74]. Analysis of the structure reveals layers of isolated $CuCl_4^{2-}$ tetrahedra. The Cu^{2+} are situated in the centre of flattened tetrahedra with the mean Cl-Cu-Cl large angle being $\approx 139°$. Superexchange takes place in the ab-plane between tetrahedra related by C-centering through Cu-Cl-Cl-Cu magnetic pathways.

The distance between adjacent in-plane Cl-Cl ions is $d_{Cl-Cl} = 4.34$ Å and determines in-plane antiferromagnetic coupling between Cu ions. The planes of $CuCl_4^{2-}$ are separated, along the c-axis, by organic pyridinium (5CAP) molecules. The out-of-plane interaction is antiferromagnetic and also takes place via Cl-Cl contacts [77] but these are longer $d_{Cl-Cl} = 4.94$ Å than the in-plane contacts and so the inter-plane coupling J′ is weaker. Each crystallographic unit-cell contains two planes of Cu atoms situated at 0.25 and 0.75 along c, with a separation of c/2 between them. Each Cu site is related to one in the adjacent layer by the c-glide symmetry operation. In-plane, each Cu atom is linked to 4 nearest neighbours and although geometrically they do not form a square lattice, from the magnetic exchange point of view, they can be considered as an effective square lattice in the ab-plane [76].

Previous high-temperature susceptibility measurements [74] have revealed a maximum at T = 1.1 K. Fitting the data to a high-temperature expansion, a value for the in-plane coupling has resulted as J = 1.14 K or J = 0.098 meV. Heat capacity measurements suggested a transition to an ordered phase below $T_N = 0.74$ K [74]. This is confirmed by a later study of Coomer et al. [77] from which $T_N = 0.754$ K. In the study of Hammar et al. [74], at T = 0.065 K, the dominant feature in χ(B) was a sharp spike at $B_{c1} = 3.78$ T. At higher fields the magnetic response dropped rapidly as the sample got saturated. This has been interpreted as a transition into a field-induced saturated phase. A higher peak at $B_{c2} = 4.37$ T was identified but its origin could not be explained. Please note that the orientation of the single crystal sample was unknown. Coomer et al. [77] have found for the deuterated version of CAPCC, the value $B_s = 3.62$ T for the saturation field B ∥ b-direction which is lower than what Hammar et al. [74] have reported and indicates the presence of small anisotropy.

3.4 Experimental Details

We performed a time-of-flight inelastic experiment on the high resolution multi-chopper spectrometer LET, at the ISIS Neutron Source, UK. The spectrometer was described in detail in Chapter 2. The aim of the experiment was two-fold. The first objective was to determine the magnetic Hamiltonian of CAPCC with better precision than before and get a value for the inter-layer coupling constant J′ by direct measurement as opposed to an estimate which was available at the time of the experiment. A reliable value for the intra-plane and inter-plane couplings J and J′ is

a prerequisite in order to provide a quantitative comparison between experimental data and the $1/S^2$ spin-wave theory for the dynamical structure factor $S(\mathbf{Q}, \omega)$. The parameters of the Hamiltonian were extracted from excitations collected at B = 7 T ($B_s = 3.95$ T) where the spins are forced to align with the field direction and the excitations are accurately described by linear spin-wave theory. The second aim was to measure the excitation spectrum in the canted phase in order to check for presence of magnon decay.

The sample used on LET was a m = 2.0 g single crystal of deuterated-CAPCC grown by Dr. Gøran Nilsen that was aligned and mounted on a dilution stick insert kept at base temperature of T = 60 mK, with $a^\star - b^\star$ in the horizontal scattering plane of the instrument and $c^\star$ making an angle of 85.63° with respect to $a^\star$ and pointing downwards. The sample was inserted in the vertical field 9T magnet with the magnetic field applied along the c-direction, with a small component in the ab-plane.

The long pulse from the ISIS Target Station 2, together with a particular choice of chopper settings, allowed simultaneous measurements with three distinct incident energies. A setting of the double disk resolution and pulse removal chopper frequency of $\omega_{res} = 150$ Hz and $\omega_{pr} = 100$ Hz allowed for the selection of $E_i = 1.25$ meV, $E_i = 2.0$ meV and $E_i = 3.67$ meV. Due to the trade-off between incident flux and energy resolution, the datasets with $E_i = 1.25$ meV (highest resolution) were not usable because of very low flux. We collected data with the sample in two orientations. One covers wave vectors around the $Q = (\pi/2, \pi/2, 0)$ square lattice point and we will refer to it as orientation I, and the second orientation, which covers wave vectors around the $Q = (\pi, 0, 0)$ point and we call orientation II. See Fig. 3.9 which best illustrates the two orientations. We determined the experimental energy resolution for each orientation and incident energy by fitting a Gaussian profile to the incoherent elastic signal. The mean values for $E_i = 2.0$ meV are $\Delta E = 25.4$ μeV and for $E_i = 3.67$ meV, $\Delta E = 61.6$ μeV. These values are in excellent agreement with the predictions of the chopper software which give for the same incident energies $\Delta E = 26$ μeV and $\Delta E = 63$ μeV respectively. This software computes what the expected energy resolution is at a given energy transfer, information which we will use in section 3.6. See table 3.1 for a summary of measurement conditions.

Table 3.1: Summary of collected data. The sample orientation is given in terms of the angle $\psi(^\circ)$ between k_i and $a^\star$. $\psi = -78^\circ$ corresponds to orientation I, which covers wave vectors around $Q = (\pi/2, \pi/2, 0)$ and $\psi = -193^\circ$ corresponds to orientation II which covers wave vectors around $Q = (\pi, 0, 0)$. The energy resolution for $E_i = 2.0$ meV is $\Delta E = 25.4$ μeV and for $E_i = 3.67$ meV it is $\Delta E = 61.6$ μeV.

E_i (meV)	Field (T)	Orientation	Q point	Time (h)
2.0	7	I	$(\pi/2, \pi/2, 0)$	24
2.0	3.35	I	$(\pi/2, \pi/2, 0)$	50
2.0	7	II	$(\pi, 0, 0)$	12
2.0	3.35	II	$(\pi, 0, 0)$	59.5
3.67	7	I	$(\pi/2, \pi/2, 0)$	24
3.67	3.35	I	$(\pi/2, \pi/2, 0)$	50
3.67	7	II	$(\pi, 0, 0)$	12
3.67	3.35	II	$(\pi, 0, 0)$	59.5

The misalignment of the sample during the experiment was determined to be 1.5 degrees. This gives the mismatch between the $a^\star - b^\star$ plane of the sample and the horizontal scattering plane of the LET spectrometer. The misalignment was quantified by analysing two diffraction datasets collected during the preliminary stage of the experiment and the knowledge of the scattering geometry. As a result, we accounted for this sample misalignment when we transformed the data from raw format to sqw format.

The raw data from LET contains information about the time-of-flight and intensity of scattered neutrons for each of the detector elements that make up the banks. From knowledge of the scattering geometry such as incident energies, lengths of the instrument, monitor positions, positions of the detector elements, this data is reduced into standard format using the 'Iliad' algorithm in the Mantid Software [88]. We performed the majority of the data handling and analysis using the Horace suite of programs [89]. Horace represents a suite of programs that work with large multiple-measurement datasets collected from time-of-flight neutron spectrometers equipped with arrays of position-sensitive detectors. The software allows exploratory studies of the four dimensions of reciprocal space and excitation energy to be undertaken, enabling multi-dimensional subsets to be visualized, algebraically manipulated, and models for the scattering to be simulated or fitted to the data [89].

3.5 Hamiltonian Parametrisation from High Field Data

In this section we show how we measured the dispersion relation in the polarised phase of $(5CAP)_2CuCl_4$ and extracted the parameters of the Hamiltonian which include the in-plane J and out-of-plane J′ exchange constants as well as the g-factor. The accurate knowledge of these parameters allows for a direct quantitative comparison between 1/S spin-wave theory which depends on the J′/J ratio and the data for the part where we investigate the presence of spontaneous magnon decay.

The magnetic Hamiltonian of a spin system can be very accurately determined by measuring its magnetic excitation spectrum using inelastic neutron scattering. It allows the parametrisation of the Hamiltonian in terms of exchange constants and anisotropy parameters through fits of the measured excitation spectrum to theoretical predictions. In the case of antiferromagnets where the true ground state is not the Néel state the excitations spectrum is not known exactly due to the effect of quantum fluctuations which is non-trivial. In contrast, for a ferromagnet where the true quantum ground state and the classical ground state coincide, the excitations are classical magnons and the spectrum is exactly given by linear spin-wave theory (LSWT) so a fit to the measured magnon dispersion gives the true exchange coupling constants. Coldea et al. [90] exploited this difference between an antiferromagnet and a ferromagnet and determined the Hamiltonian of the low-dimensional frustrated quantum magnet Cs_2CuCl_4 by applying a magnetic field strong enough to overcome all exchanges and fully polarise the sample, thus transforming it into an effective ferromagnet. A simple fit of the linear spin-wave theory dispersion to the measured magnon dispersion in this polarised state gave values for the exchange constants. Here we take the same route to obtain the spin Hamiltonian of $(5CAP)_2CuCl_4$. In the following paragraphs we show the predictions of linear spin-wave theory for the dispersion and present the data collected at B = 7 T and the details of the fitting routine.

The Hamiltonian of $(5CAP)_2CuCl_4$ is given by

$$\mathcal{H} = \mathrm{J} \sum_{<\mathrm{i,j}>} \mathbf{S}_\mathrm{i}\mathbf{S}_\mathrm{j} + \mathrm{J}' \sum_{<\mathrm{j,k}>} \mathbf{S}_\mathrm{j}\mathbf{S}_\mathrm{k} - \mathrm{g}\mu_\mathrm{B}\mathrm{B} \sum_\mathrm{i} \mathrm{S}^\mathrm{z}_\mathrm{i} \tag{3.7}$$

which includes nearest neighbour in-plane J, out-of-plane coupling J′ and coupling to the applied magnetic field B.

The most wide-spread method of tackling spin Hamiltonians is spin-wave theory [37, 45–49] which consists of mapping the spin operators onto boson creation and annihilation operators using the Holstein-Primakof [91] transformation

$$\begin{aligned} S_i^z &= S - n_i \\ S_i^+ &= \sqrt{(2S - n_i)}a_i = \sqrt{2S}(a_i - \frac{n_i a_i}{4} - \frac{n_i^2 a_i}{32} - \ldots) \\ S_i^- &= a_i^\dagger \sqrt{(2S - n_i)} = \sqrt{2S}(a_i^\dagger - \frac{a_i^\dagger n_i^2}{4} - \ldots) \end{aligned} \tag{3.8}$$

where $n_i = a_i^\dagger a_i$ and one needs to Taylor series expand the square root in powers of $n_i/(2S)$ and keep terms up to a given order. The zeroth-order approximation is the linear approximation taking

$$\begin{aligned} S_i^z &= S - n_i \\ S_i^+ &= \sqrt{(2S - n_i)}a_i = \sqrt{2S}a_i \\ S_i^- &= a_i^\dagger \sqrt{(2S - n_i)} = a_i^\dagger \sqrt{2S} \end{aligned} \tag{3.9}$$

After Fourier transforming the bosonic operators

$$\begin{aligned} a_i &= 1/\sqrt{N} \sum_{\mathbf{q}} e^{-i\mathbf{q}\mathbf{r}_i} a_{\mathbf{q}} \\ a_i^\dagger &= 1/\sqrt{N} \sum_{\mathbf{q}} e^{-i\mathbf{q}\mathbf{r}_i} a_{\mathbf{q}}^\dagger \end{aligned} \tag{3.10}$$

one ends up with the Fourier transformed bosonic Hamiltonian which has to be diagonalized to give the energy of the excitations. For our case one effectively ends up with the following Hamiltonian

$$\begin{aligned} \mathcal{H} &= \mathcal{H}_{nn} + \mathcal{H}'_{nn} + \mathcal{H}_z \\ &= -S^2 N(2J + J') - g\mu_B SNB - \ldots \\ &\quad \sum_{\mathbf{q}} 4JS(1 - \gamma_{\mathbf{q}}) a_{\mathbf{q}}^\dagger a_{\mathbf{q}} - \sum_{\mathbf{q}} 2J'S(1 - \gamma_{\mathbf{q}_c}) a_{\mathbf{q}}^\dagger a_{\mathbf{q}} + g\mu_B B \sum_{\mathbf{q}} a_{\mathbf{q}}^\dagger a_{\mathbf{q}} \end{aligned} \tag{3.11}$$

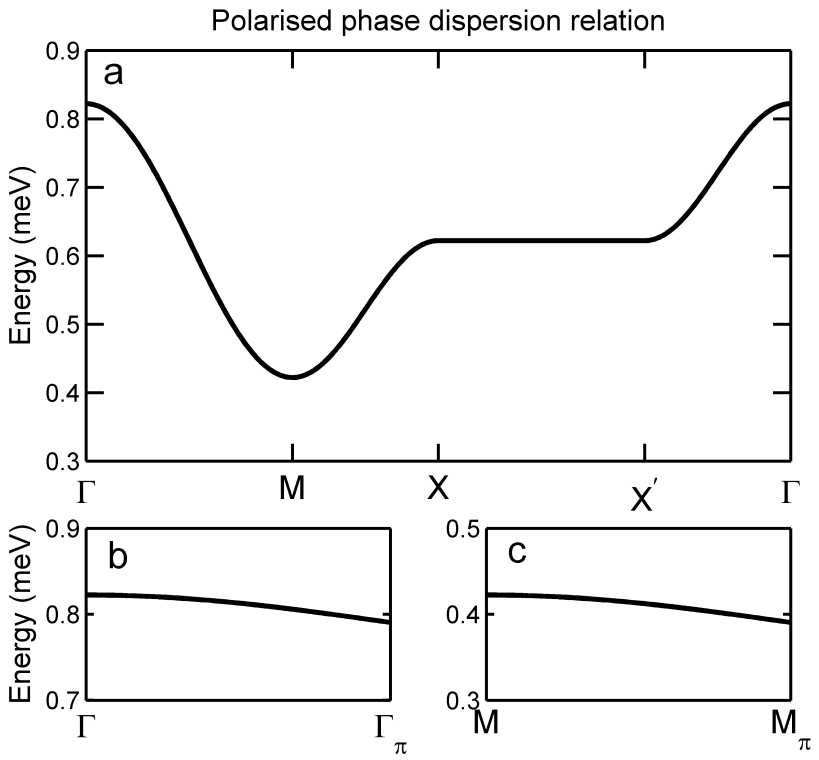

Figure 3.5: Polarised phase linear spin-wave theory prediction for the dispersion a) along a specific path in the (hk0) plane and along the l-direction from b) Γ to Γ_π and from c) M to M_π. The energy scale is set by the values of J = 0.1 meV, J′ = 0.032 meV and g = 2.03 obtained from the data. The definition of high symmetry points in the Brillouin zone is the one in Fig. 3.3.

where N is the number of spins. The second line of equation 3.11 is the ground state energy and the one-magnon dispersion for S=1/2 reads

$$\mathrm{E}_{\mathbf{q}} = \mathrm{g}\mu_{\mathrm{B}}\mathrm{B} - 2\mathrm{J}(1-\gamma_{\mathbf{q}}) - \mathrm{J}'(1-\gamma_{\mathbf{q}_\mathrm{c}}) \tag{3.12}$$

where momentum transfer in the crystal frame is labelled $\mathbf{q} = \mathrm{ha}^\star + \mathrm{kb}^\star + \mathrm{lc}^\star$ and the lattice sums are $\gamma_{\mathbf{q}} = \cos(\pi\mathrm{h})\cos(\pi\mathrm{k})$ and $\gamma_{\mathbf{q}_\mathrm{c}} = \cos(\pi\mathrm{l})$. The c-component of the Landé factor is given by g. This dispersion is plotted in Fig. 3.5 along different high symmetry directions of the 3D Brillouin zone. In the l = 0 plane, it has a maximum at the origin Γ, a minimum at the zone centre M and it is constant along the magnetic zone boundary X − X′ line. The notation of high symmetry points of the square lattice Brillouin zone is given in Fig. 3.3.

We present the strategy for extracting the Hamiltonian parameters from the

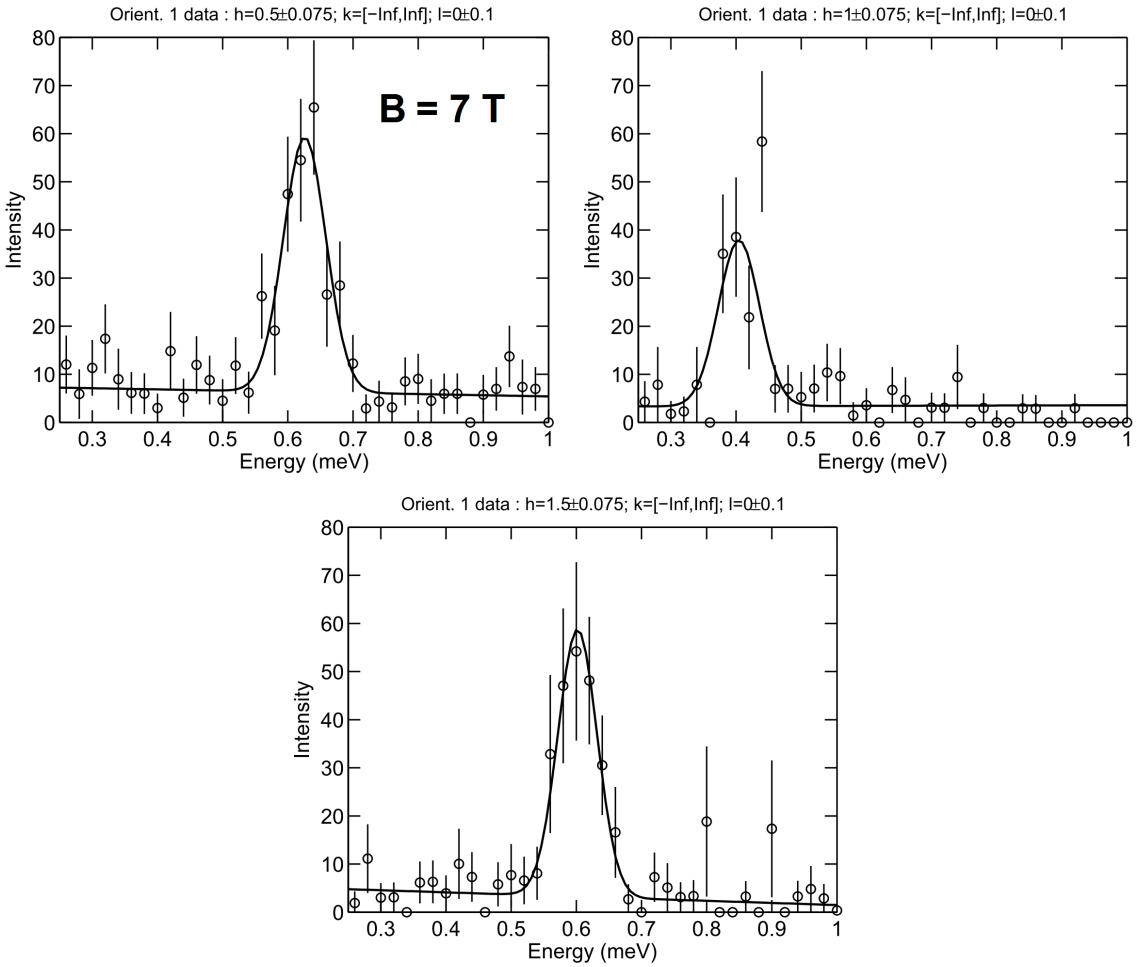

Figure 3.6: Selection of B = 7 T one-dimensional cuts along energy transfer (black circles) from which we extract the peak position in energy by fitting to a Gaussian profile on a linear background (black line).

measured data in the polarised phase by first referring back to the section where we described the LET spectrometer and reminding that on LET one has access to only three independent variables out of the four that describe the scattering function $S(\mathbf{Q}(h,k,l),\omega)$. In general this means that there will always be an implicit variation of two of the wave vector transfer components and of energy transfer with the third component of wave vector transfer. Due to our particular choice of sample orientation, the h-component of wave vector transfer and energy transfer will depend on the k-component, with the l-component being totally independent. With this remark in mind, we extract several subsets from the measured $S(\mathbf{Q},\omega)$ by averaging the scattered intensity along the k- and l-component directions. We end up with two-dimensional datasets with scattered intensity as a function of the

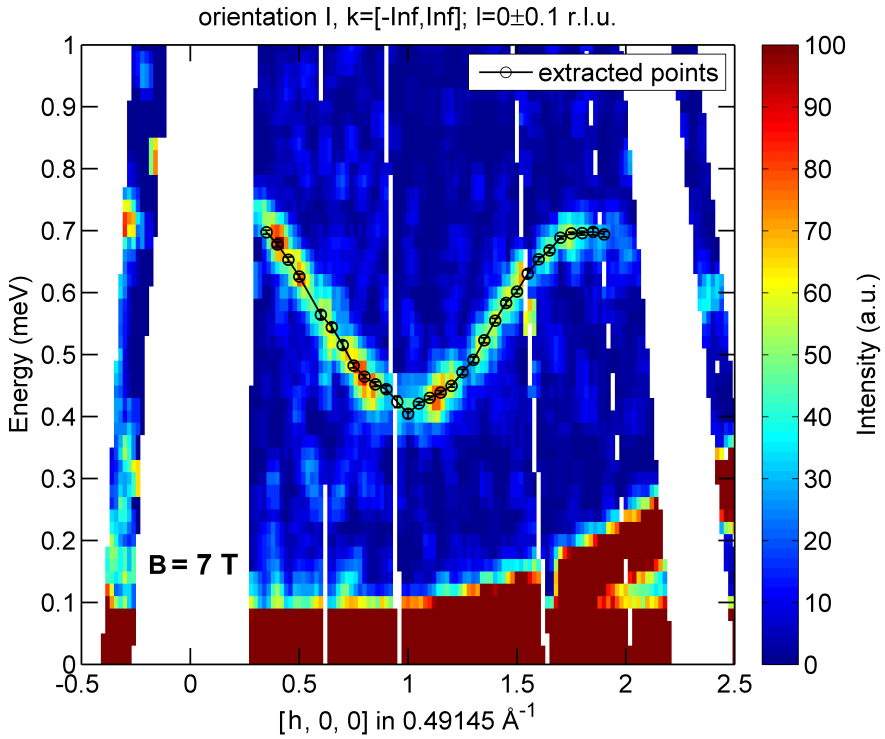

Figure 3.7: Two-dimensional false colour plot showing measured dispersion at B = 7 T in the (hk0) plane for one orientation of the sample. It is obtained by averaging over k = $[-\infty, +\infty]$ and l = $[-0.1, 0.1]$ r.l.u. Black circles represent the extracted data points along the measured dispersion using the procedure detailed in the text.

h-component of wave vector transfer and energy transfer. A further averaging along the h-direction gives one-dimensional cuts with intensity as a function of energy transfer. The cuts are fitted to a Gaussian profile on a linear background (see Fig. 3.6) in order to extract the energy of the excitations at several wave vector transfers thus obtaining the full dispersion relation. The dispersion is fitted to the dispersion predicted by linear spin-wave theory in Eq. 3.12.

For the purpose of extracting the dispersion from the data, we used the lower resolution (ΔE = 61.6 μeV) datasets collected with both sample orientations with E_i = 3.67 meV - see Table 3.1. This data has the advantage of better statistics and larger coverage of momentum space as compared to the E_i = 2.0 meV data. Energy resolution is worse than for the E_i = 2.0 meV data but for the purpose of extracting the Hamiltonian parameters it is more important to map the dispersion over a larger momentum region then to have the best energy resolution. As mentioned above, sample orientation in the spectrometer and the kinematics of the experiment lead

to a momentum coverage which is quite restricted in the k-direction and so we chose to integrate the signal along this direction. For all subsequently presented data we integrated along k from $[-\infty, +\infty]$. The other direction to integrate over has to be chosen between the l- and h-directions. The h coverage is largest so we chose to keep the h dependency together with energy transfer and integrate over finite regions along the l direction to obtain two-dimensional datasets. To extract information about the dependency of the energy on l and thus about the strength of inter-layer coupling J′, we extracted a series of two-dimensional datasets with explicit intensity dependence on h and energy transfer for several mean $< l >$ values ($< l > \pm 0.1$ r.l.u.). From each of the two-dimensional datasets we took constant h ($< h > \pm 0.075$ r.l.u.) cuts along energy transfer which were fitted to a Gaussian profile on a linear background as presented in Fig. 3.6 from which we extracted the peak position in energy. We obtained the dispersion relation for a given path through reciprocal space (see Fig. 3.7) for which we know the dependency on energy, h and l. For each extracted energy data point the k value is determined by the other variables from the kinematic constraints of the experiment. At the end we were left with the momentum dependence of extracted data along the 3-dimensional dispersion (black circles in Fig. 3.7). The integration ranges for the cuts as well as binning step sizes in energy were chosen such that the statistical quality of the resulting data would allow for decent fits while keeping the effects of averaging over finite momentum to a minimum.

A global fit of data extracted from two orientations of the sample to the prediction of linear spin-wave theory gives the following parameters for the Hamiltonian: J = 0.100(2) meV, J′ = 0.032(2) meV and g = 2.03(1) (see Tab. 3.2). The quality of the fits is given by the covariance matrix which gives a measure of the correlations between parameters. We give the global fit covariance matrix in Tab. 3.3 and see that there is almost no correlation between J and J′, whereas g is strongly correlated with both J and J′ because of the nature of the time-of-flight data. We present data extracted from several $< l >$ datasets along with the results of the global fit to the dispersion in Fig. 3.8. The data points on the left side of each subfigure come from orientation II datasets whereas the points on the right, come from orientation I datasets. One can see that the model dispersion given by Eq. 3.12 with the parameters given in Tab. 3.2 accounts very well for the measured dispersion.

We also performed a global fit of the data to the same model given by linear spin-wave theory which includes further neighbour interactions in the plane for which

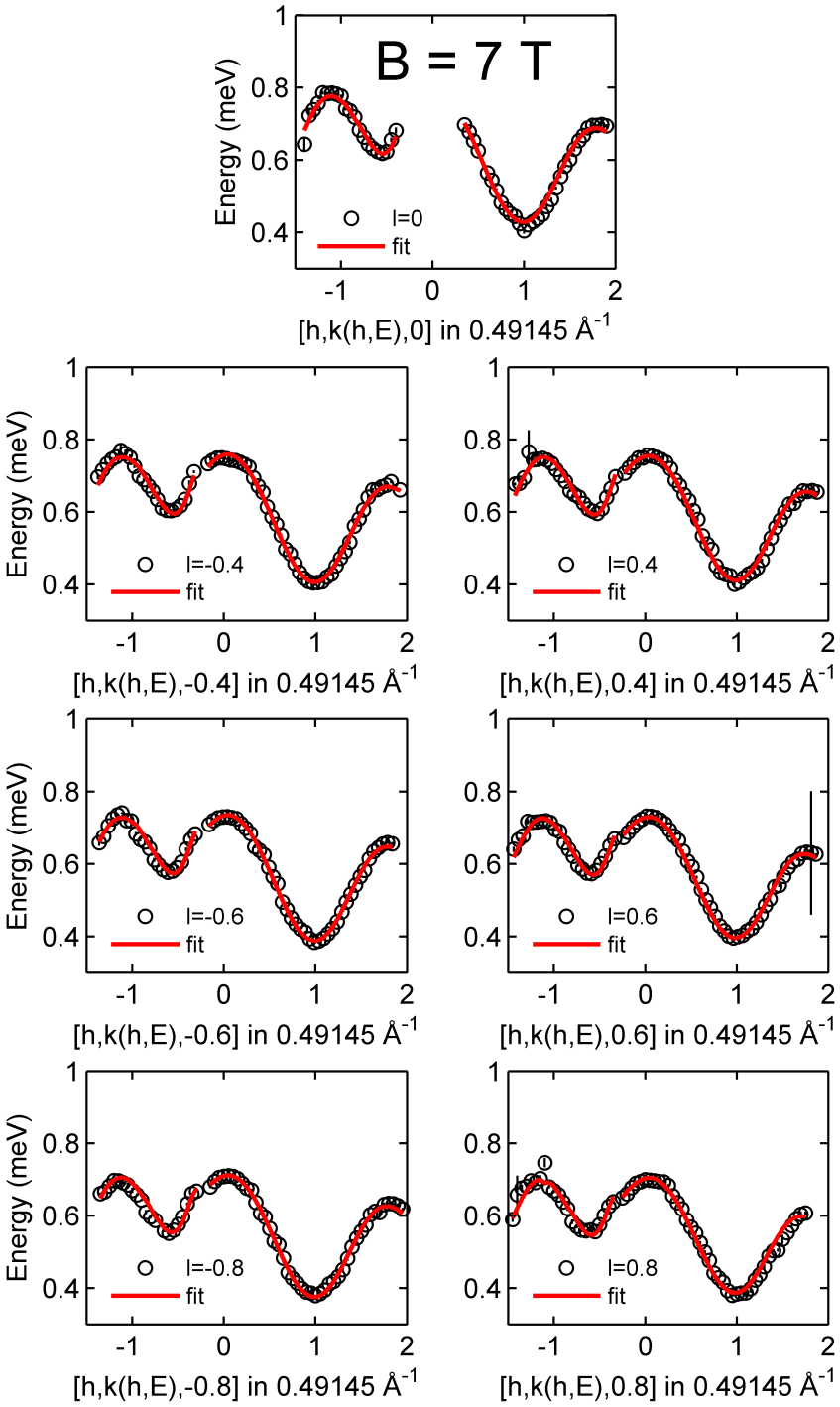

Figure 3.8: Extracted data points along the dispersion measured at B = 7 T (black circles) together with results of the global fit to the linear spin-wave theory dispersion (red line) for data with different mean $< l >$ values.

Table 3.2: CAPCC Hamiltonian parameters extracted from the high field data.

J (meV)	J′ (meV)	g
0.100(2)	0.032(2)	2.03(1)

Table 3.3: Covariance matrix for global fit that shows parameter correlations.

	J	J′	g
J	1	0.0467	0.6057
J′	0.0467	1	0.7306
g	0.6057	0.7306	1

the resulting Hamiltonian parameters are $J = 0.100(2)$ meV, $J_2 = 0.001(2)$ meV, $J' = 0.032(2)$ meV and $g = 2.02(1)$, with J_2 being the next-nearest neighbour in-plane coupling. This fit does not significantly improve the description of the data and shows that if there is any next-nearest neighbour coupling in the plane, it is most likely of the order of 1% of the main J and for most purposes it can safely be ignored.

We measured the excitation spectrum of $(5CAP)_2CuCl_4$ at $B = 7$ T where the system is forced into an effective ferromagnetic state. In this state the dispersion of magnon excitations is given exactly by linear spin-wave theory. By fitting the observed dispersion to the theoretical prediction, we extracted the parameters of the Hamiltonian and saw that only including nearest-neighbour in-plane exchange and inter-plane exchange accounts very well for the measured dispersion with $J = 0.100(2)$ meV, $J' = 0.032(2)$ meV and $g = 2.03(1)$. These values agree nicely with an empirical relationship which relates the Néel temperature to the exchange constants and is valid for quasi-2D systems. From the quantum Monte-Carlo study of Yasuda et al. [92] results that for S=1/2 systems the following relationship holds

$$T_N = \frac{0.732\pi J}{2.43 - \ln(J'/J)} \tag{3.13}$$

which for our values of the exchanges gives $T_N = 0.75$ K, in excellent agreement with the value for $(5CAP)_2CuCl_4$ given in Refs. [74, 77]. The value of the *c*-component of the g-factor determined in this study is also in good agreement with the electron paramagnetic resonance measurements of Woodward and collaborators [76] which give for $(5CAP)_2CuBr_4$, the Br analogue of $(5CAP)_2CuCl_4$, a value for $g_{c^\star} = 2.06$.

3.6 Evidence for Field-Induced Magnon Decay

In this section we present the analysis of the intermediate field data collected at $B = 3.35\ T = 0.85 \times B_s$, where spontaneous magnon decay effects are predicted to be observable in neutron scattering data. The general prediction is a broadening of the excitations around the $(\pi/2, \pi/2, 0)$ point, which is larger than the broadening at $(\pi, 0, 0)$. First, we take a purely experimental approach to the analysis and argue that the asymmetry we observe in the lineshape of the one-magnon excitations is an effect of decays. Second, we invoke results of spin-wave theory for the case of an inter-layer coupling. We show that the data is clearly not well described by the non-interacting magnon approximation or linear spin-wave theory and that going to first order in the 1/S expansion, which accounts for magnon-magnon interactions, is a clear improvement. We give details about the predicted 1/S spin-wave theory dynamical structure factor which allows for direct comparison to our data. We briefly present the case of the classical model and results of a neutron scattering experiment on the S=5/2 square lattice antiferromagnet $Ba_2MnGe_2O_7$ [83] and argue that the more pronounced continuum together with overdamped single magnon modes observed in the S=1/2 case, is favouring the presence of intrinsic decays in $(5CAP)_2CuCl_4$.

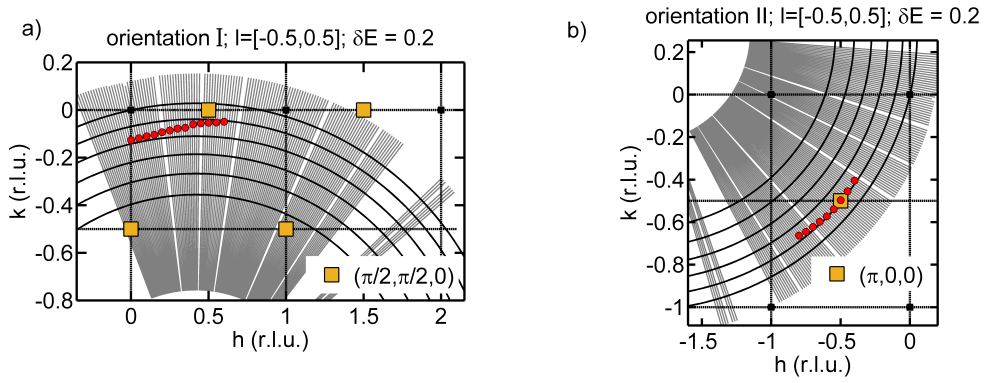

Figure 3.9: Experimental detector coverage (grey area) of the CAPCC reciprocal space in the (hk0) plane for the two orientations of the sample. The incident energy here is $E_i = 2.0$ meV. The black lines represent contours of constant energy transfer in steps of $\delta E = 0.2$ meV and the trajectory we follow through reciprocal space is plotted with red points.

We begin by showing the experimental reciprocal space coverage of $(5CAP)_2CuCl_4$ in the (hk0) reciprocal space plane in Fig. 3.9 for data collected with two orienta-

tions of the sample. When the sample is in orientation I (defined by $\psi = -78°$) the detectors cover wave vectors around the $Q = (\pi/2, \pi/2, 0)$ corresponding to $Q_{rlu} = (0.5, 0, 0)$ in crystal reciprocal space, for energy transfers between 0 and 0.4 meV (see black lines which indicate contours of constant energy transfer) and for orientation II (defined by $\psi = -193°$) the detectors cover wave vectors around the $Q = (\pi, 0, 0)$ which corresponds to $Q_{rlu} = (-0.5, -0.5, 0)$ in the crystal reciprocal space. Raw data collected with neutrons of $E_i = 2.0$ meV incident energy ($\Delta E = 25.4$ μeV - FWHM of elastic line energy resolution) is shown in Fig. 3.10. On the left column we show the intermediate-field, canted phase data and on the right column, the high-field, polarised phase data that is used as a background and which is subtracted off the canted phase data. In the canted phase, one observes two one-magnon branches, the more intense, main mode, is due to spin fluctuations in the two-dimensional planes, whereas the shadow (ghost) mode, which is shifted by the ordering wave vector $Q_{AFM} = (\pi, \pi, \pi)$ and is about 30% of the intensity of the main mode at B = 3.35 T, corresponds to spin fluctuations along the magnetic field direction and perpendicular to the two-dimensional planes.

The intensity of the shadow mode gradually decreases towards zero as the saturation field $B_s = 3.95$ T is approached due to the fact that spin fluctuations along the field direction are continuously suppressed. For the intermediate field orientation I dataset (top left), the general features are an apparent damping of the main mode and an intensity drop as one moves from h = 0 and approaches h = 0.5 r.l.u. For the intermediate field orientation II dataset (bottom left), the damping seems to be less obvious than for orientation I and the intensity of the mode at h = −0.5 r.l.u. seems to be comparable with the intensity at h = 0. A feature that is common to both datasets is the presence of extra scattering intensity close to h = 0 and at small energy transfers close to the elastic line. The extra scattering around h=0 is due to the imperfect shielding about the straight through beam stop on LET which allows for extra scattering events to occur and thus appear as extra intensity in the detectors. For the intermediate field orientation I dataset, extra scattering intensity appears for all h wave vectors and occupies a region below 0.1 meV energy transfer. We suspect this spurious feature is due to higher order scattering from our aluminium sample can and aluminium from the dilution refrigerator tail. The same feature is observed in the corresponding high-field dataset (top right in Fig. 3.10). This extra scattering below 0.1 meV does not seem to be present in the orientation II datasets, an aspect for which we do not have an explanation yet. Another spu-

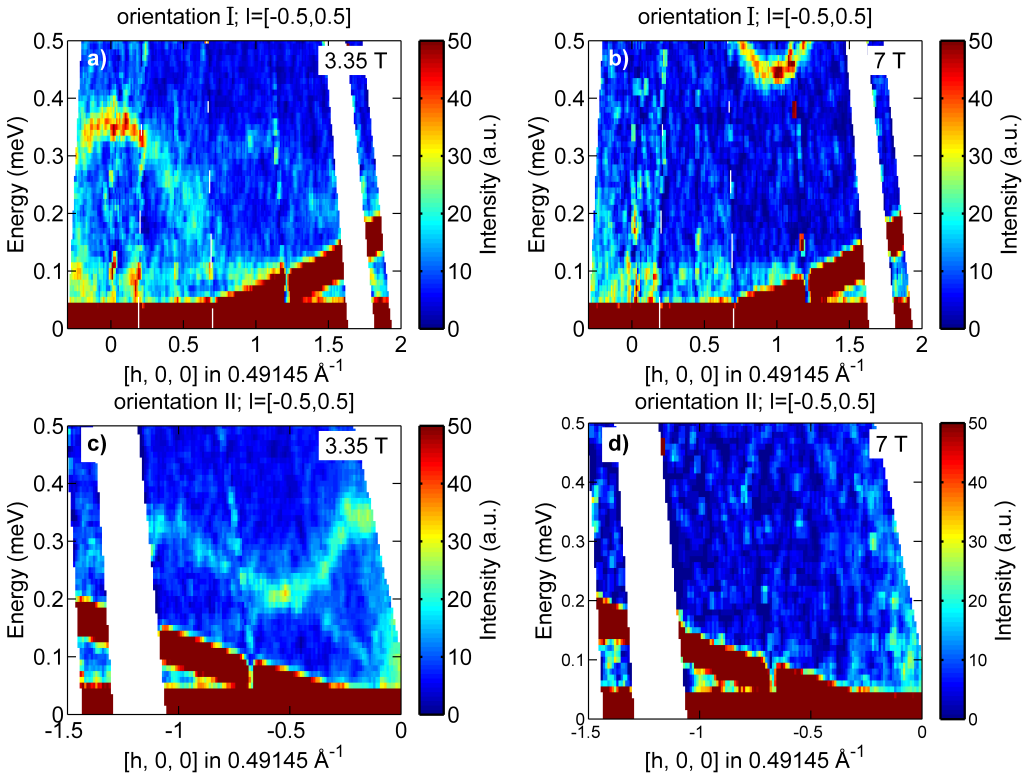

Figure 3.10: a) Raw data for wave vectors approaching $Q = (\pi/2, \pi/2, 0)$ and $B = 3.35$ T. b) Raw background data for wave vectors approaching $Q = (\pi/2, \pi/2, 0)$ and $B = 7$ T. c) Raw data for wave vectors approaching $Q = (\pi, 0, 0)$ and $B = 3.35$ T. d) Raw background data for wave vectors approaching $Q = (\pi, 0, 0)$ and $B = 7$ T. The general features are explained in the text.

rious feature which is observed in all datasets is higher scattering intensity which appears for certain detector elements which are located along vertical lines. These lines correspond to the vertical cadmium veins which separate the detector banks on LET and have the role of preventing scattered neutrons from one bank to reach detectors on another bank. The cadmium veins are not perfectly vertical and thus shadow some of the detector elements situated on the edge tubes leading to lower counts in those detectors. When the vanadium normalisation is performed the signal in the detectors with lower counts gets divided by a vanadium signal which is similar for adjacent detector elements. Due to the fact that the shadowed detectors have constantly lower signal this leads to a higher vanadium normalised signal in some detectors, as observed in the data. The odd extra scattering which branches away from the elastic line as one moves further in h and appears as neutron energy loss is related to due to neutrons that have not interacted with the sample and scatter

from the outer vacuum chamber wall of the 9 T cryomagnet we used. This can be understood if one thinks of an elastically scattered neutron at the sample position and a neutron that has not interacted with the sample, has scattered off the outer vacuum chamber of the 9 T cryomagnet and has reached the same detector as the elastically scattered neutron. The second neutron has clearly travelled an extra path, arrived later at the detector and appears to have lost energy. The neutrons that suffer a scattering process off the outer vacuum chamber and get scattered at higher and higher scattering angles, travel a longer and longer distance as compared to an elastically scattered neutron at the sample position and so appear as having lost more and more energy. This is why the extra scattering increases in energy transfer with increasing wave vector transfer.

3.6.1 Experimental Approach

In the following, we present the data analysis based on a purely experimental approach, without making reference to theoretical predictions. The objective is to check for presence of continuum scattering which would be a strong indicative of spontaneous magnon decays. The analysis of the data consists of extracting constant-h cuts with intensity averaged over a $\Delta h = 0.1$ and $\Delta l = 1$ r.l.u. interval along energy transfer and fitting these to a model of the lineshape $S(\omega)$. Final cuts are obtained after background subtraction from the raw cuts. We use the polarised phase data and generate a smooth background model for each cut. This approach is chosen instead of a point-by-point subtraction which is not valid here due to unequal statistics between the intermediate field and high field data (see Tab. 3.1). We use the polarised phase data as background because it describes well the non-sample dependent scattering as well as the non-magnetic sample scattering. For each individual one-dimensional cut we show (see Appendix A) the corresponding background cut along with the fitted smooth model which we choose to be of the form $f(\omega) = p_1 e^{-p_2\omega} + p_3$. The final cuts are individually fitted to a skew normal function on a linear background which is essentially an asymmetric Gaussian of the form

$$\begin{aligned} f(\omega) &= 2G(\omega)\Phi(\alpha\omega) \text{ with} \\ G(\omega) &= \frac{1}{\sqrt{2\pi}} e^{\frac{(\omega-\omega_0)^2}{2\sigma}} \\ \Phi(\alpha\omega) &= \frac{1}{2}[1 + \mathrm{erf}(\frac{\alpha(\omega-\omega_0)}{\sqrt{2}\sigma})] \end{aligned} \tag{3.14}$$

where the mean of the skew normal is given by $\omega_0 + \sqrt{2/\pi}\sigma\delta$, with $\delta = \alpha/\sqrt{1+\alpha^2}$, the standard deviation is given by $\sigma\sqrt{1-2\delta^2/\pi}$ and where α controls the asymmetry.

We show the results of fits in Fig. 3.11 for the orientation I which covers wave vectors around $Q = (\pi/2, \pi/2, 0)$ and in Fig. 3.12 for the orientation II which covers wave vectors around $Q = (\pi, 0, 0)$.

For wave vectors around $Q = (\pi/2, \pi/2, 0)$, corresponding to $Q_{\mathrm{rlu}} = (0.5, 0, 0)$, we see that the lineshape is asymmetric for the large majority of the cuts. From $h = -0.1$ to $h = 0.2$ the asymmetry is slightly positive (towards higher energy). In this h region we only capture the main mode and thus the asymmetry here is related to a weak continuum. For values of h larger than 0.2 and up to 0.475, the asymmetry seems to be negative, an indicative of the shadow mode approaching the main mode. For h larger than 0.475 the asymmetry becomes positive again and this is interpreted as finite continuum scattering. In terms of peak intensity, the trend seems to be an overall decrease of the peak height when moving from $h = -0.1$ to $h = 0.625$.

We propose two scenarios to explain this intensity variation. The first scenario is that the spectral weight is gradually being transferred away from the single particle peak, into a higher energy continuum, with the single particle peak having constant width. The second scenario is similar to the first one, but now in addition, the width of the single-particle peak also increases gradually, as we approach $h = 0.5$ r.l.u. We cannot distinguish between these possibilities due to the fact that we do not consider any detailed knowledge about the main and shadow modes, apart from their presence, the sensible assumption that their widths are similar and the knowledge that their integrated intensity ratio is approximately a third as predicted by 1/S spin-wave theory.

In terms of peak width, we plot the full-width half maximum of the fitted skew normal as a function of h in Fig. 3.14. We see that the width increases gradually as $h = 0.5$ r.l.u. is approached. Please note that this is not exactly the

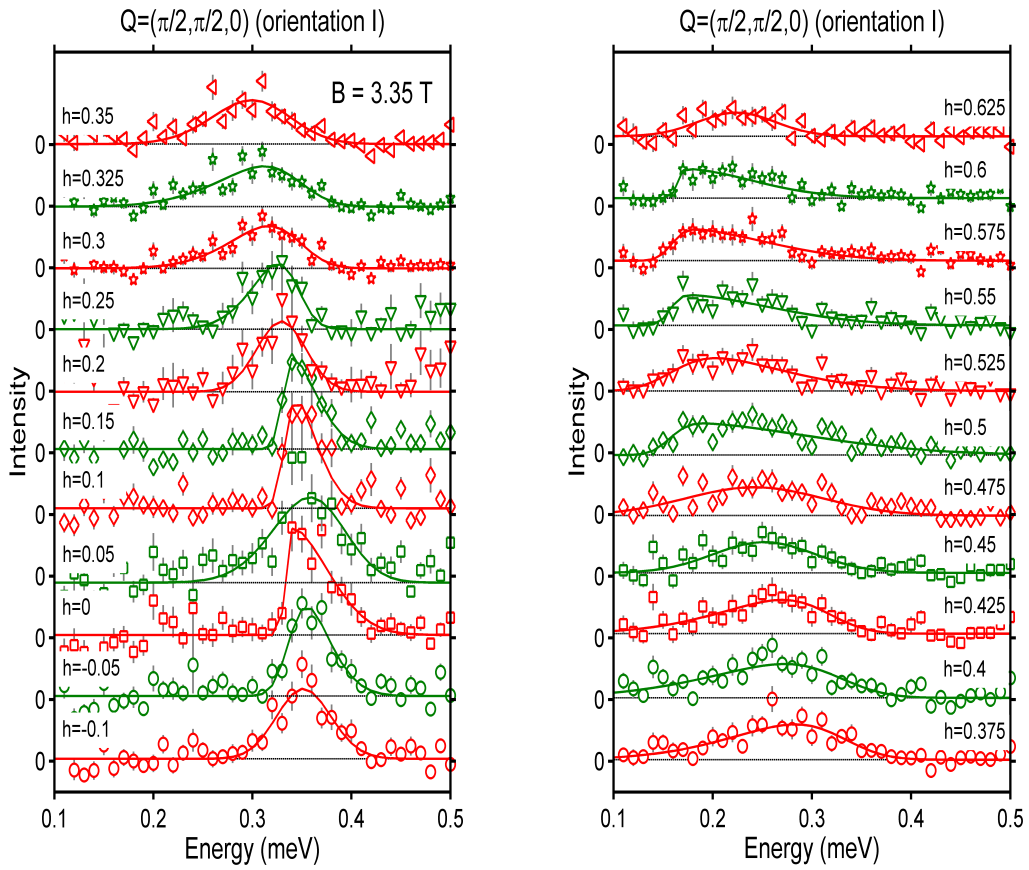

Figure 3.11: Data fits to an asymmetric lineshape described by the skew normal distribution function which show mode damping and presence of continuum scattering. The width of the peak increases as the h=0.5 r.l.u. is approached and correspondingly, the peak height decreases. There is also an increased peak asymmetry for values of h around 0.5 r.l.u. This indicates that spectral weight is being transferred away from the single particle peak into possibly a continuum at higher energy.

$Q = (\pi/2, \pi/2, 0)$ or $Q_{rlu} = (0.5, 0, 0)$ point, as there is a finite average k-component for each of the constant-h cuts. Also note that due to the quite large integration in the l-direction, the cuts have contributions from other wave vectors, where damping can be different, so what we observe is just a mean around $l = 0$. The notations below the horizontal axis are showing where wave vectors around the (0,0,0) and $(\pi/2, \pi/2, 0)$ are situated. This behaviour indicates that the modes are sharper for wave vectors around $Q = (0, 0, 0)$ and broader for wave vectors around $Q = (\pi/2, \pi/2, 0)$.

For wave vectors around $Q = (\pi, 0, 0)$, corresponding to $Q_{rlu} = (-0.5, -0.5, 0)$,

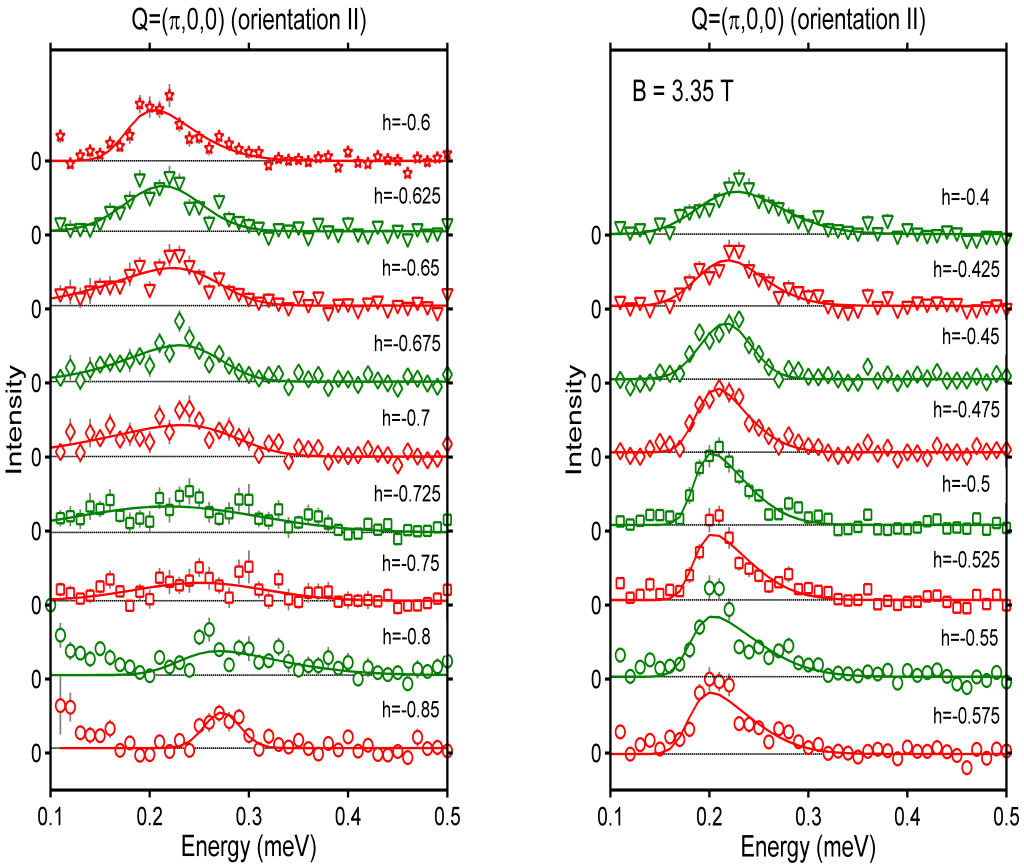

Figure 3.12: Data fits to an asymmetric lineshape described by the skew normal distribution function which show mode damping and presence of continuum scattering. The width of the peak decreases as the h=-0.5 r.l.u. is approached and correspondingly, the peak height increases. There is also an increased peak asymmetry towards higher energy, for values of h around -0.5 r.l.u. This indicates that spectral weight is being transferred away from the single particle peak into possibly a continuum at higher energy.

the lineshape is asymmetric for the majority of the cuts. Between h = −0.75 and h = −0.625, the asymmetry is negative, which is an indication of the presence of the shadow mode at energies smaller than the main mode energy. Starting from h = −0.6 and moving towards h = −0.4, the asymmetry is positive, which signals the presence of continuum scattering. This claim is also backed-up by the fact that the shadow mode appears always at energies below the main mode single particle peak. The peak height increases when moving from h = −0.625 to h = −0.5, which is an indication that spectral weight is transferred from the continuum to the single-particle peak. In terms of extracted width, the mode is broad for wave vectors

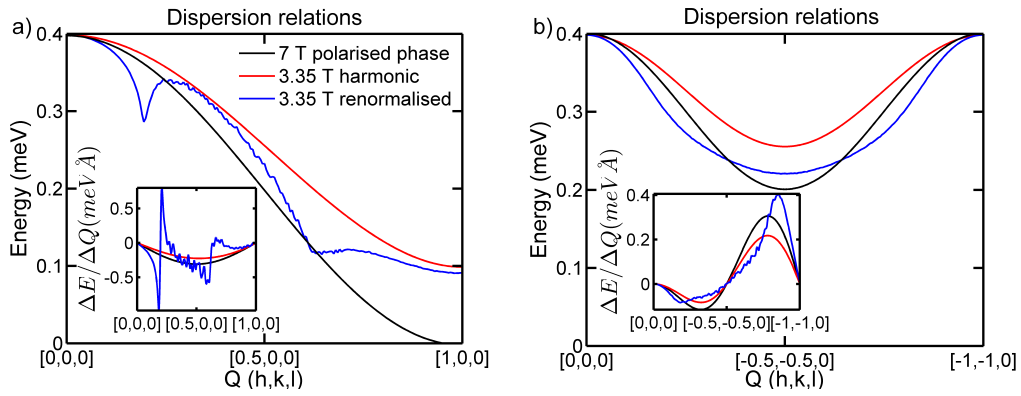

Figure 3.13: Dispersion relations for two high symmetry paths in the (hk0) plane. Paths are close to the paths we follow with the data, for a) orientation I and b) orientation II. The polarised phase dispersion has been shifted down in energy so that at the $(0, 0, 0)$ point, the energies match. In the insets we show the dispersion derivatives with respect to Q, which give the slope. We see that slopes are similar for the three dispersion relations.

around h = −0.75 when compared to wave vectors around h = −0.5. This variation of the width shows that as one approaches h = −0.5, the mode is better defined as can be seen in Fig. 3.15.

In order to show more convincingly that we observe damping, we choose to compare the width of the mode in the canted phase with the width of the polarised phase mode. We argue that such a direct comparison is valid due to several considerations. First of all, we know that in the polarised phase, where the spin structure is fully collinear and parallel to the magnetic field direction, the excitations are well-defined and no broadening beyond instrumental resolution effects is expected. Second, a difference in energy transfer of about 0.4 meV which is approximately the difference between the polarised and canted phase dispersions, does not significantly change the instrumental resolution. In fact, the energy resolution changes by about 0.004 meV whereas the Q resolution is the same, according to data provided by Dr. Rob Bewley, instrument scientist on LET. A third point concerns the mode broadening which is induced by averaging the signal over a finite range in Q and is due to the dispersion. This is easily understood if one thinks about the fact that for any dispersion a finite integration range in Q leads to a finite broadening in energy. The size of the induced broadening depends on the Q range and the change in the dispersion slope over the respective Q range. We argue that the induced broadening is the same for the polarised phase dispersion as compared to the canted

phase dispersion, due to the similar dispersions and slopes. To support this claim we plot in Fig. 3.13 the polarised phase dispersion (black lines), which is shifted down in energy so that at $Q = (0, 0, 0)$ the energy matches that of the canted phase dispersion, the canted phase harmonic dispersion given by linear spin-wave theory (red lines) and an approximation to the 1/S canted phase renormalised dispersion (blue lines), for two different paths through reciprocal space. These paths are close to the paths we follow with the data and correspond to a) wave vectors close to $Q = (\pi/2, \pi/2, 0)$ and b) wave vectors close to $Q = (\pi, 0, 0)$. We show the derivative of the dispersions in the insets of Fig. 3.13. The approximation to the 1/S dispersion includes corrections to the linear spin-wave theory dispersion that come from the mean-field decoupling of the $\mathcal{H}_3$ and $\mathcal{H}_4$ terms in the Hamiltonian. It does not consider the contribution that arises from the $\mathcal{H}_3$ self-energies. Details about all the contributions to the 1/S order are given in the appendix of Ref. [81]. We include the contribution of the self-energies only when we compute the dynamical structure factor due to the fact that the self-energies require an involved computational effort to be calculated and for our purposes this approximation to the dispersion illustrates the point. The canted phase harmonic dispersion (red line) and the approximation to the 1/S renormalised dispersion (blue line) are quite similar so the derivative of the harmonic canted phase dispersion gives a good approximation to the derivative of the renormalised dispersion. The canted phase harmonic dispersion (red lines) is also very similar in terms of slope with the polarised phase dispersion (black lines) and so we conclude that the induced broadening is expected to be quite similar for the polarised phase modes and canted phase modes. Together with the other two points stated above, this means that a direct comparison between polarised phase mode widths and canted phase widths constitutes a valid approach.

We plot the experimentally extracted mode widths from orientation I data in Fig. 3.14. For wave vectors close to $h = 0$ the mode widths are comparable, which indicates well-defined canted phase modes and small damping. As the $h = 0.5$ r.l.u. region is approached the canted phase mode width starts to significantly increase and at $h = 0.5$ r.l.u., where the main and ghost mode overlap in energy, it is about three times the width of the polarised phase mode. This large difference cannot be accounted for by the difference in induced broadening discussed above, nor by the marginal difference in the energy resolution for the canted phase and polarised phase mode. We conclude that this constitutes strong evidence that an intrinsic broadening mechanism is at play here, most likely spontaneous magnon decay. We

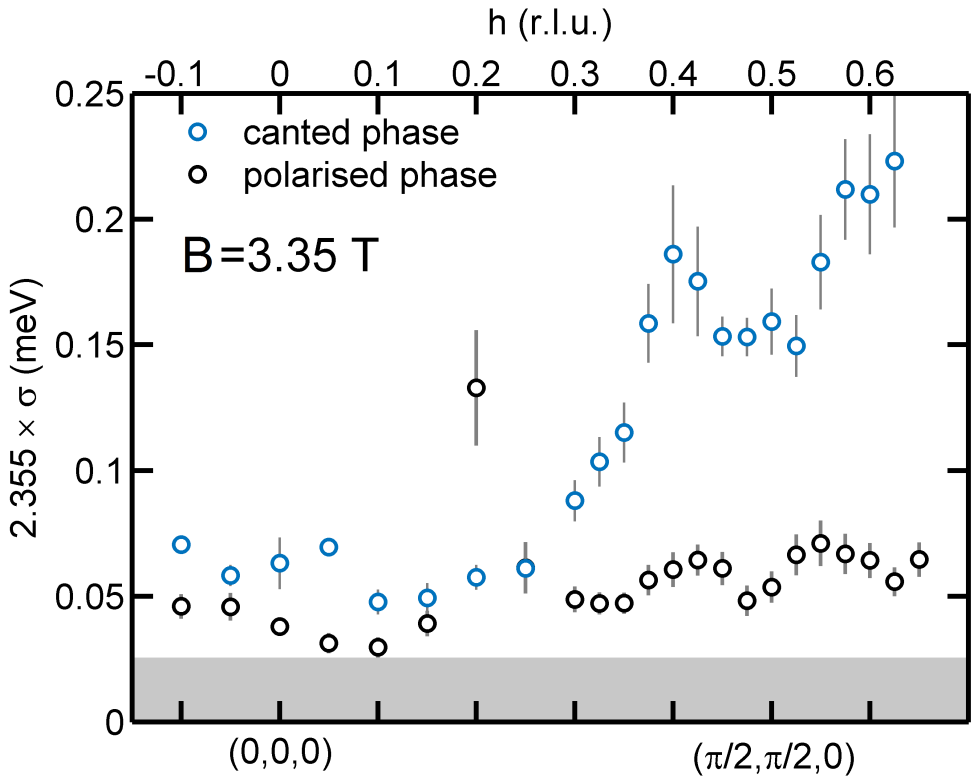

Figure 3.14: Comparison between experimentally extracted mode widths in the canted phase (blue circles) and polarised phase (black circles) as a function of h. The full-width at half maximum of the energy resolution at the elastic line is shown in grey. This plot shows that as one moves from h = 0 to h = 0.5 r.l.u. the width in the canted phase increases. If compared to the width of the polarised phase mode (see text for arguments why such a direct comparison is valid), the canted phase mode width becomes significantly larger (almost a factor of three) than the width of the polarised phase mode. For data around h = 0 the mode widths are comparable which is an indication that damping is small for this Q point. Around h = 0.5 r.l.u. where the main and ghost mode overlap in energy our data shows that the canted phase mode width is still considerably larger than the width of the polarised phase mode where only one mode is present thus providing strong evidence for significant mode damping.

plot the experimentally extracted mode widths from orientation II data in Fig. 3.15 and see that for wave vectors around h = −0.75 r.l.u. the canted phase mode width is considerably larger than the polarised phase mode width, an indication of large damping and thus strong decays. For wave vectors around h = −0.5 where the main and ghost modes overlap in energy, the extracted mode width in the canted phase is comparable to the mode width in the polarised phase. It shows that for

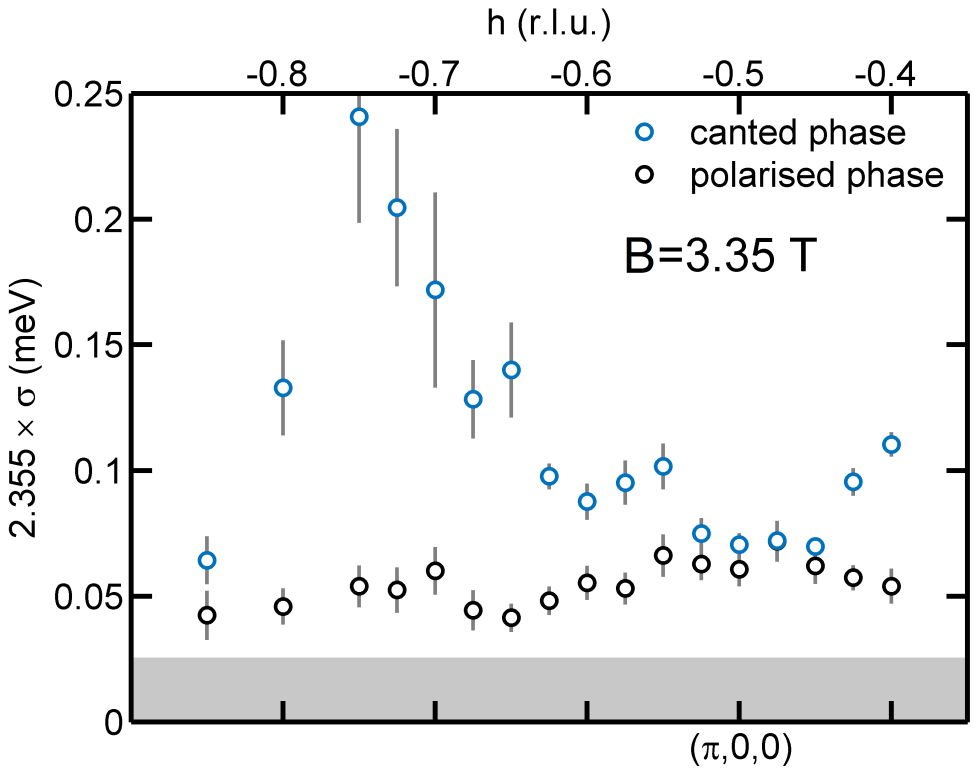

Figure 3.15: Comparison between experimentally extracted mode widths in the canted phase (blue circles) and polarised phase (black circles) as a function of h. The full-width at half maximum of the energy resolution at the elastic line is shown in grey. This plot shows that as one moves from h = −0.8 r.l.u. to h = −0.5 r.l.u. the width in the canted phase decreases. If compared to the width of the polarised phase mode (see text for arguments why such a direct comparison is valid), the canted phase mode width becomes comparable to the width of the polarised phase mode. For data around h = −0.75 r.l.u. the canted phase mode width is significantly larger than the polarised phase mode width which is an indication of considerable damping around this Q point. Around h = −0.5 r.l.u. where the main mode and ghost mode overlap in energy our data shows that mode widths are comparable and damping is small which means that the modes at this wave vector are well-defined.

this wave vector mode damping is small and the canted phase mode is well-defined, thus indicating that decays are weak. We conclude that our data clearly shows that for wave vectors around $Q = (\pi/2, \pi/2, 0)$ the mode in the canted phase is significantly damped when compared to wave vectors around $Q = (\pi, 0, 0)$ where the mode damping is small. Such a behaviour is in accord with spin-wave theory which predicts that the single magnon modes at $Q = (\pi/2, \pi/2, 0)$ are more affected by intrinsic decays than the modes at $Q = (\pi, 0, 0)$.

3.6.2 LSWT Guided Approach

Up to this point in the data analysis we ignored exact details of the ghost and main modes such as peak positions, widths and integrated intensities. In this subsection we take a step further and consider these details by analysing our data guided by results of linear spin-wave theory (LSWT) which ignores magnon interactions. The aim is to see how the measured mode width compares with the width predicted for two infinitely long-lived excitations without magnon decay that correspond to the ghost and main modes.

The linear spin-wave theory predictions for the dispersion and intensity of excitations in the canted phase are computed with the help of Matlab code written by Dr. Martin Mourigal. The dispersion is obtained starting from the Hamiltonian of the two-dimensional Heisenberg antiferromagnet on a square lattice with nearest neighbour interactions in the plane J and inter-plane coupling J′, in applied magnetic field

$$\mathcal{H} = \mathrm{J} \sum_{<\mathrm{i,j}>} \mathbf{S}_\mathrm{i}\mathbf{S}_\mathrm{j} + \mathrm{J}' \sum_{<\mathrm{j,k}>} \mathbf{S}_\mathrm{j}\mathbf{S}_\mathrm{k} - \mathrm{g}\mu_\mathrm{B}\mathrm{B} \sum_\mathrm{i} \mathbf{S}_\mathrm{i}^\mathrm{z} \tag{3.15}$$

with the inter-plane coupling parametrised by $\alpha = \mathrm{J}'/\mathrm{J}$. If one starts from the zero field collinear Néel state with the order described by $\mathrm{Q}_\mathrm{AFM} = (\pi, \pi, \pi)$, in a finite magnetic field, the spin components in the laboratory frame $(\mathrm{x}_0, \mathrm{y}_0, \mathrm{z}_0)$ are related to the ones in a rotating frame $(\mathrm{x}, \mathrm{y}, \mathrm{z})$, where the z-direction is the spin direction, via the transformations

$$\begin{aligned} \mathrm{S}_\mathrm{i}^{\mathrm{x}0} &= \mathrm{S}_\mathrm{i}^\mathrm{z}\cos\theta \exp(\mathrm{i}\mathbf{Q}\cdot\mathbf{r}_\mathrm{i}) + \mathrm{S}_\mathrm{i}^\mathrm{x}\sin\theta \\ \mathrm{S}_\mathrm{i}^{\mathrm{y}0} &= \mathrm{S}_\mathrm{i}^\mathrm{y} \\ \mathrm{S}_\mathrm{i}^{\mathrm{z}0} &= \mathrm{S}_\mathrm{i}^\mathrm{z}\sin\theta - \mathrm{S}_\mathrm{i}^\mathrm{x}\cos\theta \exp(\mathrm{i}\mathbf{Q}\cdot\mathbf{r}_\mathrm{i}) \end{aligned} \tag{3.16}$$

where the canting angle is θ. After performing the Holstein-Primakoff transformation, the bosonic Hamiltonian can be written as the sum of three terms (keeping only terms up to second order in the creation and annihilation operators)

$$\mathcal{H} = \epsilon_0 + \mathcal{H}_1 + \mathcal{H}_2 \tag{3.17}$$

where ϵ_0 gives the classical ground state energy, which if minimized, gives the value

of the canting angle $\theta = \sin^{-1}(B/B_s)$ and $B_s = 4JS(2+\alpha)$. For this choice of θ, $\mathcal{H}_1$ vanishes and the second term is

$$\mathcal{H}_2 = \sum_k (A_k a_k^\dagger a_k - \frac{1}{2} B_k (a_k^\dagger a_{-k}^\dagger + a_k a_{-k})) \tag{3.18}$$

where the coefficients read

$$A_k = 2JS(2+\alpha)[\cos 2\theta + \sin^2\theta \gamma_k] + B\sin\theta \tag{3.19}$$

$$B_k = 2JS(2+\alpha)\cos^2\theta \gamma_{k_z} \tag{3.20}$$

The lattice sums in this case are defined as $\gamma_k = (\cos(k_x) + \cos(k_y) + \alpha\cos(k_z))/(2+\alpha)$ and $\gamma_{k_z} = \cos(k_z)$. After a Bogoliubov transformation and substitution of the canting angle, one finally gets the dispersion relation

$$\epsilon_k = 2JS(2+\alpha)\sqrt{(1+\gamma_k)(1-\cos(2\theta)\gamma_k)} \tag{3.21}$$

see Ref. [81] for a detailed derivation of the dispersion.

In order to make $S(\mathbf{Q},\omega)$ obtained in the linear spin-wave theory approximation directly comparable with the data, we need to address the issue of the instrumental resolution. For each constant-h cut the effective resolution has three components. One is the Q resolution that is determined by the uncertainties in $\mathbf{k_i}$ and $\mathbf{k_f}$ which arise as a direct consequence of finite size moderator, sample and detector sizes. The second component is the energy resolution which comes about from uncertainties in the neutron flight path and time of flight. The third component is an induced energy resolution which is due to the choice of a finite integration range in h,k, and l components of Q and is determined by the change in slope of the dispersion relation over the respective integration ranges. For the first component, the Q resolution is always less than a half of the typical integration interval in h used to obtain each cut, so to a good approximation, it can be ignored. The third component is correctly accounted for because the Horace software computes $S(\mathbf{Q},\omega)$ using the underlying Q and energy information of each cut. For the second component, as there is no full energy resolution function calculation available for LET, we do not have access to the energy resolution component. This is approximated using knowledge of the polarised phase dispersion and the polarised phase mode widths extracted for each h. We use identical Q integration ranges for the polarised phase data as for the

canted phase data, and fit the resulting cuts to a Gaussian on a linear background in order to get the polarised phase widths. To extract the broadening coming from the energy resolution, we use the polarised phase dispersion which we convolve with a very small full width at half maximum of energy broadening. We then extract the energy resolution as $\mathrm{FWHM}_\epsilon = \sqrt{\mathrm{FWHM}_{\mathrm{pf}}^2 - \mathrm{FWHM}_{\mathrm{ind}}^2}$, assuming uncorrelated distributions and where $\mathrm{FWHM}_{\mathrm{pf}}$ is the width of the polarised phase mode and $\mathrm{FWHM}_{\mathrm{ind}}$ is the dispersion induced width. We use these numbers as an effective energy resolution to convolve the linear spin wave theory $S(\mathbf{Q},\omega)$ with. To compute $S(\mathbf{Q},\omega)$ we use $J = 0.1$ meV (intra-plane exchange), $J' = 0.032$ meV (inter-plane exchange), $g = 2.03$ (g-factor), $B = 3.35$ T (applied magnetic field), $B_s = 3.95$ T (saturation magnetic field), $T = 0.06$ K (temperature). In terms of intensity, we use a global prefactor to $S(\mathbf{Q},\omega)$ which is set such that the integrated intensity of the linear spin-wave theory prediction for the polarised phase mode is matched to the experimentally extracted integrated intensity of the polarised phase mode. In other words, we set the intensity scale factor according to the intensities predicted by linear spin-wave theory for the polarised phase mode. By using a global intensity scale for all the constant-h cuts extracted from a single sample orientation dataset, we get an integrated intensity mismatch between the experimentally extracted integrated intensities and intensities predicted by linear spin-wave theory of the order of 10%. In conclusion, we use the effective energy resolution to convolve the linear spin-wave theory dynamical structure factor for each constant-h cut with a Gaussian function of given full width at half maximum in ω and set the scale of $S(\mathbf{Q},\omega)$ according to the integrated intensities given by linear spin-wave theory.

LSWT First Approach We proceed and compare the predictions of linear spin-wave theory to the data by two separate means. The first approach consists in using the theory as a guide to fit the data as follows: in the h region where the main and ghost mode are well separated, we fit the data to two Gaussians on a linear background corresponding to the ghost and main mode. We fix the ratio of integrated intensities and ratio of full width half maxima to the values given by linear spin-wave theory for each cut. In the h region where the ghost mode approaches the main mode or more specifically when the separation between the modes is less than 0.075 meV, we fit the data to the skew normal function given by Eq. 3.14. We compare the extracted widths with the widths predicted by theory for the main and shadow modes. We show result of the fits for individual constant-h cuts in Fig. 3.16

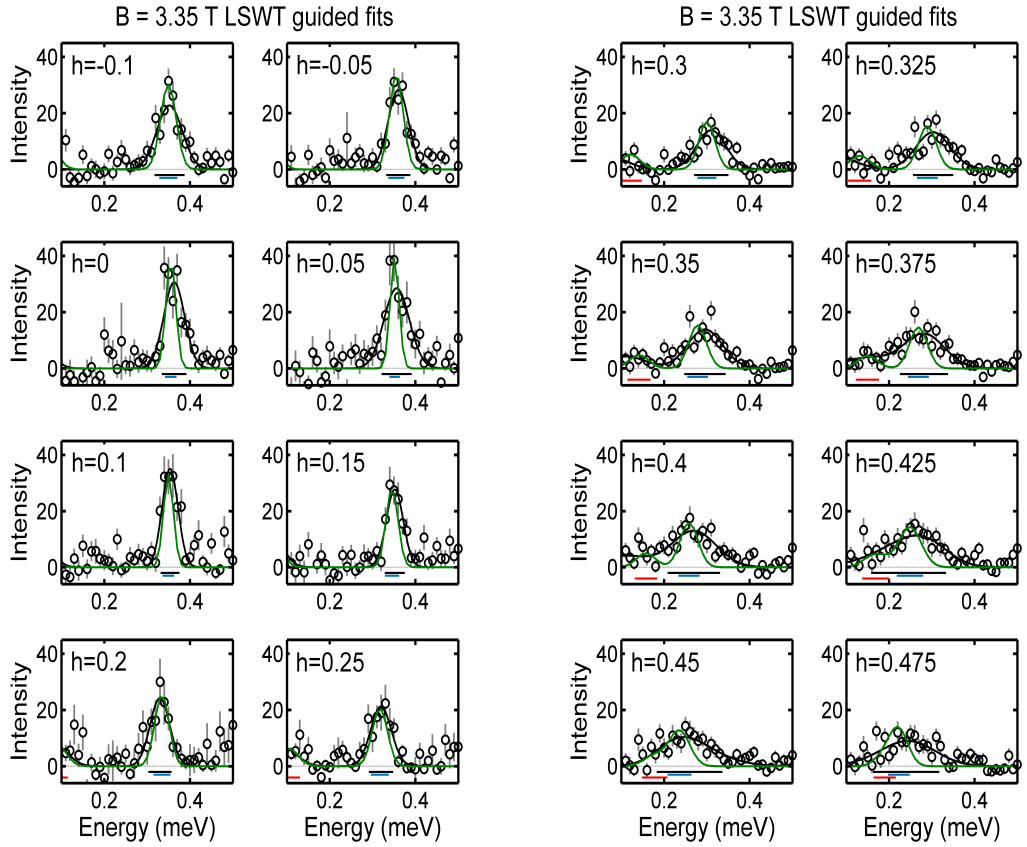

Figure 3.16: Orientation I, intermediate field, constant-h cuts plotted together with the linear spin wave-theory prediction for $S(\mathbf{Q}, \omega)$ (green line) and experimental data fitting (black line). For cuts where the ghost and main mode are well separated, we fit the data to two Gaussians on a linear background whereas for cuts where the two modes begin to overlap we fit the data to a skew normal function on a linear background. See the text for more details. Below the background line (dotted black) we plot the width (FWHM) extracted from the fit (horizontal black line) and the width of the main mode (horizontal blue line) and shadow mode (horizontal red line) as predicted by linear spin-wave theory.

and Fig. 3.17 for wave vectors close to $Q = (\pi/2, \pi/2, 0)$ and in Fig. 3.18 for wave vectors close to $Q = (\pi, 0, 0)$.

We observe that for $h = -0.1$ r.l.u. and up to $h = 0.25$ r.l.u. the fitted width (solid black horizontal line) is comparable to the linear spin-wave theory result for the main mode width (blue horizontal line). This means than for these wave vectors the data is well described by undamped modes without presence of continuum or a weak continuum. For wave vectors between $h = 0.3$ r.l.u. and $h = 0.4$ r.l.u., where

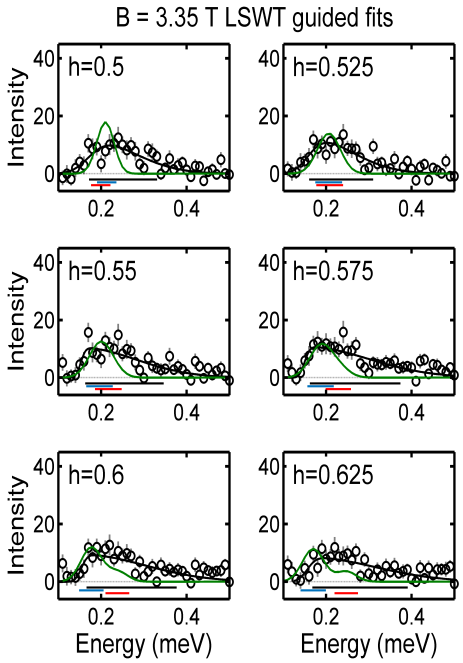

Figure 3.17: Orientation I, intermediate field, constant-h cuts plotted together with the linear spin wave-theory prediction for $S(\mathbf{Q}, \omega)$ (green line) and experimental data fitting (black line). For cuts where the ghost and main mode are well separated, we fit the data to two Gaussians on a linear background whereas for cuts where the two modes begin to overlap we fit the data to a skew normal function on a linear background. See the text for more details. Below the background line (dotted black) we plot the width (FWHM) extracted from the fit (horizontal black line) and the width of the main mode (horizontal blue line) and shadow mode (horizontal red line) as predicted by linear spin-wave theory.

the ghost and main mode are still separated in energy, the fitted width is approximately twice the main mode width. We interpret this as evidence for damping of the main mode. For $h > 0.4$ r.l.u., the extracted width is considerably larger than the combined main and shadow mode widths. This is unambiguously shown for cuts where the two modes almost overlap in energy (see $h > 0.5$ r.l.u.). For these cuts the asymmetry is positive and large. For example, for the $h = 0.525$ r.l.u. cut, where the modes are almost degenerate, we observe that the extracted width is much larger than the ghost and main mode widths. This shows that the extra observed broadening is a result of damping and presence of a continuum.

If we turn our attention to cuts from the orientation II data, we see that the extracted widths are much larger than can be accounted for by the ghost and main mode widths for wave vectors from $h = -0.8$ r.l.u. to $h = -0.725$ r.l.u. As we

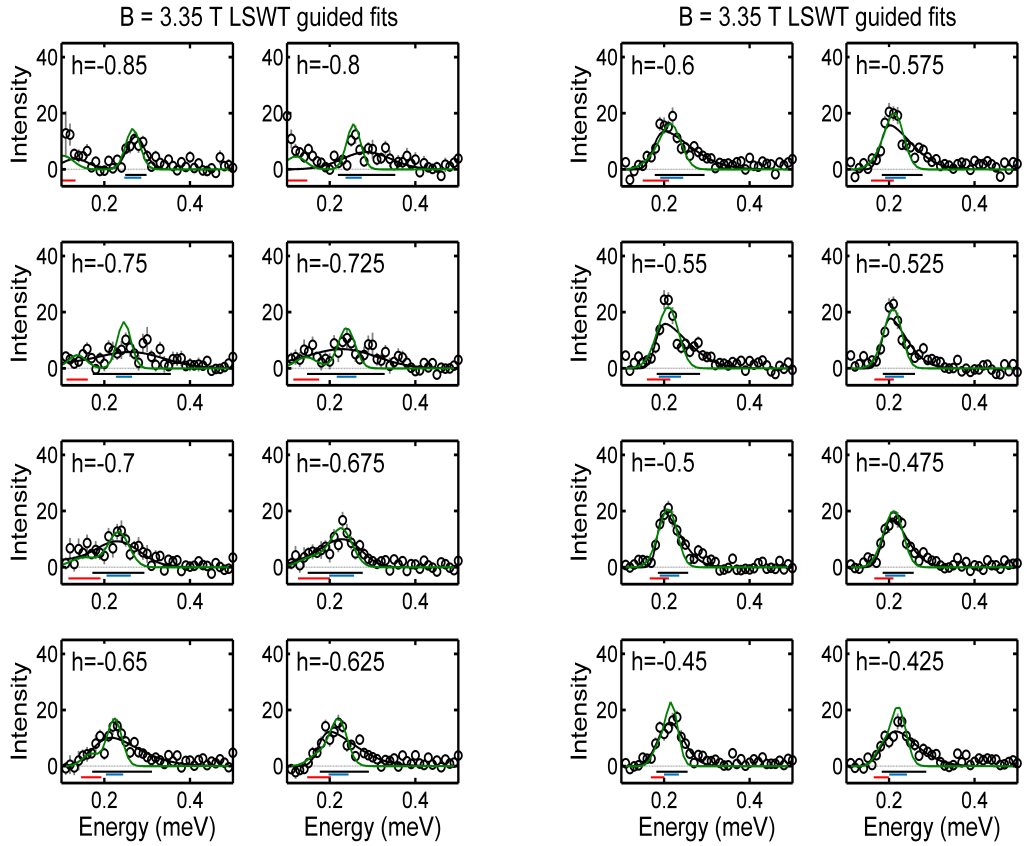

Figure 3.18: Orientation II, intermediate field, constant-h cuts plotted together with the linear spin wave-theory prediction for $S(\mathbf{Q}, \omega)$ (green line) and experimental data fitting (black line). For cuts where the ghost and main mode are well separated, we fit the data to two Gaussians on a linear background whereas for cuts where the two modes begin to overlap we fit the data to a skew normal function on a linear background. See the text for more details. Below the background line (dotted black) we plot the width (FWHM) extracted from the fit (horizontal black line) and the width of the main mode (horizontal blue line) and shadow mode (horizontal red line) as predicted by linear spin-wave theory.

approach the h = −0.5 r.l.u. cuts, we observe that the extracted width is comparable to the main and ghost mode widths and that there is also a small positive asymmetry of the lineshape. This is indicative of the fact that the modes around $(\pi, 0, 0)$ are only weakly damped. The small asymmetry signals the presence of a weak continuum due to multimagnon scattering and not due to mode overlap as for this orientation the ghost mode energy is always smaller than the main mode energy. We conclude that the data cannot be described accurately in terms of two resolution limited,

infinite lifetime modes, and that some other intrinsic process must be responsible for the observed extra broadening, which most likely comes from magnon decays.

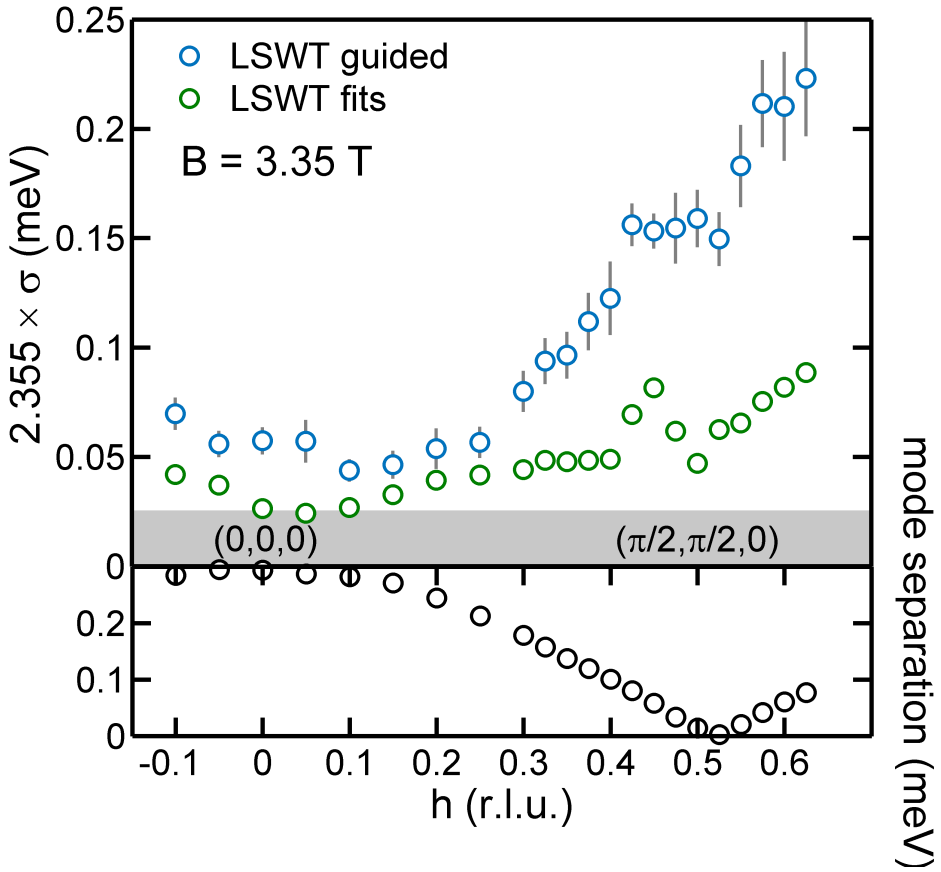

Figure 3.19: Top panel: Canted phase mode widths extracted from the linear spin-wave theory guided fits (blue circles) for wave vectors approaching $Q = (\pi/2, \pi/2, 0)$ and plotted together with the perceived widths given by linear spin-wave theory (green circles - errorbars smaller than symbols). The extra broadening of the data is clearly visible for values of h close to 0.5 r.l.u. The full width at half maximum of the elastic line energy resolution is plotted in grey. The peculiar jump of the perceived width at h = 0.45 r.l.u. is due to the approach of the shadow mode to the main mode position. Bottom panel: Corresponding energy separation between the shadow mode and main mode (black circles). This plot shows that even when the modes overlap at h = 0.525 r.l.u. the data is broader than what linear spin-wave theory perceived width predicts.

LSWT Second Approach We now discuss the second approach we take to compare the widths of the data with predictions given by linear spin-wave theory. We fit the data in the same manner as described in the first approach and extract the

width. We compute the linear spin-wave theory prediction for the main and ghost mode separately. We shift the peaks to the experimentally extracted energy positions. To get the correct integrated intensity ratio of the ghost mode to main mode, we need to be aware of the fact that the one dimensional cuts we take from the data are not constant Q cuts in the true sense. Due to the fact that for a single sample orientation, LET is able to measure only three independent variables out of the four variables that fully characterise $S(\mathbf{Q}, \omega)$, as argued in the section where we describe the LET spectrometer, means that one component of wave vector transfer will vary with energy transfer. In our particular case, each cut has an average h- and l- wave vector transfer component but the k-component varies as a function of energy transfer for fixed h and l. This means that the intensity predicted by linear spin-wave theory is computed at a slightly different Q and energy. To account for this we compute the linear spin-wave theory intensities for the main and ghost mode at the correct Q and energy of the peaks in the data and then adjust the integrated intensity ratio accordingly. The process allows then to add the ghost and main mode lineshapes and fit them identically as the data in order to obtain a perceived mode width. The widths extracted in this way are what is expected from two resolution limited, single particle peaks and reflect the perceived width due to mode overlap. We present summary plots for the two orientations in Fig. 3.19 and Fig. 3.20.

For h going from -0.1 r.l.u. to 0.625 r.l.u. (see Fig. 3.19), the comparison between the canted phase width and the linear spin-wave theory perceived width reveals that for wave vectors around $Q = (0, 0, 0)$, the data width is comparable to what is predicted by linear spin-wave theory, whereas by approaching the $Q = (\pi/2, \pi/2, 0)$ point, the width considerably deviates from the theoretical prediction. This behaviour indicates that close to $Q = (0, 0, 0)$ the canted phase mode width is fairly well described by two infinitely long lived modes and if there is any decay, this tends to be negligible. In contrast, the canted phase widths close to the $Q = (\pi/2, \pi/2, 0)$ point are much larger than what can be accounted for by two non-interacting excitations. This is obvious by looking at the $h = 0.525$ r.l.u. cut where the ghost and main mode are degenerate in energy but the extracted width is still considerably larger than a single mode width.

For wave vectors around $h = -0.75$ r.l.u. the width of the canted phase mode is larger than the perceived width given by linear spin-wave theory, a clear indication of the presence of intrinsic broadening which we attribute to spontaneous magnon decay. For wave vectors close to $h = -0.5$ r.l.u. the canted phase mode width

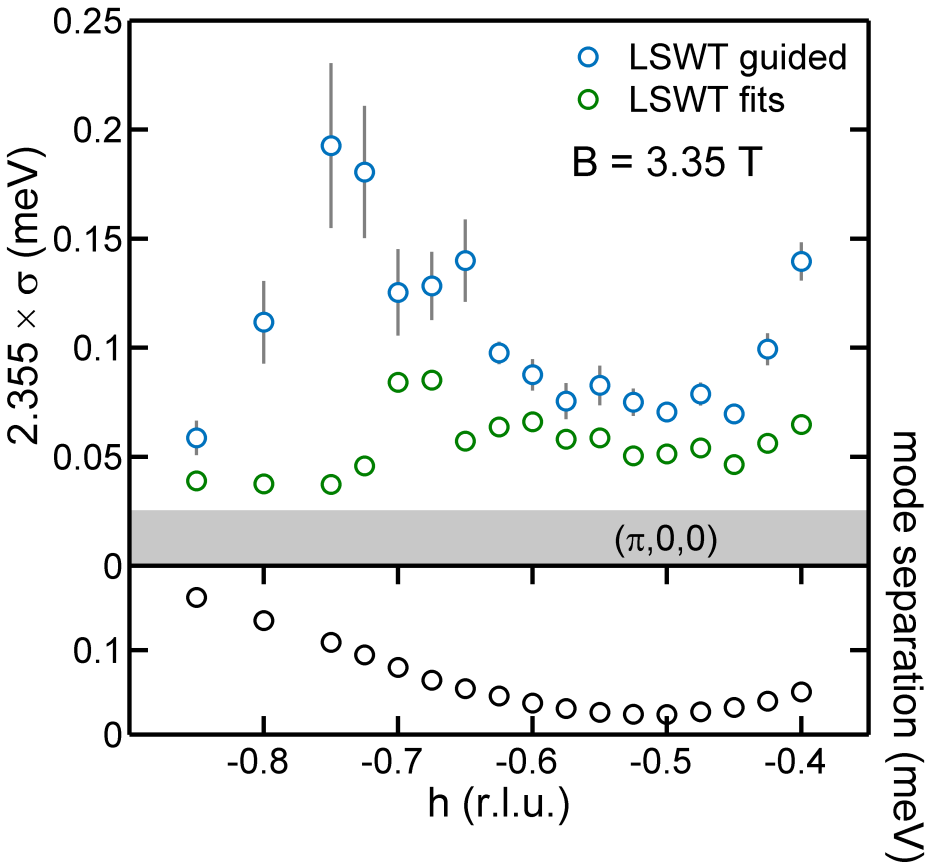

Figure 3.20: Top panel: Canted phase mode widths extracted from the linear spin-wave theory guided fits (blue circles) for wave vectors approaching $Q = (\pi, 0, 0)$ and plotted together with the perceived widths given by linear spin-wave theory (green circles - errorbars smaller than symbols). For values of h close to -0.5 r.l.u. the extracted width is comparable to the perceived width. The full width at half maximum of the elastic line energy resolution is plotted in grey. The jump of the perceived width at $h = -0.7$ r.l.u. is due to the approach of the shadow mode to the main mode position. Bottom panel: Corresponding energy separation between the shadow mode and main mode (black circles). This plot shows that when the modes almost overlap at $h = -0.5$ r.l.u. the canted phase width is comparable to the linear spin-wave theory predicted width.

becomes comparable to the linear spin-wave theory prediction. This means that for wave vectors close to the $Q = (\pi, 0, 0)$ the excitations can be considered to a good approximation as non-interacting which means effects of magnon decay, if present, must be small.

Based on the results of the two approaches we took to analyse the data and compare it with the predictions of linear spin-wave theory, we conclude that this

comparison shows unambiguously that the theory which assumes two infinitely long lived excitations with no interaction between them, fails to describe the canted phase mode width for the majority of sampled Q points. As compared to theory, we observe larger widths at the single particle peak positions and also identify the presence of considerable spectral weight at higher energies, indicative of continuum scattering. This favours the interpretation that interactions between the excitations are responsible for the extra observed broadening.

3.6.3 1/S SWT Comparison

To test and predict the effects of magnon-magnon interaction, we compute the dynamical structure factor S(**Q**,ω) by going to the 1/S order in spin-wave theory. This calculation is described in detail by Fuhrman et al. [87] for the case of a finite inter-layer coupling $\alpha = J'/J = 0.2$ at $B = 0.9B_s$ and $B = 0.95B_s$. We take the same approach and compute S(**Q**,ω) for $\alpha = 0.32$, the value which characterises $(5CAP)_2CuCl_4$ and at $B = 0.85H_s$, where B = 3.35 T and B_s = 3.95 T.

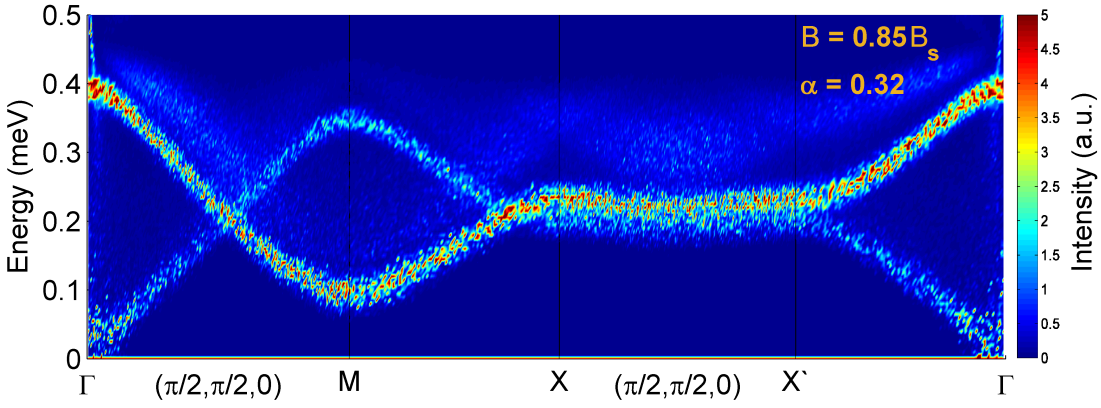

Figure 3.21: Dynamical structure factor computed using the 1/S spin-wave theory plotted along the $\Gamma - M - X - X' - \Gamma$ reciprocal space path. See Fig. 3.3 for definition of the high-symmetry points of the Brillouin zone. Two magnon continuum scattering is predicted to occur everywhere in the (hk0) plane above the single magnon energies. A convolution with a Gaussian of full width at half maximum 0.025 meV has been performed.

The starting point is the Hamiltonian given by Eq. 3.15, where the bosonic Hamiltonian now contains terms up to fourth order in the creation and annihilation operators

$$\mathcal{H} = \epsilon_0 + \mathcal{H}_1 + \mathcal{H}_2 + \mathcal{H}_3 + \mathcal{H}_4 \tag{3.22}$$

where the exact form of the terms in the equation are given in the appendix of Ref. [87].

The computation is performed using Matlab code based on work in Ref. [87]. It is a perturbative approach where the effects of magnon-magnon interactions are explicitly considered at the 1/S order in spin-wave theory. Frequency independent contributions to the harmonic dispersion which come from canting angle renormalisation and Hartree-Fock mean-field decoupling of the quartic term in the Hamiltonian are also included. The cubic self-energies are computed using a Monte-Carlo integration scheme with adjustable number of integrals over which the energies are evaluated. The dynamical structure factor is first computed in the local spin frame ($\hat{z}$ along the spin direction) and then transformed in the laboratory frame ($\hat{z_0}$ along the field) using the transformations

$$\begin{aligned} \mathrm{S}^{\mathrm{x_0x_0}}(\mathbf{Q},\omega) &= \sin^2\theta \mathrm{S}^{\mathrm{xx}}(\mathbf{Q},\omega) + \cos^2\theta \mathrm{S}^{\mathrm{zz}}(\mathbf{Q}-(\pi,\pi,\pi),\omega) \\ \mathrm{S}^{\mathrm{y_0y_0}}(\mathbf{Q},\omega) &= \mathrm{S}^{\mathrm{yy}}(\mathbf{Q},\omega) \\ \mathrm{S}^{\mathrm{z_0z_0}}(\mathbf{Q},\omega) &= \cos^2\theta \mathrm{S}^{\mathrm{xx}}(\mathbf{Q}-(\pi,\pi,\pi),\omega) + \sin^2\theta \mathrm{S}^{\mathrm{zz}}(\mathbf{Q},\omega) \end{aligned} \tag{3.23}$$

where θ is the canting angle and S^{xx}, S^{yy} and S^{zz} are the local frame dynamical structure factor components.

In order to obtain the full dynamical structure factor, as measured by neutron scattering, the g-factor components, magnetic form factor and the Bose population factor are added. Finally, an ω convolution of $\mathrm{S}(\mathbf{Q},\omega)$ with a Gaussian of 0.0255 meV full width at half maximum (FWHM) is performed in order to mimic the instrumental energy resolution. The result is plotted in Fig. 3.21 for a high symmetry path through reciprocal space, in the (hk0) plane.

The 1/S dynamical structure factor shows the presence of two transverse one magnon branches corresponding to the main (more intense) and ghost modes. Two magnon continuum is predicted for all wave vectors above the single magnon energies, apart from the Γ point which is predicted not to be affected by spontaneous decays. At the middle of the magnetic zone boundary point, $\mathrm{Q} = (\pi/2, \pi/2, 0)$, the continuum starts immediately after the one magnon energy and goes up to approxi-

mately 0.4 meV. For the the X point, Q = $(\pi, 0, 0)$, there seems to be a gap between the one magnon peak and the start of the continuum, at approximately 0.3 meV. The continuum occurs at energies between 0.3 to 0.4 meV for this wave vector.

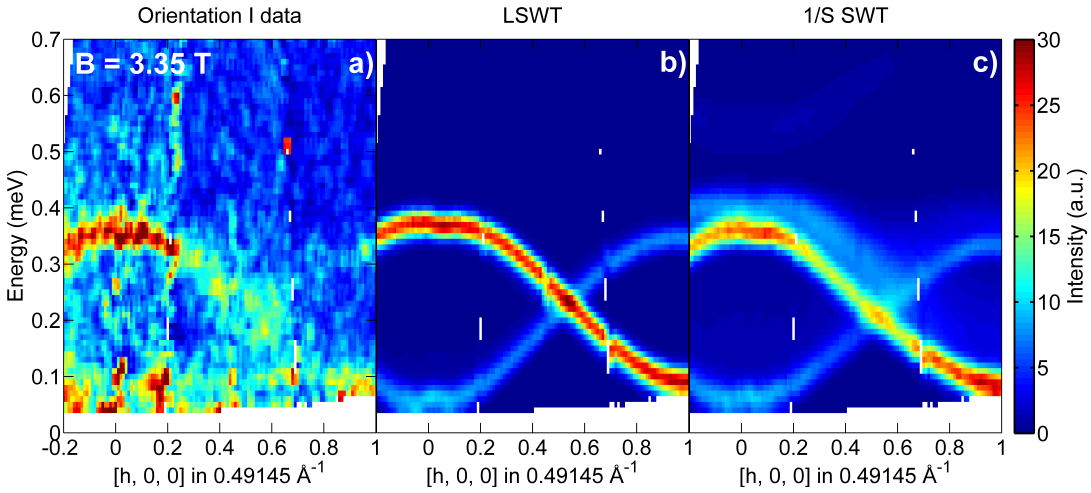

Figure 3.22: Two dimensional scattering false colour plots extracted from the a) data collected in the orientation I that covers wave vectors close to $(\pi/2, \pi/2, 0)$. Alongside we plot the corresponding S($\mathbf{Q}$,ω) predictions of b) linear spin-wave theory and c) 1/S spin-wave theory. Theoretical predictions were convolved with a Gaussian of 0.0255 meV FWHM to account for the instrumental energy resolution.

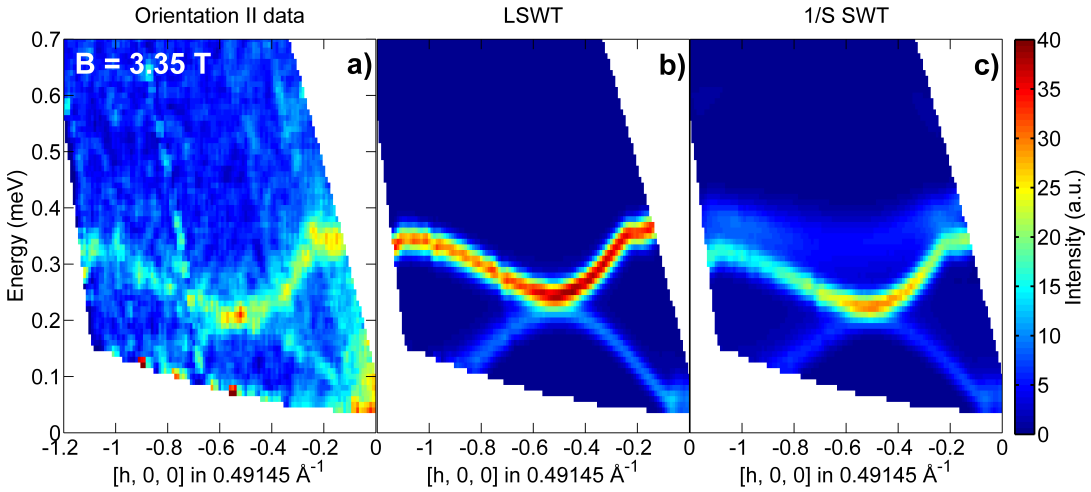

Figure 3.23: Two dimensional scattering false colour plots extracted from the a) data collected in the orientation II that covers wave vectors close to $(\pi, 0, 0)$. Alongside we plot the corresponding S($\mathbf{Q}$,ω) predictions of b) linear spin-wave theory and c) 1/S spin-wave theory. Theoretical predictions were convolved with a Gaussian of 0.0255 meV FWHM to account for the instrumental energy resolution.

In Fig. 3.22 and Fig. 3.23 we plot the experimentally measured dynamical structure factor together with predictions of linear spin-wave theory and 1/S spin-wave theory, for wave vectors along two given paths in reciprocal space. The data shows the presence of the main and ghost mode dispersions and evidence for continuum scattering spread over significant portions of reciprocal space. A visual comparison of the data with linear spin-wave theory (LSWT) shows that LSWT fails to reproduce the intensity variation of the data, by predicting an almost constant intensity as a function of h and does not predict continuum scattering. On the other hand, the 1/S spin-wave theory predicts continuum scattering for all wave vectors above the single magnon energies. It also captures the data intensity variation better than LSWT, with higher intensity around h = 0 and h = 1 r.l.u. and lower intensity around h = 0.5 r.l.u. for orientation I data and higher intensity around the h = −0.5 r.l.u. as compared to h = −0.2 r.l.u. for orientation II data. We conclude that visually, going to 1/S in spin-wave theory, accounts better for the observed $S(\mathbf{Q},\omega)$ than the linear spin-wave theory. This indicates that including interactions between excitations explicitly is necessary in order to correctly describe the data.

To confirm that 1/S spin-wave theory does a better job in describing the data as compared to the linear approximation, we plot the 1/S spin-wave theory $S(\mathbf{Q},\omega)$ for the same series of constant-h cuts as before, in Fig. 3.24 and Fig. 3.25 for orientation I data and in Fig. 3.26 for orientation II data. The 1/S approximation predicts a complex lineshape with a continuum at higher energies which overall agrees with the data. The widths of the single particle modes are well described by the 1/S approximation, with peak positions in good agreement with the data. The momentum dependence of the intensity is also captured acceptably by the 1/S approximation. On closer inspection of individual cuts though, we see that it is difficult to exactly assess the exact level of agreement between theory and data with respect to the shape of the continuum and subtle features of the main peak shapes such as asymmetry. We think that improved statistical quality of the data would allow for a much more in-depth investigation of the shape of the continuum. Due to the overall quality of the data and the various approximations we have made in the analysis we are restricted from making a fully quantitative comparison between data and 1/S theory mainly due to the fact that the data is not sensitive to fitting such a complex lineshape as is predicted by the 1/S spin-wave theory.

It is instructive to compare theoretical predictions for S=1/2 with predictions for the S=5/2 classical case. For the classical case, the damping of the one-magnon

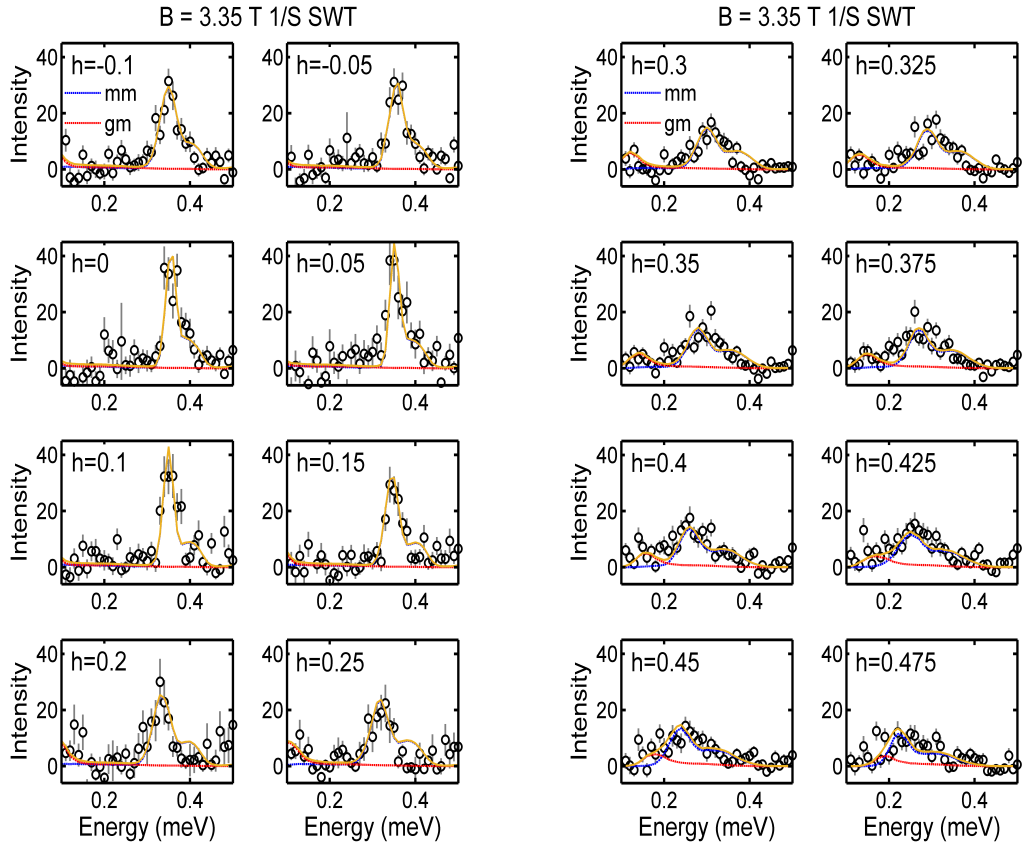

Figure 3.24: Orientation I, intermediate field constant-h cuts (black circles) plotted together with the 1/S spin-wave theory prediction for $S(\mathbf{Q},\omega)$(yellow line). For each constant-h cut the corresponding contribution from the main mode (blue interrupted line) and ghost mode (red interrupted line) is plotted as well. The renormalised theory predicts a complex lineshape with presence of continuum scattering at higher energies above the single particle peaks.

mode is much weaker due to the reduced coupling between one and two magnon excitations for large spin values. Although the width of the single particle peak is broadened (magnons acquire finite lifetimes), the excitations remain well-defined throughout the Brillouin zone and the predicted continuum is weak for S=5/2. This is in contrast to the S=1/2 case, where the redistribution of spectral weight into a higher energy continuum determines the complete disappearance of single-particle peaks for some wave vectors. Neutron experiments on the S=5/2 layered material $Ba_2MnGe_2O_7$ [83] have shown indication of magnon decay although the widths extracted from the data were 2-3 times larger than what is predicted by

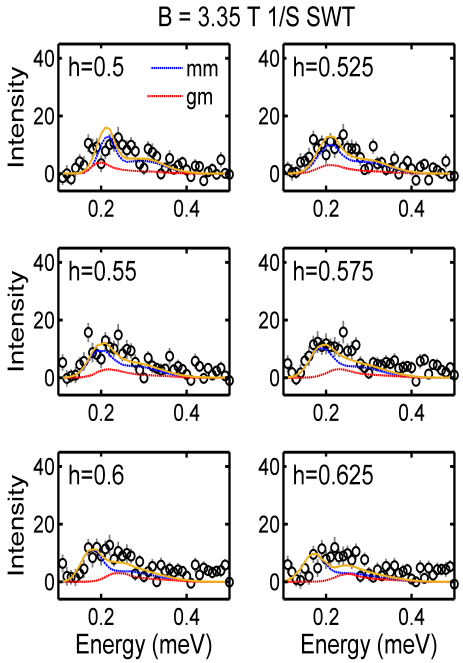

Figure 3.25: Orientation I, intermediate field constant-h cuts (black circles) plotted together with the 1/S spin-wave theory prediction for $S(\mathbf{Q},\omega)$ (yellow line). For each constant-h cut the corresponding contribution from the main mode (blue interrupted line) and ghost mode (red interrupted line) is plotted as well. The renormalised theory predicts a complex lineshape with presence of continuum scattering at higher energies above the single particle peaks.

the 1/S theory, so it is still unclear whether the observed broadening comes solely from intrinsic decays or whether it is the result of mode overlap and experimental resolution.

In conclusion, we measured the spin excitation spectrum of $(5CAP)_2CuCl_4$ at $B = 0.85H_s$, in the canted spin phase, for wave vectors close to $Q = (\pi/2, \pi/2, 0)$ and $Q = (\pi, 0, 0)$. For the S=1/2 case one-magnon modes are predicted to lose coherence and become overdamped within most of the Brillouin zone. A sign of the presence of intrinsic decays is considered to be a more pronounced broadening of the one-magnon peaks for $(\pi/2, \pi/2, 0)$ as compared to $(\pi, 0, 0)$, where the peaks should remain better defined. Another indication of decays is a redistribution of spectral weight away from the one particle peak, towards the two particle continuum. Our measurements qualitatively support these predictions and show that the observed modes are broader than what is predicted by linear spin-wave theory in the absence of interactions. Including interactions to 1/S order in spin-wave theory predicts a

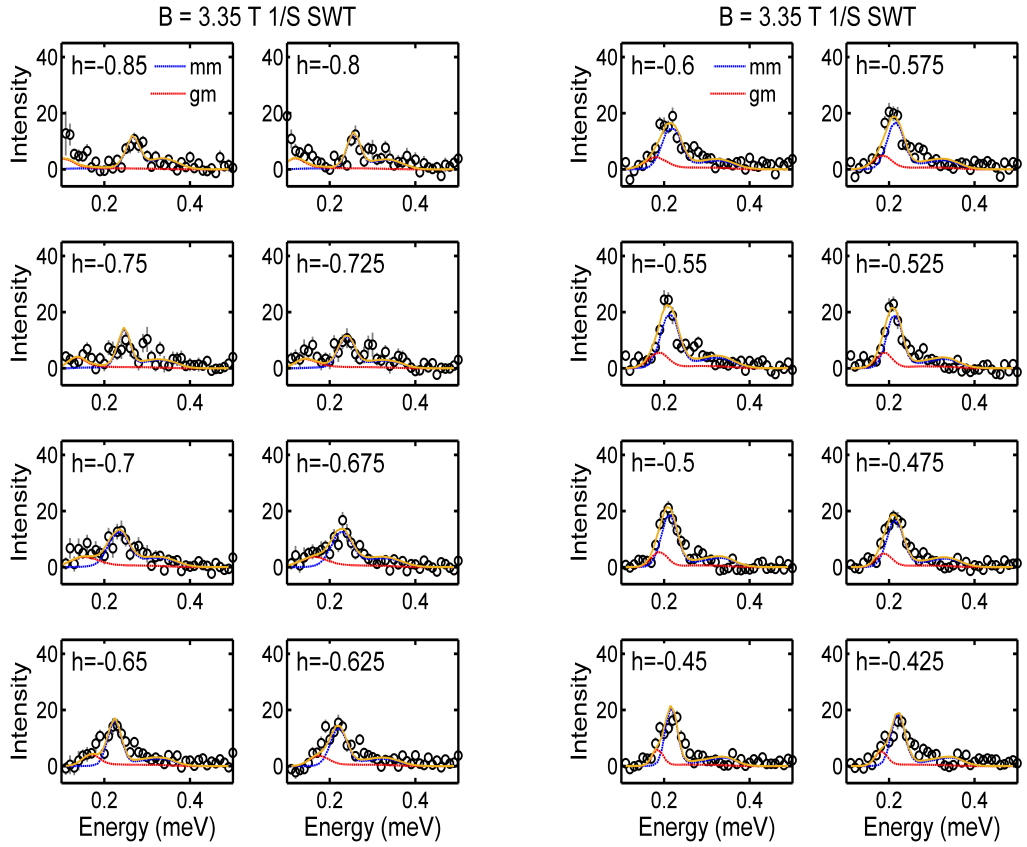

Figure 3.26: Orientation II, intermediate field constant-h cuts (black circles) plotted together with the 1/S spin-wave theory prediction for $S(\mathbf{Q},\omega)$ (yellow line). For each constant-h cut the corresponding contribution from the main mode (blue interrupted line) and ghost mode (red interrupted line) is plotted as well. The renormalised theory predicts a complex lineshape with presence of continuum scattering at higher energies above the single particle peaks.

continuum and agrees better with the measured data. As the $(\pi/2, \pi/2, 0)$ point is approached, the measured lineshape becomes more and more asymmetric as fitted to a normal skew distribution and the spectral weight is redistributed towards higher energies into the continuum. As the $(\pi, 0, 0)$ point is approached, the lineshape becomes asymmetric with the development of a high energy shoulder which is associated with the two-magnon continuum. There is a corresponding increase in the intensity of the one-magnon mode. This behaviour is in general good agreement with the predictions of the 1/S spin-wave theory.

Proposal of Definitive Experiment We propose here a definitive inelastic neutron scattering experiment to confirm theoretical predictions of magnon decay in $(5CAP)_2CuCl_4$ by allowing for a full quantitative comparison between data and 1/S spin-wave theory for the decay rates and shape and intensity of the two-magnon continuum.

In this chapter we showed experimental evidence which qualitatively supports the presence of magnon decay in $(5CAP)_2CuCl_4$. From spin waves measured at $B = 0.85 \times B_s$ we extracted the magnon linewidth and identified mode damping, with increased mode widths for wave vectors around $Q = (\pi/2, \pi/2, 0)$ as compared to mode widths for wave vectors around $Q = (\pi, 0, 0)$, which is in accord with predictions of 1/S spin wave theory. The data we collected from LET prevents a full quantitative comparison with theory due to several reasons: a) the insufficient statistical quality of the data does not allow for fitting to such a complex lineshape as is predicted by 1/S spin-wave theory; b) the presence of two, almost degenerate magnon modes, which almost overlap at the magnetic zone boundary, with the shadow mode intensity of approximately a third of the main mode intensity, makes the increased broadening extracted from the data appear as decays; c) due to the fact that at the time of the LET experiment we were not aware that the g-factor is slightly anisotropic for $(5CAP)_2CuCl_4$ the saturation field known from literature was lower than in our sample geometry. The experiment was thus not performed at an ideal value of the applied magnetic field in order to maximize the effects of magnon decay such as the predicted complete disappearance of the single magnon peaks with almost all spectral weight found in the two-magnon continuum and the appearance of double-peak lineshapes in the dynamical structure factor.

For the proposed experiment we want to use LET at the ISIS neutron source and plan to overcome the issues presented above by: a) using a deuterated sample mass twice to three times larger than what we had, which although expensive, was successfully grown before. The installation of a new elliptical guide system on LET in the summer of 2016 will increase the neutron flux at the sample position by a factor of three compared to what was available at the time of the original experiment. Combined with a larger sample mass, it will lead to an overall gain of approximately nine times in effective flux; b) At a higher applied magnetic field such as $B = 0.95 \times B_s$, magnon decay effects are predicted to be more severe (see Fig. 3.27) with overdamped modes almost indistinguishable from a continuum for wave vectors close to $Q = (\pi/2, \pi/2, 0)$ and presence of double-peak lineshapes along

the $\Gamma - X$ reciprocal space path. The higher applied magnetic field will also have the advantage of changing the integrated intensity ratio between the shadow mode and main mode from approximately 1/3 to approximately 1/10. This would then make the data interpretation straightforward by eliminating the possibility that the observed mode broadening comes from mode overlap as the measured dynamical structure factor will be dominated by the main mode. The 1/S spin-wave theory calculation gives exact predictions for the shape and intensity of the two-magnon continuum and the one-magnon decay rate, which are to be directly compared with the data.

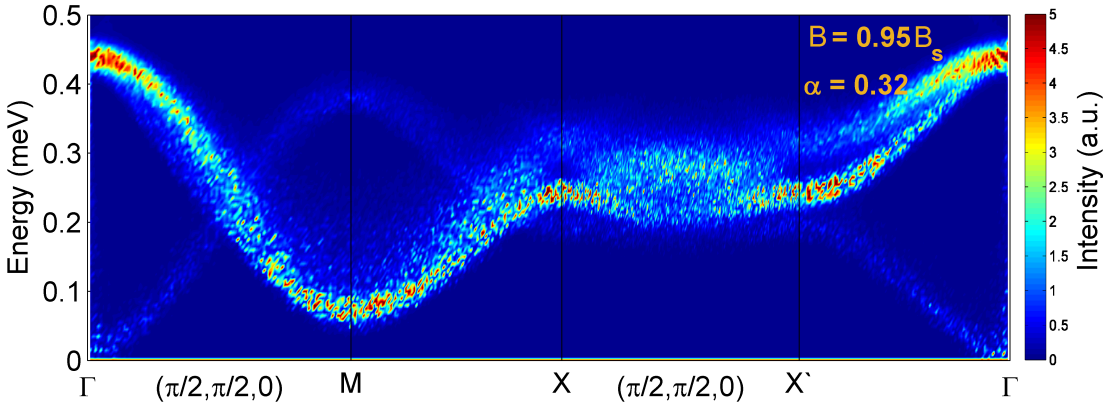

Figure 3.27: 1/S spin wave theory prediction for $S(\mathbf{Q}, \omega)$ for an inter-layer coupling $\alpha = 0.32$ (value for CAPCC) and at $B = 0.95B_s$. A convolution with a Gaussian of full-width at half maximum 0.025 meV has been performed.

LET has a complete detector bank covering horizontal scattering angles from -40 to +140 degrees and from -30 to +30 degrees in the vertical direction which will allow the excitations to be measured in a large region of momentum space. Such a large Q coverage makes LET preferable to a standard triple-axis instrument where one can only perform measurements at specific points in Q space.

In view of extracting magnon decay rates (mode widths) and the shape of the two-magnon continuum, we argue that the energy resolution typically obtained on LET is high enough. We back this up by referring to Fig. 3.14 and Fig. 3.15 where we show the polarised phase mode is approximately resolution limited, with the extra broadening coming from the finite Q range over which we average the signal. For example for $E_i = 2$ meV incident energy neutrons the full width at half maximum of the energy resolution at the elastic line is approximately $\Delta E = 0.025$ meV.

In conclusion, a better optimised, inelastic neutron experiment will allow for the

unambiguous confirmation of field-induced magnon-decay in CAPCC by allowing a quantitative comparison of the extracted two-magnon continuum and one-magnon decay rates with the predictions of 1/S spin-wave theory. The presence of magnon-decay in the case of the square-lattice and quantum limit S=1/2 is important to be firmly established as decays are predicted for a large class of spin systems, but have only been experimentally observed in the classical S=5/2 square-lattice [83] and the S=2 triangular lattice [93], and not for S=1/2.

Chapter 4

Triplon Lifetime and Blue Shift in the Haldane Chain Y_2BaNiO_5

In this chapter we extend the experimental study of magnon lifetime effects in a model Haldane spin chain to very high resolution using neutron spin-echo techniques. In the introductory part we motivate the study, we introduce the Heisenberg spin model in one dimension and show the difference in properties that arises from considering half-integer or integer spins. We briefly present the ground state properties and excitations of half-integer antiferromagnetic spin chains and then focus on the ground and excited states of the S=1 Heisenberg antiferromagnetic chain. In section 4.2, we give details about theoretical predictions based on the non-linear sigma model for the lifetime of the triplet excitations and gap energy evolution with temperature. In section 4.3, we present the properties of Y_2BaNiO_5, an excellent realisation of the S=1 Heisenberg chain, and in the next section we describe neutron spin-echo experiments performed on Y_2BaNiO_5. In sections 4.5 and 4.6 we present experimental results for the temperature evolution of the triplet excitations and gap energy, giving a physical interpretation to the data. We end the chapter with conclusions and closing remarks.

4.1 Introduction

Quantum spin chains are paradigmatic model systems whose study provides insight into the physics related to collective, quantum many-body effects. For example, quantum spin chains are ideal for the study of quantum fluctuations which are greatly enhanced in one-dimension and which give rise to disordered quantum ground states with short range correlations and exotic excitations with no classical analogues. Quantum spin chains are also studied in connection to quantum computation where understanding quantum correlations in the ground state plays a crucial role in the manipulation of quantum states. Due to their reduced spatial dimensionality, quantum spin chains provide a considerable theoretical simplification to the many-body problem, while at the same time retaining enough complexity to give rise to rich physics. Theoretical methods and predictions can be tested against experiments performed on suitable materials which are very good representations of model chains. The most utilised theoretical methods to study quantum spin chains are exact calculations such as the Bethe ansatz, quantum field theoretical approaches such as conformal invariance, semi-classical non-linear σ-model (NLSM), bosonisation, many-body methods such as the Schwinger boson mean field, series expansion and numerical methods such as exact diagonalisation (ED), density matrix renormalisation group (DMRG) and quantum Monte-Carlo (QMC). Experimentally there are a lot of excellent realisations of the different variations of quantum spin chains which can be studied by several techniques which include neutron scattering, magnetic susceptibility, magnetization and specific heat measurements, electron spin resonance (ESR) and nuclear magnetic resonance (NMR) to name a few.

In this chapter we present a neutron spin-echo study of Y_2BaNiO_5, an excellent realisation of a famous quantum spin chain model, the S=1 Heisenberg antiferromagnetic chain, also known as the Haldane chain [94, 95]. We have chosen to study the S=1 Heisenberg chain because it offers the possibility of investigating symmetry protected topological states with short range quantum entanglement which are of major importance to quantum computing. The singlet ground state of the Haldane chain constitutes a symmetry protected topological state because it does not break SO(3) spin rotational symmetry and has a gap to the first triplet excited state. Despite the absence of classical long range antiferromagnetic order, the ground state is quantum coherent due to the presence of finite quantum string order [12, 96]. The excitations above the ground state are predicted to be infinitely long lived, protected

from external perturbations by the Haldane gap thus preserving the coherence of the ground state. An excitation can be interpreted [97] as introducing a defect in the string order which can propagate along the chain until it encounters another defect, interacts with it and decays. The finite lifetime which results from this interaction is reflected in the degree of coherence of the ground state. For a real system, defects are of two major types. Static defects which arise from chemical impurities and break the chains, and thermally excited defects or excitations which are mobile and can travel along the chain. This study aims at understanding how robust the triplet excitations are and what are the possible mechanisms that lead to finite lifetimes and decoherence in a real S=1 Haldane chain material, Y_2BaNiO_5.

The starting point in the study of the static and dynamic properties of quantum spin chains is the spin Hamiltonian which encapsulates the symmetries, types of interactions and strengths of interactions for the models under consideration. The Hamiltonian of a general anisotropic XYZ antiferromagnetic chain is written as

$$\mathcal{H} = \mathrm{J}\sum_{\mathrm{i}}[(1+\gamma)\mathbf{S}_{\mathrm{i}}^{\mathrm{x}}\mathbf{S}_{\mathrm{i+1}}^{\mathrm{x}} + (1-\gamma)\mathbf{S}_{\mathrm{i}}^{\mathrm{y}}\mathbf{S}_{\mathrm{i+1}}^{\mathrm{y}} + \Delta\mathbf{S}_{\mathrm{i}}^{\mathrm{z}}\mathbf{S}_{\mathrm{i+1}}^{\mathrm{z}}] \tag{4.1}$$

where J represents the intra-chain nearest neighbour exchange coupling and γ and Δ parametrise the anisotropy. The general case of the anisotropic XXZ chain ($\gamma = 0$, $\Delta \neq 0$) with the properties of its different phases is nicely presented in chapter one of the book on quantum magnetism by Richter and Bishop [98]. Here, we will focus on the isotropic Heisenberg case ($\gamma = 0$, $\Delta = 1$) and will consider the S=1/2 and S=1 cases to illustrate the major differences between half-integer and integer quantum spin chains.

We start with a brief presentation of the S=1/2 Heisenberg antiferromagnetic chain. The T=0 ground state is a macroscopic singlet as a result of large quantum fluctuations which prevent magnetic long range order to establish, as first shown by Bethe [39]. The ground state energy is given by $\mathrm{E}_0 = -\mathrm{NJln2}$ where N is the number of spins in the chain. The static spin-spin correlation function behaves as $\langle \mathrm{S}_0\mathrm{S}_\mathrm{n}\rangle \propto (-1)^{\mathrm{n}}\frac{\sqrt{\ln(\mathrm{n})}}{\mathrm{n}}$ which shows that the correlation between spins decays as a power-law with increasing distance. The elementary excitations form a particle-hole continuum and have fermionic character as opposed to magnons which have bosonic character [99]. They are S=1/2 quasiparticles known as spinons and give rise to an excitation continuum which has a lower and upper bound [99, 100]

$$E_l(Q) = \frac{\pi}{2} J \sin(Q) \tag{4.2}$$

which corresponds to the lower bound of the dispersion in Fig. 4.1 (left). The upper bound on the continuum is given by

$$E_u(Q) = \pi J \sin(Q/2) \tag{4.3}$$

and corresponds to the upper limit of the dispersion in Fig. 4.1 (left). The excitations are gapless and they are unbound so they are able to travel independently along the chain. They share energy and momentum between them and give rise to a continuum of scattering as observed experimentally from inelastic neutron scattering measurements [3, 71, 72, 101, 102].

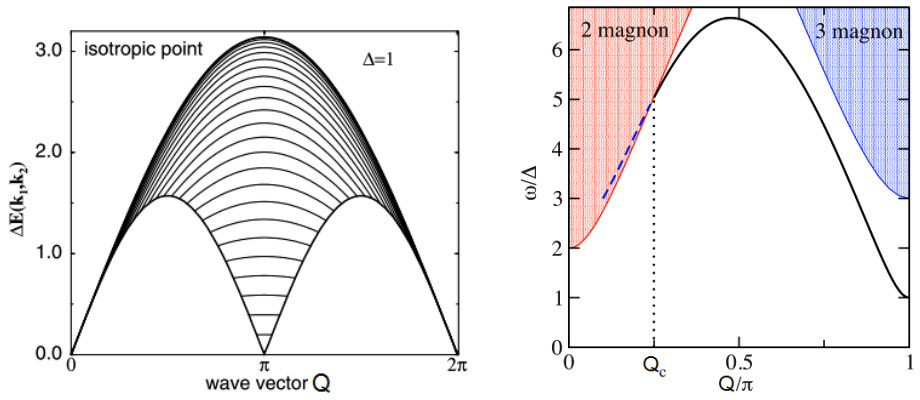

Figure 4.1: Left: Continuum spin excitation spectrum of the isotropic S=1/2 Heisenberg antiferromagnetic chain (shaded area). Right: Triplet excitation dispersion of the S=1 Heisenberg antiferromagnetic chain (black line) and higher energy two and three magnon continua (red and blue shaded areas). Taken from Refs. [98, 103].

Depending on the spin quantum number, antiferromagnetic Heisenberg chains have totally different ground and excited state properties, as first conjectured by Haldane [94, 95]. Using field theory arguments he showed that the ground state of an integer-spin Heisenberg chain is disordered with exponentially decaying spin-spin correlations. It is separated from the first excited state by a spectral gap which is sizeable for S=1 and exponentially small in the large spin limit. In the following paragraphs we will concentrate on the properties of the S=1 Heisenberg antiferromagnetic chain or as it is better known, the S=1 Haldane chain.

A coherent picture of the properties of the Haldane chain has resulted from several theoretical approaches which include finite-size Monte Carlo [104], density

matrix renormalisation group [103, 105, 106] and exact diagonalisation [107]. The ground state energy per spin is $E_0 = -1.4J$ and the correlation length is $\xi \approx 6$ (in units of spin-spin distance) with the spin-spin correlations decaying exponentially as $\langle S_0^\alpha S_n^\beta \rangle \propto (-1)^n \delta_{\alpha,\beta} n^{-1/2} e^{-n/\xi}$ which is in contrast with the power-law decay that characterises half-integer Heisenberg antiferromagnetic chains. The singlet ground state of the S=1 Haldane chain can be naturally understood in terms of the Affleck-Kennedy-Lieb-Tasaki (AKLT) model [108]. In this model each S=1 can be viewed as being locally formed of two S=1/2 spins that combine on each site in a fully symmetric triplet state with total S=1. Each of the two S=1/2 spins then pairs with a neighbouring S=1/2 from the next site on the left and right, in an antisymmetric singlet state (see Fig.4.2). The model predicts that in the case of finite size chains the ground state can be considered to have an effective S=1/2 at each end. The effective spins have been observed in experiments on both doped NENP using EPR [109] and in Mg doped Y_2BaNiO_5 using NMR [110] and INS [111].

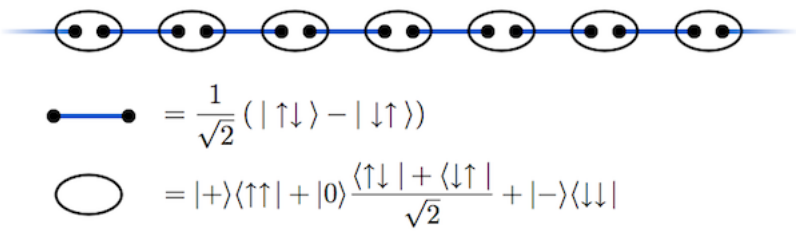

Figure 4.2: The Valence Bond Solid (AKLT) model for the ground state of the S=1 Haldane chain. Black ellipses represent the triplet state formed by two S=1/2 spins at each site. Blue lines represent the pairing of S=1/2 spins on different sites into a singlet state.

An important property of the S=1 Haldane chain is the presence of quantum coherence in the ground state. The coherence arises as a result of 'hidden' string order [12] that has a strong non-local character and is described by the string correlation function $\langle S_i^z \exp(i\pi \sum_{i<j<i'} S_j^z) S_{i'}^z \rangle$, which for large distances tends to a constant [112]. This highly non-classical order can be understood in terms of the three possible eigenstates of the S^z operator with basis states $|+1\rangle$, $|-1\rangle$ and $|0\rangle$. The states $|\pm 1\rangle$ have a classical analogue in the sense that out of them one can build a Néel state as $|\ldots, +1, -1, +1, -1, \ldots\rangle$, whereas $|0\rangle$ does not. String order is carried by states where spin sites with $S^z = 0$ are inserted in the Néel state. A good approximation to the ground state wave function is a coherent superposition of all such states with a weighting factor that decreases exponentially with the number of

$S^z = 0$ sites [108].

The nature of the singlet ground state and the presence of a gap which separates it from the first excited triplet state have a direct consequence for the spin dynamics of the Haldane chain. The low energy excitation spectrum of the S=1 Haldane chain is markedly different from that of the S=1/2 Heisenberg antiferromagnetic chain as seen in Fig. 4.1. The T=0 Haldane spectrum predicted by theory is dominated by well-defined, infinitely long-lived, one-magnon excitations which disperse with wave vector Q according to

$$E(Q) = \sqrt{\Delta^2 + v^2 \sin^2(Q - \pi)} \tag{4.4}$$

where Δ is the Haldane gap and v is the spin-wave velocity which is connected to the main intra-chain exchange by $v = 2.49J$ (for an isotropic chain) [106]. The one-magnon dispersion has a minimum $E_{min} = \Delta$ at $Q = \pi$ and a maximum $E_{max} = 2.7J$ near $Q = \pi/2$. The one-magnon spectrum terminates abruptly at a critical value of the wave vector $Q_c = 0.23\pi - 0.24\pi$, and the dynamical response is dominated by two-magnon excitations for $Q < Q_c$. At $Q = 0$ the two-magnon continuum begins at energies $E > 2\Delta$. The spectrum at $Q = \pi$ and energies $E > 3\Delta$ is dominated by a three-magnon continuum of excitations. The asymmetry in the excitation spectrum is indicative of the absence of broken translational symmetry in the ground state of the S=1 chain, unlike the case of the S=1/2 chain.

In real materials there is always a finite anisotropy which has to be taken into account when investigating the properties of the S=1 Haldane chain. In general the spin Hamiltonian with anisotropy has the form

$$\mathcal{H} = J \sum_i \mathbf{S}_i \mathbf{S}_{i+1} + \sum_i D(\mathbf{S}_i^z)^2 \tag{4.5}$$

where D sets the strength of the single-ion anisotropy.

The effect of anisotropy on the properties of the Haldane chain was theoretically considered by Golinelli et al. [113–115]. They studied the effect of single-ion anisotropy of the easy-plane type (D) on the gap energy and showed that the Haldane gap is split into a lower lying doubly degenerate doublet and a higher singlet. Their numerical data fitted quite well a linear dependence of the gap, for small values of D/J up to 0.25, by

$$\Delta^{-} = \Delta(0) + 1.41\mathrm{D} \tag{4.6}$$

$$\Delta^{+} = \Delta(0) - 0.57\mathrm{D} \tag{4.7}$$

where $\Delta(0) = 0.4105\mathrm{J}$ is the value of the purely isotropic model and D is the single-ion anisotropy parameter. When D is increased, the lowest gap continuously closes and it is exactly zero at $\mathrm{D} = \mathrm{J}$. At this value of D, a transition takes place between the Haldane phase and the large-D phase [114]. In the large-D phase the spectral gap which separates the ground state from the first excited state is due to anisotropy only, whereas in the Haldane phase with $\mathrm{D} = 0$, the gap arises due to purely quantum considerations. The effect of a more general single-ion anisotropy which includes an easy-plane (D) term and an in-plane term (E), on the isotropic Hamiltonian, was considered by Golinelli et al. [115]. They found that for non-zero E, the following holds true

$$\Delta_{\mathrm{x}} = \Delta(0) - \alpha\mathrm{D} + 3\alpha\mathrm{E} \tag{4.8}$$

$$\Delta_{\mathrm{y}} = \Delta(0) - \alpha\mathrm{D} - 3\alpha\mathrm{E} \tag{4.9}$$

$$\Delta_{\mathrm{x}} = \Delta(0) + 2\alpha\mathrm{D} \tag{4.10}$$

for the gaps along three directions and where $\alpha \approx 2/3$. One can see that the effect of E is to lift the degeneracy of the doublet state. The values predicted for the gaps and anisotropy parameters match well with experimentally determined values for NENP and Y_2BaNiO_5 [116, 117].

Ever since the initial proposal of Haldane [94,95] that the integer spin Heisenberg antiferromagnetic chain has qualitatively different properties than the half-integer spin chain, experimental efforts were focused on finding suitable candidate materials to study the Haldane conjecture.

The first material to be studied was the isotropic Heisenberg $CsNiCl_3$ which has an intra-chain exchange $\mathrm{J} = 2.28$ meV and an inter-chain exchange $\mathrm{J}' = 0.044$ meV which leads to long-range magnetic order below $\mathrm{T_N} = 4.8$ K. Above $\mathrm{T_N}$, the system behaves one-dimensionally and presents many of the characteristics predicted for the S=1 Haldane chain [118, 119]. These include a disordered ground state with no long-range magnetic order, a spectrum of excitations dominated by a single-magnon

dispersion which has a measured gap $\Delta \approx 1.2$ meV [120] at the antiferromagnetic zone centre $Q = \pi$ and a continuum of two-magnon excitations for wave vectors close to $Q = 0$ [121].

Another system which was found to be a good realization of the S=1 Haldane chain is the organic compound $Ni(C_2H_8N_2)_2NO_2ClO_4$ (NENP). It has a very good one-dimensional character with J = 4 meV and no experimental evidence of a transition to long-range magnetic order which implies that inter-chain coupling is negligible. The system is quite anisotropic with $D/J \approx 0.2$ [116, 122, 123]. This anisotropy splits the Haldane gap into three gaps ($\Delta_{\parallel} = 2.4$, $\Delta_{\perp 1} = 1.23$, $\Delta_{\perp 2} = 1.05$ meV) corresponding to fluctuations polarised along the chain and perpendicular to the chain respectively [124].

Another realisation of the S=1 Haldane chain is $AgVP_2S_6$ [125, 126]. It is well described by an isotropic Heisenberg model with $J \approx 58$ meV and very weak inter-chain $J'/J < 10^{-5}$ [127]. The Haldane gap measured at the minimum of the triplet dispersion $Q = \pi$ is given by $\Delta = 26$ meV and the correlation length in units of spin-spin distance is $\xi = 5.5 \pm 1$ [127]. The disadvantage of $AgVP_2S_6$ is that large single crystals are unavailable for detailed neutron scattering studies.

The material studied here is Y_2BaNiO_5 [128]. It was chosen due to several reasons. Firstly, detailed investigations using inelastic neutron scattering can easily be performed due to the availability of high quality single crystals. Secondly, Y_2BaNiO_5 has been shown not to order magnetically down to the lowest experimentally reachable temperatures. Thirdly, it is only slightly anisotropic $D/J \approx 0.03$ and has a mean gap $\Delta = 8.55$ meV. It has a very good one-dimensional character as evidenced by the small intra-chain to inter-chain exchange ratio $J'/J < 5 \times 10^{-4}$ with J = 24.5 meV. Y_2BaNiO_5 is one of the best experimental realisations of the S=1 Haldane chain and all its characteristics make it ideal for inelastic neutron scattering studies of the temperature evolution of the excited triplet state.

4.2 Predictions for Triplet Lifetime and Gap Evolution with Temperature

At T = 0 the excitation spectrum of the S=1 Haldane chain is well understood as evidenced by the good agreement between theory and experiments on various physical realisations of the model which include $CsNiCl_3$ [118–121, 129], NENP [116, 124, 130],

$AgVP_2S_6$ [125–127] and Y_2BaNiO_5 [117, 131–134]. The low energy excitation spectrum is dominated by well-defined, infinitely long lived (δ-function lineshape) one-magnon (triplon) excitations between $Q = 0.25\pi$ and $Q = \pi$. For wave vectors around $Q = 0$ and at energies larger than 2Δ the spectrum consists of two-magnon excitations. For wave vectors around $Q = \pi$ and at energies larger than 3Δ the excitations are three-magnon excitations.

At $T \neq 0$ the triplet excitations are theoretically predicted to become unstable due to interactions with static defects and other thermally excited particles. This damping should be reflected in the dynamical structure factor as a broadening of the one-magnon lineshape, which is described by an activated behaviour across the Haldane gap. The excitation instability can be understood if one considers that at $T = 0$ there are no excitations on the chain but as temperature increases, thermal fluctuations create new triplet excitations. Interaction between the triplet excitations leads to their instability and determines their finite lifetimes. Another consequence of $T \neq 0$ is that the Haldane gap energy is predicted to change with respect to its $T = 0$ value, an effect known as blue shift. The blue shift arises due to the fact that as the temperature increases, the number of thermally excited quasi-particles increases so any one of them is confined to move between boundaries imposed by neighbouring quasi-particles. Such a constraint clearly changes their energy and instead of being created with energy Δ, they are created with larger energies which reflect an increase in their kinetic energy. Both the blue shift and the excitation damping have been experimentally confirmed in NENP [130], $CsNiCl_3$ [129, 135], NINAZ [136], $SrNi_2V_2O_8$ [137] and Y_2BaNiO_5 [97, 134].

Xu et al. [97] measured the temperature evolution of the Haldane gap energy Δ and inverse lifetime of triplet excitations Γ in Y_2BaNiO_5 ($\Delta \approx 100$ K), in a temperature range from $T \to 0$ K to $T = 100$ K, using inelastic neutron scattering. For temperatures $T < 20$ K the resolution function of the triple-axis spectrometer they used, limited the inverse lifetime to $\Gamma \geq 0.1$ meV for a Gaussian lineshape and to $\Gamma \geq 0.05$ meV for a Lorentzian lineshape. The objective of our study was to measure the inverse lifetime for temperatures $T < 50$ K with a focus on the region of temperatures close to $T = 0$, by using the neutron spin-echo technique (NSE). NSE has an energy resolution of about two orders of magnitude better than a typical triple-axis technique, thus allowing a more accurate determination of Γ as $T \to 0$. The evolution of $\Gamma(T)$ in this low temperature region is expected to be revealing of the nature of the decoherence mechanisms that lead to finite lifetimes.

In the remainder of this section we present a quantitative model for the temperature evolution of the inverse lifetime of triplet excitations, which adds to the semi-classical model based on the non-linear sigma model (NLSM) [138]. We supplement the NLSM model by taking into account two further aspects which are of importance when considering real Haldane systems. The first is the contribution to the inverse lifetime which is expected due to static defects alone (impurities) and the second is the contribution to the inverse lifetime due to the fact that in a real sample, impurities will lead to a Poisson distribution of chain lengths. For the blue shift we present the predictions of the NLSM of Jolicoeur and Golinelli [139].

In the large S limit, the low energy properties of the Haldane chain are described by the NLSM [94, 95]. Although it has not been rigorously proved, there is strong evidence [140] that the mapping of the Heisenberg model onto the NLSM is exact even for S=1. In the NLSM, the low energy excitations are triplets which are separated by an energy gap Δ from the ground state and which propagate either ballistically or diffusively, depending on the temperature regime. We are interested in the regime at $T < \Delta$ where strong quantum fluctuations create a singlet ground state and there are a few thermally excited triplets propagating along the chain. At $T = 0$, near $Q = \pi$ and at energy Δ, the dynamical structure factor is typical for a single-particle excitation and is well-described by a δ-function lineshape [138, 141]. As the temperature increases, an asymmetric lineshape develops and at $T = \Delta/2$ (where $\Delta = 100$ K for Y_2BaNiO_5) the asymmetry is quite pronounced as predicted by the NLSM study of Essler and Konik [141] and shown in Fig. 4.3.

In terms of transport, excitations are viewed as particles which at T=0 and for an infinite chain are perfectly stable, long-lived and propagate ballistically along the chain. Their density is zero and they are treated as non-interacting. At $T > 0$ the presence of thermally excited particles (thermal defects) increases the total triplet density and interactions between particles have to be explicitly considered. The consequence of this fact is that the particles acquire finite lifetimes and as their density increases, their mean lifetimes decrease, which is reflected in $S(Q, \omega)$ as a broadening in energy.

In order to quantify the real expected lifetime we consider that at T=0 the ideal, infinitely long chains are broken into finite segments by chemical impurities. The distribution of resulting chain lengths is well described by a Poisson distribution with the mean chain length given by L_0 spin-spin distances. For a finite chain of length L_0, an excitation can, on average, travel half the length of the

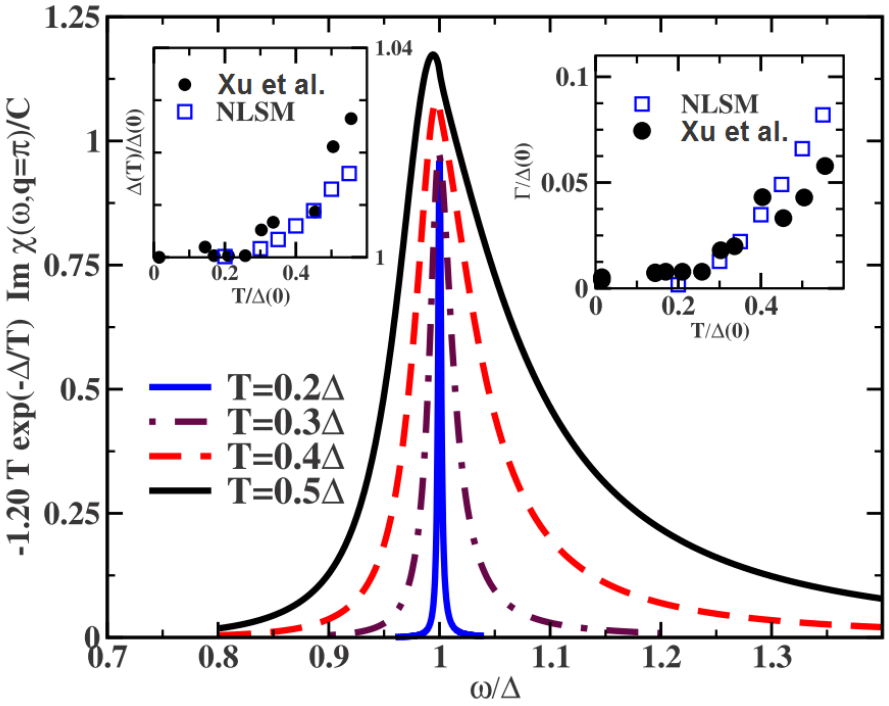

Figure 4.3: Temperature dependence of the lineshape of S=1 Haldane chain triplet excitations at $Q = \pi$ as predicted by the non-linear sigma model (NLSM). The predictions for the Haldane gap energy Δ and inverse lifetime Γ are compared with measurements of Xu et al. [97] and plotted in the insets. Adapted from Essler and Konik [141].

chain until it encounters a chain termination and decays. The distance over which it travels is its mean free path $\lambda_0 = L_0/2$, and is interpreted as the distance over which the excitation is coherent. The mean free path can be translated in terms of an effective density of static defects as $\rho_0 = 1/L_0$. At finite temperatures, thermal fluctuations create excitations which can be effectively considered as mobile defects. The density of thermal defects increases with temperature according to $\rho_T = 3\sqrt{k_B T\Delta/(2\pi v^2)}\exp(-\Delta/k_B T)$ [138, 142] and determines the triplet excitation mean free path λ_T due to interactions with thermal excitations. The density of thermal defects is determined by the Haldane gap energy and the spin-wave velocity of the quasi-particles. It reflects the presence of the Haldane gap through the expected activated behaviour given by the exponential factor. This expression can be understood from simple arguments involving the density of momentum states which arises as a result of space confinement of particles. If one assumes that the triplet interaction with static and thermal defects are uncorrelated processes, then the total

mean free path of the triplets is given as $1/\lambda_t = 1/\lambda_0 + 1/\lambda_T$ or $\rho_t = \rho_0 + \rho_T$ and shows that there is a direct correspondence between the total density of defects and an effective chain length. The way of adding the mean free paths is in analogy to Matthiessen's rule which describes the electrical resistivity of materials as a result of the combined effect of electron scattering from independent processes such as impurities, phonons, defects and other electrons. The static and thermal defects were experimentally shown to have the same effect on the mean free path of the triplet excitations by Xu et al. [97] (see Fig. 3(A) in Ref. [97]).

As a result of interaction with static and thermally activated defects, the triplet excitations become unstable and decay. Their instability is quantified in terms of the decay rate or mean inverse lifetime $\Gamma =< 1/\tau >$. The mechanisms that contribute to the lifetime are the distribution of chain lengths as a result of impurities $1/\Gamma_L$, the interaction with static defects $1/\Gamma_0$ and the interaction with other thermally activated defects $1/\Gamma_T$.

It is theoretically known from finite chain calculations that the Haldane gap energy changes with chain length according to Lou et al. [143] as

$$\Delta(L) = \sqrt{\Delta^2 + v^2 \sin^2(\frac{\pi}{L+2})} \tag{4.11}$$

where L is the chain length, Δ is the gap for the infinite ideal chain and v is the spin-wave velocity. In order to determine the contribution to Γ coming from a distribution of chain lengths, we calculate what is the corresponding spread in gap energy for a finite spread in chain length. Γ_L is then given by the spread in Δ. We associate the spread in chain length with the full-width at half maximum of a Gaussian distribution because in the limit of a large mean chain length, the Poisson distribution becomes a Gaussian distribution characterised by the full-width at half maximum. Basically we know that in the vicinity of $L = L_0$ we can write down a linear relationship which connects a spread in Δ to a spread in L in the following way

$$\Delta(L) - \Delta(L_0) = \frac{d\Delta}{dL}(L - L_0) \tag{4.12}$$

which for a Gaussian distribution of chain lengths becomes

$$FWHM(\Delta) = \frac{d\Delta}{dL} FWHM(L) \tag{4.13}$$

and where we want to determine $d\Delta/dL$ from knowledge of Eq. 4.11. For wave vectors close to $Q = \pi$ and for $L \gg 2$ (Xu et al. [97] measured the impurity concentration for the same Y_2BaNiO_5 sample as ours and inferred that the mean chain length is $L_0 = 70$ spin-spin distances), Eq. 4.11 becomes $\Delta(L) = \sqrt{\Delta^2 + \pi^2 v^2/L^2}$, the derivative of which evaluated at $L = L_0$ is

$$\frac{d\Delta}{dL}\Big|_{L_0} = -\frac{\pi^2 v^2}{\sqrt{\Delta^2 + \pi^2 v^2/L_0^2} L_0^3} \tag{4.14}$$

The inverse triplet lifetime which results from a distribution of chain lengths with mean L_0 is given by the half-width at half maximum of the corresponding distribution of gap energies and has the following expression

$$\Gamma_L = \frac{\pi^2 v^2}{\sqrt{\Delta^2 + \pi^2 v^2/L_0^2} L_0^3} \cdot \frac{2.355\sqrt{L_0}}{2} \tag{4.15}$$

where Δ is the Haldane gap for the infinite chain, L_0 is the mean chain length and $2.355\sqrt{L_0}/2$ is the half-width at half maximum of the Gaussian distribution of chain lengths, taking the standard deviation of the Gaussian as simply the standard deviation of the parent Poisson distribution with mean L_0, which is $\sqrt{L_0}$. The expression for Γ_L is independent of temperature and shows that as $T \to 0$ the lifetime of the triplet excitations is only limited by the distribution of chain lengths which results from considering impurities.

The second contribution to the inverse lifetime that we consider is Γ_0 which results from the interaction of the triplet excitations with static defects only. We begin the derivation by considering the density of momentum states which is available for the triplet excitations when they are confined by thermally activated excitations in a one-dimensional box of typical length L. The size of the box in momentum space is given by $q = 2\pi n/L$ with n being the number of triplets that can be fitted in the box. The density of triplets in the range $[q, q + dq]$ is given as

$$\frac{dn}{L} = \frac{1}{2\pi} \exp(-\sqrt{\Delta^2 + v^2 q^2}/k_B T) dq \tag{4.16}$$

which accounts for temperature by weighing with the Boltzmann factor. For $k_B T \ll \Delta$ we expand the argument of the exponential around $q = 0$ as

$$\frac{\Delta}{k_B T}\left(\sqrt{1 + \left(\frac{vq}{\Delta}\right)^2}\right) = \frac{\Delta}{k_B T}\left(1 + \frac{1}{2}\left(\frac{vq}{\Delta}\right)^2 + \cdots\right) \tag{4.17}$$

and keep only the first two terms. The density of triplets becomes

$$\begin{aligned}\rho_T(q) &= 3\int_{-\infty}^{+\infty}\frac{dn}{L}dq = \frac{3}{2\pi}\exp\Big(-\frac{\Delta}{k_BT}\Big(1+\frac{1}{2}\Big(\frac{vq}{\Delta}\Big)^2\Big)\Big)\\ \rho_T(q) &= \frac{3}{2\pi}\exp\Big(-\frac{\Delta}{k_BT}\Big)\exp\Big(-\frac{1}{2}\frac{(vq)^2}{k_BT\Delta}\Big)\end{aligned} \tag{4.18}$$

and gives the total number of triplets per length as a function of momentum. The factor 3 is due to the presence of three distinct types of triplets ($|+1\rangle$, $|0\rangle$, $|-1\rangle$).

The second thing we consider is the the group velocity v_g of quasi-particles with a dispersion relation given by Eq. 4.4 which in the vicinity of $Q=\pi$ becomes $E(q)=\sqrt{\Delta^2+v^2q^2}$ with $q=Q-\pi$. The group velocity is given by

$$v_g = \frac{dE}{dq} = \frac{v^2q}{\sqrt{\Delta^2+v^2q^2}} \tag{4.19}$$

and in the limit of small q it becomes $v_g = v^2q/\Delta$. We want to determine what is the mean inverse lifetime due to the dispersion of triplet excitations that are characterised by the group velocity v_g knowing that the total density of triplets varies as a function of momentum according to Eq. 4.18. We compute the mean inverse lifetime as

$$\langle\frac{1}{\tau}\rangle = \Gamma_0 = \frac{1}{L_0}\frac{\int_{-\infty}^{+\infty}v_g\rho_T(q)dq}{\int_{-\infty}^{+\infty}\rho_T(q)dq} \tag{4.20}$$

The denominator of the last fraction in Eq. 4.20 represents the total density of triplet excitations irrespective of momentum q. It is calculated in the following way

$$\begin{aligned}\rho_T &= \int_{-\infty}^{+\infty}\rho_T(q)dq\\ &= \frac{3}{2\pi}\exp\Big(-\frac{\Delta}{k_BT}\Big)\int_{-\infty}^{+\infty}\exp\Big(-\frac{1}{2}\frac{q^2}{(\sqrt{k_BT\Delta}/v)^2}\Big)\\ &= \frac{3}{2\pi}\exp\Big(-\frac{\Delta}{k_BT}\Big)\sqrt{2\pi}\frac{\sqrt{k_BT\Delta}}{v}\\ \rho_T &= 3\sqrt{\frac{k_BT\Delta}{2\pi v^2}}\exp\Big(-\frac{\Delta}{k_BT}\Big)\end{aligned} \tag{4.21}$$

which is a nice result, as it is identical with the total density of thermal excitations

given by Sachdev and Damle [138, 142]. It shows that the density of thermal excitations behaves as expected for an activation across the Haldane gap. With this firm result in place we return to the determination of the mean inverse lifetime. Replacing the expression for the group velocity in the limit of small wave vector q and the result for the total density of thermal excitations, in Eq. 4.20, we obtain

$$\begin{aligned}
\Gamma_0 &= \frac{1}{L_0}\frac{v^3}{\sqrt{2\pi}\sqrt{k_B T\Delta}\Delta}\int_{-\infty}^{+\infty} q\cdot\exp\Big(-\frac{1}{2}\frac{q^2}{(\sqrt{k_B T\Delta}/v)^2}\Big)dq \\
&= \frac{1}{L_0}\frac{v^3}{\sqrt{2\pi}\sqrt{k_B T\Delta}\Delta}2\int_{0}^{+\infty} q\cdot\exp\Big(-\frac{1}{2}\frac{q^2}{(\sqrt{k_B T\Delta}/v)^2}\Big)dq \\
&= \frac{1}{L_0}\frac{2v^3}{\sqrt{2\pi}\sqrt{k_B T\Delta}\Delta}\frac{k_B T\Delta}{v^2} \\
&= \rho_0\frac{1}{\sqrt{\pi}}2v\sqrt{\frac{k_B T}{2\Delta}} \\
\Gamma_0 &= \rho_0\langle v_g\rangle
\end{aligned} \tag{4.22}$$

where we have written $1/L_0 = \rho_0$. We see that the inverse triplet lifetime that results from interaction with static defects can be written as the density of static defects multiplied by an effective velocity. We interpret this velocity as the mean group velocity of the triplets which is given as

$$\langle v_g\rangle = \frac{2v}{\sqrt{\pi}}\sqrt{\frac{k_B T}{2\Delta}} \tag{4.23}$$

The inverse lifetime due to static defects varies with the square root of temperature $\Gamma_0 \propto \sqrt{T}$ and should be the dominant contribution at $T \ll \Delta/k_B$.

The contribution to the inverse lifetime which results from interactions with thermally activated excitations Γ_T is obtained by Damle and Sachdev [138] using a semi-classical approach based on the non-linear sigma model. They give for the inverse lifetime

$$\begin{aligned}
\Gamma_T &= \frac{3k_B T}{\sqrt{\pi}}\exp\Big(-\frac{\Delta}{k_B T}\Big) \\
&= 3\sqrt{\frac{k_B T\Delta}{2\pi v^2}}\exp\Big(-\frac{\Delta}{k_B T}\Big)\cdot 2v\sqrt{\frac{k_B T}{2\Delta}} \\
\Gamma_T &= \rho_T v_{rms}
\end{aligned} \tag{4.24}$$

The inverse triplet lifetime which comes from interactions with thermal defects has the same form as Γ_0 in the sense that it is written as the product of a density of quasi-particles and a velocity. In this case the velocity is the root mean square velocity which has the form

$$v_{rms} = 2v\sqrt{\frac{k_B T}{2\Delta}} \tag{4.25}$$

and it gives the mean velocity of a thermally excited quasi-particle. The inverse lifetime of the triplet excitations due to thermally activated defects varies with temperature as $\Gamma_T \propto T \cdot \exp(-1/T)$ and is the dominant contribution at large temperatures, $T < \Delta/k_B$.

The contributions to the lifetime of the triplet excitations derived above all combine to give the total triplet lifetime in an identical manner as we combined mean free paths. If one deals with three independent processes which each lead to a finite lifetime, than the consideration of all processes together should give rise to a total lifetime which is smaller than each individual lifetime contribution. This is simply written as $1/\tau = 1/\tau_L + 1/\tau_0 + 1/\tau_T$ or $\Gamma = \Gamma_L + \Gamma_0 + \Gamma_T$. Explicitly we write

$$\begin{aligned}
\Gamma(T) &= \frac{\pi^2 v^2}{\sqrt{\Delta^2 + \pi^2 v^2/L_0^2}} \frac{1}{L_0^3} \cdot \frac{2.355\sqrt{L_0}}{2} \\
&+ \frac{1}{L_0} \cdot \frac{2v}{\sqrt{\pi}} \sqrt{\frac{k_B T}{2\Delta}} \\
&+ 3\sqrt{\frac{k_B T \Delta}{2\pi v^2}} \exp\Big(-\frac{\Delta}{k_B T}\Big) \cdot 2v\sqrt{\frac{k_B T}{2\Delta}}
\end{aligned} \tag{4.26}$$

This equation gives the temperature dependence of the inverse triplet lifetime when we account for a distribution of chain lengths as a result of the presence of chemical impurities in a real system, the interaction with chain-breaking, static defects and the interaction with thermally activated mobile defects. Three regimes are identified, at $T = 0$ where the lifetime is given by the distribution of chain lengths, at $T \ll \Delta/k_B$ where the density of thermally activated defects is small and the lifetime arises due to interactions with chain-breaking defects and at $T < \Delta/k_B$ where the lifetime is determined by thermally activated defects.

We have seen that due to finite chain effects and thermal effects, we can consider

the excitations in the S=1 Haldane chain to be confined in one-dimensional boxes. This gives rise to quantum behaviour of the quasi-particles and the consequence is that when they are created, instead of being created with energy Δ, they are created with an extra kinetic energy due to the constraints of having to move between fixed boundaries. The amount of extra energy is proportional to the density of thermally excited triplets and so, as the temperature increases, the energy of the gap is expected to increase exponentially. This effect is known as the blue shift of the gap energy. The evolution of the gap with temperature has been computed by Jolicoeur and Golinelli [139] in the framework of the NLSM. They state that although their calculations assume the purely isotropic case, the effect of anisotropy should not change their conclusions qualitatively. They give for temperature approaching zero, an activated behaviour

$$\Delta(\mathrm{T}) = \Delta + \sqrt{2\pi}\sqrt{\Delta \mathrm{k_B T}}\exp\Big(-\frac{\Delta}{\mathrm{k_B T}}\Big) \tag{4.27}$$

where Δ is the value of the Haldane gap for the infinite chain in the limit of $\mathrm{T} = 0$.

4.3 Sample Properties

The nickelate compound Y_2BaNiO_5 was first successfully synthesized by Buttrey et al. [128]. Their phase equilibrium studies revealed a new stable phase of the Y-Ba-Ni-O system. They managed to grow single crystals of Y_2BaNiO_5 via an RF induction melting technique and show that the structure symmetry belongs to the Immm space group with lattice parameters a = 3.765 Å, b = 5.755 Å, c = 11.324 Å at 10 K [144]. X-ray and neutron scattering measurements on powder samples revealed that each Ni atom is surrounded by 6 oxygen atoms in a distorted octahedral environment. The Ni-O distance along the a-axis is d = 1.885 Å whereas the Ni-O distance in the bc-plane is d = 2.186 Å [131]. Considering the magnetic superexchange paths the structure can be considered as made up of chains of Ni atoms which run along the a-axis, with every chain isolated from its neighbouring chains by Y and Ba atoms (see Fig. 4.4). Magnetic susceptibility measurements on a powder sample revealed a broad maximum at T = 400 K, an indicative of one-dimensional behaviour of the magnetic correlations. At T < 25 K the susceptibility was very well described by a Curie law which was interpreted as either being due to the presence of paramagnetic impurities or the presence of finite length chains as expected from a policrystalline

sample. A fit of the measured susceptibility to theoretical predictions for a S=1 chain gave the intra-chain exchange J = 285 K or J = 24.7 meV [131]. Subsequent susceptibility measurements have revealed that there is no magnetic long range order down to T = 1.8 K [145]. Neutron scattering on a powder sample has shown the presence of an energy gap in the excitation spectrum $\Delta = 8.5 \pm 0.5$ meV [131]. Inelastic neutron scattering data on a single crystal of Y_2BaNiO_5 determined the value of the intra-chain exchange J = 24.1 meV and gave a value for the gap along the chain direction as $\Delta_{\|} \approx 10$ meV [133].

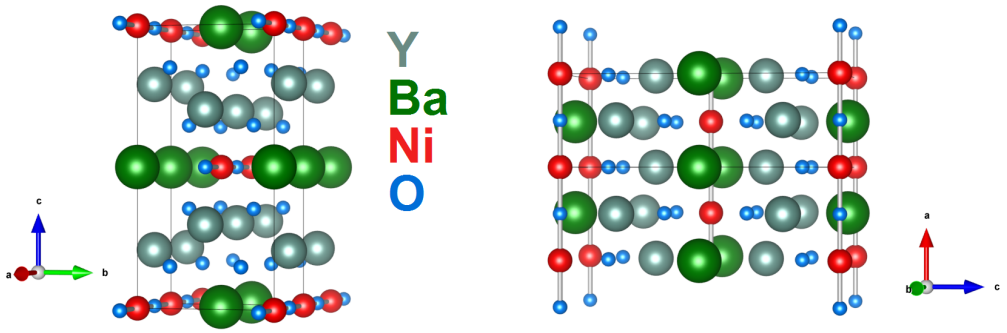

Figure 4.4: Crystal structure of Y_2BaNiO_5 viewed from two different directions. The colour legend for the atoms is: Y (grey), Ba (green), Ni (red), O (blue). We show the bonds between the nickel atoms along the chain direction with light grey.

The inelastic neutron scattering experiments of Xu et al. [117] and Sakaguchi et al. [134] have revealed similar features of the excitation spectrum of Y_2BaNiO_5. Xu et al. [117] found that the excitation gap at the triplet minimum at $Q = \pi$ is split into three separate gaps $\Delta_a = 7.5$ meV, $\Delta_b = 8.6$ meV, $\Delta_c = 9.6$ meV corresponding to spin fluctuations polarised along the a-,b- and c-directions respectively. By taking the value of the mean gap $(\Delta_a + \Delta_b + \Delta_c)/3 = 8.55$ meV they inferred for the intra-chain exchange a value of J = 21 meV, assuming $\Delta/J = 0.4105$, which is theoretically predicted for the Haldane chain [103]. The spin-wave velocity v = 70(5) meV was determined by a fit of the observed excitations to the dispersion $E(Q) = \sqrt{\Delta^2 + v^2 \sin^2(Q-\pi) + A\cos^2((Q-\pi)/2)}$ but is too large when comparing the computed dispersion using v = 70 meV with the data, as evident from the data of Xu et al. [117] given in Fig. 4.5. The energy of the excitations computed with v = 70 meV is overestimating the measured energies and thus a smaller value for v must clearly describe the data better. An accurate value for v is essential in order to perform reliable corrections to the neutron spin-echo data as we will see in the

section on results. The uncertainty in v has motivated us to remeasure the one-magnon dispersion in Y_2BaNiO_5 and extract a more reliable value for the spin-wave velocity v. The measurement will be described in detail in section 4.5.

The correlation length computed using the experimentally extracted values for the mean gap and the spin-wave velocity is $\xi = v/\Delta = 8.1$, which is larger than $\xi = 6$ predicted for the ideal Haldane chain. The splitting of the Haldane gap into three separate gaps is an indication of finite anisotropy. The data does not allow to distinguish between exchange and single-ion anisotropy, but Xu et al. [117] assume that the observed anisotropy is of single-ion type. They give values for the anisotropy parameters $D = -0.81$ meV ($D/J = -0.04$) and $E = 0.25$ meV ($E/J = 0.01$). The strength of the inter-chain coupling is found to be $J'/J < 5 \times 10^{-4}$ which can be considered negligible and reinforces the idea of one-dimensional magnetic character.

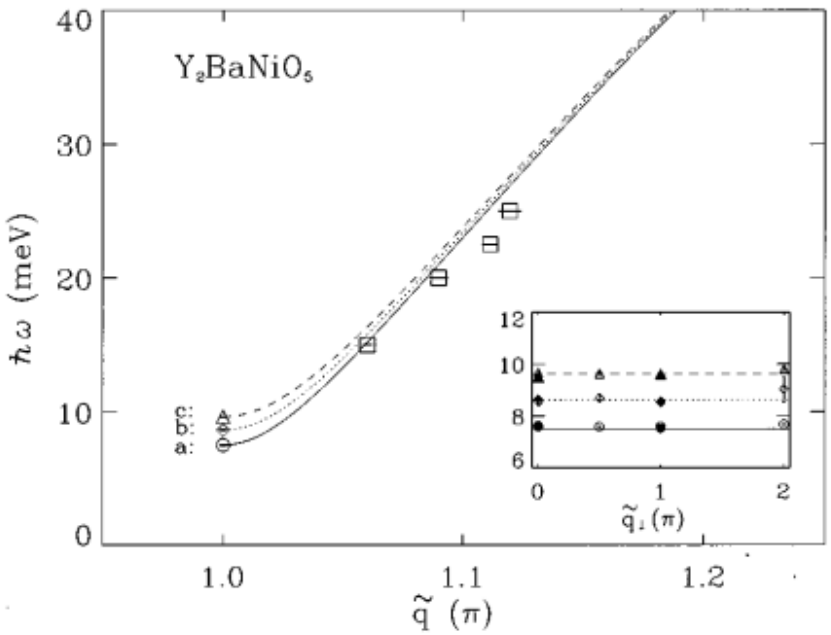

Figure 4.5: One-magnon excitation energy variation with wave vector transfer $\tilde{q}$ in Y_2BaNiO_5 as measured by Xu et al. [117] and plotted alongside the computed dispersions (lines) using the spin-wave velocity $v = 70$ meV and the three values of the Haldane gap $\Delta_a = 7.5$ meV, $\Delta_a = 8.6$ meV and $\Delta_a = 9.6$ meV. It shows that the computed dispersions are overestimating the energy for the last three measured points and for a better agreement with the data, a smaller value of v should be used. Taken from Ref. [117].

Sakaguchi et al. [134] measured the one-magnon dispersion around $Q = \pi$ and from a fit to the single-magnon dispersion given by $E(Q) = \sqrt{\Delta^2 + (2.7JS)^2 \sin^2(Q - \pi)}$

they obtained J = 24.1 ± 1 meV for the intra-chain exchange and $\xi = 6.9 \pm 0.6$ Ni-Ni spacings for the correlation length. The gap values extracted for spin fluctuations along the three orthorhombic crystal axes are $\Delta_a = 7.5$ meV, $\Delta_b = 8.6$ meV and $\Delta_c = 9.5$ meV. From the measurement of the gaps, Sakaguchi et al. [134] compute the single-ion anisotropy parameters D = −0.78 meV (D/J = −0.03) and E = 0.23 meV (E/J = 0.01). By following the temperature dependence of the single magnon peak at the triplet minimum they observed an increase of the peak width and a shift of its position towards higher energies. This observation is in accord with the prediction of the existence of a blue shift in Y_2BaNiO_5. The data shows that the prediction of the NLSM given in Eq. 4.27 overestimates the temperature dependence of the gap energy for T > 40 K. From the peak width, Sakaguchi et al. [134] extract the inverse lifetime Γ of the excitations as a function of temperature and show that the NLSM prediction accounts acceptably for the data, for $T < \Delta/k_B$. A better description is found if the value of the gap is replaced with the experimentally determined gap at each temperature.

The most recent study of the triplet lifetime and blue shift of the Haldane gap in Y_2BaNiO_5 was performed by Xu et al. [97]. This study should be regarded as more reliable as compared to older studies due to the increased experimental energy resolution ($\Delta E_{Xu} = 0.1$ meV) which is at least an order of magnitude better that of Sakaguchi et al. [134] ($\Delta E_{Sa} = 1.3$ meV). Xu et al. [97] measured the blue shift of the Haldane gap energy and showed that the NLSM prediction of Jolicoeur and Golinelli [139] given in Eq. 4.27 (black line in Fig. 4.6 A) severely overestimates the measured energy for T > 20 K. The data is much better described in terms of a model which combines the effects of static and thermal defects using the mean free paths as $1/\lambda = 1/\lambda_0 + 1/\lambda_T$. The mean free path due to thermal defects is given by the density of thermal defects as $\lambda_T = 1/2\rho_T$ with ρ_T from Eq. 4.21. The mean free path due to static defects is deduced from the Monte Carlo study of Nightingale and Blote [104] which give the T = 0 gap energy as a function of chain length L. Taking $\lambda_0 = L/2$ and combining it with λ_T an effective mean free path or chain length is obtained. The gap energy computed with this effective chain length at each temperature is obtained and plotted in Fig. 4.6 A with a solid blue line and accounts very well for the data.

Xu et al. [97] measured the inverse lifetime Γ of the triplet excitations as a function of temperature. Their data was not able to distinguish between a Gaussian and a Lorentzian spectral function so they fitted the data to both lineshapes. The

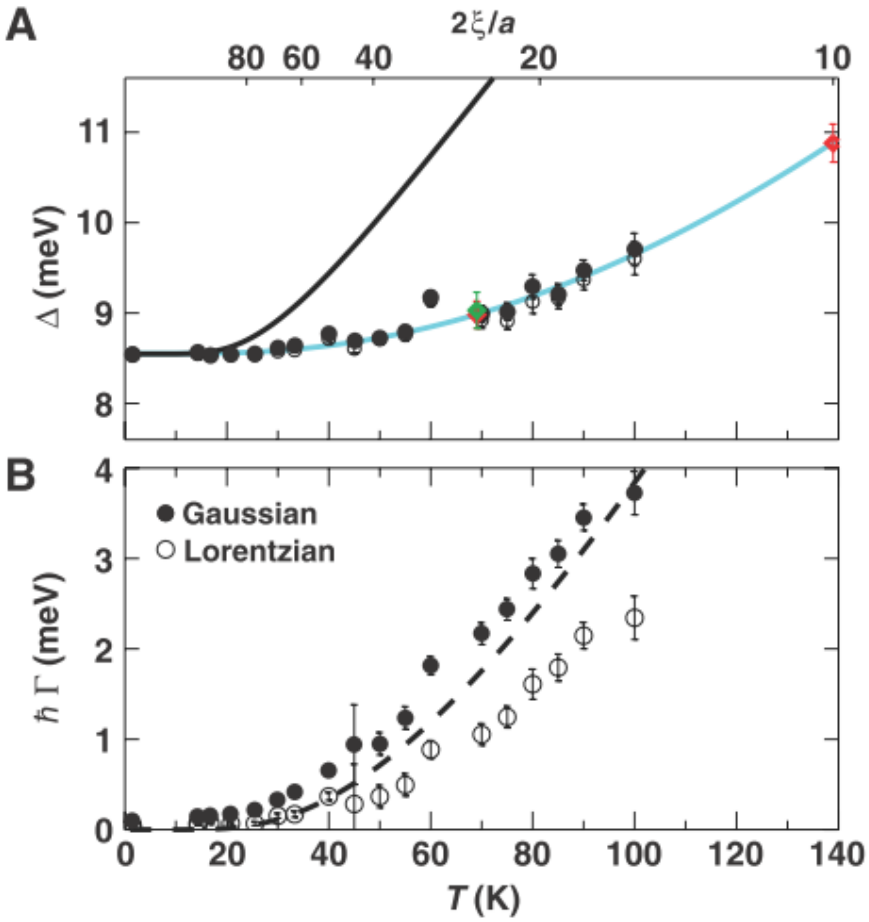

Figure 4.6: A) Blue shift of the Haldane gap measured by Xu et al. [97] (black points) together with the prediction of the NLSM [139] (black line) and the prediction of the model described in the text (blue line). The base temperature gaps measured for Ca (red diamonds) and Mn (green diamond) doped Y_2BaNiO_5 samples are also plotted. The inclusion of impurities of Ca and Mn breaks the infinite chains into finite segments. The measured gap energy matches very well with the gap energies measured for the pure compound and shows that static defects and thermal defects have an identical effect on the Haldane gap. B) Inverse lifetime Γ extracted from the data by fitting the lineshape to a Gaussian profile (filled circles) and a Lorentzian profile (open circles). The theoretical prediction of the NLSM is plotted with black interrupted line. Taken from Ref. [97].

result for the inverse lifetime extracted from the fits is plotted in Fig. 4.6 B alongside the prediction of the NLSM (interrupted black line). There is a significant difference between the Γ extracted from a Gaussian fit and a Lorentzian fit which increases with increasing temperature, with almost a factor two difference for 50 K < T < 100 K. This signals the fact that the tails of the magnon peaks play an important role and

understanding the behaviour in the tails is crucial in order to correctly extract the inverse lifetime. At low temperatures T < 20 K, the measured inverse lifetime is limited to $\Gamma \geq 0.1$ meV by the resolution of the triple-axis instrument. The current study of the triplet lifetime evolution with temperature is motivated by the fact that it is important to establish the evolution of Γ in this low temperature region in order to reveal whether the inverse lifetime goes to zero as predicted by the NLSM or whether it is limited to a finite value, what is its behaviour as approaching T = 0 and what are the possible mechanism which limit it.

4.4 Experimental Details

In order to study the temperature dependence of the triplet lifetime and gap energy, a high-resolution inelastic neutron scattering experiment was performed at the neutron resonant spin-echo triple-axis spectrometer (NRSE-TAS) TRISP located at the FRM-II reactor in Garching, Germany. Details about the technique and underlying theoretical concepts were presented in Chapter 2. In essence, NRSE allows for the measurement of single particle dispersive excitation energies and lineshapes with energy resolution in the μeV range, about two orders of magnitude smaller than what current triple-axis spectrometers can achieve. The basic idea behind NRSE is to use differences in the Larmor phase of a polarised incident neutron beam which runs through a uniform magnetic field before and after the sample, to determine the energy transfer between the neutron and the sample.

The mass of our Y_2BaNiO_5 sample was m = 2 g and it consisted of two cylindrically shaped single crystals which were co-aligned to less than one degree by Dr. Toby Perring and were mounted on an aluminium base plate with the $a^\star - b^\star$ crystallographic plane in the horizontal scattering plane of the spectrometer. The co-alignment was confirmed during preliminary measurements. The sample was mounted at the end of a stick which was introduced into a standard closed-cycle refrigerator to reach temperatures as low as T = 3.5 K. The lattice parameters were refined at 3.5 K to give a = 3.758 Å, b = 5.755 Å and c = 11.334 Å.

TRISP was run in a configuration with the scattering senses at the monochromator SM=-1, at the sample SS=-1 and at the analyzer SA=-1, which gave the highest outgoing beam polarization. A negative sense means that the scattering angle as measured with respect to the incident neutron beam is measured in a clockwise sense. We used a pyrolytic graphite (PG) monochromator with a vertical curvature

radius of rmv = 0.8 m^{-1} and zero curvature horizontally. We chose to do this in order to increase the incident flux at the sample position. A vertical focusing worsens the vertical Q resolution but this is unimportant in the case of scattering from a 1D chain where the chain direction is in the horizontal scattering plane because the scattering is featureless for Q directions perpendicular to the chain direction. The analyser used for the inelastic measurements was a Heusler alloy with small horizontal curvature radius rah = 0.2 m^{-1} and vertical focusing fixed with a curvature radius of (rav = 1 m^{-1}), for better beam focusing, with the beam size at the sample position being 50 mm × 20 mm (H×V). A velocity selector was used before the sample to filter out higher order incident neutron wavelengths and allowed a large incident wavelength distribution $\Delta\lambda/\lambda \approx 10\%$. This broad distribution does not affect the energy resolution of the experiment because the resolution does not depend, to first order, on the wave vector transfer. The final wave vector was fixed to $k_f = 2.51$ $Å^{-1}$ and TRISP was operated in the Larmor mode where the magnetic fields in the two spectrometer arms were parallel. We operated in Larmor mode because there is a spin-flip process which occurs at the sample position.

The spectrometer was set to measure at the Q = (0.5, 1.5, 0) r.l.u. and E = 7.6 meV, which corresponds to the magnetic zone centre and minimum of the triplon dispersion corresponding to spin fluctuations polarised along the chain direction. Q was chosen such that the polarisation factor in the neutron scattering cross section minimises the intensity of the second triplet mode at energy $\Delta_b = 8.6$ meV. This ensures that within the experimental resolution ellipsoid we only pick up fluctuations from the mode at $\Delta_a = 7.6$ meV and minimize any contribution from Δ_b. The third mode at energy $\Delta_c = 9.6$ meV is too far away in energy to contribute to the scattering we observe as the full-width at half-maximum (FWHM) of the TAS resolution ellipsoid is $\Delta E = 1.2$ meV.

For the inverse lifetime, the experiment consisted in first measuring the echo amplitude at a number of spin echo times τ and then extracting the corresponding outgoing neutron beam mean polarisation by fitting the oscillation of the spin-echo intensity to a model given in Ref. [146]. The spin-echo time was changed by varying the frequencies in the RF spin-flip coils in the first and second arm of the spectrometer. The true outgoing beam polarisation as a function of spin-echo time τ was obtained after the raw measured polarisation was divided by a polarisation correction which takes into account several depolarising mechanisms. As the neutron beam travels through space, it naturally depolarises. Stray fields and field inhomo-

geneities also cause beam depolarisation. All three effects were accounted for by calibration measurements. These measurements consisted in measuring the polarisation as a function of coil frequency and with an empty instrument (without the sample), using the same experimental conditions as for the spin-echo scans. The depolarisation coming from sample dependent factors such as crystal mosaic, spread in lattice spacing and curvature of the dispersion surface probed within the TAS resolution ellipsoid, is taken into account using a standard formalism [146,147]. The measured raw polarisation at each spin-echo time τ was then divided by the combined polarisation correction from extrinsic effects at the same τ. $P(\tau)$ uniquely determines the spectral function because $P(\tau) \propto \int S(\omega)\cos(\omega\tau)d\omega$, the cos-Fourier transform of $S(\omega)$. The characteristic width of the spectral function, which is inversely proportional to the lifetime of the triplet excitations was extracted from the fit of $P(\tau)$ to the Fourier transform of a model for $S(\omega)$. The temperature dependence of the inverse lifetime was determined by performing identical measurements of $P(\tau)$ at several temperatures.

For the blue shift, phase sensitive measurements were performed. These consist in choosing a fixed spin-echo time, measuring the echo amplitude and then extracting the Larmor phase for different temperatures. In the simple case where the excitation lineshape is symmetric, the energy transfer is directly proportional to the difference in phase between two temperatures which gives the energy difference between the single-particle peaks that translates into the gap energy or blue shift. In the next sections we discuss in detail the data analysis and limitations of the measurements which arise from both sample dependent properties and possible asymmetry of the lineshape of triplet excitations.

4.5 Triplon Lifetime Measurements

In this section we present the TRISP measurements performed in order to probe the linewidth temperature dependence of the triplet excitations which correspond to spin fluctuations along the chain direction in the Haldane chain material Y_2BaNiO_5. Details about the configuration of the instrument were given in the previous section.

The linewidth of the excitations is extracted from the dependence of the outgoing beam polarisation on the spin-echo time $P(\tau)$, which is the Fourier transform of the excitation spectral function. The minimum frequency which can be applied in the radio-frequency (RF) coils dictates the minimum spin-echo time that can

be accessed, which in this case is $\tau = 4.087$ ps. The maximum frequency which is applied to the RF coils dictates the final energy resolution of the experiment. In order to cover a region $\tau < 4.087$ ps, we used an instrument setup where we replaced the two RF coils in each spectrometer arm with normal static (DC) coils. We extracted the polarisation at several spin-echo times by either translating the last RF coil in the second spectrometer arm by a few millimetres or by varying the current in one of the two DC coils and then measuring the oscillation of the echo amplitude. We show such typical scans in Fig. 4.7 and Fig. 4.8.

Each scan is fitted to the following equation to extract the raw polarisation

$$\mathrm{I}(\Delta\mathrm{L}, \mathrm{I}_2) = \mathrm{I}_0\{1 + \mathrm{P}\cos[2\pi(\Delta\mathrm{L}, \mathrm{I}_2 + \Delta\mathrm{L}_0)/\Delta\mathrm{L}_\mathrm{p}]\} \tag{4.28}$$

where P is the polarisation and the intensity I can depend either on translation distance ΔL (RF coils setup) or on the current I_2 (DC coils setup). I_0 is the average intensity, $\Delta\mathrm{L}_0$ is an offset and $\Delta\mathrm{L}_\mathrm{p} = 2\pi\hbar\mathrm{k}_2/(\mathrm{m}\omega_2)$ is a fixed known constant that depends solely on instrumental parameters and represents the oscillation period.

In NRSE the true polarisation is the product of the Fourier transform of the scattering function $\mathrm{S}(\omega)$ and a τ-dependent function which accounts for resolution [147]. The true polarisation is obtained by dividing the raw polarisation by the τ-dependent resolution function which takes into account the natural beam depolarisation, the mosaicity of the sample, the TAS resolution ellipsoid and the curvature of the dispersion surface which is sampled by the TAS resolution ellipsoid. $\mathrm{P}(\tau)$ is fitted to the Fourier transform of the excitation lineshape and a width Γ is extracted which characterises the assumed lineshape of the excitations.

In the case of $\mathrm{Y_2BaNiO_5}$ there is theoretical evidence due to Essler and Konik [141] that apart from broadening, the lineshape of the excitations also develops an asymmetry with increasing temperature (see Fig. 4.3). To parametrise the asymmetry we used the following lineshape as given by Stancik and Brauns [148]

$$\mathrm{S}(\omega) = \frac{\mathrm{A}}{\pi\Gamma}\frac{1}{1 + [(\omega - \omega_0)(1 + \exp[\mathrm{a}(\omega - \omega_0)])/2\Gamma]^2} \tag{4.29}$$

which is a Lorentzian with area A, centred on ω_0, with a half-width at half maximum Γ and asymmetry parametrised by a. In the limit of $\mathrm{a} = 0$ this function reduces to a symmetric Lorentzian. The sigmoid form in the denominator has the role of limiting the width between 0 and 2Γ thus preventing the lineshape from becoming unphysical.

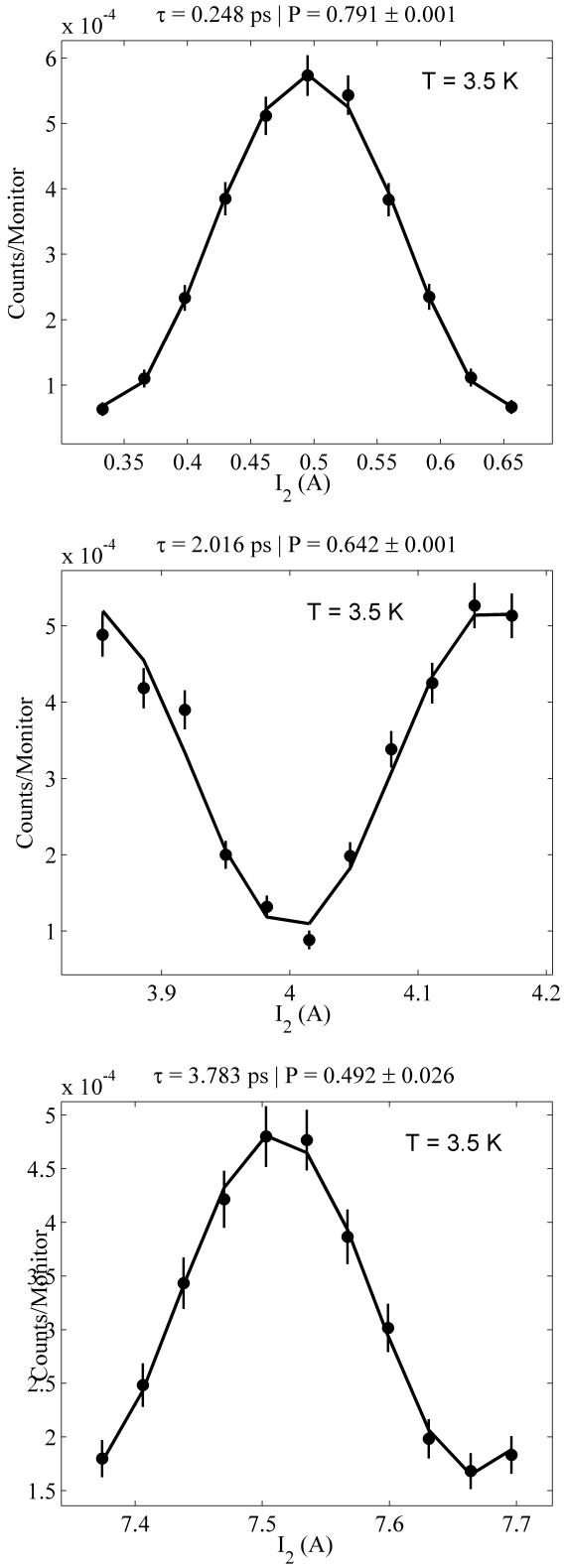

Figure 4.7: Echo amplitude oscillations at T = 3.5 K and $\tau = 0.248$ ps, $\tau = 2.016$ ps and $\tau = 3.783$ ps (from top to bottom) where I_2 is the current in the coils. The raw polarisation is extracted as the amplitude of the oscillations.

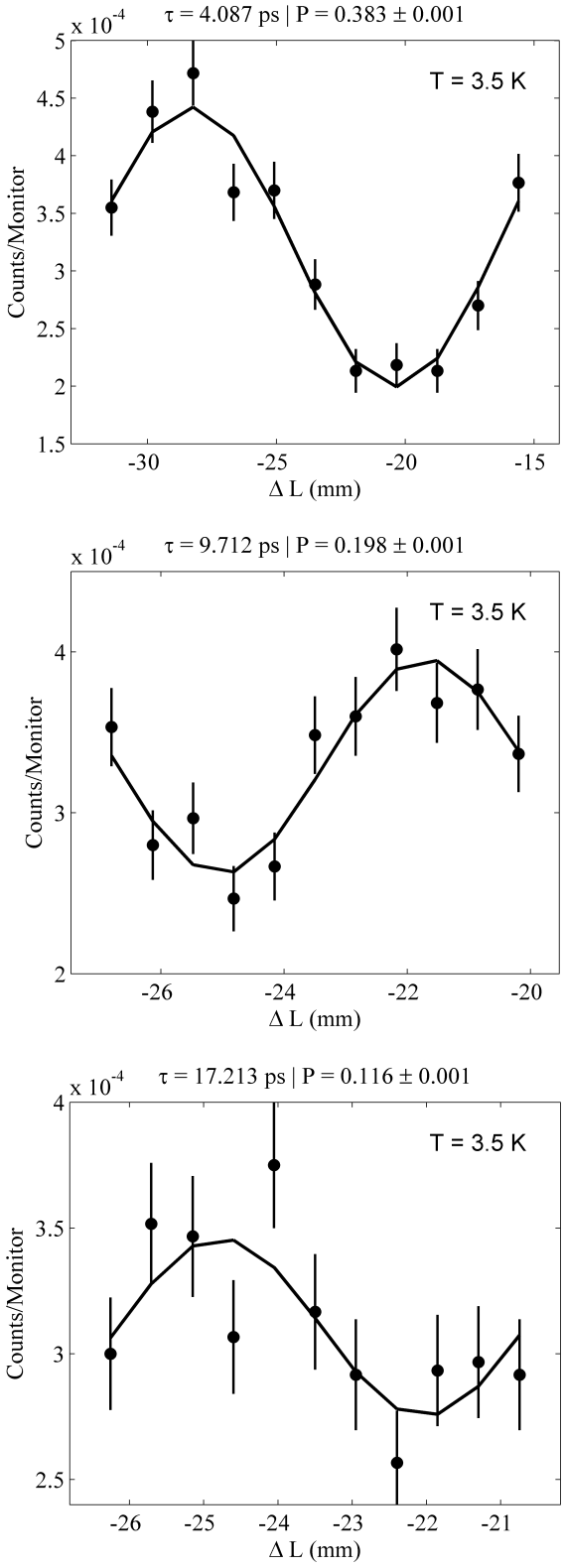

Figure 4.8: Echo amplitude oscillations at T = 3.5 K and $\tau = 4.087$ ps, $\tau = 9.712$ ps and $\tau = 17.213$ ps (from top to bottom) where ΔL is the coil translation distance. The raw polarisation is extracted as the amplitude of the oscillations.

We fitted the data assuming the lineshape is described by the asymmetric model in Eq. 4.29 but the results of the fits were inconclusive due to the fact that we always extracted an errorbar on the asymmetry parameter which was larger than the parameter itself. Please note that we also used the asymmetric skew normal function in Eq. 3.14 to parametrise the asymmetry but the fit also resulted in an errorbar larger than the asymmetry parameter itself. This behaviour is an indication that either our data is not sensitive to the predicted temperature dependent asymmetry or that the lineshape remains symmetric up to at least T = 60 K.

We now present the results of the data analysis by assuming the lineshape is symmetric Lorentzian and thus its Fourier transform follows an exponential decay of the polarisation as a function of spin-echo time. For temperatures 3.5 K, 10 K, 15 K, 20 K, 25 K, 30 K, 35 K, 45 K and 60 K, and correlation time τ in the range $\tau = 0$ to $\tau = 20$ ps, the extracted mean polarisation is plotted in Figs. 4.9, 4.10 and 4.11. The plotted polarisation is corrected for natural beam depolarisation, beam depolarisation which comes from the resolution of the underlying TAS, curvature of the dispersion and deviations from an ideal sample.

In order to make sure the extracted inverse lifetime is due to intrinsic effects of quasi-particle interactions with both static and mobile defects, we tested for possible extra linewidth broadening which might be due to the presence of two excitation modes within the TAS resolution ellipsoid. In Y_2BaNiO_5, the small single-ion anisotropy D splits the gap excitations into fluctuations polarised along the three orthorhombic crystal directions $S^{aa} = 7.6$ meV, $S^{bb} = 8.6$ meV and $S^{cc} = 9.6$ meV. To test whether the S^{bb} mode contributes to the extracted Γ, we fitted the data to a model given by Dr. Felix Groitl (Eq. 3.26 in Ref. [149]). The presence of the S^{bb} mode within the TAS resolution would lead to oscillations in $P(\tau)$ whose period and amplitude give the energy separation and integrated intensity ratio for the two modes. The results of the fits proved that no significant oscillation is present in the polarisation, thus indicating that indeed our setup is sensitive exclusively to S^{aa}. This is actually expected for two reasons. First, $S^{aa} = 7.6$ meV and $S^{bb} = 8.6$ meV are separated in energy by 1 meV which is comparable to the FWHM of the TAS energy resolution $\Delta E = 1.2$ meV (FWHM) and thus S^{bb} lies outside of the resolution ellipsoid and second, at $Q = (0.5, 1.5, 0)$ r.l.u., the magnetic scattering polarisation factor gives a mode intensity ratio of $S^{bb} = 0.26 \times S^{aa}$, making the contribution from S^{bb} insignificant.

The principal features one can observe in the corrected polarisation data are the

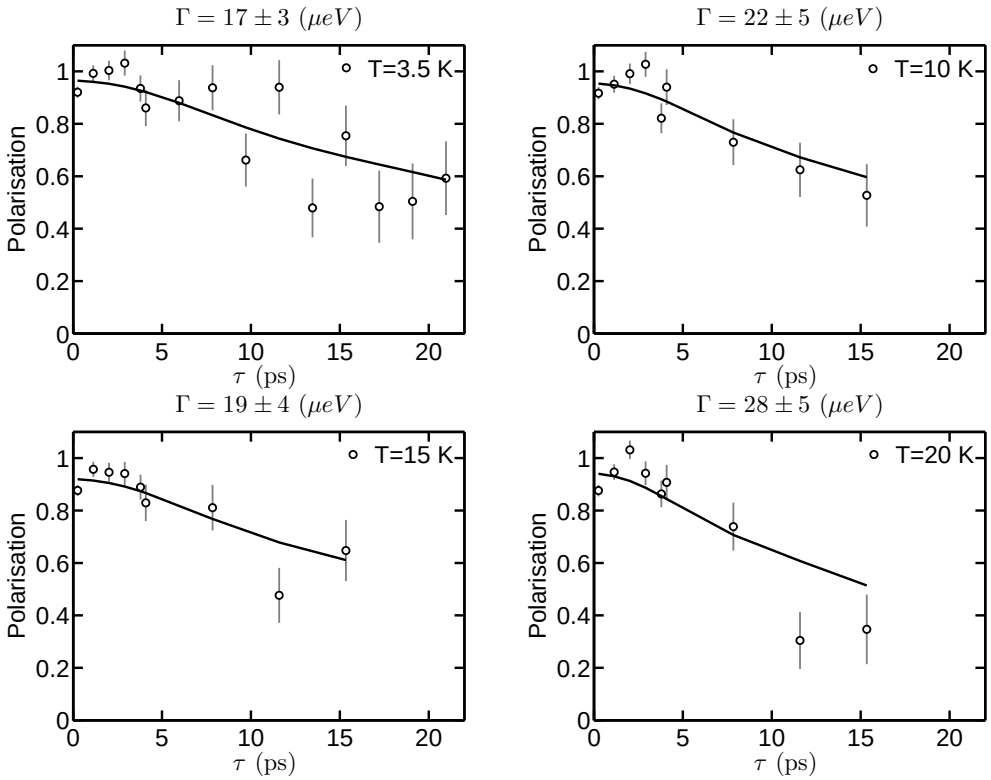

Figure 4.9: Corrected polarisation versus spin-echo time τ for T = 3.5 K, T = 10 K, T = 15 K and T = 20 K. The width of the excitations (HWHM of Lorentzian broadening) is extracted by fitting an exponential decay to the polarisation. The extracted values for Γ are given at the top of each plot.

low statistical quality and the errorbars on the points that increase with increasing spin-echo time and temperature. This behaviour of the errorbars is due to the low intensity of the excitation at high temperatures and a faster decay of the spin-echo signal due to linewidth broadening. One can also see that with increasing temperature, the extrapolated polarisation at $\tau = 0$, decreases from about $P_0 = 1$ at T = 3.5 K to about $P_0 = 0.8$ at T = 60 K. This is an indication of the presence of significant non-spin-flip scattering events as the polarisation at $\tau = 0$ should remain constant as a function of sample temperature. The spectrometer is set to detect spin-flip scattering events and so it is totally defocused with respect to non-spin-flip events, which results in a depolarised background.

We now discuss the extrinsic effects that lead to depolarisation of the outgoing neutron beam in more detail. In Fig. 4.13 we show the expected depolarisation when taking into account the instrumental TAS resolution, the mosaic spread of the sample and the curvature of the dispersion surface sampled by the TAS resolution

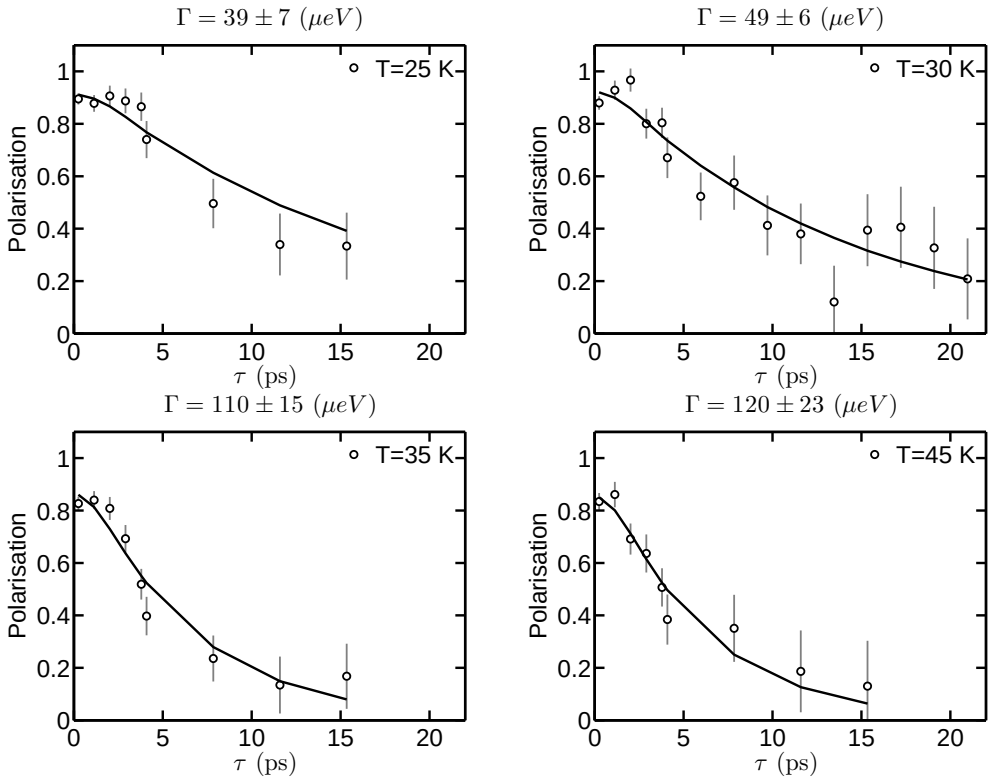

Figure 4.10: Corrected polarisation versus spin-echo time τ for T = 25 K, T = 30 K, T = 35 K and T = 45 K. The width of the excitations (HWHM of Lorentzian broadening) is extracted by fitting an exponential decay to the polarisation. The extracted values for Γ are given at the top of each plot.

ellipsoid. In this calculation, an ideal excitation with zero linewidth is considered and the spin-echo conditions are assumed to be satisfied. One can see that the dominant contribution to the depolarisation of the beam comes from the local curvature of the dispersion in Y_2BaNiO_5 (cyan solid line).

We computed the value for the local curvature based on the dispersion in Eq. 4.4 (see appendix B for the full derivation) using the value of the Haldane gap $\Delta_a = 7.6$ meV corresponding to spin fluctuations along the chain direction and for the spin-wave velocity $v = 60.5 \pm 1.5$ meV. This value of v was re-measured for Y_2BaNiO_5 by us using the high-resolution cold chopper spectrometer LET at the ISIS neutron source. As seen previously, the dominant contribution to the polarisation correction is due to the local curvature of the dispersion. The dispersion relation in Y_2BaNiO_5 is extremely steep, with a minimum energy $E_{min} = 7.6$ meV at the magnetic zone centre point $Q = \pi$ and a maximum around $Q = \pi/2$ of $E_{max} \approx 65$ meV. The values for the spin-wave velocity found in literature have shortcomings. For example, the

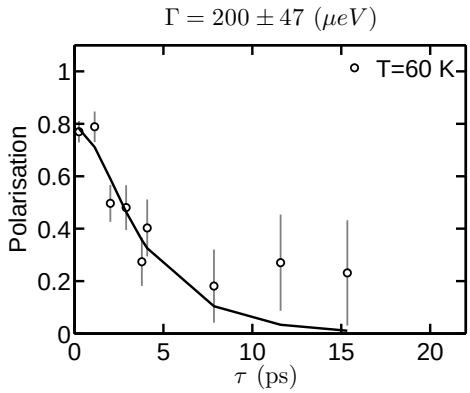

Figure 4.11: Corrected polarisation versus spin-echo time τ for T = 60 K. The width of the excitations (HWHM of Lorentzian broadening) is extracted by fitting an exponential decay to the polarisation. The extracted value for Γ is given at the top of the plot.

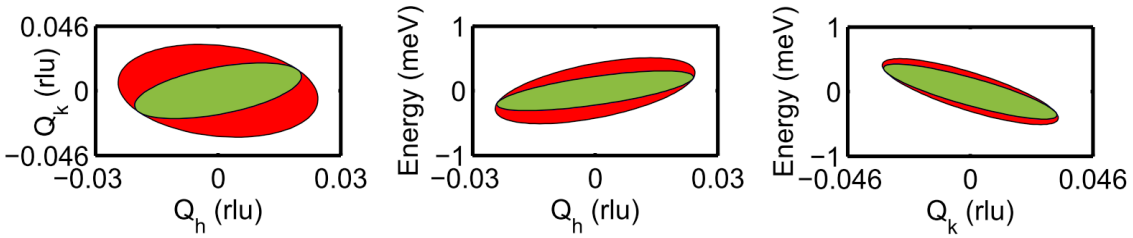

Figure 4.12: TAS resolution function for the setup used on TRISP at Q = (0.5, 1.5, 0) r.l.u. and E = 7.6 meV. The FWHM of the resolution function are ΔE = 1.2 meV, ΔQ_h = 0.05 r.l.u. and ΔQ_k = 0.065 r.l.u.

difference in the values given by Sakaguchi et al. [134] v = 65.1 ± 2.7 meV and Xu et al. [117] v = 70 ± 5 meV is quite significant. The value extracted from inelastic neutron scattering measurements by Sakaguchi et al. [134] seems to be a bit too large because they used v = 2.7J with J = 24.1 ± 1 meV, whereas theory predicts v = 2.5J for the S=1 Haldane chain. The value extracted by Xu et al. [117] is also too large as discussed in section 4.3 and as is obvious from Fig. 4.5. The value we extracted from the LET measurements is more reliable because the (Q,E) resolution of LET (δQ_{ch} = 0.027 r.l.u. and δE = 0.83 meV - based on McStas calculations by Dr. Rob Bewley) was better than what Xu et al. [117] had for their experiment (δQ_{ch} = 0.04 r.l.u. and δE = 2.4 meV). From measurements at T = 4 K we extracted the spin-wave velocity v = 60.5 ± 1.5 meV which constitutes the most accurate value for the spin-wave velocity currently known for Y_2BaNiO_5 and which gives for the local curvature $\delta^2E/\delta Q^2 = 6866 \pm 336.5$ meVÅ^2. There are no restrictions on how large

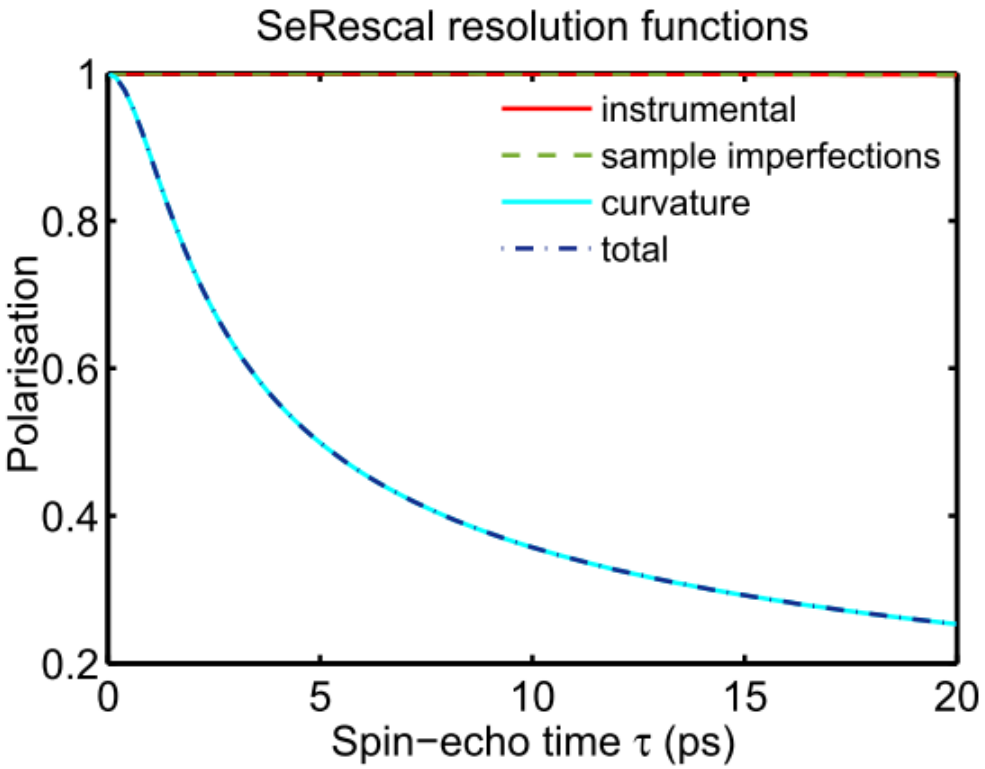

Figure 4.13: NRSE resolution function which includes effects of the instrumental TAS resolution (continuous red line), sample imperfections (dashed green line) and dispersion surface curvature (continuous cyan line).

the curvature can be, until the estimation of the depolarisation becomes unreliable (see Ref. [147] for the full treatment of the resolution function for NRSE). Other effects that contribute to beam depolarisation are the natural beam depolarisation and depolarisation due to the DC and RF coils. They are taken into account by performing calibration measurements with an empty instrument. Deviations from a perfect single crystal sample such as mosaicity and lattice spacing uncertainties are accounted for using the SeRescal Matlab program written by Dr. K. Habicht [150]. The total expected depolarisation is then obtained by multiplying all the individual correction terms. The true polarisation, which only reflects intrinsic lineshape broadening, is obtained by dividing out the contributions to the polarisation coming from the combined effect of all terms presented above.

The polarisation data was fitted to an exponential decay $P = P_0 \exp(-\Gamma\tau)$ from which the HWHM Γ of the assumed symmetric Lorentzian lineshape broadening was extracted. The individual fits are shown in Figs. 4.9, 4.10 and 4.11 with a solid

black line. The results for the inverse lifetime as a function of temperature are then plotted in Fig. 4.14 (blue circles) alongside data from the work of Xu et al. [97] (green circles) and the fit to a phenomenological model [136] (solid blue line) which gives for the temperature dependence of the inverse lifetime

$$\Gamma(T) = \Gamma_0 + I\frac{3k_BT}{\sqrt{\pi}}\exp(-\Delta/k_BT) \tag{4.30}$$

The thermal activated part is identical to what we derived in Eq. 4.24 and with the expression in Damle and Sachdev [138]. It describes the temperature activated behaviour of the inverse lifetime due to collisions with thermally excited particles. The first term, which is temperature independent, gives a measure of the residual $T = 0$ inverse lifetime.

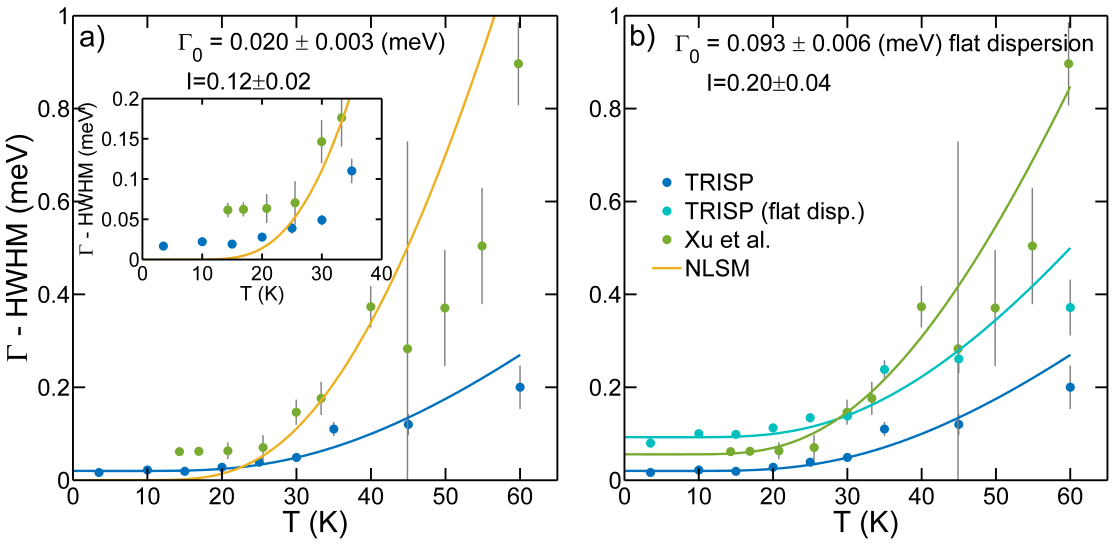

Figure 4.14: Inverse lifetime of lowest lying triplet excitations with the a) local curvature of the dispersion taken into account and b) with both the local curvature of the dispersion and a flat dispersion considered. The residual inverse lifetimes Γ_0 are given in the top of the plots. The fits to the phenomenological model given by Eq. 4.30 are shown with solid lines. The prediction of the non-linear σ model [138] is plotted with a yellow line. It is identical to the black dashed line in Fig. 4.6 B.

Our data (blue circles) and the TAS data of Xu et al. [97] (green circles) disagree over the whole domain of overlapping temperatures from $T = 0$ to $T = 60$ K. For $T < 25$ K, where the TAS data is resolution limited, our data gives an inverse lifetime at least twice smaller, with a residual $\Gamma_0 = 0.020 \pm 0.003$ meV at $T = 0$ (blue line). For $T > 25$ K, where the TAS data should be reliable, our data still

predicts a considerably smaller inverse lifetime, with approximately a factor two difference at T = 50 K. We currently do not understand where this discrepancy might come from but there are several factor one needs to be aware of. First, the TAS data has its uncertainties as evidenced by the large difference in the extracted Γ when fitting to either a Lorentzian or a Gaussian lineshape (see Fig. 4.6 B), which indicates that the tails of the peaks play an important role in extracting the correct width. The data collected on TRISP has its uncertainties as well, due to the very steep dispersion which leads to a large polarisation correction. As the polarisation correction coming from the curvature is computed approximately, we suspect there might be a threshold value above which this approximation becomes unreliable. If that is the case, it indicates a limitation of the NRSE-TAS technique when measuring excitation lineshapes with a large dispersion within the resolution ellipsoid of the underlying TAS spectrometer. Another aspect to be considered is the fact that we are unable to fit our data using an asymmetric model for the lineshape despite theoretical indications [141], which might lead to systematically wrong values for Γ with increasing temperature. Nonetheless, the inverse lifetime should be reliable for T → 0, as in this temperature range the lineshape is theoretically predicted to show a vanishingly small asymmetry.

The theoretical prediction for the inverse lifetime based on the non-linear sigma model [138] is plotted with a yellow line in Fig. 4.14. This prediction is identical to the one used by Xu et al. [97] to compare their TAS data with (see dashed black line in Fig. 4.6 B). The NLSM is overestimating the inverse lifetime for T > 25 K when compared to our data (blue circles). Extrapolated to T = 0, it predicts an infinite lifetime for the excitations. When compared to the TAS data, the NLSM seems to give a slightly better description of the temperature dependency of Γ for T > 25 K.

In Fig. 4.14 b) we plot the inverse lifetime Γ extracted from the TRISP data by using the best estimate for the dispersion curvature (blue points) and by assuming a zero curvature, flat dispersion surface within the TAS resolution ellipsoid (cyan points). Such a comparison has the merit of showing that the correction to Γ coming from a curved dispersion just shifts the extracted width without effectively changing the relative curvature. This is somehow revealing in view of finding a possible explanation of the discrepancy between the TRISP data and the data of Xu et al. [97], in the sense that it shows that in order for the TRISP data to increase more rapidly with temperature, some other effect, apart from the curvature correction, must come into play. The $\Gamma_0 = 0.093 \pm 0.006$ meV extracted from assuming a

flat dispersion does not constitute an upper bound on the residual inverse lifetime because we clearly know that the dispersion is not flat at the triplet minimum but rather very steep. A more reliable upper bound on the residual dispersion is provided by the TAS data. By fitting the phenomenological model in Eq. 4.30 to the Xu et al. [97] Lorentzian data, we obtain $\Gamma_0 = 0.056 \pm 0.005$ meV and $I = 0.39 \pm 0.01$ (solid green line).

Using the phenomenological model of Eq. 4.30 we are able to extract an upper and lower bound on the residual inverse lifetime as $0.020 \text{ meV} \geq \Gamma_0 \geq 0.056$ meV which means the triplet lifetime is limited to $12 \text{ ps} \leq \tau_0 \leq 33$ ps. This model does not provide any information about the mechanisms which give rise to finite inverse lifetime as $T \to 0$, so in the following paragraphs we show and discuss how the quantitative model for $\Gamma(T)$ we developed in section 4.2 compares with the TRISP data.

We remind that in our model there are three distinct contributions to the inverse lifetime $\Gamma = \Gamma_L + \Gamma_0 + \Gamma_T$. The first contribution Γ_L (Eq. 4.15) is temperature independent and arises due to the random distribution of chain lengths as a result of a finite impurity concentration. The second contribution Γ_0 (Eq. 4.22) depends on the square root of temperature and is due to interactions with static defects or chain terminations. The third contribution Γ_T (Eq. 4.24) is attributed to Damle and Sachdev [138], depends exponentially on temperature and describes the temperature activated behaviour expected from interactions with thermally activated defects or excitations.

In Fig. 4.15 a) we plot the TRISP data with the best estimate of the dispersion curvature alongside the individual contributions (interrupted lines) and total inverse lifetime (solid line) as predicted by our quantitative model with the parameters fixed to $L_0 = 70$ Ni-Ni spacings (for a 1% impurity concentration - as estimated by Xu et al. [97] for the same sample), spin-wave velocity $v = 60.5$ meV and Haldane gap $\Delta = 7.6$ meV. The model predicts a residual value, an initial increase in the inverse lifetime $\propto \sqrt{T}$ and a crossover to an activated $\exp(-1/T)$ behaviour. The measured Γ is much smaller than what the model predicts. If one assumes that the spin-wave velocity and the Haldane gap are accurately known, the residual inverse lifetime, which is independent of temperature, gives a measure of the mean chain length L_0. If we take the value estimated by Xu et al. [97] for this parameter we see that it severely overestimates the residual inverse lifetime. The measured residual inverse lifetime gives a mean chain length of $L_0 = 148$ Ni-Ni spacings which only differs by

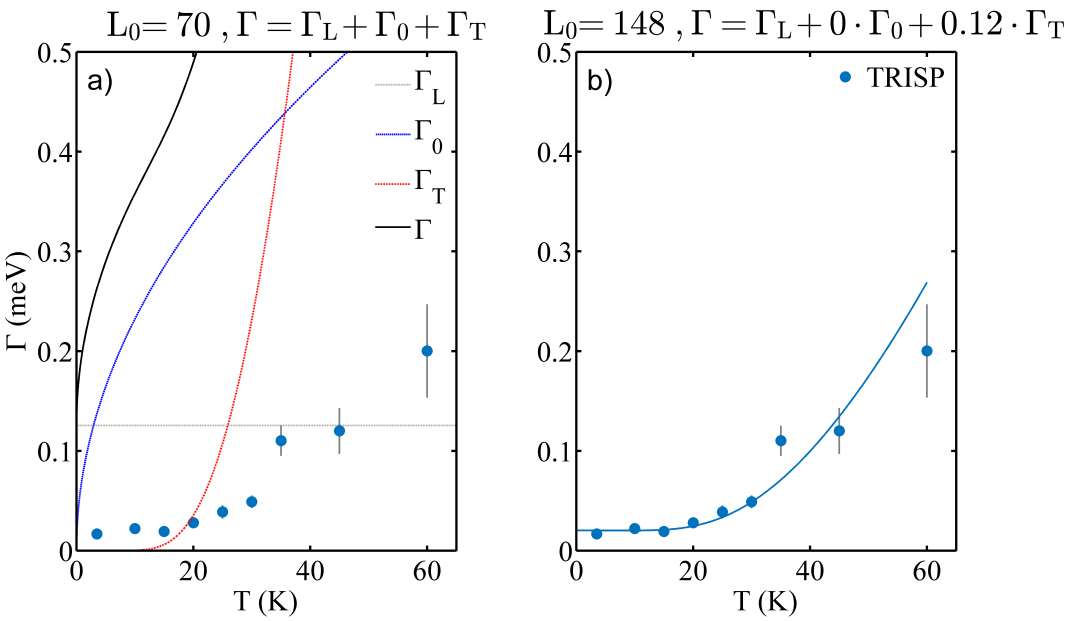

Figure 4.15: Inverse triplet lifetime as a function of temperature, as measured on TRISP with our best estimate of the dispersion curvature. In a) we plot the individual contributions to the inverse lifetime and the total inverse lifetime (solid black line) as given by our quantitative model with $L_0 = 70$, v = 60.5 meV and $\Delta = 7.6$ meV. In b) we plot the TRISP data (blue circles) and the result of a fit of the quantitative model to the data with L_0 and the weights of Γ_0 and Γ_T as free parameters. The best fit is obtained for $L_0 = 148$, $I_0 = 0$ and $I_T = 0.12$.

a factor of two from the estimated value of 70. A concentration of impurities twice smaller is not inconceivable, given the precision of the susceptibility measurements used for its estimation.

In Fig. 4.15 b) we plot the TRISP data together with a fit of the quantitative model where the only free parameters are the weights of Γ_0 and Γ_T and fixed parameters $L_0 = 148$, v = 60.5 meV and $\Delta = 7.6$ meV. The result of the best fit to the data with weights $I_0 = 0$ and $I_T = 0.12$ is plotted with a black line. The fit indicates that our data is not sensitive to the Γ_0 contribution and that only the residual Γ_L and Γ_T are enough to provide a good description of the data. This result is in fact identical to the result of fitting the phenomenological model of Eq. 4.30 to the data.

In conclusion, we used high resolution inelastic neutron resonant spin-echo (NRSE) to measure the inverse lifetime of the triplet excitations that propagate along the chain direction in Y_2BaNiO_5. We showed how NRSE can be used in general to extract excitation lifetimes. The fit of the data to an asymmetric lineshape model was unsuccessful due to low statistical quality of data and due to a large dominant

depolarisation correction coming from the curvature of the dispersion surface sampled by the underlying TAS resolution ellipsoid. We concluded that either the data is not sensitive to an asymmetry of the lineshape or the lineshape remains symmetric up to at least T = 60 K, despite strong theoretical evidence that support an asymmetric development with temperature [138, 141]. Due to large uncertainties in literature values given for the spin-wave velocity that characterises the triplet excitation dispersion in Y_2BaNiO_5, we re-measured it using high-resolution time-of-flight inelastic neutron scattering, thus providing the most reliable and accurate value currently known for this parameter $v = 60.5 \pm 1.5$ meV. This analysis indicates a possible limitation of the NRSE technique when measuring excitation lineshapes with a very steep dispersion due to the large corrections that need to be applied to the polarisation. All the subsequent analysis was performed assuming a symmetric Lorentzian lineshape and the inverse triplet lifetime was extracted as the HWHM Γ of the Lorentzian. Compared to previous TAS measurements, our data deviates substantially from the TAS data, even above T = 25 K, where the TAS data is expected to be reliable because the energy resolution is smaller than the measured lineshape broadening. Below T = 25 K, our data predicts a smaller inverse lifetime and a residual (T = 0) value between $0.02 \text{ meV} < \Gamma_0 < 0.056$ meV or lifetime $12 \text{ ps} \leq \tau_0 \leq 33$ ps, as fitted to a phenomenological model for $\Gamma(T)$. To try and understand the mechanisms that give rise to finite excitation lifetimes we developed a quantitative model with three expected contributions. A finite lifetime due to a random distribution of chain-breaking defects due to impurities, a finite lifetime due to interactions with chain terminations or static defects and a finite lifetime due to interactions with mobile defects or thermal excitations. We showed that using the most accurate known values for the mean chain length, spin-wave velocity and Haldane gap, the quantitative model severely overestimates the inverse lifetime over the whole range of measured temperatures. A fit of the TRISP data to the quantitative model showed that the best description is obtained if the mean chain length is $L_0 = 148$ Ni-Ni spacings (approximately twice of that estimated for a 1% impurity concentration for the same sample as ours) and that our data is not sensitive to the contribution to Γ coming from interactions with chain terminations and only two terms are sufficient in order to provide a good description of the measured inverse lifetime $\Gamma = \Gamma_L + 0.12 \cdot \Gamma_T$. The non-linear sigma model prediction of Damle and Sachdev [138] fails to describe both our data and the TAS data over the whole range of temperatures from T = 0 to T = 60 K. For $T \to 0$ this is not surprising as the

theory accounts only for interactions with mobile thermally excited defects and ignores static defects. For larger temperatures though, the NLSM should provide an accurate description of the data because here the dominant mechanism that leads to finite lifetimes is the interaction with thermally excited particles.

4.6 Blue Shift of the Gap Energy

The gap energy shift towards higher values with increasing temperature, which is predicted by the NLSM [138, 139], has been experimentally confirmed in several gapped antiferromagnetic systems [120, 129, 136, 151, 152] as well as in Y_2BaNiO_5 [97, 134]. All these experiments were performed using either time-of-flight or TAS spectroscopy. First attempts to measure the temperature dependence of the gap using high resolution NRSE-TAS spectroscopy, were made by Dr. Felix Groitl and Dr. Thomas Keller [149]. They performed phase sensitive measurements in copper nitrate and $Sr_3Cr_2O_8$, where the spin-echo phase was determined with high precision by measuring the echo amplitude oscillations over two and a half periods. The most important conclusion from their study was that NRSE can reliably be used to measure the blue shift of the gap in the case of a symmetric lineshape of the excitations. In this case, the spin-echo phase is a linear function of the spin-echo time and it is thus directly proportional to the change in energy according to [149]

$$\Delta \mathrm{E}(\mathrm{T}) = \hbar \frac{\phi(\mathrm{T}) - \phi(\mathrm{T}')}{\tau} \tag{4.31}$$

where at a given temperature T, the change in energy transfer is given by ΔE. For a fixed spin-echo time τ, the difference between the phase at two different temperatures gives the difference in the energy gap.

The choice of spin-echo time is determined by the fact that the sensitivity of the energy shift increases with increasing τ (period of the echo amplitude decreases) but the error on the extracted phase increases due to lower polarisation.

In the case of an asymmetric lineshape, the relationship in Eq. 4.31 does not hold anymore because the phase becomes a non-linear function of the spin-echo correlation time. In order to correctly analyse the data one needs to predict what this dependency is for a given lineshape.

Due to the fact that we were not able to reliably extract the lineshape asymmetry from the measurements of the excitation lifetime, we assumed a symmetric

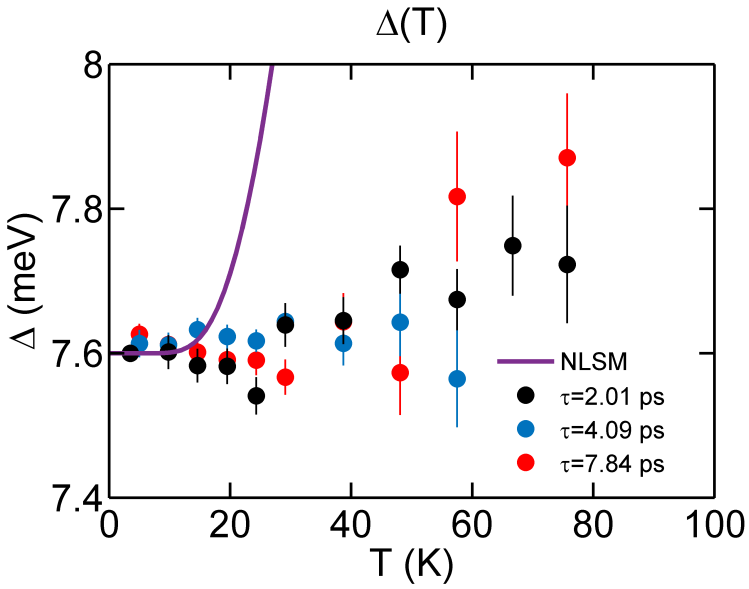

Figure 4.16: Blue shift of the gap energy extracted from phase sensitive measurements performed at three different spin-echo times assuming a linear relationship between the Larmor phase and the spin-echo time.

lineshape of the excitations and extracted the gap energy blue shift accordingly. In Fig. 4.16 we present the blue shift extracted from measuring the spin-echo phase for three different fixed spin-echo times. We see that for $\tau = 2.01$ ps and $\tau = 7.84$ ps the data shows an increase of the gap energy with increasing temperature. For $\tau = 4.09$ ps the energy seems to remain constant with increasing temperature. It is quite difficult to conclude quantitatively on the energy shift due to the fact that we assumed a symmetric Lorentzian lineshape of the excitations and used the linear relationship between the Larmor phase and the spin-echo time to extract the blue shift. There is strong theoretical indication that this assumption might not be correct due to the predicted asymmetric development of the lineshape with increasing temperature [138, 141]. The inability to extract the lineshape asymmetry from the lifetime measurements prevents us from correctly extracting the gap energy from the data. On a qualitative level we can confirm the predicted blue shift of the gap energy. When compared to theory, we see that the NLSM prediction [139] (violet line) seriously overestimates the blue shift. The NLSM also overestimates the blue shift for other Haldane gap systems [134, 136, 137] and a good description is provided only for a very narrow range of temperatures close to T = 0. This mismatch between NLSM and experimental results indicates the need for including the effects of anisotropy and possible further neighbour interactions in order to provide

a theoretical description of the blue shift in real materials.

Chapter 5

Entanglement Transition, Order and Excitations in Cs_2CoCl_4

In the first half of this chapter we study the entanglement transition, a phenomenon that is purely driven by quantum correlations, in a one-dimensional anisotropic antiferromagnetic chain, using time-of-flight magnetic neutron diffraction. In the second part of this chapter we study the applied magnetic field dependence of the magnetic ordering which arises when the field is applied parallel to the chain direction, using triple-axis neutron scattering. We begin with an introduction about the recent success of the cross-fertilisation between quantum information and condensed matter theory in characterising the low-temperature properties of quantum spin systems through the analysis of correlations determined by quantum entanglement. We then present the concept of concurrence and its importance in providing a quantitative characterization of entanglement present in the XXZ antiferromagnetic spin chain. We show that in principle the concurrence can be extracted from neutron scattering measurements and used to compute the entanglement between microscopic degrees of freedom. In sections 5.3 and 5.4 we give details about Cs_2CoCl_4, a realisation of the XXZ chain, and the neutron scattering experiments devised to detect an entanglement transition. In section 5.5, we present results from two diffraction experiments and comment on the possible causes why the predicted entanglement transition signatures might not be visible. Motivated by the unknown field phase diagram of Cs_2CoCl_4 with applied field along the crystallographic b-direction, we describe in section 5.6, the results from a dedicated triple-axis neutron scattering experiment performed in order to establish the magnetic field evolution of the ground state. We then present spin-wave data collected at B = 4 T, in the fully polarised

state, used to extract possibly relevant additional terms in the magnetic Hamiltonian that are responsible for the observed ordering. We end the chapter with conclusions and future outlook regarding the entanglement transition and the complex observed magnetic ordering of Cs_2CoCl_4.

5.1 Introduction

In recent years extensive theoretical work has been carried out that has proven successful in describing various aspects of many-body physics using concepts from the field of quantum information theory (QIT) [153–155]. The application of concepts from QIT to the study of well-established models of condensed matter systems such as spin chains, has revealed novel features in their phase diagram. For example, a new type of T = 0 phase transition is predicted, which is markedly different from a quantum phase transition because none of the traditional thermodynamic quantities show discontinual behaviour. Quantum entanglement is a QIT concept which constitutes a basic resource for quantum computation, quantum cryptography and quantum teleportation [156] and which is fairly well-understood for a bipartite system made of two subsystems [157]. Not so much is known for the more complicated case of multipartite entanglement where the entanglement is shared between more than two subsystems. In this respect, the study of spin chains offers the possibility to investigate properties of multipartite entanglement for many-body systems with Hamiltonians that can be controlled and manipulated [153].

Entanglement is a defining feature of quantum mechanics which describes nonlocal correlations between quantum systems. These quantum correlations cannot be explained using classical arguments as they arise due to the fundamental superposition property and the Heisenberg principle of uncertainty of conjugate variables such as position and momentum or different components of spin. A useful way to illustrate the strangeness of entanglement is using the traditional example of two spin-1/2 particles. Assume that at time t_0 the decay of a S = 0 particle takes place with the emission of an electron and a positron in opposite directions in space. Conservation of total spin dictates that the electron spin and the positron spin are opposite. At a later time t, the particles have travelled an arbitrary large distance in space which prevents them from interacting classically. If a measurement of the spin of the electron is performed at time t along the x-direction with the result +x ($+\frac{1}{2}\hbar$), the measurement of the positron spin along the same direction will have

an outcome which depends on the result of the measurement on the first electron, namely -x ($-\frac{1}{2}\hbar$). It turns out that such measurements are perfectly anti-correlated revealing that the electron and positron are entangled and the state of the system is the singlet state. The obvious question is how can the positron know what spin state to adopt if measurements are done independently and simultaneously, as the two particles cannot exchange information (no signal travels faster than the speed of light). The answer lies in the fact that before measurements neither of the two particles had definite spin state, but were in a superposition of negative and positive spin along the x-direction. Once a measurement is performed on one particle, its spin chooses a state whereas for the other particle its spin chooses the opposite state. The experimental confirmation of the existence of quantum entanglement as an intrinsic property of quantum mechanics came from experiments on photon polarizations [158] and electron spins [159].

Real systems have a large number of interacting spins. Understanding the quantum correlations between spins and how these can be manipulated is crucial because of fundamental and practical reasons. In this context, the investigation of quantum phase transitions in spin systems with the help of entanglement estimators [21, 154, 155] has led to previously hidden features in their phase diagrams, of which the most notable is a completely new type of transition known as an entanglement transition (ET) [21, 22]. The ET has no clear signature in any of the thermodynamic quantities that can be computed or measured due to a smooth variation of these quantities upon crossing the transition. There is though experimental evidence that magnetic measurements [160] and neutron scattering [2] are sensitive to the entanglement present in a system. This has led to the idea that a method for experimentally detecting an entanglement transition in a quantum spin system could be devised with the help of neutron scattering techniques. The objective of the present study is to develop a method that can unmistakably detect an entanglement transition in a real system, and the focus of our study is a one-dimensional system with localized spins, the quasi-1D spin-1/2 XXZ antiferromagnet Cs_2CoCl_4 in applied magnetic field.

5.2 Model and Concurrence

The theoretical investigations were performed by Dr. Jorge Quintanilla and Dr. Luigi Amico. They have focused on the one-dimensional anisotropic S=1/2 XXZ

antiferromagnetic model in applied magnetic field, which is the model that best describes Cs_2CoCl_4 for fields applied along the b-axis, in a range of temperatures $0.22\ \mathrm{K} < \mathrm{T} < 0.6\ \mathrm{K}$. The Hamiltonian of the general anisotropic Heisenberg chain model is written as

$$\mathcal{H}_{\mathrm{XYZ}} = \mathrm{J}\sum_{\mathrm{i}}\left[(1+\gamma)\mathrm{S}_{\mathrm{i}}^{\mathrm{x}}\mathrm{S}_{\mathrm{i+1}}^{\mathrm{x}} + (1-\gamma)\mathrm{S}_{\mathrm{i}}^{\mathrm{y}}\mathrm{S}_{\mathrm{i+1}}^{\mathrm{y}} + \Delta\mathrm{S}_{\mathrm{i}}^{\mathrm{z}}\mathrm{S}_{\mathrm{i+1}}^{\mathrm{z}}\right] - \sum_{\mathrm{i}}\mathbf{h}\cdot\mathbf{S}_{\mathrm{i}} \qquad (5.1)$$

where the first term is the XYZ term and the second term is the Zeeman term which describes the interaction with the applied magnetic field. The constants γ and Δ parametrize the anisotropy of the interactions and where $\mathbf{h} = \mathrm{g}\mu_{\mathrm{B}}\mathbf{B}/\mathrm{J}$ and represents the reduced applied magnetic field in units of J, the exchange interaction strength. For $\Delta = 0$ the model interpolates between the isotropic antiferromagnetic XY model ($\gamma = 0$) and the antiferromagnetic Ising model ($\gamma = 1$). The anisotropic antiferromagnetic XY model then sits between the two, with $0 < \gamma < 1$.

Two shared features of anisotropic spin chains in an external applied magnetic field are the presence of a factorised ground state at a field $\mathrm{h_f}(\Delta)$ and the presence of a QPT at $\mathrm{h_c}(\Delta)$ [21]. A factorised ground state means that the total spin wave function can be written as a product of individual wave functions for each spin in the chain and corresponds to the classical Néel state. The factorised field always occurs for $\mathrm{h_f} < \mathrm{h_c}$ with $\mathrm{h_f} = \sqrt{2(1+\Delta-\gamma)}$ (for the magnetic field pointing in the XY plane [23]). At $\mathrm{h_c}$ the quantum critical point separates a region with long-range antiferromagnetic order from a disordered phase with short-range antiferromagnetic order [23, 161].

For the Ising model ($\Delta = 0$, $\gamma = 1$), the factorising field is at $\mathrm{h_f} = 0$ and $\mathrm{h_c} = 0.5$ so the zero field ground state is factorisable. This means that by applying a magnetic field one is always on the same side of the factorising field. For the isotropic XY model ($\Delta = 0$, $\gamma = 0$) the factorising field is at $\mathrm{h_f} = \sqrt{2}$ and the critical field $\mathrm{h_c} = 1.5$ with the entanglement transition taking place in the magnetically ordered phase at $\mathrm{T} = 0$. For the anisotropic XXZ model ($\gamma = 0$) with $\Delta = 0.25$, the ground state phase diagram is presented in Fig. 5.1. Quantum Monte-Carlo [21] gives the quantum critical point at $\mathrm{h_c} = 1.605$, which separates a Neél ordered phase from a disordered phase with short range order [23, 161] while the value of the factorising field is $\mathrm{h_f} = 1.581$. The XXZ model is not exactly solvable but the anisotropic XY model does admit an exact solution both at zero and finite temperature. This is

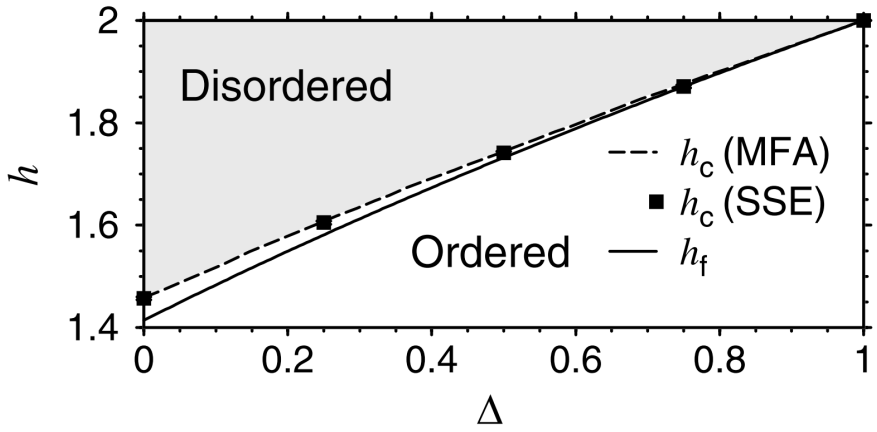

Figure 5.1: Ground state phase diagram of the XXZ model in an applied magnetic field. The evolution of the quantum critical field (h_c) and the factorizing field (h_f) with the anisotropy parameter (Δ) is shown. Broken line corresponds to the results of a mean-field approximation and black rectangles to stochastic series expansion quantum Monte Carlo. Taken from [21].

important as we will argue in the next section that the pattern of correlations for the two models are expected to be similar. A study of the XY model thus provides useful information about the XXZ model.

A theoretical method has been proposed for detecting a factorised state with high accuracy [21]. It makes use of several multipartite entanglement witnesses such as the one-tangle, two-tangle and concurrence. The one-tangle [154] gives a measure of the degree of entanglement of one spin with the rest of the system in the ground state. The concurrence [162] describes the level of entanglement between pairs of spins and is defined as

$$C_r = 2\max\{0, C'_r, C''_r\} \tag{5.2}$$

$$C'_r = |g_r^{xx} + g_r^{yy}| - \sqrt{\left(\frac{1}{4} + g_r^{zz}\right)^2 - M_z^2} \tag{5.3}$$

$$C''_r = |g_r^{xx} - g_r^{yy}| + g_r^{zz} - \frac{1}{4} \tag{5.4}$$

where C'_r and C''_r quantify the two-spin entanglement of the anti-parallel and parallel Bell states respectively (see Fig. 5.2) for pure and mixed states alike. Here $g_r^{\alpha\beta} = \langle S_0^\alpha S_r^\beta \rangle$ (with $\alpha, \beta = x, y, z$) is the correlation function in real space between two spins separated by distance r. The magnetisation is $M_z = \langle S_z \rangle$. The one-tangle

and two-tangle [155] read

$$\tau_1 = 1 - 4\sum_{\alpha} M_{\alpha}^2 \tag{5.5}$$

$$\tau_2 = 2\sum_{r} C_r^2 \tag{5.6}$$

with the ratio τ_2/τ_1 that gives a measure of the fraction of the total entanglement that is stored in two-spin entanglement [21]. An important point has to be made here, namely the fact that at $T = 0$ for $h > h_f$ the concurrence is a measure of bipartite entanglement whereas for $h < h_f$ it only gives a lower bound to the entanglement in the system [21, 163].

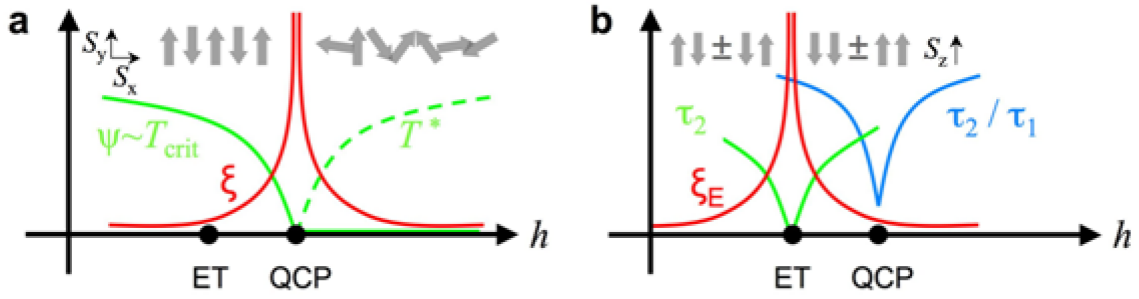

Figure 5.2: a) conventional and b) quantum information theoretic view of quantum criticality. In a) the type of magnetic order qualitatively changes upon crossing the transition point whereas in b) the type of entanglement in the system changes. Taken from [164].

With these ideas in mind, quantum criticality can now be viewed from two distinct perspectives as pictured in Fig. 5.2. The well-established view where an order parameter vanishes continuously as the quantum critical point is approached and the correlation length diverges (sub-figure a), and a novel, quantum information theoretical view (sub-figure b), where the ratio of the two-tangle to one-tangle has a minimum at h_{QCP}. This novel perspective can also signal a factorisation point where the concurrence goes through zero having different values on both sides of this point. The associated entanglement range diverges at the so-called entanglement transition, at $h_f \equiv h_{ET}$.

5.2.1 From Magnetic Scattering to Concurrence

In order to experimentally detect a factorised state we have focused our efforts in devising a neutron scattering experiment that we thought would show clear signatures of such a state. The essential feature which connects the theory of entanglement in spin systems and neutron scattering is that neutron magnetic scattering is a direct probe of the spin-spin correlation function which depends on the entanglement between spins. If we analyse the analytic form of the concurrence (see Eq. 5.4) we see that what is actually needed is the static spin-spin correlator. This is written as

$$\mathrm{S}^{\alpha\beta}(\mathbf{Q}) = \int_{-\infty}^{+\infty} \mathrm{S}^{\alpha\beta}(\mathbf{Q},\omega)\mathrm{d}\omega \tag{5.7}$$

by integrating the components of the dynamical structure factor over all frequencies (energy transfers). In practice this is achieved by either performing an inelastic neutron scattering experiment, obtaining $\mathrm{S}(\mathbf{Q},\omega)$ and calculating the integral $\mathrm{S}(\mathbf{Q}) = \int_{-\infty}^{+\infty} \mathrm{S}(\mathbf{Q},\omega)\mathrm{d}\omega$ or by performing an elastic neutron scattering experiment that directly yields $\mathrm{S}(\mathbf{Q})$. At this point an extra step is necessary to obtain the correlators in real space, namely performing a Fourier transform of the correlators which neutron scattering gives in reciprocal space. After this step has been performed, the concurrence can be computed.

An ansatz for the $\mathrm{T} = 0$ real-space correlators has been developed [164]. It applies to the exactly solvable anisotropic XY model. The XXZ model ($\gamma = 0$) with $\Delta = 0.25$ for which Cs_2CoCl_4 is a good realisation of, has no exact solution. Its $\mathrm{T} = 0$ properties have been studied numerically with quantum Monte Carlo by Roscilde et al. [21] and by Caux et al. [161] through a mean-field approach. Density matrix renormalisation group (DMRG) has been performed on the XY model with $\gamma = 0.2$ (for this value of γ the factorising field and the quantum critical field are 2% apart as in the case of the XXZ($\Delta = 0.25$) model) and it gives excellent agreement with the ansatz [164] for the behaviour of the correlation functions. The assumption we make from this point onward is that the pattern of correlations is very similar for the XY and XXZ models close to the entanglement transition because the XY and the XXZ models belong to the same universality class and have the same symmetries.

The main result of the ansatz is that measuring $\mathrm{S}^{\alpha\beta}(\mathbf{Q})$ close to the factorising field in a neutron scattering experiment, will result in a peak with two components: a sharp component (ideally a δ-function) due to long-range correlations in the ground state and a broad component due to finite range quantum correlations which depend

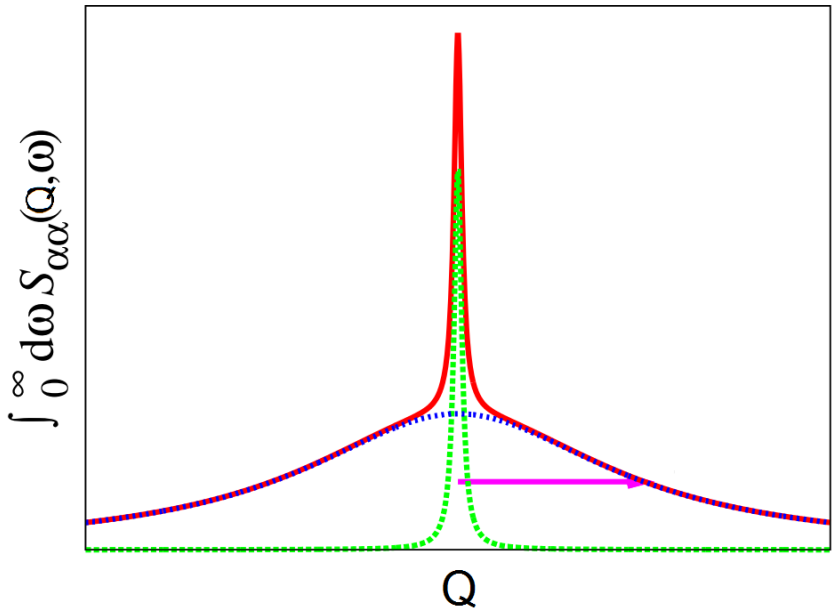

Figure 5.3: Integrated $S^{\alpha\alpha}(\mathbf{Q},\omega)$ over all frequencies in the low temperature limit near the factorising field. A narrow peak (green colour) centred at $Q_{chain} = \pi$ (antiferromagnetic) and a broad component (blue colour) due to entanglement. This latter component vanishes as the factorising field is approached. Taken from [164].

in turn on the entanglement. The expected peak shape is illustrated in Fig. 5.3. The broad component is expected to vanish as the factorising point is approached and resurface for fields larger than h_f. A crucial point here is that the vanishing of this component takes place through the decrease of the amplitude as the external magnetic field is varied and not through a decrease of the width which would correspond to a diverging correlation length characteristic to a quantum phase transition. This implies that the neutron scattering signatures of an entanglement transition and a quantum phase transition are different. The key signature of the entanglement transition is a decrease of the total weight of the diffuse scattering over a wide range of fields $h < h_f$ which is indicated by the integrated diffuse scattering weight

$$\mathcal{I}_{\alpha\beta} = \int_{BZ} \left[S^{\alpha\beta}(\mathbf{Q}) - S^{\alpha\beta}(\mathbf{Q}=0)\right] d\mathbf{Q} \tag{5.8}$$

where in the case of a one-dimensional system of spin chains $\mathbf{Q} = Q_{chain}$ and the integral is performed over one Brillouin zone. The details of how $\mathcal{I}_{\alpha\beta}$ was derived can be found in [165]. At $T = 0$ this quantity shows a non-monotonic behaviour. We plot the results from DMRG on the XY model in Fig. 5.4 where the non-

monotonic behaviour of the correlation functions marks the entanglement transition. If an entanglement transition can be detected by the method described earlier, in principle, by choosing a narrow range around the factorising field, obtaining the parameters in the ansatz and calculating the correlators, leads to the determination of the concurrence. The concurrence can then be used to quantify the level of pairwise (two-spin) entanglement present in the system as well as check that the entanglement range diverges at h_f.

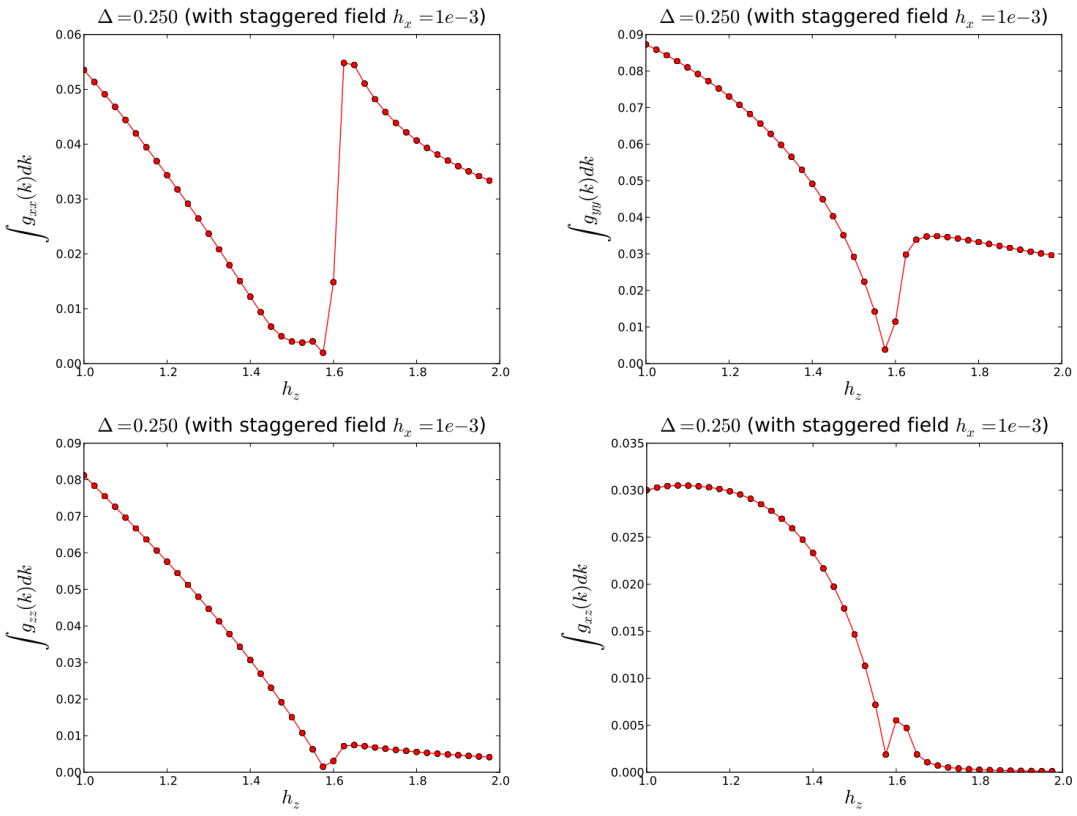

Figure 5.4: DMRG results for the T = 0 ground state of the XY model showing (top left) $\mathcal{I}_{xx}$, (top right) $\mathcal{I}_{yy}$, (bottom left) $\mathcal{I}_{zz}$, (bottom right) $\mathcal{I}_{xz}$ as a function of applied magnetic field (in units of J), corresponding to different components of the pair spin correlation function. A non-monotonic behaviour that is used to identify the entanglement transition can be observed. The factorising point occurs at $h_f = 1.58$. Taken from [164].

5.3 Sample Properties

Cs_2CoCl_4 crystallizes in an orthorhombic β-K_2SO_4 type structure, Pnma (No. 62) space group [166]. Its lattice parameters at T = 0.3 K are a = 9.71 Å, b = 7.27 Å and c = 12.73 Å [167]. Each unit cell contains four Co^{2+} ions, each surrounded by four Cl^- ions, arranged in a slightly distorted tetrahedral environment (see Fig. 5.5). Earlier heat capacity [168] and susceptibility [169] measurements suggested that Cs_2CoCl_4 has a one-dimensional character. The heat capacity measurements revealed a small λ-type anomaly at $T_N = 0.22$ K that suggested a transition to a magnetic ordered phase below this temperature. The in-plane susceptibility measurements also pointed to magnetic order below 222 mK. Both these studies were in excellent agreement with numerical work [170], an indication that Cs_2CoCl_4 can be well described by a one-dimensional antiferromagnetic XXZ ($\Delta = 0.25$) model. A more recent analysis of new high-resolution specific heat and thermal expansion data [171] has revealed that while Cs_2CoCl_4 is indeed very well described by an effective S=1/2 XXZ model, the anisotropy of the exchange is smaller ($\Delta = 0.12$) than what was previously assumed. This conclusion emerged due to the necessity of including virtual excitations of the higher $|\pm 3/2\rangle$ spin states to correctly explain the data. From a magnetic point of view Cs_2CoCl_4 can be considered as made up of one-dimensional parallel spin chains running along the crystallographic b-direction with exchange coupling proposed as J = 0.23 meV and small inter-chain couplings $J'/J < 0.1$ [167,172] that lead to frustration. Neutron diffraction measurements [167] have shown that the static spin-correlation function has a sheet-like structure perpendicular to the crystallographic b-axis thus confirming the one-dimensional magnetic character of the compound. They have also revealed incommensuration in the magnetic ordering that has been interpreted as the effect of finite inter-chain coupling.

In Cs_2CoCl_4 there are two types of spin chains, one shifted with half a unit cell along the b-direction with respect to the other. Spin orbit coupling and crystal field effects determine XY easy-plane anisotropy at the Co^{2+} sites with adjacent chains that have a different orientation of the XY easy-planes and make a large angle with each other (see Fig. 5.5). In zero field, the competition between magnetic exchange and crystal-field leads the Co moments to lie in the b-c plane making a small angle $\phi = 15°$ with respect to the b-axis [173].

The investigation of possible exchange paths has revealed that superexchange

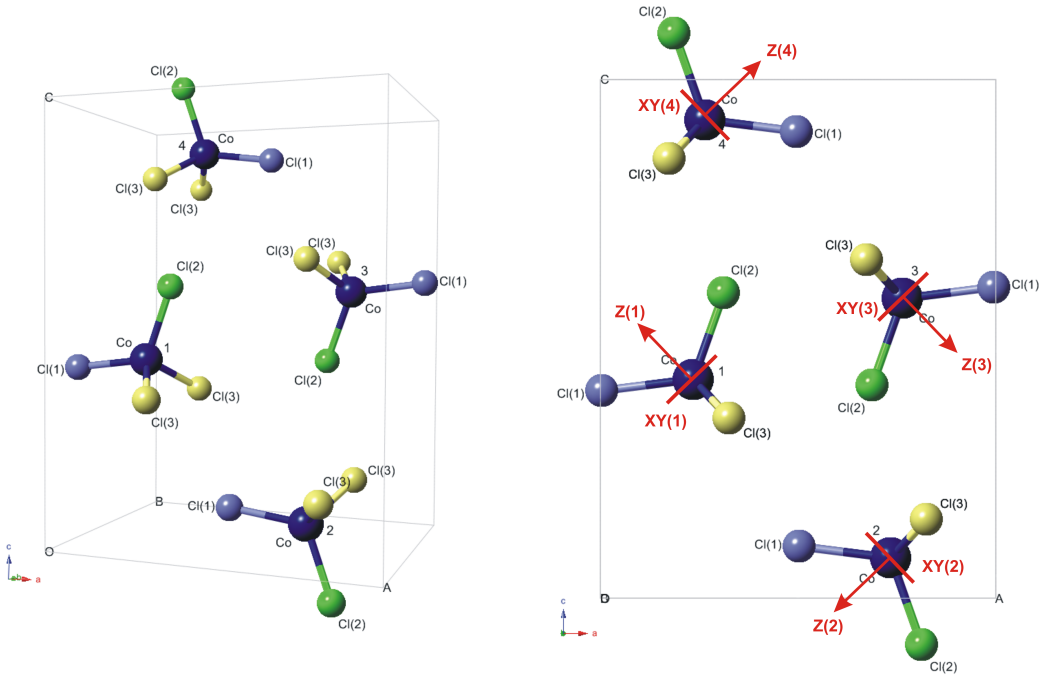

Figure 5.5: Left: Crystal structure of Cs_2CoCl_4 showing the Wyckoff 4c positions of the four Co^{2+} ions in the unit cell. Antiferromagnetic chains run along the b-axis. Right: Projection onto the a-c plane showing the XY easy planes in each chain; the normal to these planes defines the local Z axis and bisects the largest angle of the distorted Cl^- tetrahedra.

through the Cl^-, along the chains, is strongest and that coupling between chains leads to magnetic frustration. As a result, the possibility of helical spin-order has been proposed [167]. This was backed up by observation of a modulation in the correlation function even in the paramagnetic phase. Spins interact through $Co-Cl-Cl-Co$ paths with the angle between $Co-Cl$ and $Cl-Cl$ bonds being $\approx 145°$ [168]. The shortest distance is $d_{Cl-Cl} = 3.61$ Å along the b-axis. Other possible exchange paths are J_{12} ($d_{Cl-Cl} = 4.05$ Å), J_{13} ($d_{Cl-Cl} = 4.04$ Å) and J_{14} ($d_{Cl-Cl} = 4.01$ Å). These distances come to support the picture of weakly coupled parallel spin chains running along the b-axis.

The true orbital ground state of the magnetic ions is a singlet with $\tilde{S} = 3/2$. Every Co^{2+} ion is tetrahedrally coordinated with four Cl^- ions. Spin-orbit coupling and the crystal field environment split the true ground state into two Kramers doublets [173] with separation $2D \approx 1.3$ meV [174]. Because the magnetic exchange energy is smaller than the inter-doublet separation, for most purposes, only the

lowest energy Kramers doublet gets populated at low temperatures ($k_BT << 2D$) and the system can be well-described by a ground state with effective $S = 1/2$.

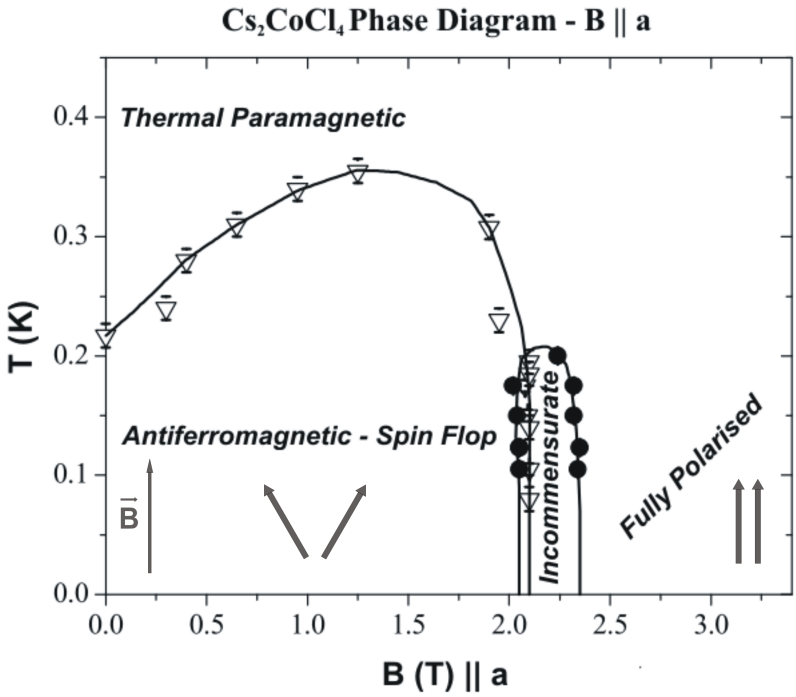

Figure 5.6: Cs_2CoCl_4 experimental temperature - field phase diagram for the case when the magnetic field is applied along the a-direction, perpendicular to the spins. Solid lines are guides to the eye. Adapted from [175, 176].

The results of the neutron scattering study of Kenzelmann et al. [173], reveal that for $T < T_N$ and zero applied magnetic field, Cs_2CoCl_4 is in the ground state and shows antiferromagnetic ordering ($\mathbf{k} = (0, 0.5, 0.5)$) with spins lying in the b-c plane, making a small angle with b. In these conditions the coupling between the chains leads to 3D magnetic order. As the temperature is increased, thermal fluctuations come into play and have the effect of disordering the system. A phase transition from antiferromagnetic to thermal paramagnetic takes place at $T_N = 0.22$ K [168]. At zero temperature but finite and small value of the applied field parallel to the a direction, the system displays canted antiferromagnetic order described by a spin-flop phase [173] which we will refer to, from now on, as canted antiferromagnetic phase (CAF). At higher fields, an incommensurate ordering emerges which is stable from $B_c = 2.04$ T to $B = 2.36$ T. This phase has been proposed to be an incommensurate longitudinally-modulated spin-density wave propagating along the magnetic chain direction [176]. In the narrow region where commensurate and incommensurate or-

dering overlap the ordering wave vector was found to be $\mathbf{k} = (0, 0.5 - \delta, 0)$ with $\delta = 0.055$ r.l.u. [176]. For higher magnetic fields, the system makes a smooth transition to a fully polarised state. The experimental temperature-field phase diagram is illustrated in Fig. 5.6.

The more recent study of Breunig et al. [171,177,178] makes use of high-resolution specific heat and thermal expansion measurements on single crystals of Cs_2CoCl_4 to provide information about the magnetic field dependency of magnetic ordering. For magnetic fields applied along the a- and c- crystallographic directions, the temperature-field phase diagram is very similar to the one proposed by Kenzelmann et al. [173] (see Fig. 5.6 and the top and bottom panels of Fig. 5.7). At the lowest of temperatures and small applied field, the magnetic phase is an ordered canted antiferromagnetic phase (CAF). Such a phase is expected to occur as the magnetic field is applied perpendicular to the Co moments. In the canted phase, the transition temperature increases with increasing magnetic field up to about B = 1 T, where it reaches a maximum of approximately 0.325 K (a-direction) and 0.3 K (c-direction), after which the transition temperature decreases. This behaviour indicates that the canted phase is initially stabilised by the magnetic field, in accord with an increased perpendicular antiferromagnetic moment measured by Kenzelmann et al. [173]. At about B = 2.1 T (B ∥ a) and B = 2.25 T (B ∥ c) there is a phase transition into another magnetic phase denoted in Fig. 5.7 as phase II. The exact nature of this phase is unknown and various scenarios have been proposed. The main possibilities include an incommensurate magnetic phase and a magnetic nematic phase [177]. For fields higher than approximately 2.5 T, the system transitions into a fully polarised state where the magnetic moments tend to align parallel with the direction of the applied field.

The b-direction is a special crystallographic direction because it is the only XY in-plane common direction for both types chains. The application of a magnetic field along the b-direction makes the chains equivalent from an anisotropy point of view and leads to a much more complex phase diagram as a function of applied magnetic field strength than for the case of the field applied along the a-direction. At low temperatures and for fields up to B = 0.25 T, the magnetic ordering is characterised by a Neél-type phase (AF) with moments aligned antiferromagnetically along the chain. For fields between $B = 0.25$ T and B = 2 T, the order has been proposed to be described by two different spin-flop phases. In the field region from B = 0.25 T to B = 0.7 T, the ordering can be described by a spin-flop phase (SF1) where only half

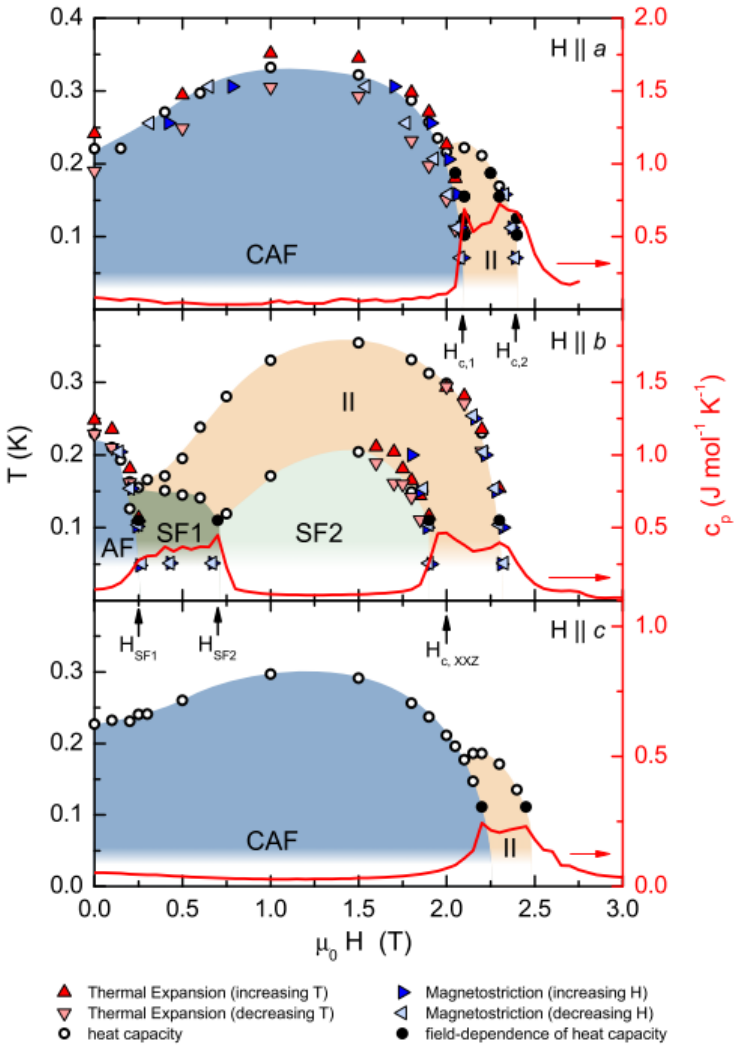

Figure 5.7: Cs_2CoCl_4 temperature-field phase diagram based on specific heat and thermal expansion measurements for magnetic field applied along the a direction (top panel), b direction (middle panel) and c direction (bottom panel). The measured specific heat C_p at 0.11 K is plotted in red. Taken from [177].

of the chains make the spin-flop transition and the other half remain in a Neél-type order. For fields larger than B = 0.7 T and up to approximately B = 2 T (SF2), all chains make the transition into the spin-flop arrangement. This two-stage spin-flop transition is believed to be driven by the inter-chain Dzyaloshinskii-Moriya (DM) interaction. The antisymmetric DM exchange is written as $\mathbf{H}\mathrm{DM} = \mathbf{D}_{ij} \cdot (\mathbf{S}_i \times \mathbf{S}_j)$ and gives a contribution to the magnetic exchange between two magnetic spins. It arises due to finite spin-orbit coupling and favours spin canting. For higher fields, the spin-flop phases are followed by the same phase II as identified before. In this

case, phase II has a much wider spread in the T-B parameter space, occupying a significant portion of the phase diagram at temperatures higher than the zero field Neél temperature (see Fig. 5.7 middle panel). For B > 2.5 T, the magnetic moments align parallel to the applied field and the system is classical polarised.

For all three orientations of the magnetic field, the measured specific heat C_p is plotted in Fig. 5.7 with red lines. Whenever a phase transition occurs, there is also a significant change in the specific heat. The enhanced specific heat in the field range of phase II as well as the power-law scaling $C_p \propto T^{\alpha}$ that is almost identical for all three field directions, constitutes a strong indicative that the nature of phase II is similar for all fields [177].

5.4 Experimental Details

The objective of the present study was to use neutron scattering to identify experimental signatures of a newly predicted transition which was shown to occur in one-dimensional quantum antiferromagnetic chains and which is totally driven by quantum entanglement between spins along the chain. This quantum transition is known as an entanglement transition and it describes the transition, inside the same magnetic phase, between two distinct phases which differ from each other in their respective type of entanglement between spins. To identify the entanglement transition an entanglement estimator has been constructed which can be extracted from neutron scattering data. It requires the static structure factor measured over at least one Brillouin zone along the momentum transfer along the chain direction as in Eq. 5.8.

After a survey of possible candidate materials [163], Cs_2CoCl_4 has been chosen due to several reasons. First of all, Cs_2CoCl_4 is well described by an effective S=1/2 XXZ model for temperatures between T = 0.22 K and T = 2 K, and magnetic fields up to B = 3 T. This means that experimentally the regime of 1D behaviour can be easily reached. Theoretically, although the XXZ model is not an exactly solvable model, useful information can be obtained from the study of the quantum XY model. The two belong to the same Ising universality class and are expected to have very similar patterns of spin correlations near the factorisation field. Also, large single crystals of Cs_2CoCl_4 can be grown via an established method, thus making it a good candidate material for such a study.

The magnetic diffuse scattering experiment was performed on a single crystal of

m = 2 g of Cs_2CoCl_4 grown by Dr. Karl Krämer and Dr. Daniel Biner from the University of Bern, which we aligned with the $(h, 0, l)$ plane in the horizontal plane of the instrument (see right side of Fig. 5.8) and mounted on a custom made aluminium mount piece. The crystal was glued onto the mount with a very small amount of red araldite and a thin copper bonnet was used to ensure enough contact between the crystal surface and the mount in order to facilitate the cooling of the crystal to dilution temperatures. The whole mount was enclosed in a He filled aluminium can and sealed with indium wire. The sample mount was introduced in a dilution refrigerator insert into a vertical field magnet with maximum field of $B_{max} = 9$ T. This setup was placed on the high resolution cold neutron diffractometer WISH at the ISIS Neutron Source, UK. The main reason for choosing WISH is that it has large detector banks (covering horizontal scattering angles from $-10°$ to $-170°$ - at the time of the experiment) made up of 1 m long ^{3}He detector tubes (covering $\pm 15°$ vertically) which are pixellated vertically (128 individually addressable elements per tube) and allow one to measure a vast portion of reciprocal space in one go. The experiment was performed in applied vertical magnetic fields using a magnet with a vertical opening of $\pm 15°$. Due to the high fields generated by this magnet, the sample geometry is quite restricted. The in-plane magnet window allowed the coverage of detectors placed at horizontal scattering angles ranging from $-10°$ to $+22.5°$.

The crystallographic b-direction is the only common in-plane direction for both types of chains in Cs_2CoCl_4. By applying the magnetic field along this direction we ensure that all chains are treated identically from the anisotropy point of view. Our sample was oriented such that the chain direction (b-direction) was parallel to the applied magnetic field and vertical in the coordinate frame of the instrument. This means that the diffuse scattering along the chain direction was measured in the out-of-plane detectors. In Fig. 5.8 we show that in order to cover a full Brillouin zone along the chain direction, which is a prerequisite to extracting the integrated spectral quantity $\mathcal{I}$ that is predicted to signal the entanglement transition, one has to use neutrons of wavelengths smaller than 2 Å. Also in order to cover at least one Brillouin zone in the chain direction, one is forced to use wave vectors at small scattering angles with consequently poor in-plane momentum resolution.

All measurements were performed with a fixed sample orientation described by the angle $\psi = -27°$, the angle between the incident beam direction defined by $\mathbf{k}_i$ and the $a^\star$ direction. This orientation has two major advantages. One of them is that neutron absorption is minimized and the second is that the weight of the S^{xx}

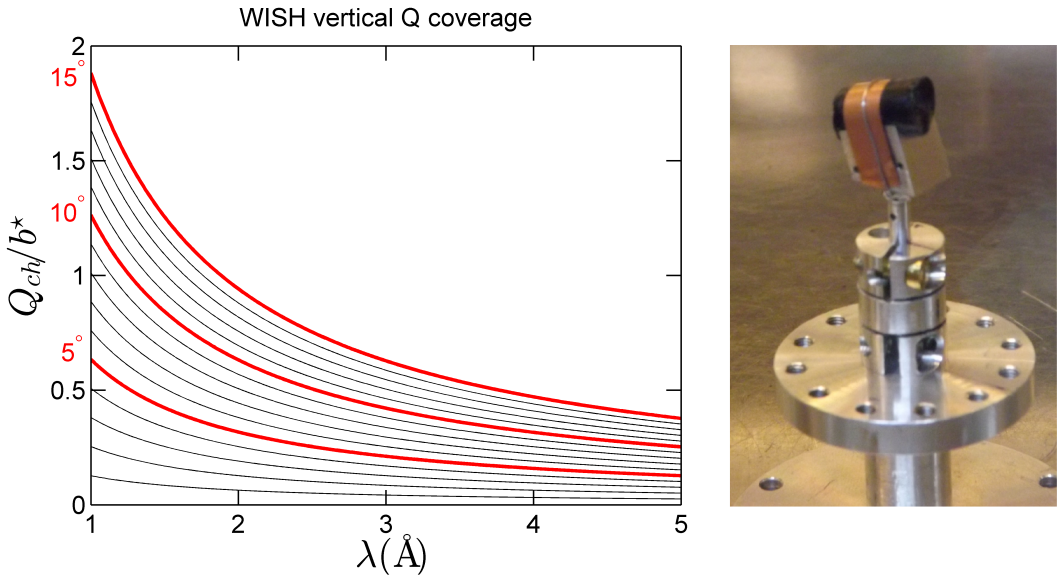

Figure 5.8: Left: Vertical coverage in Q_{chain} as a function of wavelength for different vertical magnet openings given in degrees. This shows that in order to get a full Brillouin zone coverage (0 to 1) in the Q_{chain} direction, we need to use neutrons of wavelength smaller than 2 Å. Right: Aligned single crystal sample of Cs_2CoCl_4 as used on WISH, with the b-direction vertical.

component of the scattering function is maximised due to the polarisation factor in the magnetic scattering cross-section. This is essential because DMRG calculations (see Fig. 5.4) predict the most non-monotonic behaviour (largest dip) for the integrated S^{xx} component.

The determination of the static scattering function $S(\mathbf{Q})$ is made via the measurement of the diffuse magnetic scattering expected in the case of a one-dimensional magnetic system with short range correlations. The low-dimensional character of Cs_2CoCl_4 leads to observation of features in the magnetic scattering cross section that are essentially independent of two of the components of momentum transfer perpendicular (Q_h and Q_l in our case) to the momentum transfer along the chain. As such, the focus will be on the momentum along the chain direction ($Q_k = Q_{chain}$), with the momentum perpendicular being integrated over a carefully chosen volume. This integration volume is chosen in order to improve the statistics of $S(Q_k)$ in such a manner as to avoid Bragg reflections.

The experimental investigations have concentrated on two distinct temperature regimes. First, the diffuse scattering in the 1D phase was measured, at T = 400 mK which is above the zero field transition temperature of T_N = 220 mK. The diffuse

signal was measured at a series of applied magnetic fields between B = 0.025 T and B = 6.5 T. At a later date, due to the continuously developing theory, the magnetic field dependency of the magnetic scattering was also measured in the 3D ordered phase at T = 50 mK. Results from these measurements are presented and discussed in the next section.

5.5 WISH Results

Neutron scattering data is always presented in standard physical units for momentum and energy transfer in order to be directly comparable between experiments and between experiments and theory. In the following, we describe the steps needed to transform the raw WISH data into data given in units of $Å^{-1}$ and meV which can be directly read into the Horace suite of programs [89] used for the data analysis.

For a given detector element on WISH, the raw data is stored as a two-dimensional histogram of the form (X,Y,E), with X that contains a large neutron time-of-flight window which is binned into fine steps (usually as dictated by the time channel resolution of the acquisition electronics). Correspondingly, Y contains the number of neutrons that have hit the detector in each time-of-flight interval and E contains the error associated with the counting statistics. A full raw dataset contains such information for all the detector elements on the detector bank.

The raw data is restructured and transformed into ascii column data with information of the accessible momentum **Q** space. It is structured as columns with Q_h-Q_k-Q_l-C-E information (wave vector transfer components, counts and error for each scattering event). This first step is done using the Mantid software [88] which given a run number, loads and rebins the data, extracts the monitor spectrum, performs a smoothing algorithm and normalises the raw data to the monitor data in order to account for the incident flux. To correct for detector efficiency, a standard vanadium run is treated almost identical to the data, with an extra smoothing algorithm applied to iron out statistical fluctuations in the spectrum. In the next step, the normalised data is divided by the normalised vanadium data. As background dataset we use the B = 6.5 T dataset (fully polarised state), which is transformed identically and subtracted from the data collected at different values of the magnetic field.

In a next step, we read the ascii files, together with the instrument parameter file, sample lattice constants and sample orientation into Horace [89] which trans-

forms the data into SQW 4-dimensional data format. Horace is an analysis and visualisation software written specifically for inelastic experiments, but by clever design, it can also handles elastic data by integrating over all energy transfers.

5.5.1 $T > T_N$ Investigation

In this subsection we present data collected on WISH at $T = 400$ mK, above the transition temperature $T_N = 220$ mK to 3D magnetic long-range order. At this temperature, Cs_2CoCl_4 has a strong one-dimensional magnetic character. It can be considered as made up of decoupled spin chains with two different orientations of the XY easy-planes. The application of the magnetic field **B** along the crystallographic b-direction ensures the scattering is identical for both types of chains.

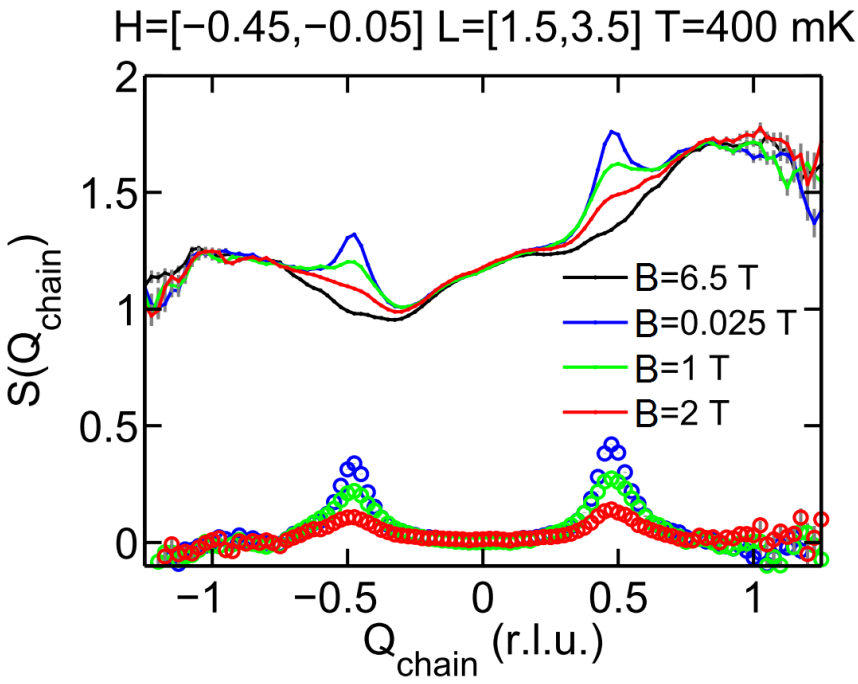

Figure 5.9: One-dimensional raw data (lines) and background subtracted data (circles) that cover two Brillouin zones along the chain direction, collected at $T = 400$ mK for several magnetic field values. We show that the background at 6.5 T is very large and introduces uncertainties in the interpretation of the data, as explained in the main text.

We begin with illustrating the major difficulty of the data analysis by plotting, in Fig. 5.9, a few raw one-dimensional cuts of $S(Q_{chain})$ versus Q_{chain}. We remind that we use the data collected at $B = 6.5$ T $> B_{sat}$ (black line) as a background

dataset because it gives a good description of the non-magnetic sample dependent scattering and the non-sample dependent background scattering. One observes that the overall background scattering is very large compared to data collected at lower fields (blue, green and red lines). This is due to the fact that the 9 T magnet we used for the experiment is incompatible with the oscillating collimator on WISH so we measured without the collimator. The oscillating collimator has the role of suppressing all background scattering from the magnet, the dilution fridge and scattering from beamline components in general. Without the collimator in place we pick-up all the scattering from the magnet and the dilution fridge aluminium tails. We had to use this particular magnet because it had a vertical opening that allowed to cover at least one Brillouin zone along the chain direction (see Fig. 5.8). Another problem we highlight is the fact that the sample moved in the magnetic field due to a slight bending of the dilution fridge stick. This would not constitute a major problem if the background were small compared to the diffuse signal, but as illustrated in Fig. 5.9, the background is comparable to the diffuse signal. As a result, the subtraction of the background from the raw data becomes a sensitive operation which introduces large uncertainties in the subtracted data (blue, green and red circles). The uncertainty transfers to the integrated spectral weight $\mathcal{I}$ (which is the key quantity predicted to signal the entanglement transition), so our level of confidence in the measured diffuse scattering signal is quite limited and care must be taken when interpreting the results.

The background subtracted $S(\mathbf{Q})$ is plotted in Fig. 5.10 in the form of two-dimensional scattering intensity maps in the $(-0.25, \mathrm{K}, \mathrm{L})$ plane, for a few selected values of the applied magnetic field. These maps were obtained though an averaging of the signal in the H direction from -0.45 r.l.u. to -0.05 r.l.u. The scattering is of magnetic origin and is one-dimensional in nature as evidenced by the presence of scattering rods at antiferromagnetic half-integer positions whose intensity variation is due to the magnetic form factor. The small modulation of the scattering intensity along the L direction is consistent with what was observed in the earlier study of Yoshizawa et al. [167] and it indicates the presence of finite inter-chain couplings. The scattering signal is diffuse and is spread over a fairly large area in the $(-0.25, \mathrm{K}, \mathrm{L})$ plane. As a function of magnetic field, the diffuse scattering intensity decreases with increasing field, which is consistent with an evolution of the magnetic structure from antiferromagnetic at small fields to polarised at fields $\mathrm{B} \gtrsim 2.3$ T.

In order to compare the predicted behaviour of the magnetic field dependence of

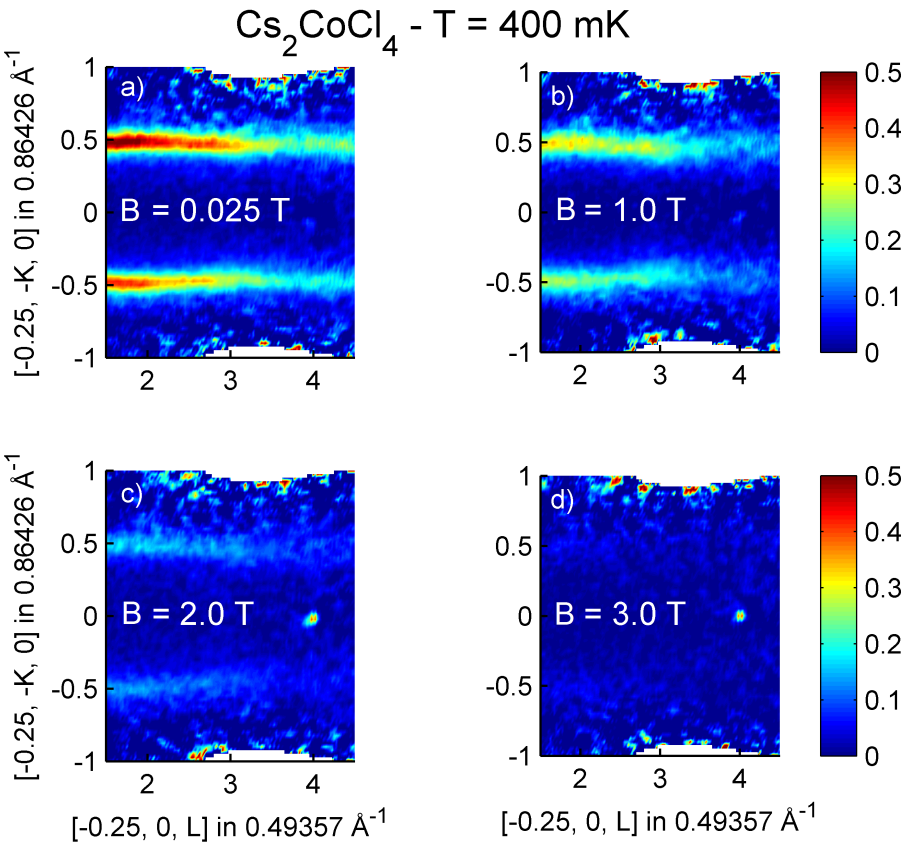

Figure 5.10: Two dimensional scattering maps for selected number of applied magnetic fields along the chain direction.

$\mathcal{I}$, the integrated static structure factor along the chain given by Eq. 5.8, with the experimental data, we extract one-dimensional cuts from the full datasets by averaging the signal in the momentum transfer directions perpendicular to $Q_{chain} \equiv K$. To avoid any scattering coming from structural Bragg reflections, we choose to average the signal in $H = [-0.45, -0.05]$ r.l.u. and $L = [1.5, 3.5]$ r.l.u. The results are plotted in Fig. 5.11 where we show the static structure factor dependency on the momentum transfer along the chain direction for a given set of applied magnetic fields. The diffuse scattering intensity decreases with increasing applied field and becomes flat when saturation is reached.

The integrated scattering intensity $\mathcal{I}$ that is predicted to signal a factorised state, is obtained from the data by subtraction of $S(Q_{chain} = 0)$, obtained in practice by extracting the average $S(Q_{chain})$ over an interval of [-0.1,0.1] r.l.u. around $Q_{chain} = 0$, from the total integrated $S(Q_{chain})$ over two Brillouin zones from $Q_{chain} = -1$ to $Q_{chain} = 1$. This integrated quantity is predicted by theory to display a non-

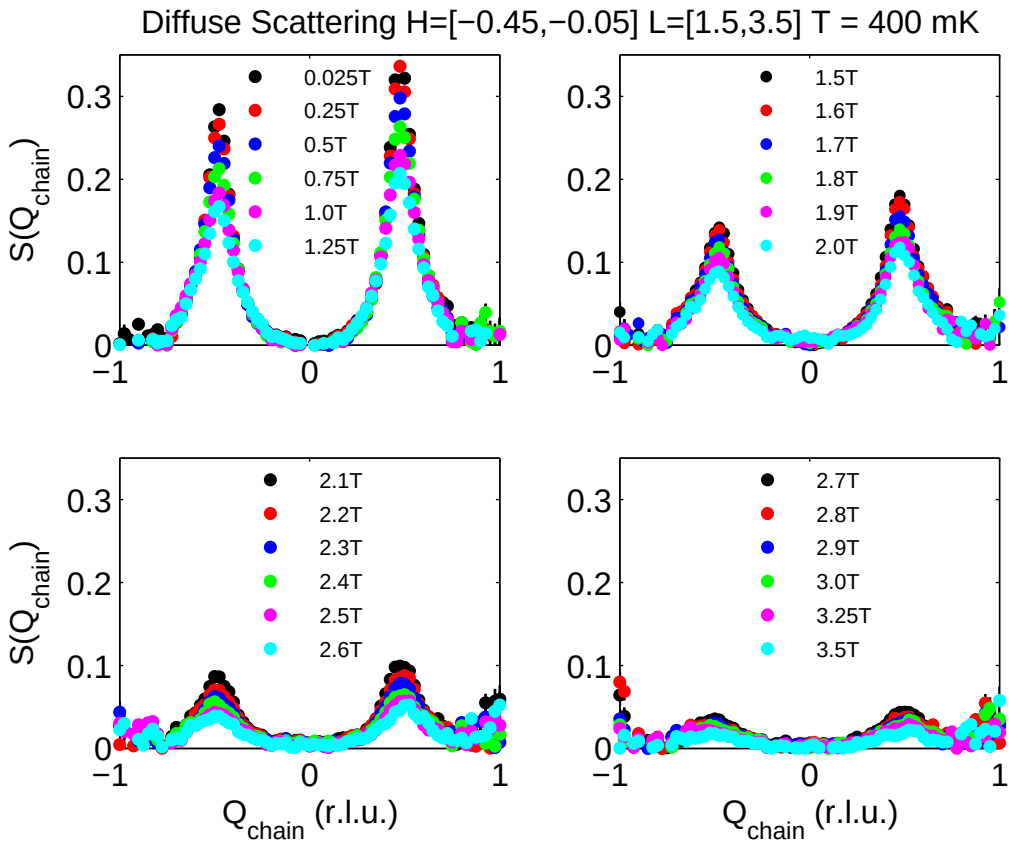

Figure 5.11: Static structure factor as a function of momentum transfer along the chain direction for a set of applied magnetic fields.

monotonic behaviour as a function of applied magnetic field, with a minimum value at the entanglement transition field and a rise and local maximum at the quantum critical field. $\mathcal{I}$ extracted from the data is plotted in sub-figure b) of Fig. 5.12, with blue circles. In sub-figure a) we plot the integrated spectral weight from -1 to 1 in Q_{chain} with violet circles and the integrated spectral weight from -0.1 to 0.1 with orange rectangles. The total spectral weight decreases monotonically with increasing applied field, whereas the integrated spectral weight around $Q_{chain} = 0$ increases initially, reaches a maximum around B = 2.0 T and then decreases towards zero at full saturation. As a consequence, the difference of the two shows a steeper decrease in the region around B = 2.0 T, but the evolution remains monotonic with no obvious minimum.

We think we do not observe the predicted non-monotonic behaviour of the entanglement witness $\mathcal{I}$ due to both the uncertainties of the background subtraction discussed at the beginning of this section and also due to finite temperature ef-

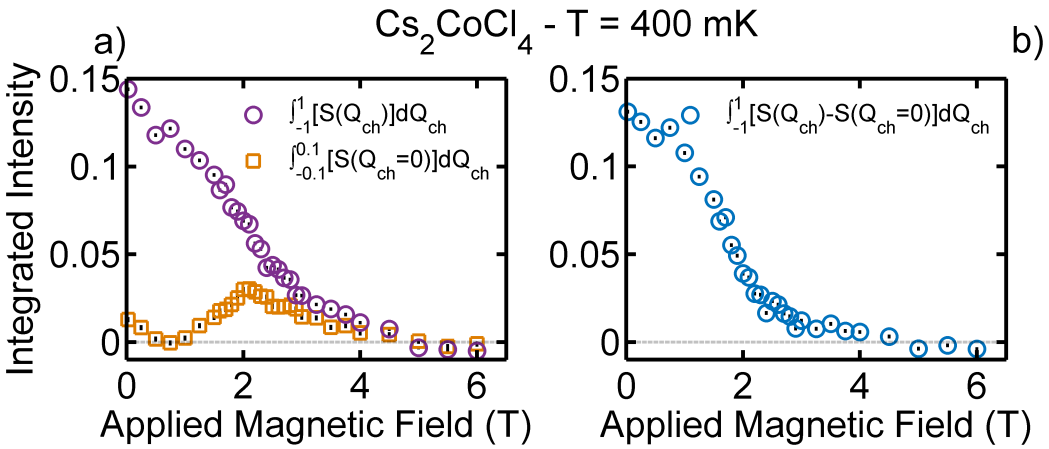

Figure 5.12: Integrated spectral weight extracted from the data collected at T = 400 mK that is predicted to signal the entanglement transition through a non-monotonic behaviour as a function of field. In a) we plot the integral of $S(Q_{chain})$ over two Brillouin zones and the integral of $S(Q_{chain})$ over a 0.2 r.l.u. interval around $Q_{chain} = 0$. In b) we plot $\mathcal{I}$ according to the definition in Eq. 5.8 and extracted as the difference between the two quantities plotted in a).

fects which smear out the factorisation signature [165]. New theoretical investigations [165] on the anisotropic XY model with $\gamma = 0.2$ have revealed the fact that a less pronounced non-monotonic behaviour of $\mathcal{I}$ should still be visible for temperatures up to $T = 0.03$J (see Fig. 5.13). This temperature corresponds to the value of the spectral gap. With a logic similar to quantum phase transitions, the presence of the entanglement transition is visible at finite temperature as soon as the thermal energy is smaller than the energy of the gap. For the XY model with $\gamma = 0.2$, the gap energy is $E_g = 0.03$J, whereas the experiment was performed at T = 0.15J (for J = 0.23 meV) of T = 0.26J (for J = 0.13 meV - as fitted from the measured polarised dispersion) which are both too high. For the ideal 1D case, this means that performing the same experiment at T < 80 mK (J = 0.23 meV) or T < 45 mK (J = 0.13 meV) and extracting the integrated spectral weight $\mathcal{I}$ one should see the predicted non-monotonic behaviour. In reality things are never truly 1D due to finite inter-chain couplings. As the current theory does not account for inter-chain couplings, our motivation for performing the experiment at T = 50 mK, in the 3D magnetically ordered state, was based on a more hand-wavy argument. For finite but small inter-chain couplings, the 1D T = 0 ground state and the 3D T = 0 ground state are similar. As the 3D T = 0 state is adiabatically connected to the 3D finite T

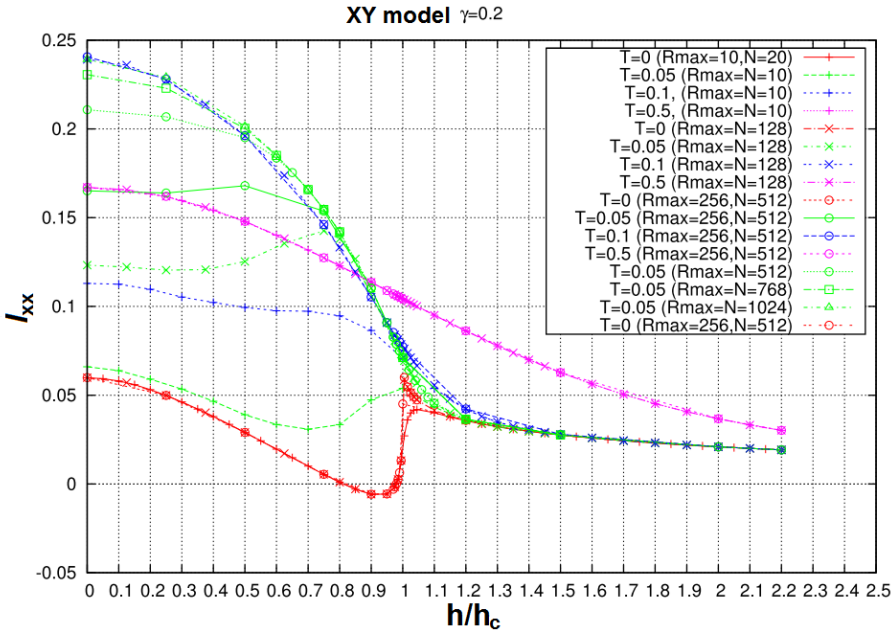

Figure 5.13: Integrated spectral weight $\mathcal{I}_{xx}$ versus applied magnetic field h in units of the quantum critical field h_c for the anisotropic XY model with $\gamma = 0.2$. Each curve corresponds to a different temperature T (in units of J) and value of numerical parameters R_{max} (cut-off chain length) and N (chain length). Adapted from Ref. [165].

state, the 3D ordered state 'freezes' the 1D T = 0 state at small finite temperatures.

5.5.2 $T < T_N$ Investigation

In this subsection we present results from neutron scattering measurements on Cs_2CoCl_4 at T=50 mK. At this temperature and at B=0, the system is characterised by long range antiferromagnetic order [173]. As a function of field, there are qualitative changes in the type of order, and at around B = 2.3 T there is a quantum phase transition from antiferromagnetic to quantum paramagnetic order [177].

The experimental uncertainties related to background subtraction as described in the previous section, apply for the data in this section as well due to identical experimental conditions as for measurements at 400 mK.

We plot the neutron scattering intensity distribution in the $(-0.25, K, L)$ crystallographic plane in Fig. 5.14 for several applied magnetic fields. One observes that the scattering is spread all over reciprocal space, resembling what is seen at T = 400 mK. At 50 mK we are below the Néel temperature and the diffuse scattering is

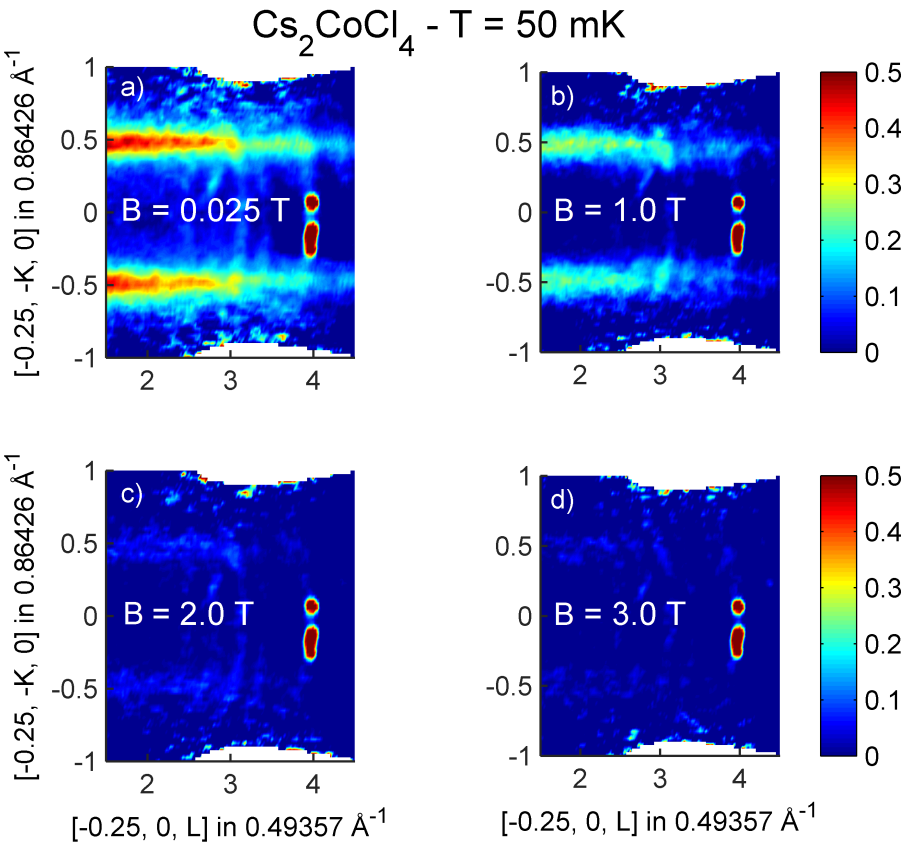

Figure 5.14: Two dimensional scattering maps for different applied magnetic fields along the chain direction.

due to the presence of quantum fluctuations. This observation is in accord with the proposed adiabatic connection argument discussed at the end of the previous subsection.

The principal feature one observes is the presence of scattering rods of intensity localised at antiferromagnetic wave vector positions along the chain direction. For every applied field value, the intensity drops for increasing Q due to the magnetic form factor. As a function of magnetic field, the scattering looses intensity as the field is increased, a sign that antiferromagnetic order is gradually suppressed. One also observes what seems to be circular aluminium powder lines. We do not have an explanation for the increased scattering intensity around L = 4 r.l.u.

We analyse and present the data identically to data collected at T = 400 mK, with one-dimensional cuts plotted in Fig. 5.15. To obtain these, we have chosen an averaging range in H from [-0.45,-0.05] r.l.u. and in L from [1.5,2.5] r.l.u. The intensity of the cuts decreases with increasing applied field. The data close to

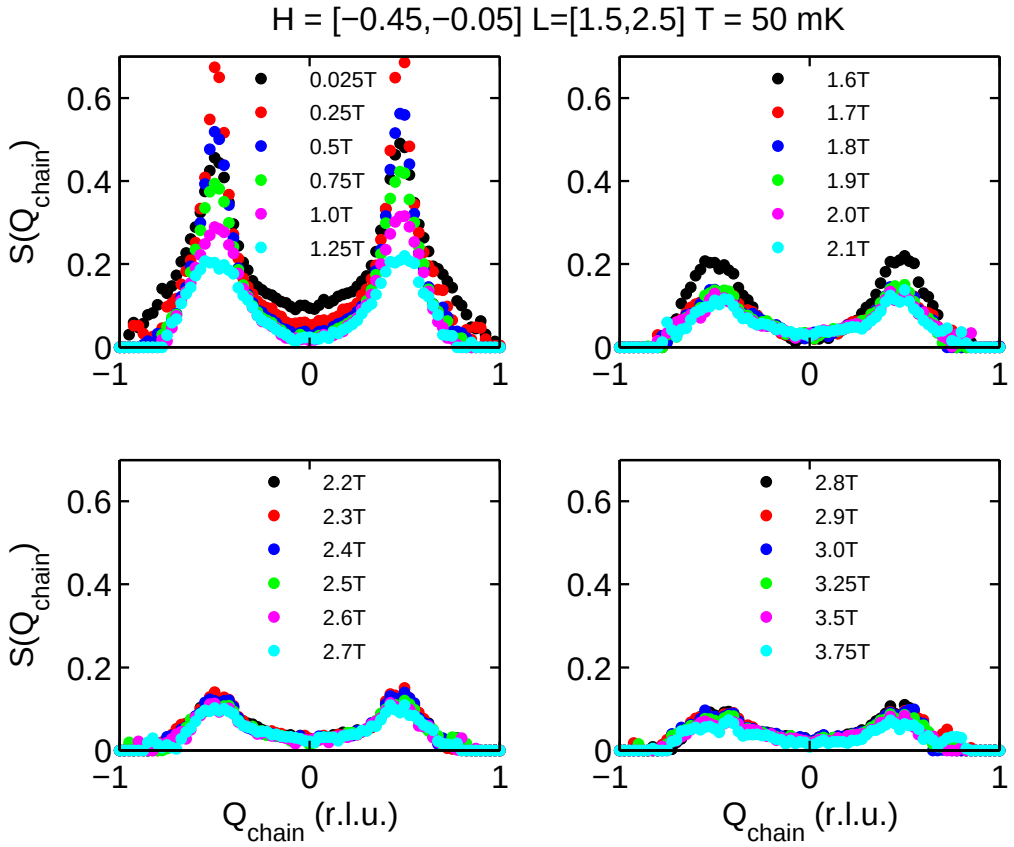

Figure 5.15: Static structure factor as a function of momentum transfer along the chain direction for a set of applied magnetic fields.

$Q_{chain} = \pm 1$ goes to negative values due to a poor background subtraction. This is due to the inability of using the standard oscillating collimator on WISH which is not compatible with the magnet used. As a consequence the background scattering is very large, comparable to the signal coming from the sample and the background subtraction performs poorly at the ends of the interval. For data presented in Fig. 5.15 we set the intensity to zero for data points whose intensity is negative and keep the original errorbars.

The integrated spectral weight is extracted and plotted in Fig. 5.16 where in sub-figure a) we plot the whole integrated spectral weight from -1 to 1 r.l.u., with violet circles, alongside the integrated spectral weight from -0.1 to 0.1 r.l.u., with orange rectangles. In sub-figure b) we show $\mathcal{I}$ with blue circles. The total integrated weight (violet circles) decreases continuously as the field is varied from 0 to 6 T. The spectral weight integrated between -0.1 and 0.1 r.l.u. (orange rectangles), decreases abruptly at small fields and then shows a slight increase with a local maximum at

B ≈ 2 T. As a consequence, $\mathcal{I}$ (blue circles) first increases at low fields, reaches a maximum at 0.25 T and then decreases monotonically for increasing field.

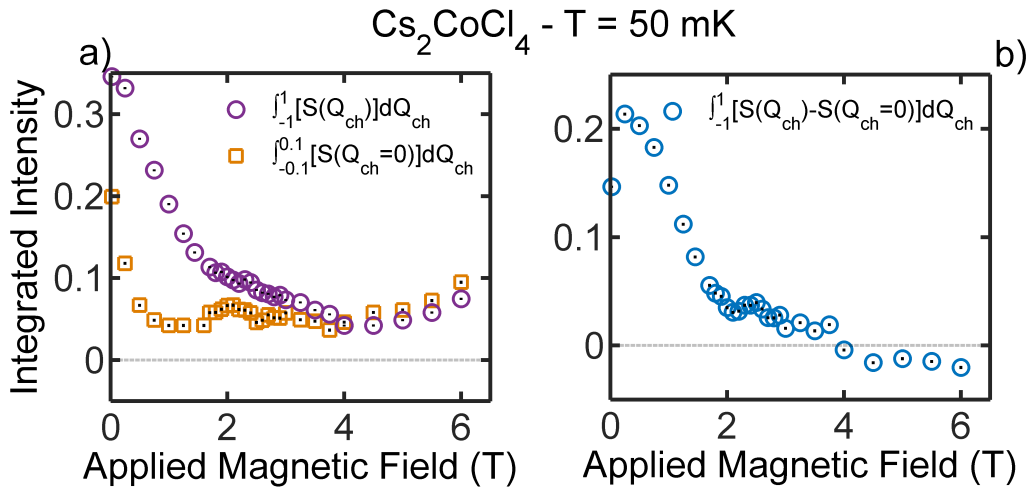

Figure 5.16: Integrated spectral weight extracted from the data collected at T = 50 mK that is predicted to signal the entanglement transition through a non-monotonic behaviour as a function of field. In a) we plot the integral of $S(Q_{chain})$ over two Brillouin zones and the integral of $S(Q_{chain})$ over a 0.2 r.l.u. interval around $Q_{chain} = 0$. In b) we plot $\mathcal{I}$ according to the definition in Eq. 5.8 and extracted as the difference between the two quantities plotted in a).

Over the whole field range covered by the experiment, $\mathcal{I}$ continuously decreases from a maximum value at small fields towards zero at saturation, in a monotonical way which is in disagreement with theory that predicts a non-monotonic behaviour of this quantity. We believe that at 50 mK we could be in one of two situations. The first scenario is that at this temperature we observe the true 1D T = 0 behaviour and the other is that we observe the 1D finite T behaviour. If we were in situation one, then we would expect to see quite clearly the non-monotonic behaviour of $\mathcal{I}$, which is clearly not the case. If we were in situation two, following the same argument as at the end of the previous section, that in order to see the signature of the ET, the temperature has to be smaller than the gap energy, one sees that T = 50 mK≡ 0.019J (J = 0.23 meV) or T = 50 mK≡ 0.033J (J = 0.13 meV) might be right at the border. Together with the now known strength of the inter-chain interactions ($5\% - 15\%$ of J - as determined from the measured polarised dispersion in section 5.6), it is unclear what the expected behaviour is, because the current theory does not include effects of inter-chain interactions, which might as well just wash-out any signature of the ET for significant inter-chain couplings. We mention

here that the unknown strength of the inter-chain couplings partly motivated our measurements of the high-field polarised dispersion. As a conclusion, because it is still unclear what the expected behaviour of $\mathcal{I}$ is and because of the experimental uncertainties about the data, it is difficult to find a proper explanation for our measurements on Cs_2CoCl_4.

When we started this project, we believed that Cs_2CoCl_4 was a promising candidate for experimentally observing signatures of the predicted entanglement transition, but we now see that in practice there are problems. One aspect is related to experimental uncertainties and the sensitive operation which is the background subtraction. Another aspect is related to the fact that in Cs_2CoCl_4 the quantum critical field h_c and the factorising field h_f are predicted to be less than 2% apart and field inhomogeneities and deviations from an ideal sample could potentially suppress the entanglement transition. On the theoretical side we mention that the theory has been developed in parallel with the experiments in order to try to better understand the measured data. Finite temperature and non-zero inter-chain couplings make the predictions of the original 1D chain $T = 0$ theory unusable in case of real systems.

As future outlook there might be systems where the entanglement transition could be experimentally observed with much more success. For example, for the ideal transverse-field Ising model, the factorisation field is $h_f = 0$, meaning that for an Ising-like system the factorisation field would be well separated from the quantum critical field. One advantage of this is that the factorisation point remains accessible even if the quantum critical point is at experimentally unreachable high fields, so materials that might have been discarded for investigations of quantum criticality could be usable. One such system that could be studied experimentally is $CoNb_2O_6$ [179,180], a quasi-1D Ising chain in transverse applied magnetic field. This will require detailed theoretical investigation to obtain experimentally measurable quantities either using neutron scattering or another experimental probe which is sensitive to spin correlations. Another example would be finite-sized systems because some of the results of theoretical investigations carried out as part of this project have hinted to an alternative scenario where signatures of a factorised state could be visible in a finite-size system at non-zero temperature. Experimental realisations of such models include molecular-based magnets where the elementary building blocks are 1D rings of spins [181–183] and broken spin-chains [184].

Preliminary magnetic order At the time of the second WISH experiment (May 2014), the magnetic ordering of Cs_2CoCl_4 was only known for the case of a magnetic field applied along the crystallographic a-direction with no data available in literature for other directions of the applied field. The fact that the evolution of the magnetic ground state with a field applied along the b-direction was not known, motivated us to do a preliminary investigation of the magnetic field evolution of a few magnetic reflections. The results for the field dependence of the integrated intensity of the $Q = (0, 0.5, 1.5)$, $Q = (0, 0.5, 1)$ and $Q = (0, 0, 4)$ reflections is summarised in Fig. 5.17. We found three different ordering wave vectors for the magnetic field applied along the b-direction. At fields smaller than 0.25 T the magnetic order is characterised by propagation vector $k = (0, 0.5, 0.5)$, consistent with what is known from zero field. For fields between 0.25 T and 2.2 T, the propagation vector is $k = (0, 0.5, 0)$ and it coexists between 1.9 T and 2.2 T with an incommensurate order described by $k = (0, 0.5 - \xi, 0)$.

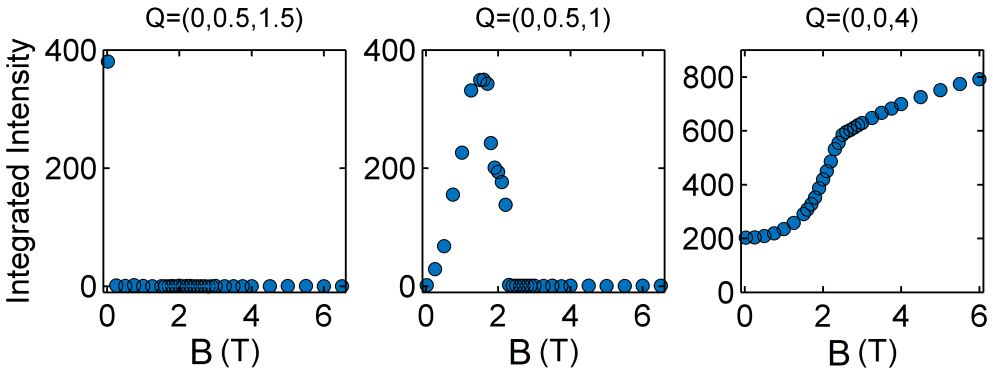

Figure 5.17: Integrated intensity of three reflections as a function of applied magnetic field B ∥ b as collected on WISH.

The induced ferromagnetic component of the magnetic moment measured at $Q = (0, 0, 4)$ increases over the whole range of applied fields with two different distinguishable regimes. At small fields the integrated intensity has a quadratic-like increase followed by a crossover to a linear regime at fields $B > 2.4$ T. The quadratic regime is indicative of a linear increase of the magnetic moment where the low-lying and higher Kramers doublets are intermixed and both participate in the dynamics at low fields. The crossover signals the almost full saturation of the low-lying $|\pm 1/2\rangle$ states and the linear increase of the integrated intensity shows that the dynamics is dominated by the $|\pm 3/2\rangle$ spin states. We see that even at the highest fields B = 6 T

the system has not yet reached full saturation, an indication that there is a non-zero fluctuating moment which is possibly due to finite quantum fluctuations.

This very brief survey shows that the magnetic ordering evolution in the case of an applied field parallel to the b-direction is much more complex than in the case where the field is applied along the a-direction [173]. A strong confirmation of the complexity of the magnetic field (|| b) dependency of the magnetic order came recently from high-resolution specific heat and thermal expansion measurements on Cs_2CoCl_4 [177,178]. In order to investigate the magnetic ordering evolution in more detail, we have performed a neutron diffraction experiment on a single crystal of Cs_2CoCl_4 at the RITA-II spectrometer at Paul Scherrer Institute. The details of the experiment and results for the magnetic ordering and high-field excitations of Cs_2CoCl_4 for fields applied along the crystallographic b-direction are presented in the next section.

5.6 RITA-II Results

In this section we present results from a dedicated neutron scattering experiment performed in order to investigate in detail the field phase diagram of Cs_2CoCl_4 when a magnetic field is applied along the b-axis and to gain a better understanding of the possibly relevant additional terms in the magnetic Hamiltonian that may be responsible for the observed ordering. This study was motivated by the previous findings from WISH which indicated that the magnetic ordering of this material is quite complex for the case of the field along the b-direction. Although the phase diagram was recently mapped out using specific heat and thermal expansion measurements [177,178], the exact nature of the magnetic phases could not be established and only possible scenarios were given for each phase, using simplified microscopic models. Here we wish to use neutron scattering to reveal the exact nature of the magnetic ordering as the field is increased from zero to saturation.

The experiment was performed at the cold neutron triple-axis spectrometer RITA-II at the Paul Scherrer Institute (PSI) in Villigen, Switzerland and it was divided into two parts. The first part concentrated on elastic scattering to investigate the magnetic ordering as a function of field, in a range of fields from B = 0 up to B = 4 T and at T = 0.05 K. The second part used inelastic scattering and focused on measuring the excitation spectrum at B = 4 T, in the field polarised phase, to get the parameters of the Hamiltonian.

The single crystal sample of m = 2 g Cs_2CoCl_4 used at RITA-II was aligned with the (0, K, L) plane in the horizontal scattering plane of the spectrometer. It was placed on a custom made aluminium mount and sealed in an aluminium can with helium exchange gas. The sample was attached to a dilution insert stick and introduced in the horizontal field MA7 cryomagnet with a base temperature of 50 mK and maximum field of 6.5 T. After preliminary checks of the alignment, the sample was oriented in the magnet such that B ∥ b-direction, horizontally. Due to the magnet design, its geometry is quite restrictive with four 45° horizontal openings, two of them with ±22.5° vertical openings and the other two with ±6.5° vertical openings. The constrains from the magnet together with neutron kinematic constrains lead to observation of a restricted number of magnetic reflections.

For the diffraction measurements, RITA-II was run in three-axis mode with a vertically focusing pyrolitic graphite (002) monochromator that selects an incident neutron energy of $E_i = 5$ meV. After the sample position, a cooled BeO filter was used to filter out higher order scattering. A pyrolitic graphite analyser was used to select final energy neutrons $E_f = 5$ meV. It was used in focusing mode to improve counting statistics and lower the background scattering. Scattered neutrons were detected using a position sensitive ^{3}He detector with 128x128 pixels. This setup allowed the measurement of several magnetic Bragg reflections at Q = (0, 1.5, −2.5), Q = (0, 0.5, 0), Q = (0, 0.5, −2), Q = (0, 0.5, −3) and Q = (0, 0.5, −4).

For inelastic measurements, RITA-II was run in three-axis mode with the following elements in the beam: vertically focusing PG monochromator - collimator 80′ - diaphragm - Cs_2CoCl_4 in MA7 - BeO filter - PG analyser focusing mode - PSD - $E_f = 3.7$ meV. The spectrometer was run with fixed final energy neutrons of 3.7 meV. At B = 4 T and T = 50 mK the dispersion relation was measured along four directions in reciprocal space.

5.6.1 Field Dependence of the Magnetic Ordering

Our interest in mapping out the experimental phase diagram of Cs_2CoCl_4 when a magnetic field is applied along the b-axis was initially driven by the original observations from the WISH experiment that indicated the presence of commensurate order described by $\mathbf{k} = (0, 1/2, 0)$ in a field range from B = 0.25 T to B = 1.9 T and incommensurate magnetic reflections for fields close to B = 2 T. The phase diagram was only known for a field applied along the a-direction [173] and so it was important

to understand what happens to the ordering for fields along the chain direction.

Recently, the temperature-field phase diagram of Cs_2CoCl_4 was mapped out for magnetic fields applied along all three orthorhombic crystal axes, using high-resolution specific heat and thermal expansion measurements [177,178]. These have revealed that the scenarios where the field is applied either along the a or c axes are very similar, whereas the case of fields applied along the b-axis is much more complex and interesting.

The general features of the a-axis and c-axis phase diagrams were discussed earlier in this chapter (see section 5.3). We will now focus on the b-axis phase diagram and present in detail the findings of Breunig et al. [177].

At T = 50 mK the magnetic ground state changes as a function of applied magnetic field, with at least five distinct phases between zero field and saturation. At low fields B < 0.25 T an antiferromagnetic phase is identified. For fields between 0.25 < B < 1.9 T two consecutive spin-flop phases are believed to exist. The transition from the antiferromagnetic phase is proposed to occur via a two-stage spin-flop transition [177]. For fields 1.9 < B < 2.4 T another phase intervenes and is followed, at B > 2.4 T, by the almost fully polarised effective ferromagnetic state. As a function of temperature, the antiferromagnetic phase extends up to $T_N = 0.22$ K, in zero field, and is followed by a thermal paramagnetic phase. In the field range of the two spin-flop phases, the specific heat data shows two distinct transitions which indicate the presence of a phase between the magnetically ordered states and the paramagnetic state. It turns out that this phase is the same phase that occurs between the spin-flop phase and the effective ferromagnetic phase at low temperature and spreads over a large region in the temperature-field plane. The thermodynamic measurements of Breunig et al. [177] allow for a clear identification of different phases but do not provide information about the exact nature of the magnetic ground state ordering.

In the following we present the results of neutron scattering measurements performed with the aim of revealing the nature of each of the low temperature phases identified from thermodynamic measurements.

AF commensurate phase In Fig. 5.18 we show the integrated intensity of the $Q = (0, 1.5, -2.5)$ magnetic reflection as a function of temperature which confirms the zero field $T_N = 0.22$ K. This phase is a commensurate antiferromagnetic (AF) phase described by an ordering wave vector $k = (0, 1/2, 1/2)$. It is the same phase

previously identified by Kenzelmann et al. [173], which is characterised by antiferromagnetic correlations along the $(0, \mathrm{K}, 0)$ and $(0, 0, \mathrm{L})$ reciprocal lattice directions. It extends up to $\mathrm{B_{c1}} = 0.25$ T as can be seen from Fig. 5.19. The small shift of the peak position from the commensurate $\mathrm{K} = 1.5$ r.l.u. value is due to a small misalignment of the sample.

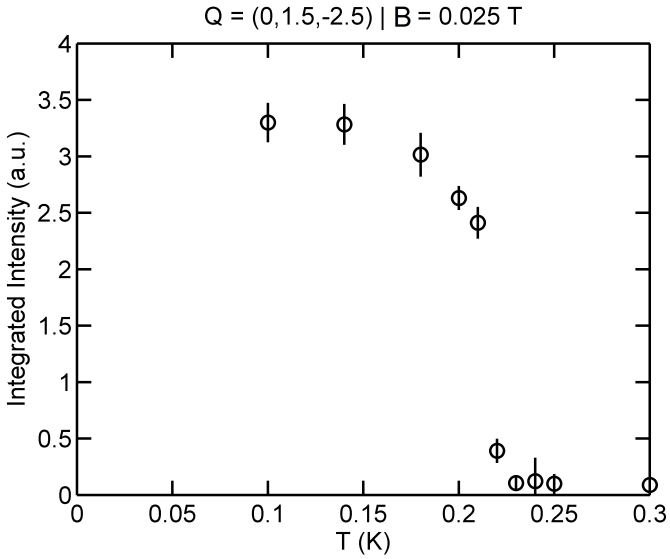

Figure 5.18: Integrated intensity of $\mathrm{Q} = (0, 1.5, -2.5)$ reflection as a function of temperature in zero field that confirms the known Néel temperature of 0.22 K.

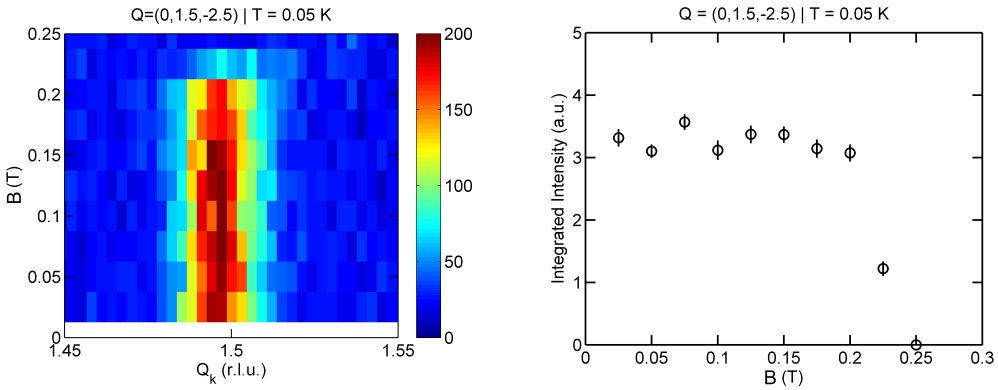

Figure 5.19: Left: Two-dimensional colourmap illustrating the disappearance of the commensurate $\mathrm{k} = (0, 1/2, 1/2)$ order; Right: Corresponding integrated intensity of the $\mathrm{Q} = (0, 1.5, -2.5)$ reflection as a function of applied magnetic field.

In the AF phase, the spins are confined to the bc-plane, almost parallel to the b-direction and make a small $\phi = 15°$ angle with the b-direction. They are oriented

anti-parallel to each other along the b-direction (chain direction) and along the c-direction, leading to a doubling of the magnetic unit cell along these two directions. This structure is described by two types of domains where the relative orientation of neighbouring chains is different [173]. In order to gain an understanding of what is responsible for the observed spin arrangement we analyse the exchange interactions. A first question we want to answer is what is responsible for the antiferromagnetic order along the b- and c-directions, and a second question is what is the origin of the small finite tilt of moments away from the b-direction. In order to answer the first question we look at each exchange interaction (see Fig. 5.20). The energy associated with the main, intra-chain J is always minimised and so this coupling gives rise to the order along the b-direction. The energy associated with the J_{ac} exchange is also always minimised and one can think of the magnetic structure as being formed of two types of coupled chains. Specifically, one type of coupled chains is formed by spins $(1, 2, 9, 10)$ and $(5, 6, 13, 14)$ and the other is formed by $(3, 4, 11, 12)$ and $(7, 8, 15, 16)$. The interactions that connect the coupled chains are J_{bc} and J_{ab} which are frustrated. In the case of isotropic Heisenberg exchange such frustrated interactions cannot be responsible for ordering because at a mean-field level, the magnetic energy does not depend on these couplings [173]. The exchange interactions in this case are not isotropic, but have a strong XY character, with a small finite coupling of the z-components of spin. This leads to an effective Ising coupling between neighbouring chains that have a finite relative orientation of the XY easy-planes. We speculate that this effective Ising coupling is in fact responsible for the observed ordering along the c-direction. Another possibility is that further neighbour interactions could stabilise the antiferromagnetic order.

The tilt of the moments away from the b-axis is surprising because this means that spins leave their local easy-planes. Such a state is unfavoured by the XY anisotropy which dictates that spins should remain in the XY planes. Considering the relative angle between easy-planes on neighbouring chains, the only common in-plane direction for all chains is the b-direction and thus spins should be parallel to b. This state is realised in practice because most probably there is another weak interaction that gains from the tilt. A possibility is the presence of a finite Dzyaloshinskii-Moriya (DM) interaction between chains, with J_{bc} being the only coupling which allows for a non-zero Dzyaloshinskii vector (D) due to symmetry considerations and is also consistent with a non-collinear spin arrangement in the bc-plane [177, 178]. From a symmetry analysis of the components of the D vec-

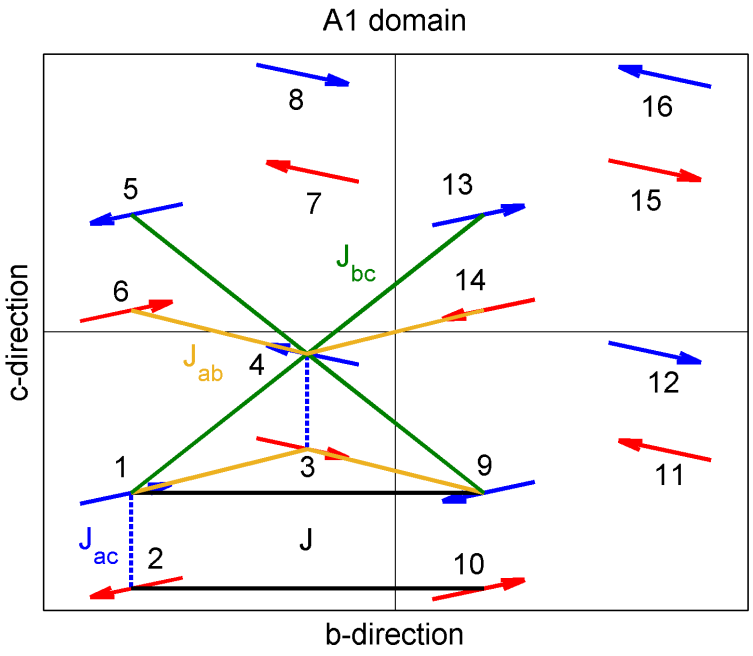

Figure 5.20: A-type domain showing the orientation of the magnetic moments in the enlarged magnetic unit cell and all nearest neighbour exchange couplings between spins. Blue and red spins indicate same height along the a-direction.

tor, Breunig [178] showed that the energy gained by DM interactions along the J_{bc} couplings is zero due to the fact that crystal symmetry dictates that the D vector cancels for the whole lattice. This means that DM interactions between chains cannot explain the departure of moments away from the b-axis. A finite DM interaction could still be responsible for the small tilt if somehow the D vector would not cancel for the whole lattice. This could be possible if the magnetic ordering was accompanied by a small structural distortion that would lower the symmetry of the lattice which in turn would give rise to finite D. This scenario is experimentally testable by performing a diffraction experiment above and below the ordering temperature.

Spin-Flop commensurate phase Considering the known zero field magnetic structure, the application of a large enough magnetic field almost parallel to the ordered moment should induce a spin-flop transition. The transition is controlled by the competition between the main intra-chain J, the single-ion anisotropy D_{si} and the magnetic field B, according to a classical treatment [14]. Our measurements are summarised in Fig. 5.21 where we present two-dimensional colourmaps of the magnetic field evolution for three wave vector transfers.

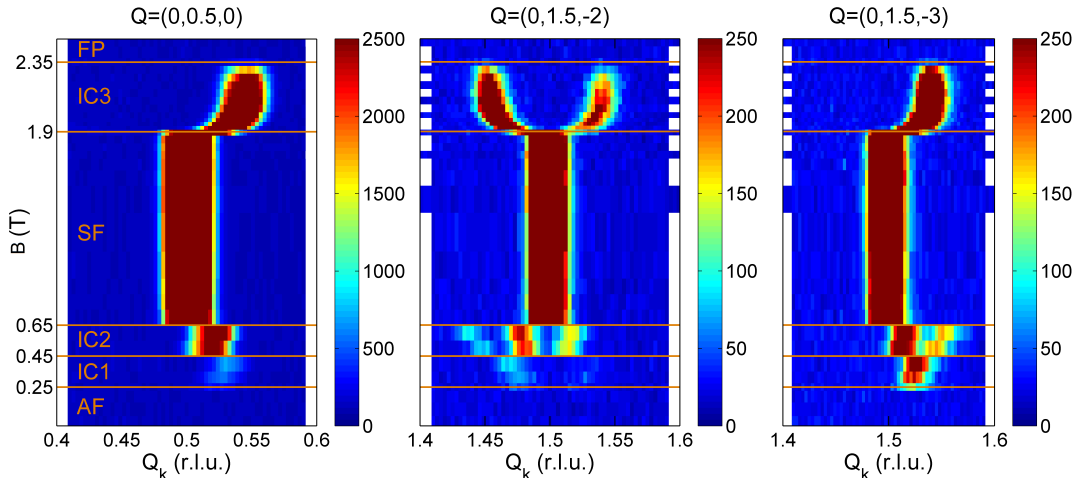

Figure 5.21: Two-dimensional colourmaps that illustrate the presence of a commensurate SF phase and three incommensurate phases as the field is swept from zero to saturation, for three different magnetic reflections measured during the RITA-II experiment. Please note that the maximum value of the colour scale is 10 times larger for the $Q = (0, 0.5, 0)$ reflection as compared to the other two which have the same scale.

We concentrate here on the SF phase which appears between $B_{c3} = 0.65$ T and $B_{c4} = 1.9$ T and is characterised by commensurate magnetic order described by the ordering wave vector $k = (0, 1/2, 0)$. We present the integrated intensity of the $Q = (0, 1.5, -3)$ and $Q = (0, 0.5, 1)$ magnetic reflections in Fig. 5.22 where we show that the measurements performed on RITA-II and WISH are very similar. The SF phase is characterised by a sudden increase of the perpendicular antiferromagnetic moment which reaches a maximum value for $B = 1.5$ T and then decreases abruptly towards zero at $B_{c4} = 1.9$ T. The integrated intensity plot in Fig. 5.22 includes the integrated intensities of all three incommensurate reflections presented in Fig. 5.21. Please note that the integrated intensity as a function of field for the other measured reflections ($Q = (0, 0.5, 0)$ and $Q = (0, 1.5, -2)$) characterised by the same $k = (0, 1/2, 0)$ is similar. Such behaviour signals a particular evolution of the spin structure throughout this phase, with two possible scenarios. The first scenario involves a pure spin reorientation with fixed moment, and the second involves a combination of spin reorientation and fluctuating moment. In order to pick the one which is in accord with our observations, we have computed the expected magnetic structure factor for a classic spin-flop phase.

We consider a SF phase evolution as depicted in Fig. 5.23 and compute the expected magnetic structure factor by assuming a continuous transition from the

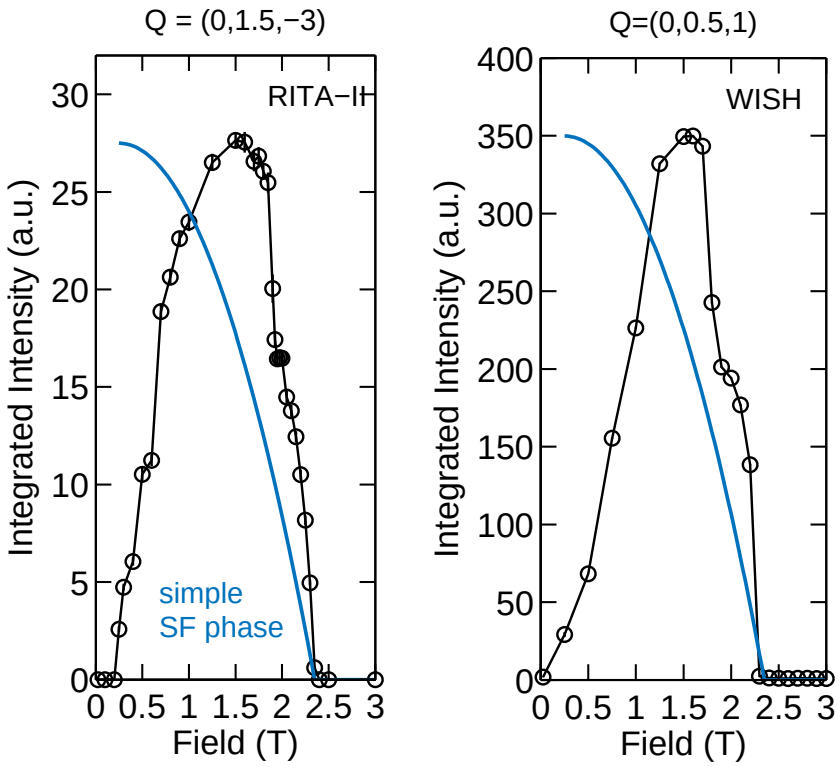

Figure 5.22: Integrated intensity of the $Q = (0, 1.5, -3)$ reflection measured on RITA-II and $Q = (0, 0.5, 1)$ as measured on WISH as a function of applied magnetic field. The corresponding magnetic structure factor squared computed assuming a spin-flop configuration for spins is plotted with blue line.

antiferromagnetic phase to the spin-flop phase and to the fully polarised phase and ignoring the incommensurate phases that border the SF phase. In the SF phase we use the canting angle θ, measured with respect to the b-direction, to describe the orientation of the spins at any given value of the applied field. The canting angle depends on the magnetic field in accordance to the classical treatment of spin-flop phases [14] as $\theta = \cos^{-1}(B/B_{sat})$ where the applied field is given by B and the saturation field by B_{sat}.

We plot the computed square of the magnetic structure factor as a function of applied magnetic field with a blue solid line in Fig. 5.22 for the corresponding measured reflections. We see that the computed structure factor is in total disagreement with the measured data. At the transition field between AF and SF, $B_{c1} = 0.25$ T, the square of the magnetic structure factor is maximum and then continuously decreases with increasing field, reaching zero at $B_{c5} = 2.35$ T. If we consider a simple spin reorientation, then the starting spin configuration must give rise to a zero struc-

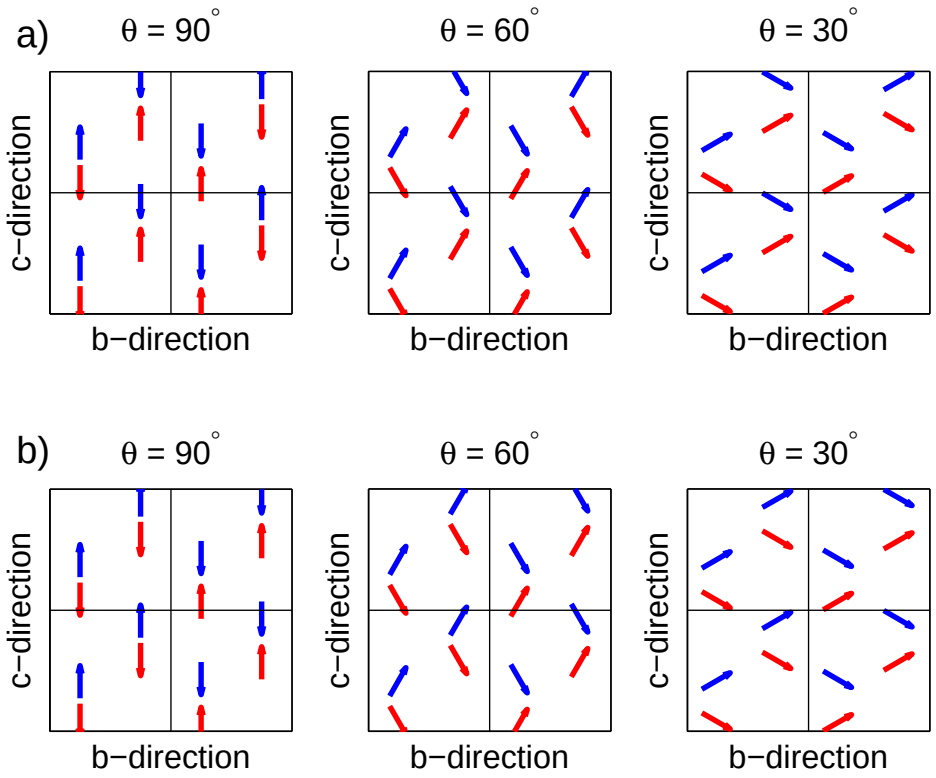

Figure 5.23: Magnetic field evolution of the spin structure assuming a classical SF phase for a) A domain type and b) B domain type. The canting angle θ is given at the top of each subfigure.

ture factor at the low field transition point. This means that spins aren't arranged antiferromagnetically along the b-direction. This is inconsistent with the fact that the largest exchange energy scale controlled by intra-chain J is still dominant over the Zeeman energy at this low field and antiferromagnetic correlations are expected to vanish only at much larger fields. The scenario where the structure factor is initially zero and then increases, implies that most probably quantum fluctuations are responsible for such behaviour. It is well-known that for low-dimensional low-spin systems the strength of quantum fluctuations is non-negligible. We believe that the same scenario as proposed by Kenzelmann et al. [173] to explain the field dependency of the magnetic structure factor in the canted phase with field applied along the a-direction, applies in this case too. Quantum fluctuations are gradually suppressed by the magnetic field and in consequence allow for more and more of the antiferromangnetic moment to order until it reaches a maximum value at around

B = 1.5 T. The system then arranges itself into a classical spin-flop configuration which leads to the gradual decrease of the antiferromagnetic moment, with increasing field, until it completely disappears at $B_{c5} = 2.35$ T and an almost fully polarised state is promoted.

Fully-Polarised phase For fields larger that 2.35 T the spins are aligned parallel to the direction of the applied field and the system is in a (almost) fully-polarised state (FP). In this phase all the antiferromagnetic correlations have been suppressed by the field and the system can be described as an effective ferromagnet. The field evolution of the ferromagnetic moment is given by the integrated intensity of the $Q = (0, 0, -2)$ reflection as measured on RITA-II, which is plotted in Fig. 5.24. We identify two magnetic field regions where the integrated intensity behaves differently. For fields up to $B_{c5} = 2.35$ T the integrated intensity shows a quadratic dependency with applied field, whereas for fields larger than B_{c5}, a linear dependency is observed. The quadratic dependency signals a linear increase of the ferromagnetic component of the moment and is in accord with what is expected for a spin-flop phase. In the low field region both the $|\pm 1/2\rangle$ and $|\pm 3/2\rangle$ contribute to the magnetisation whereas the crossover to a linear regime signals the full saturation of the lower $|\pm 1/2\rangle$ states where only the $|\pm 3/2\rangle$ contribute to the magnetisation.

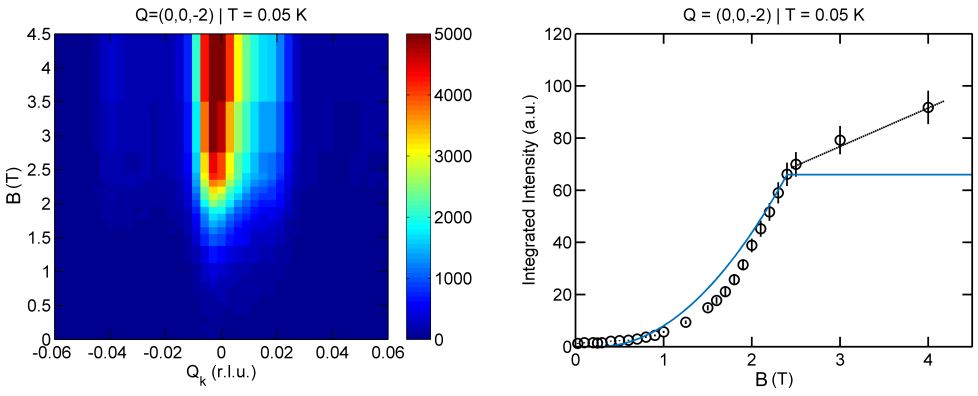

Figure 5.24: Left: Two-dimensional colourmap which shows magnetic field dependency of the $Q = (0, 0, -2)$ reflection. Right: Integrated intensity of the same reflection as a function of magnetic field. With blue line we plot the expected structure factor squared for a classical SF phase and with black line we highlight the linear regime attributed to the $|\pm 3/2\rangle$ spin states.

Thus far we have presented the results and interpretation for the main three phases that dominate the phase diagram of Cs_2CoCl_4 for an applied magnetic field

along the b-direction. At low fields the magnetic ground state is a commensurate antiferromagnetic state with antiferromagnetic order along the c- and b-directions. At intermediate fields the order is described by a commensurate state which we propose to be a spin-flop phase where the antiferromagnetic order along the c-direction is lost. At high fields, the magnetic ground state is an effective ferromagnet with no antiferromagnetic order. At the transitions between the three main phases we identify other magnetic phases which are all incommensurate as shown by the neutron scattering data. In the following paragraphs we speculate what might be responsible for the stabilisation of such incommensurate states and also what spin structures would be consistent with the observations.

IC1 and IC2 phases At the transition between the AF phase and the SF phase, two incommensurate magnetic phases intervene. The first phase (IC1) appears for magnetic fields between $B_{c1} = 0.25$ T and $B_{c2} = 0.45$ T and is characterised by an ordering wave vector $k = (0, 1/2 - \xi, 0)$ where the incommensuration $\xi = f(B)$ changes as a function of the applied magnetic field. The second phase (IC2) appears for fields between $B_{c2} = 0.45$ T and $B_{c3} = 0.65$ T and is described by two ordering wave vectors $k_1 = (0, 1/2 - \xi_1, 0)$ and $k_2 = (0, 1/2 - \xi_2, 0)$.

In Fig. 5.25 we present data measured around the antiferromagnetic $Q = (0, 1.5, -3)$ reflection as a function of applied magnetic field. We show that up to $B_{c2} = 0.45$ T the order is incommensurate described by a single propagation wave vector which is followed by a transition to a second incommensurate phase that extends up to $B_{c3} = 0.65$ T and is characterised by two ordering wave vectors. For fields larger than B_{c3}, the ordering goes back to a commensurate wave vector. The transition from the AF phase to the SF phase is thus quite complex and most probably is the result of a fine balance between different energy scales which compete and which include frustrated inter-chain interactions, DM interactions, anisotropy and the applied field. In support of this idea we mention the comprehensive study of Starykh et al. [185] which explains most of the observed features of the experimental phase diagram of Cs_2CuCl_4. Although Cs_2CuCl_4 and Cs_2CoCl_4 have the same magnetic lattice geometry, the physics is quite different for the two systems mainly due to the relative strength of the inter-chain interactions and the anisotropy point of view. The inter-chain frustrated $J_{bc} \approx J/3$ for Cs_2CuCl_4 whereas for Cs_2CoCl_4 the inter-chain $J_{bc} \approx J/10$. The different magnetic ions in the two systems also give rise to different anisotropic effects. In Cs_2CuCl_4 the quenching of the orbital moment gives

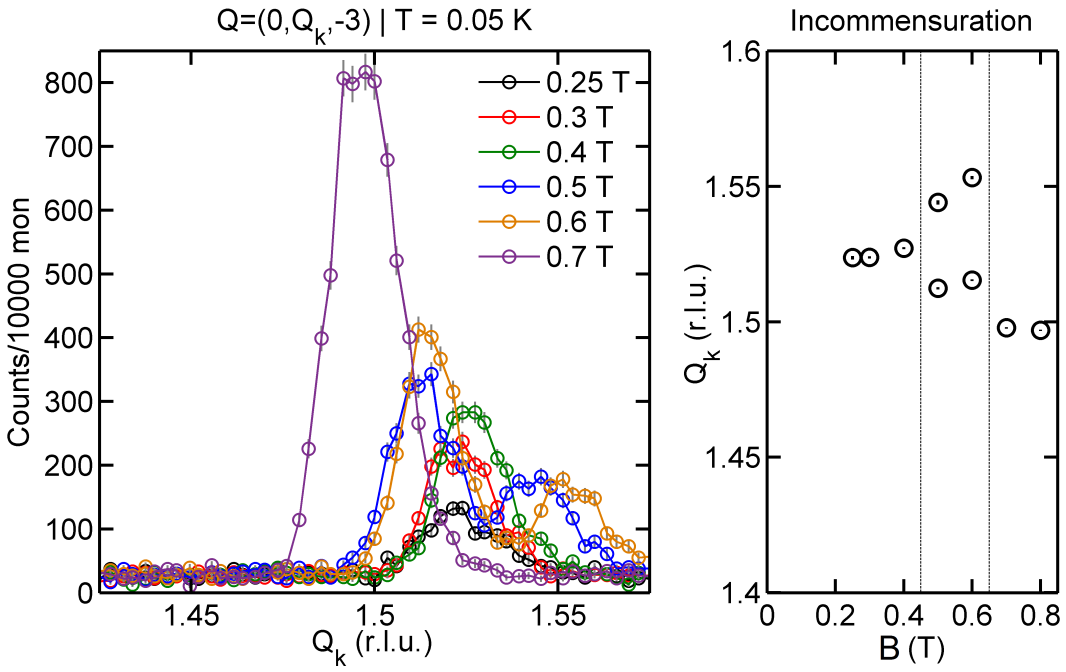

Figure 5.25: Left: Neutron scattering intensity variation of the $Q = (0, Q_k, -3)$ magnetic reflection with applied field that illustrates the presence of three distinct phases: IC1 for $0.25 < B < 0.45$ T, IC2 for $0.45 < B < 0.65$ T and SF for $B > 0.65$ T. Right: Incommensuration as a function of field.

rise to isotropic Heisenberg exchange interactions whereas for Cs_2CoCl_4 the finite orbital moment due to the Co^{2+} ions gives rise to finite spin-orbit interactions which in consequence determine XY-type exchange. The main conclusion of the theoretical study is that frustration and quasi-one-dimensionality do amplify tiny terms in the Hamiltonian to the point where they control the ground state. Also considering weak interactions induces a commensurate-incommensurate transition, very similar to what we observe in Cs_2CoCl_4.

For the low field region, our data are in excellent agreement with the magnetostriction data of Breunig et al. [177] which apart from the main transitions at 0.25 T and 0.7 T also observed a transition at 0.45 T. We disagree with the interpretation of the transition between the AF phase and the SF phase which suggests a two-stage spin-flop transition driven by DM interactions. The proposed two-stage transition implies that in a first stage only half of the chains would make the SF transition whereas the other half would remain in an AF state. This means that the observed ordering should be antiferromagnetic commensurate. We clearly show that the ordering in the transition region is incommensurate and is thus incompatible with a

two-stage spin-flop transition. We speculate that the two incommensurate phases might be a spin spiral state or distorted cycloid in the bc plane which is controlled by the DM interactions and frustrated inter-chain interactions but we currently have no solid evidence for this. Of course, a detailed theoretical study similar to the one of Starykh et al. [185] would probably serve to clarify the exact nature of the ordering in this field region in Cs_2CoCl_4.

IC3 phase Before the transition to the fully-polarised state, Cs_2CoCl_4 is described by an incommensurate phase (IC3). The IC3 is stable from $B_{c4} = 1.9$ T to $B_{c5} = 2.35$ T and is characterised by an ordering wave vector $k = (0, 1/2 - \xi, 0)$. The incommensuration ξ varies with applied field as shown in Fig. 5.26 for the $Q = (0, Q_k, -3)$ magnetic reflection. As the field is increased, it asymptotically approaches $\xi = 0.04$ r.l.u.

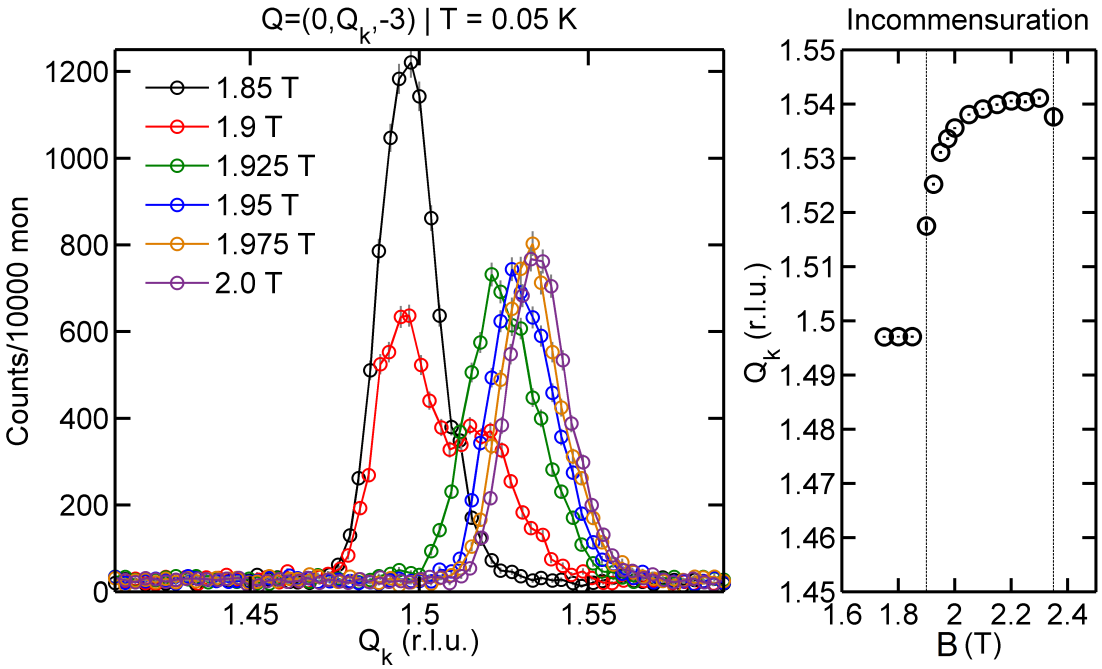

Figure 5.26: Left: Neutron scattering intensity variation of the $Q = (0, Q_k, -3)$ magnetic reflection with applied field that illustrates the presence of two distinct phases: SF for $0.65 < B < 1.9$ T and IC3 for $1.9 < B < 2.35$ T. Right: Incommensuration as a function of field.

A schematic map of the magnetic incommensurate reflections observed in the $(0, K, L)$ plane is given in Fig. 5.27 for data collected on WISH and RITA-II. For a magnetic field applied parallel to the a-direction, only nuclear peaks which satisfy

H + K = odd and L ≠ 0 are expected to have magnetic satellite peaks [176]. We see that for a field applied along the b-direction the pattern of observed reflections does not satisfy this selection rule.

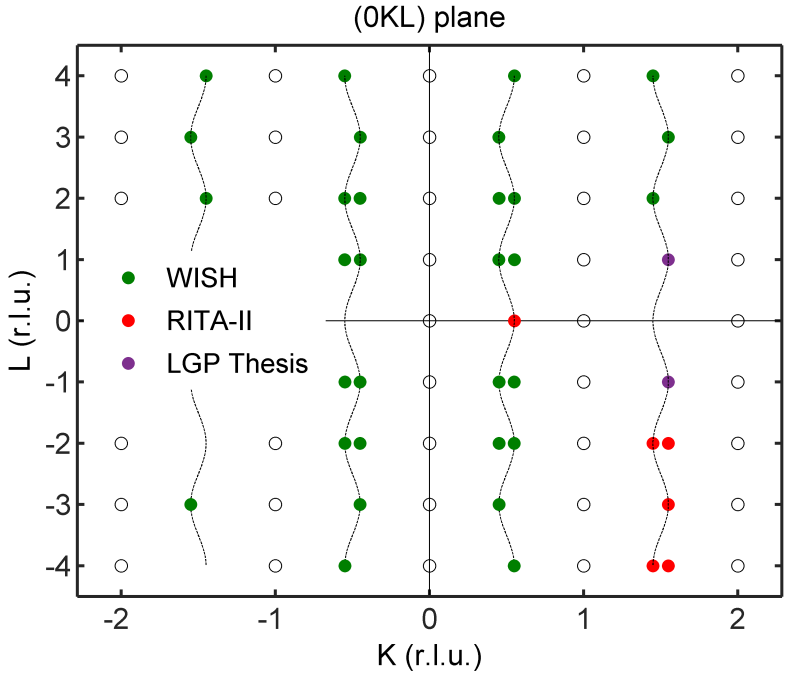

Figure 5.27: Observed magnetic reflections in the high-field IC3 phase in the (0KL) plane. Empty circles represent nuclear reflections, filled green circles represent the observed incommensurate reflections measured on WISH, red filled circles represent magnetic reflections measured on RITA-II and violet circles represent reflections observed by G. L. Pascut [176] (for a field applied along the a-direction).

For example, in the WISH data we observe the $(0, 0, \pm 2) \pm \mathrm{k}$, $(0, -1, \pm 1) + \mathrm{k}$ and $(0, 1, \pm 1) - \mathrm{k}$ reflections but only for $\mathrm{L} = \pm 1$ and $\mathrm{L} = \pm 2$ and not for any other value of L. We currently don't have an explanation for why this should be the case. In the RITA-II data we do observe a magnetic incommensurate reflection with $\mathrm{L} = 0$ component which confirms our initial guess that the field along b-direction leads to different magnetic selection rules as compared to the a-direction case. Furthermore in the RITA-II data we now observe the $(0, 2, -2) - \mathrm{k}$ and $(0, 2, -4) - \mathrm{k}$ reflections which is inconsistent with the WISH data where we see neither the $(0, 2, 2) - \mathrm{k}$ nor the $(0, 2, 4) - \mathrm{k}$ reflections. This is a worrisome inconsistency for which we currently do not have an explanation. With black interrupted line we plot the expected incommensurate peak positions in the case where satellite peaks appear only for nuclear centres satisfying $\mathrm{K} + \mathrm{L} = \text{odd}$. This shows the wave vector modulation

of the scattering perpendicular to the chain direction which was experimentally observed by Yoshizawa et al. [167].

Not withstanding the inconsistency between the WISH and RITA-II data, we clearly observe an incommensurate magnetic phase at the transition between the SF and FP states. This phase is the phase II identified by Breunig et al. [177] from thermodynamic measurements. This observation then excludes the possibility that this phase could be a nematic phase, as proposed by Breunig et al. [177]. The incommensuration arises in this case from the frustrated inter-chain interactions which shift the magnetic peaks away from the half-positions along the K direction.

In this section we have used a combination of time-of-flight neutron diffraction and triple axis measurements to explore the low temperature evolution of the magnetic ground state of Cs_2CoCl_4 when a magnetic field is applied parallel to the crystallographic b-direction.

Figure 5.28: Schematic low temperature phase diagram of Cs_2CoCl_4 as measured by neutron scattering. It shows the evolution of the magnetic ground state of Cs_2CoCl_4 as a function of applied magnetic field.

We identify a rich phase diagram with six different magnetic phases which we schematically plot in Fig. 5.28. At low fields an antiferromagnetic Néel-type commensurate state is stabilised by inter-chain couplings and possibly Dzyaloshinskii-Moriya inter-chain interactions. As the field is increased, two consecutive incommensurate phases are observed. They arise as a result of competing low energy scales associated with the frustrated inter-chain interactions, DM interactions and anisotropy. Our observations of incommensurate order are inconsistent with the proposed two-stage spin-flop transition. In the intermediate field range, a commensurate spin-flop phase which is characterised by antiferromagnetic correlations along the b-direction is present. Just before the transition to an almost fully polarised state, a third incommensurate phase is identified. It is the phase denoted phase II by Breunig et al. [177] and arises as a result of competing frustrated inter-chain interactions. Beyond this phase, a polarised state is observed where all spins tend

to align parallel to the applied field direction.

In order to provide a clearer picture of the exact nature of each phase and the mechanism responsible for their stabilization, a comprehensive theoretical investigation, similar to the one performed for the explanation of the experimental phase diagram of Cs_2CuCl_4 [185] is required. It should take into account the relative strengths of exchange interactions, the XY-type anisotropies and the direction of the applied magnetic field.

5.6.2 Spin Excitations in the Polarised Phase

The neutron scattering measurements of the magnetic ordering of Cs_2CoCl_4 for a field applied along the b-direction reveal that the evolution of the magnetic ground state is very complex, with various commensurate and incommensurate phases which are stable at the lowest of temperatures. In order to gain a better understanding of what is responsible for the appearance of these phases, an accurate knowledge of the magnetic Hamiltonian is required. The parametrisation of the Hamiltonian in terms of various exchange constants and additional smaller terms, for which there is no experimental evidence yet, would probably help to explain each of the experimentally observed phases.

An elegant solution to the experimental parametrisation of the magnetic Hamiltonian of a quantum spin system was originally provided by Coldea et al. [90] who used inelastic neutron scattering to extract the relevant Hamiltonian parameters for Cs_2CuCl_4. By measuring the dispersion of spin excitations in a field regime where the system can be considered as fully polarised and fitting the data to the predictions of linear spin-wave theory, which is accurate in the polarised state, very reliable values for the Hamiltonian parameters were extracted. In general, this technique works whenever the system is forced into a polarised state by the application of a large enough magnetic field because in this case the ground state is ferromagnetic. A ferromagnetic ground state is an exact eigenstate of the Hamiltonian and so linear spin-wave theory gives the dispersion and intensity of magnon excitations very accurately. The values for the exchange constants extracted in this way are reliable as they are not renormalised by quantum fluctuations which are totally suppressed by the field.

In the case of Cs_2CoCl_4 there have been two previous attempts to parametrise the Hamiltonian. Mukherjee et al. [186] have proposed two models to describe

the high-field excitations. The first model is based on a simplified effective S=1/2 isotropic Hamiltonian and linear spin-wave theory is used to extract the intensity and dispersion of excitations. Although this model gives an accurate description of the observed excitations at B = 4 T, it does a poor job in describing the excitations measured at B = 2.5 T. To obtain a consistent model, a second, 'exciton' model was used, that takes into account the full S=3/2 physics of the system and thus accounts for the anisotropic XY exchange. The excitations are computed using a multilevel pseudo-boson technique in an applied magnetic field.

We choose to use the simplified model to fit our data due to several reasons. Firstly, the comparison of the extracted exchanges of Mukherjee et al. [186] using both models reveals that their relative strengths are identical. Secondly, we know that the simplified model correctly describes the excitations in the polarised state at a given field. Thirdly, the lack of an analytical solution for the dispersion in the case of the exciton model means we have to computationally calculate the dispersion which is quite an involved process.

The simplified model uses only the lowest S=1/2 states, which is justified by the fact that the energy separation between the $|\pm 1/2\rangle$ and $|\pm 3/2\rangle$ Kramers doublets is much larger than the main exchange, and assumes isotropic Heisenberg exchange interactions. Although this is not a very accurate description of Cs_2CoCl_4, it allows the understanding of the major observed features and their origin in terms of exchange couplings. The magnetic lattice and exchange paths considered are identical to the ones pictured in Fig. 5.20. The Hamiltonian in this case reads

$$\mathcal{H} = \mathcal{H}_{\mathrm{ex}} + \mathcal{H}_{\mathrm{DM}} + \mathcal{H}_{\mathrm{app}} \tag{5.9}$$

where the first term is the exchange term, the second term includes a Dzyaloshinskii-Moriya interaction and the third terms describes the interaction with the applied magnetic field. The exchange term is given as

$$\mathcal{H}_{\mathrm{ex}} = \mathrm{J}\sum_{\mathbf{r},\delta} \mathbf{S}_{\mathbf{r}} \cdot \mathbf{S}_{\mathbf{r}+\delta} + \mathrm{J}_{\mathrm{ab}}\sum_{\mathbf{r},\delta} \mathbf{S}_{\mathbf{r}} \cdot \mathbf{S}_{\mathbf{r}+\delta} + \mathrm{J}_{\mathrm{bc}}\sum_{\mathbf{r},\delta} \mathbf{S}_{\mathbf{r}} \cdot \mathbf{S}_{\mathbf{r}+\delta} + \mathrm{J}_{\mathrm{ac}}\sum_{\mathbf{r},\delta} \mathbf{S}_{\mathbf{r}} \cdot \mathbf{S}_{\mathbf{r}+\delta} \tag{5.10}$$

where each $\mathbf{r}$ and δ vectors run over the nearest neighbour exchange paths connected by the corresponding exchange coupling. The DM term reads

$$\mathcal{H}_{\rm DM} = \sum_{\mathbf{r},\delta} \mathbf{D} \cdot \mathbf{S_r} \times \mathbf{S_{r+\delta}} \tag{5.11}$$

with δ running over the nearest neighbours of spin $\mathbf{S_r}$ connected by the J_{bc} exchange paths and $\mathbf{D}$ is the DM vector. The applied field term is written as

$$\mathcal{H}_{\rm app} = -g\mu_B \sum_{\mathbf{r}} \mathbf{B} \cdot S^z_{\mathbf{r}} \tag{5.12}$$

where the applied field is along the z-direction and g is the Landeé factor. In the above expressions the main exchange J connects 1 spin to 2 nearest neighbours along the chain direction, J_{ab} and J_{bc} connect 1 spin to 4 nearest neighbours, J_{ac} connects 1 spin to 2 nearest neighbours and the DM interaction vector is assumed perpendicular to the bc plane and associated with the J_{bc} exchange paths.

The transformation of the Hamiltonian in terms of bosonic creation and annihilation operators is performed via the Holstein-Primakoff transformation for spin operators. By retaining only the first order terms in the boson operator expansion, Fourier transforming them accordingly and diagonalizing the subsequent form of the Hamiltonian, the dispersion of magnon-like excitations is given as

$$\hbar\omega_{\mathbf{Q}} = A_0 + A_{\mathbf{Q}} \pm B_{\mathbf{Q}} \pm D_{\mathbf{Q}} \tag{5.13}$$

with

$$\begin{aligned}
A_0 &= g\mu_B H - J - 2J_{ab} - 2J_{bc} - J_{ac} \\
A_{\mathbf{Q}} &= J\cos(2\pi Q_k) + 2J_{bc}\cos(\pi Q_k)\cos(\pi Q_l) \\
B_{\mathbf{Q}} &= 2J_{ab}\cos(\pi Q_h)\cos(\pi Q_k) + J_{ac}\cos(\pi Q_h)\cos(\pi Q_l) \\
D_{\mathbf{Q}} &= 2D_a\sin(\pi Q_k)\cos(\pi Q_l)
\end{aligned} \tag{5.14}$$

The existence of two sublattices in the unit cell gives rise to two magnon branches which correspond to magnons residing on each sublattice. The further consideration of finite DM interactions splits each branch into two sub-branches predicting a total of 4 separate magnon branches which we will identify as $++$, $+-$, $--$ and $-+$ depending on the sign of the $B_{\mathbf{Q}}$ and $D_{\mathbf{Q}}$ terms. For a particular choice of Hamiltonian parameters of the same order of magnitude as expected for Cs_2CoCl_4, J = 0.1 meV $J_{ab} = 0$, $J_{bc} = 0.02$ meV, $J_{ac} = 0.01$ meV, D = 0.002 meV, g = 3, H = 4 T, we plot

the dispersion along the $(0, Q_k, -2)$ and $(0, 2, Q_l)$ directions as predicted by linear spin-wave theory for all 4 magnon branches in Fig. 5.29.

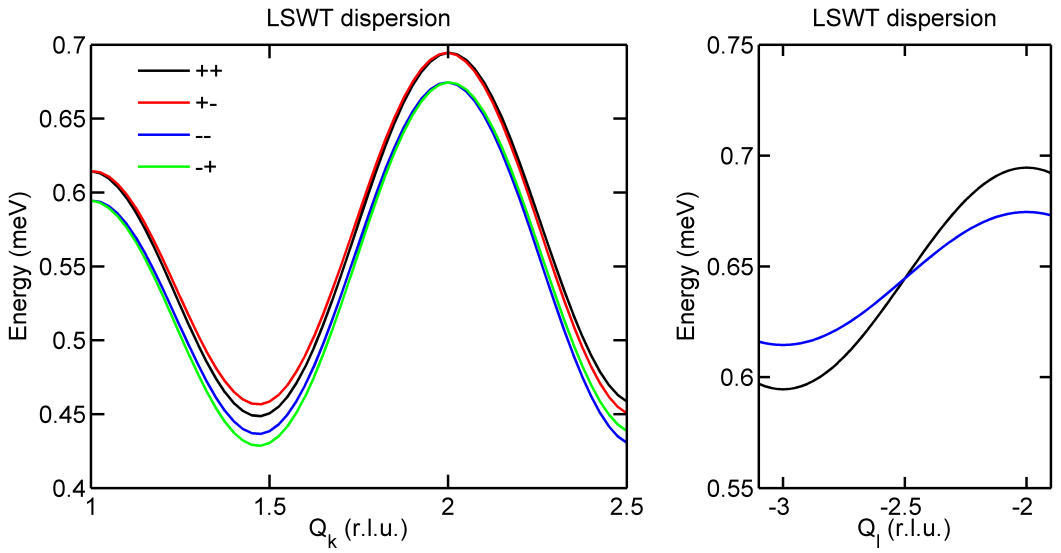

Figure 5.29: Linear spin-wave theory predictions for the dispersion along the same reciprocal space paths as measured during the experiment. Considering two sublattices in the unit cell and adding a DM interaction term gives rise to 4 non-degenerate magnon branches.

In order to get a feel for which parameters are responsible for what features of the dispersion relation, we analyse the effects of each parameter on one of the magnon branches and along the Q_k and Q_l directions. Along the Q_k direction we see that the g-factor is responsible for the overall mean dispersion energy. The main intra-chain J is fixed from the amplitude of the dispersion (i.e. the difference in energy between the maximum and minimum of the dispersion). The ratio between the inequivalent maxima as well as the shift of the minimum away from the half-integer positions in Q_k is sensitive to both frustrated J_{ab} and J_{bc} couplings so these can't be both extracted from only the dispersion along Q_k. The dispersion along Q_k for fixed Q_h and Q_l is not sensitive to the J_{ac} coupling as expected. If we turn to the dispersion along the Q_l direction we observe that J and J_{ab} have no effect on the dispersion as expected. The g-factor is responsible for the overall shift of the mean dispersion energy. The inter-chain J_{bc} and J_{ac} are both sensitive to the amplitude of the dispersion so they can't be both extracted from only the dispersion along Q_l. The effect of adding the DM term is to slightly shift the position of the Q_k dispersion minimum to higher or lower energy depending on the sign of the DM term while the maximum energy remains the same which leads to 4 non-degenerate dispersions

along the Q_k direction. The DM term has no effect on the Q_l dispersion and 2 non-degenerate dispersions are predicted. By measuring the dispersion relation along several reciprocal space paths and fitting all the data to the predictions of linear spin-wave theory, we should be able to extract reliable values for the parameters of the Hamiltonian.

Inelastic neutron scattering data was collected on RITA-II with fixed final neutron energy of 3.7 meV and fairly tight beam collimation. This provided an energy resolution at the elastic line of $\Delta E = 0.115 \pm 0.001$ meV (FWHM). The inelastic scattering signal was measured as constant-Q scans by varying the energy transfer. A typical such scan is shown in Fig. 5.30 where we fit both the elastic line and the inelastic peak to Gaussians on a linear background. We extract the position in energy of each inelastic peak which for several Q points gives the dispersion relation.

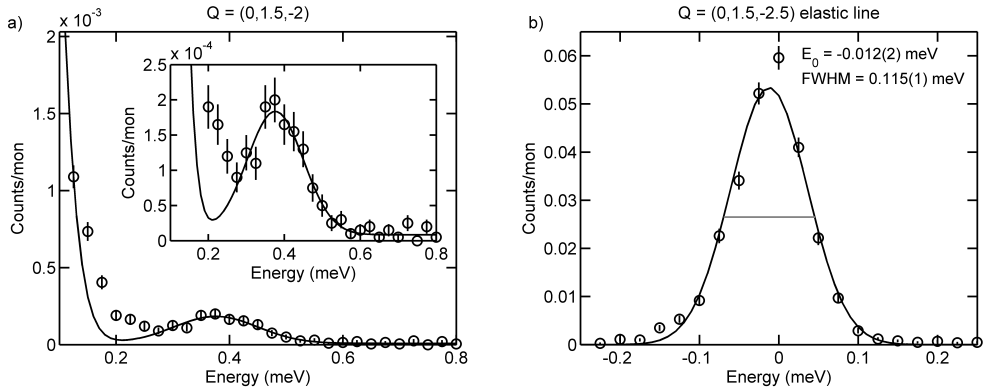

Figure 5.30: a) Typical constant-Q scan at $(0, 1.5, -2)$ together with a fit of both the elastic line and the inelastic peak to Gaussian functions on a linear background. b) Scan through the elastic line which gives the experimental energy resolution of $\Delta E = 0.115(1)$ meV (FWHM).

The summary of the measured dispersion along four different reciprocal space paths is given in Fig. 5.31. Due to the fact that the difference between the expected energy peak positions of the magnon branches are much smaller than the experimental energy resolution, we observe all the branches as being degenerate in energy. Nonetheless we can extract reliable values for the Hamiltonian parameters by assuming we only see one magnon branch, which for these purposes was chosen as the ++ branch. If we consider we see other branches, the sign of the relevant parameters will change accordingly but their modulus will not. We know that all exchange interactions are antiferromagnetic and the sign of the DM vector is important only if we want to analyse in detail the expected spin structure which we

will not do in this thesis. For the purpose of extracting the relative strengths of the exchanges and possibly show evidence for a finite DM interaction, fitting the data to one magnon branch will suffice. In a first step we have fitted the data by fixing D_a to 0. The values extracted from fitting all the data to the dispersion given by the ++ dispersion are J = 0.130(5) meV, J_{ab} = 0.004(5) meV, J_{bc} = 0.020(2) meV, J_{ac} = 0.006(2) meV and g = 2.92. In a second step we have included the DM term in the dispersion and the extracted fit parameters are in this case J = 0.130(5) meV, J_{ab} = 0.003(5) meV, J_{bc} = 0.016(4) meV, J_{ac} = 0.014(6) meV, D_a = 0.004(3) meV and g = 2.92(2). The extracted fit parameters are given in Table 5.1.

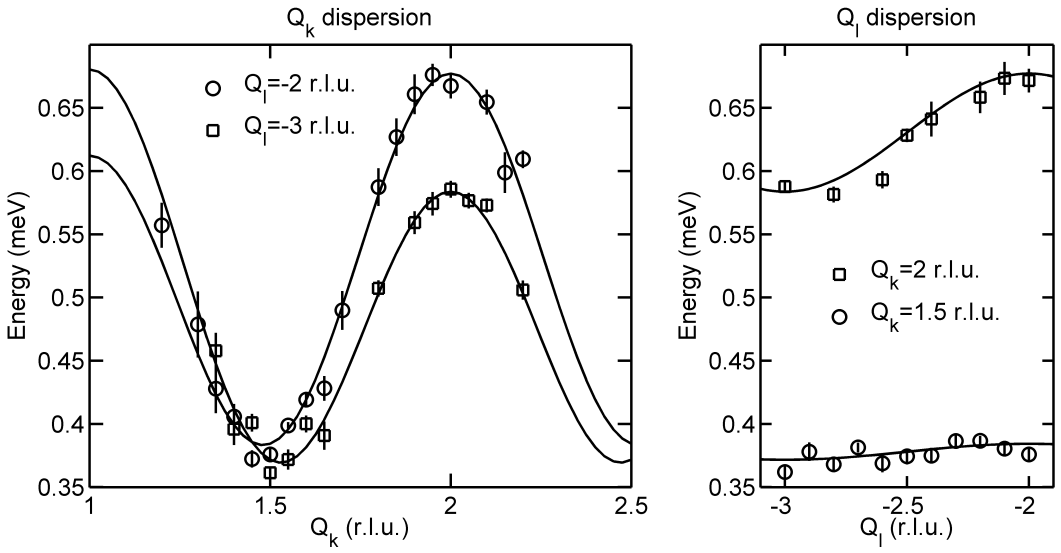

Figure 5.31: Measured dispersion (open symbols) along different reciprocal space paths together with a fit to the predictions of linear spin-wave theory for a single magnon branch (black lines).

The results of the fitting show that our data is either not sensitive to J_{ab} or it is very small $J_{ab} < 0.05J$. This is in contradiction to the values extracted by Mukherjee [186] and Pascut [176] which give J_{ab} = 0.030(5) meV and J_{ab} = 0.034(2) respectively. If one tries to fit the data by fixing J_{ab} to either of their values, the quality of our fit is worse. By including the DM term the quality of our fit does not improve significantly which leads us to conclude that if there is such a term present, then it is most likely of the order of 5% of the main intra-chain J or lower. Both our fits suggest that in order to accurately describe the data the relative strength of the exchange interactions has to be $J > J_{bc} > J_{ac} > J_{ab} \approx D_a$. As a function of the main J, the inter-chain interactions $J_{bc} = (12-15)\%J$, $J_{ac} = (5-10)\%J$, $J_{ab} < 5\%J$ and $D_a < 5\%J$, which indeed confirms the quasi-1D nature of Cs_2CoCl_4.

Table 5.1: Hamiltonian parameters as extracted from the dispersion measured at B = 4 T.

Parameter	D_a fixed	D_a free
J (meV)	0.130(5)	0.130(5)
J_{ab} (meV)	$< 5\%$J	$< 5\%$J
J_{bc} (meV)	0.020(2)	0.016(4)
J_{ac} (meV)	0.006(2)	0.014(6)
D_a (meV)	0	$< 5\%$J
g	2.92(2)	2.92(2)

In the context of the observed magnetic ordering, we now see that the combination of frustrated inter-chain interactions and their comparable strength (a few % of the main J), together with the inclusion of Dzyaloshinskii-Moryia interactions, does provide the right conditions such that a very fine balance and competition between low energy scales would determine the magnetic ground state. The application of a magnetic field then has the role of promoting one of these energy scales over the others and thus stabilize one of the many experimentally observed types of ordering. As mentioned in the previous section, we believe that the knowledge of the relative strengths of inter-chain interactions and of DM interactions can guide a thorough theoretical study of this material which should also consider the true S=3/2 physics and the anisotropies it gives rise to, in order to give an accurate description of the various low temperature phases.

Chapter 6

Conclusions and Future Outlook

In chapter 3 we presented a time-of-flight inelastic neutron scattering study aimed at identifying experimental signatures of magnon decay in the organic layered magnet $(5CAP)_2CuCl_4$ (CAPCC). We began with a description of what is theoretically and experimentally known about the static and dynamical properties of the two-dimensional S=1/2 square lattice Heisenberg antiferromagnet in zero field. We introduced the concept of spontaneous magnon decay and showed theoretical predictions for the expected anomalous spin dynamics that result as a consequence of decays. We discussed the possibility of experimentally observing the effects of magnon decays in a real system with finite inter-layer coupling. In section 3.3 we presented the properties of CAPCC and in section 3.4 we described the experimental setup of an LET inelastic neutron scattering experiment performed with the aim of testing various theoretical predictions about the high-field excitation spectrum of CAPCC. In a first step, we characterised the spin Hamiltonian of CAPCC by extracting the magnetic exchange constants from spin-wave data collected in the polarised phase, at B = 7 T, where spins are forced to align along the applied magnetic field direction and where the excitation spectrum is accurately described by linear spin-wave theory. We showed that the Hamiltonian of CAPCC is well described by a Heisenberg model with nearest neighbour in-plane coupling J = 0.100(2) meV and considerable out-of plane coupling $J' = 0.032(2)$ meV. In section 3.6 we presented and discussed results for the spin dynamics in the intermediate field, canted phase of CAPCC, where magnon decay effects are predicted to be experimentally observable. We first took an experimental approach to the data analysis and argued that the observed asymmetry in the lineshape of the excitations is an indication of decays. We then invoked results of linear spin-wave theory and showed that the measured excitations

are broader than what is predicted for two non-interacting single magnon modes, with significant spectral weight distributed away from the single particle peaks, into a higher energy continuum. We compared the data with theoretical predictions based on a 1/S spin-wave theory expansion which accounts for magnon-magnon interactions and showed that the 1/S theory captures better the general features of the data, which include a damping of the modes and the presence of continuum scattering. We showed that the excitation lineshape around the $Q = (\pi/2, \pi/2, 0)$ is broader than around $Q = (\pi, 0, 0)$, in accord with predictions of the 1/S theory. We concluded that on a qualitative level, the data supports the presence of field-induced magnon decay in CAPCC but that the overall data quality does not allow for a full quantitative comparison to theory. We proposed a better optimized, definitive experiment, which will allow for a quantitative comparison with specific theoretical predictions for the shape of the continuum and the decay rates.

Despite the fact that effects of magnon decay are predicted to be most extreme for the quantum limit S=1/2, so far signatures of decays have only been experimentally identified for classical S=2 and S=5/2 systems. This study provides the first experimental confirmation of magnon decay for the quantum case and presents as an opportunity to further study a range of related phenomena such as triplon decays in spin liquids, magnon decays in planar ferromagnets and impurity assisted magnon-magnon scattering in easy-plane collinear antiferromagnets.

In chapter 4 we presented a neutron resonant spin-echo triple-axis neutron scattering study aimed at investigating the temperature evolution of the triplet excitations and gap energy in the prototypical S=1 Haldane chain Y_2BaNiO_5. We began with an introduction about the Heisenberg antiferromagnetic chain and showed that the excitation spectrum of the integer spin model is markedly different from the half-integer model, with a gap in the spectrum for integer spin. We focused on the S=1 Heisenberg antiferromagnetic chain and presented the properties of its ground and excited states. Although the ground state is disordered from a classical point of view, there is finite string order that determines quantum coherence in the ground state. We showed that the coherence is directly reflected in the lifetime of the triplet excitations. In section 4.2 we presented a quantitative model for the lifetime of the triplet excitations and the non-linear sigma model (NLSM) prediction for the blue shift of the gap energy. We then moved on to present details of Y_2BaNiO_5, an excellent realisation of the S=1 Haldane chain. In section 4.4 we described the high-resolution NRSE-TAS experiment performed on Y_2BaNiO_5 and the strategy we

adopted to measure the lifetime and blue shift. In the next section we discussed the results for the triplet lifetime measurements and showed that although NRSE-TAS had previously been used to extract information about lineshape asymmetry [149], we were not able to reliably extract such information from the data. All the subsequent analysis was performed assuming a symmetric lineshape of the excitations. We corrected the data for depolarisation effects and extracted the intrinsic lineshape broadening as the half-width at half maximum of a Lorentzian. We showed that the non-linear sigma model is unable to capture the measured temperature dependence of the inverse excitation lifetime. Triple-axis (TAS) and NRSE-TAS measurements on Y_2BaNiO_5 were shown to disagree for a wide range of temperatures and while we were unable to identify the reasons for this mismatch, we concluded that for $T > 25$ K the TAS data should be considered reliable, whereas for $T < 25$ K, the NRSE-TAS data should describe more accurately the inverse lifetime of the triplet excitations. A phenomenological model for the temperature dependence of the inverse lifetime was fitted to the data and bounds were put on the residual inverse lifetime at $T = 0$. We attributed the residual inverse lifetime to the random distribution of static defects introduced by impurities present in the sample. A comparison of the measured $\Gamma(T)$ with predictions of the quantitative model revealed that the model severely overestimates the inverse lifetime for all temperatures. Assuming the measured residual inverse lifetime arises from static defects, we showed that a mean chain length twice as large as what was inferred by Xu et al. [97] should be used. In section 4.6 we presented results from phase sensitive measurements from which we extracted the blue shift of the triplet energy. Due to the impossibility of parametrising the lineshape asymmetry from the lifetime measurements, we analysed the data in terms of a symmetric lineshape of the excitations. While this prevents an accurate extraction of the blue shift, we showed that qualitatively one can confirm the blue shift in Y_2BaNiO_5.

As future work on the subject, it is desirable to identify the exact reasons for the TAS and NRSE-TAS lifetime measurement discrepancy by better understanding how the TAS data has been analysed and what are its limitations and also by improving ones understanding of the depolarisation corrections applied to the spin-echo data. We plan to obtain exact theoretical predictions for the lineshape asymmetry from Ref. [141] and use them to parametrise the lineshape asymmetry. In this way we can compute what is the expected relationship between the spin-echo phase and the spin-echo time and extract the blue shift of the gap energy accordingly.

In chapter 5 we presented results of neutron scattering measurements on the quasi-1D effective S=1/2 XXZ antiferromagnet Cs_2CoCl_4 performed with the aim of identifying experimental evidence for the entanglement transition predicted to occur in this system. We began by emphasizing the role of quantum information theoretical concepts in the study of condensed matter and how the methods of quantum information provide a novel view on the known properties of quantum spin systems and at the same time reveal previously unknown features. One of the predictions is the presence of a completely new type of transition which is driven by quantum entanglement correlations in the ground state, an entanglement transition. Next, we presented the concept of concurrence, an entanglement witness which signals an entanglement transition, and made the connection with the spin-spin correlation function which is measured via neutron scattering. We gave predictions of what the expected behaviour of the integrated diffuse scattering weight should be as a function of applied magnetic field in order to be consistent with the presence of an entanglement transition. An overview of the sample properties and the experimental phase diagram for an applied magnetic field along the crystallographic a-direction as measured with neutron scattering were presented in section 5.3. The results of more recent high-resolution bulk measurements were also given and the phase diagrams for applied magnetic fields along all three orthorhombic crystallographic directions were presented. In section 5.4 we gave details of the two neutron scattering experiments performed on the WISH diffractometer and in section 5.5 we discussed the data collected at $T > T_N$ and $T < T_N$. We showed that the data does not provide clear evidence for an entanglement transition and discussed possible reasons why this happens. Based on measurements performed on WISH we identified, for the first time, two new magnetic phases which are present when an applied magnetic field is parallel to the crystallographic b-direction. This motivated a dedicated neutron scattering study to investigate the unknown ground state phase diagram of Cs_2CoCl_4 for magnetic fields applied along the b-direction. In section 5.6 we described the experimental setup of triple-axis measurements on RITA-II and presented results for the field dependency of the magnetic ordering. We showed that the magnetic ground state suffers numerous changes as the field is swept from zero to beyond saturation. We identified six ordered phases, both commensurate and incommensurate and discussed possible mechanisms that stabilize each phase. From spin-wave excitations measured at $B = 4$ T in the polarised phase, we extracted the parameters of the magnetic Hamiltonian. We showed that inter-chain interactions are of the order

of $5\% - 15\%$ of the main intra-chain J. The inclusion of a Dzyaloshinskii-Moriya interaction did not significantly improve the fits and we concluded that if such an interaction is present, it is most likely of the order of a few percent of J. The observed magnetic ordering most probably arises from the fine balance of all the low energy scales set by the inter-chain exchange interactions and anisotropy.

Appendix A

Complete Datasets for $(5CAP)_2CuCl_4$

In this appendix we present the complete raw and analysed datasets collected for the study of the field-induced magnon decay in the quasi-2D square lattice quantum Heisenberg antiferromagnet $(5CAP)_2CuCl_4$. In each of the subsequent figures, the arrangement of datasets is the following. Top right: raw B = 3.35 T data; Bottom right: raw B = 7 T data and exponential model; Top left: subtracted B = 3.35 T data (raw data minus smooth exponential model for background) and fit to a skew normal distribution; Bottom left: subtracted B = 3.35 T data and predictions of renormalised 1/S spin-wave theory. Main mode (red line) and ghost mode (blue line) are plotted separately.

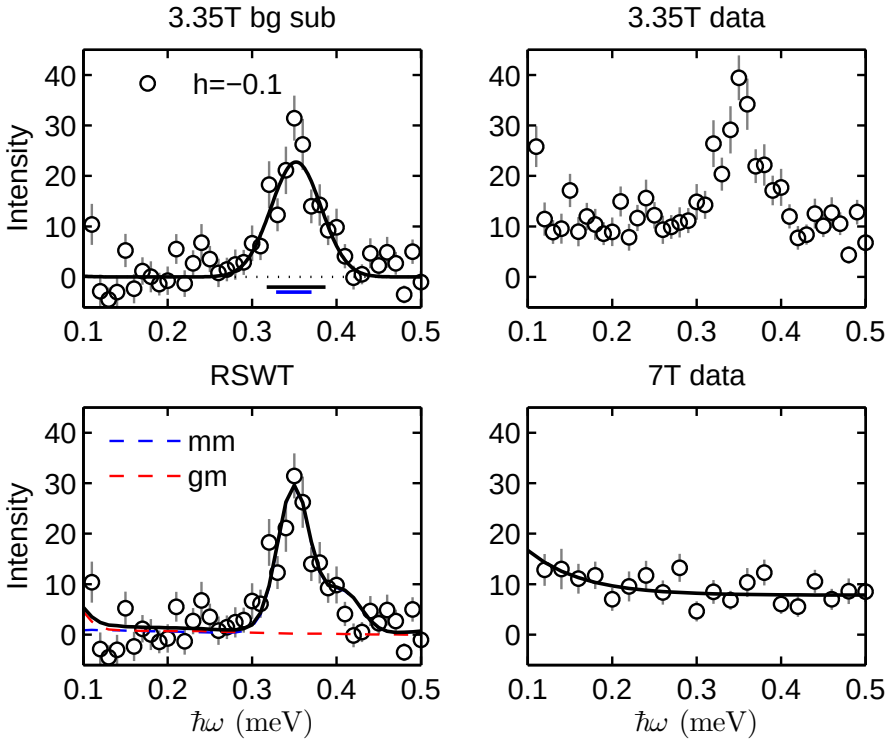

Figure A.1

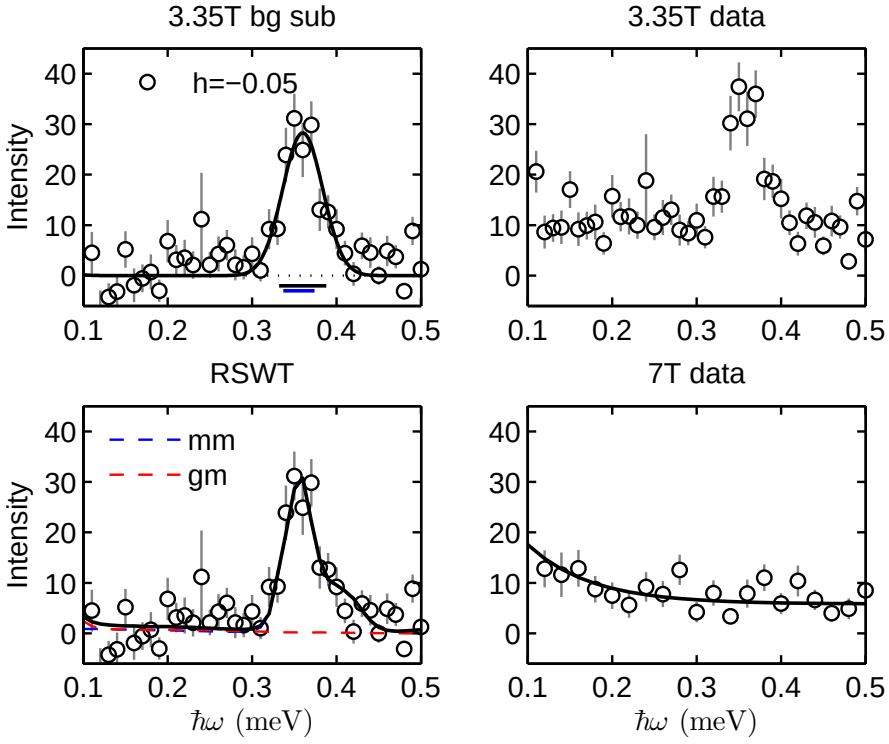

Figure A.2

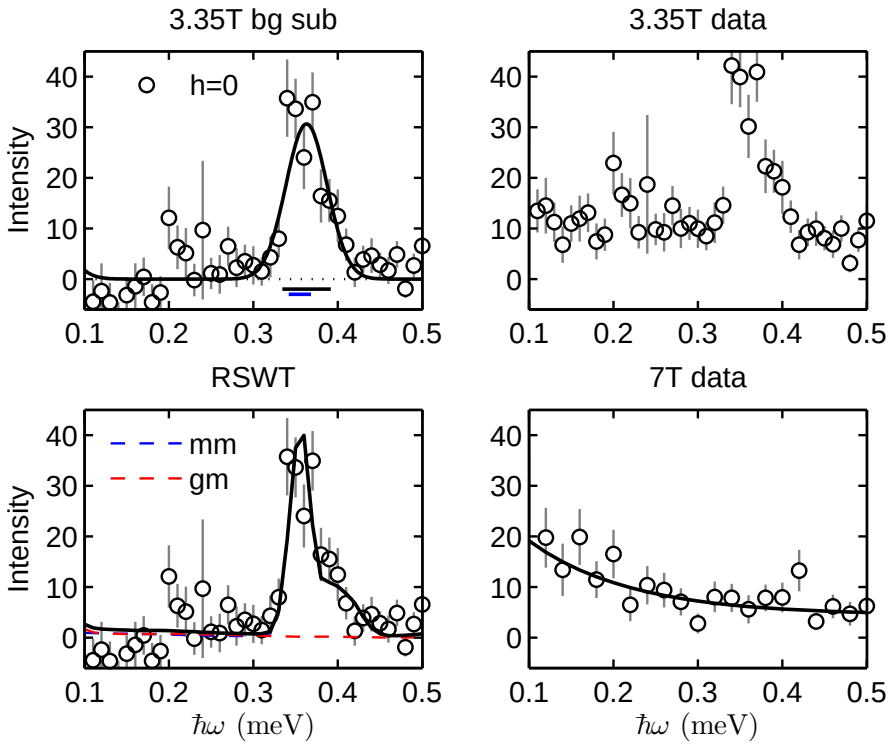

Figure A.3

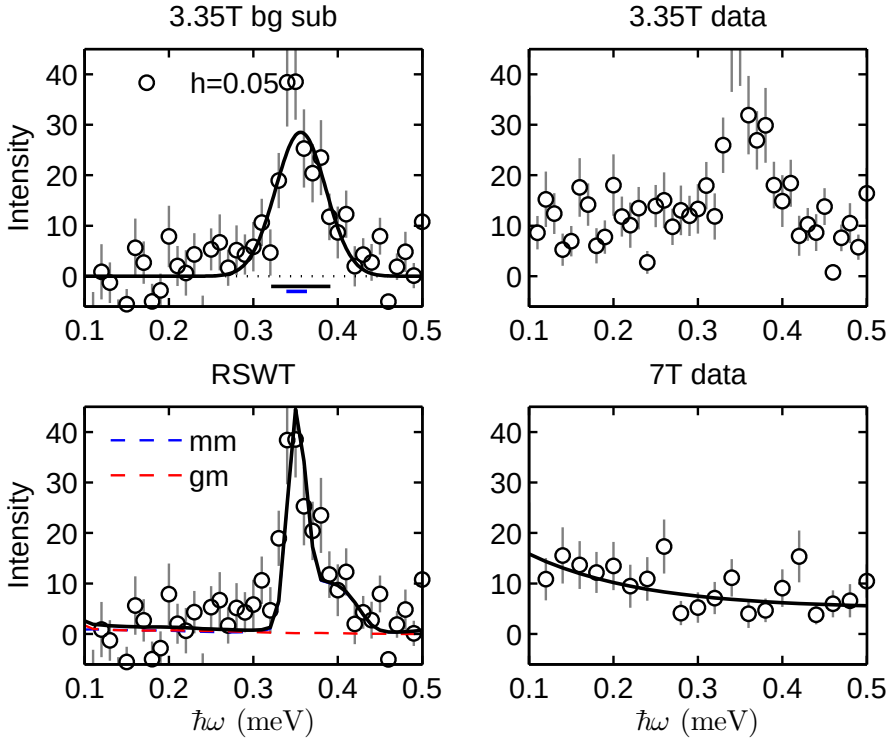

Figure A.4

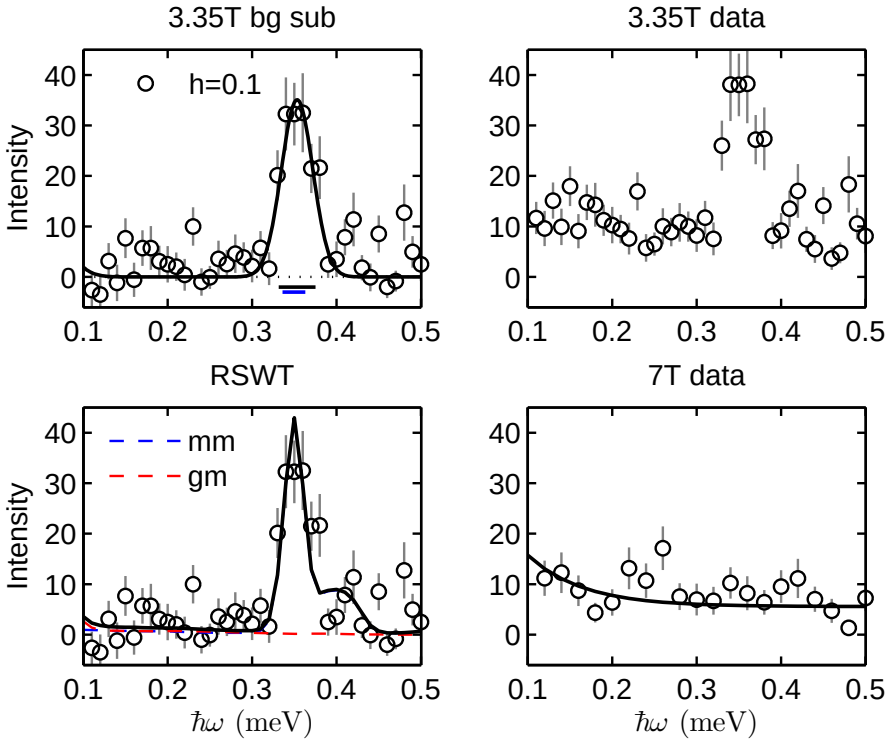

Figure A.5

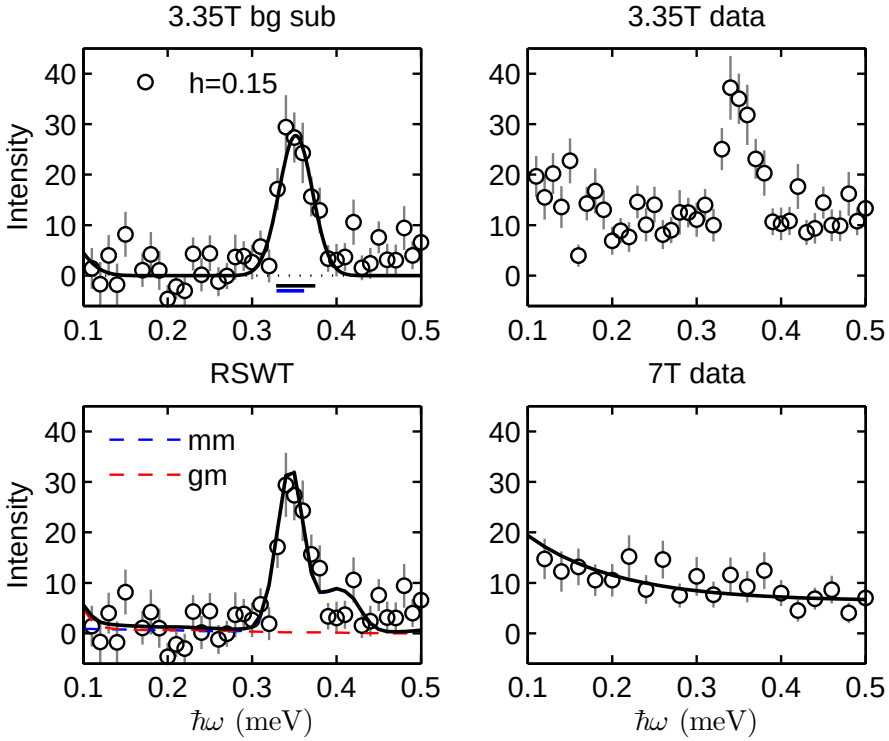

Figure A.6

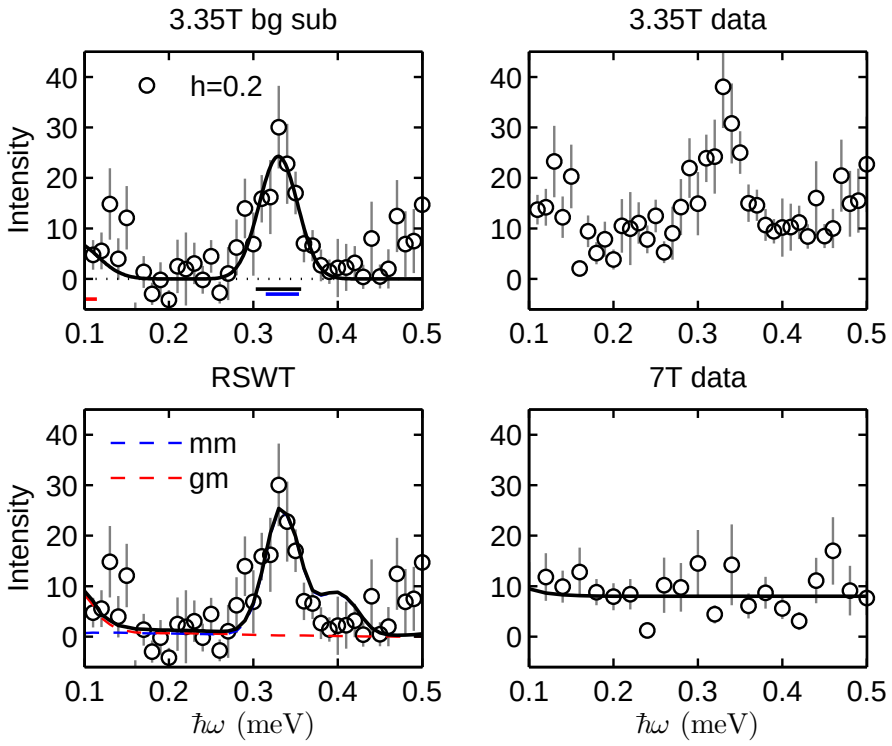

Figure A.7

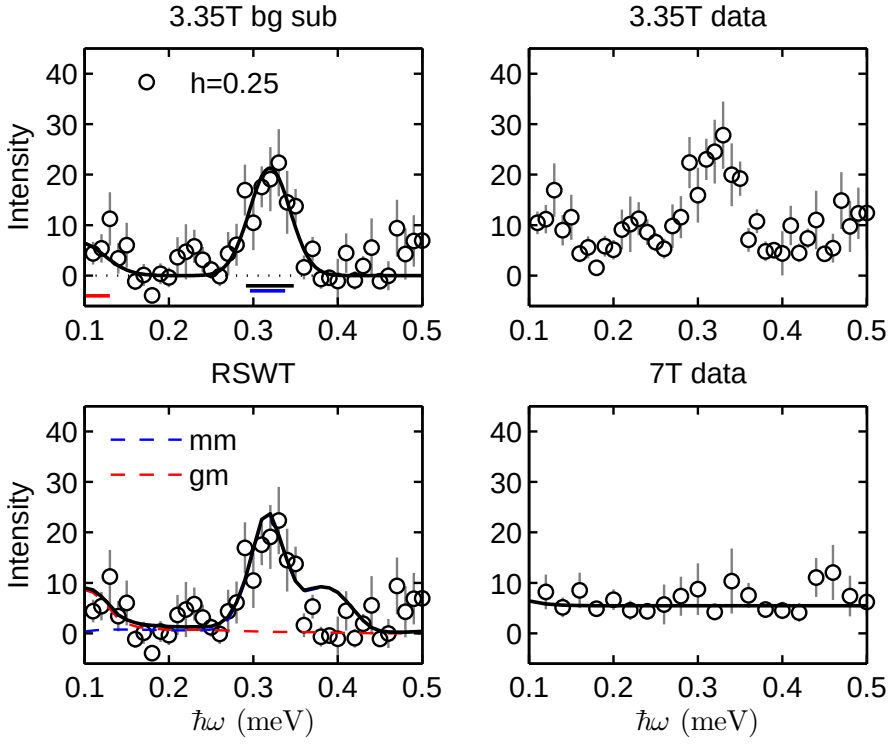

Figure A.8

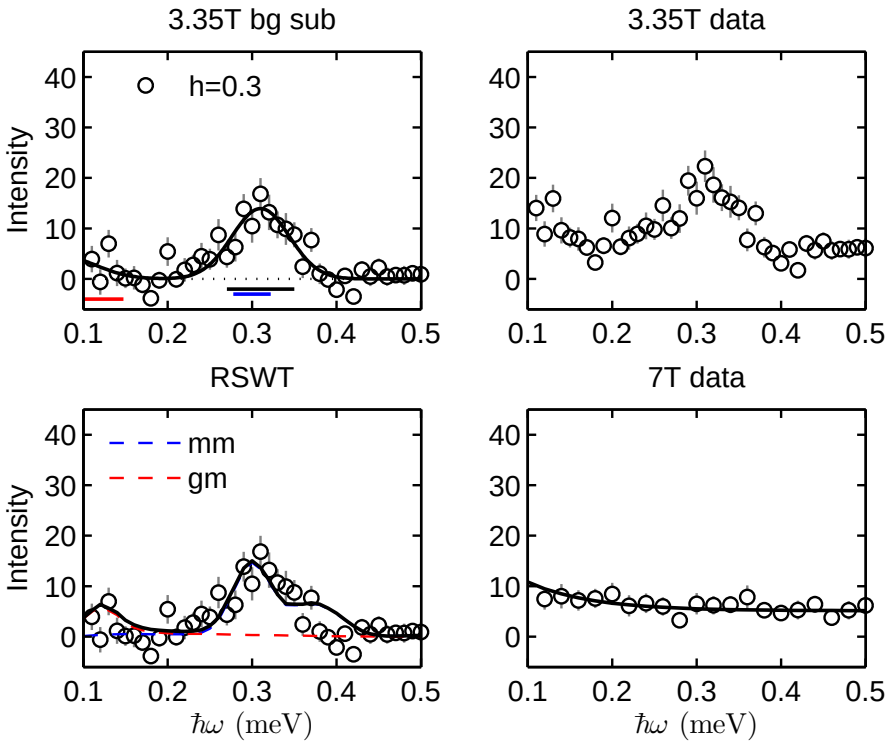

Figure A.9

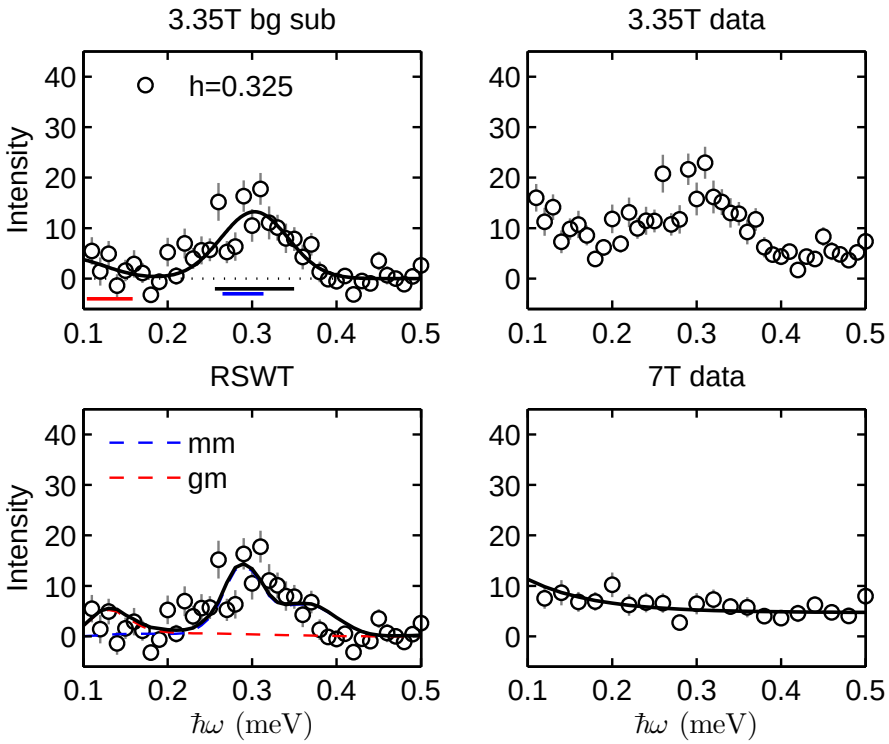

Figure A.10

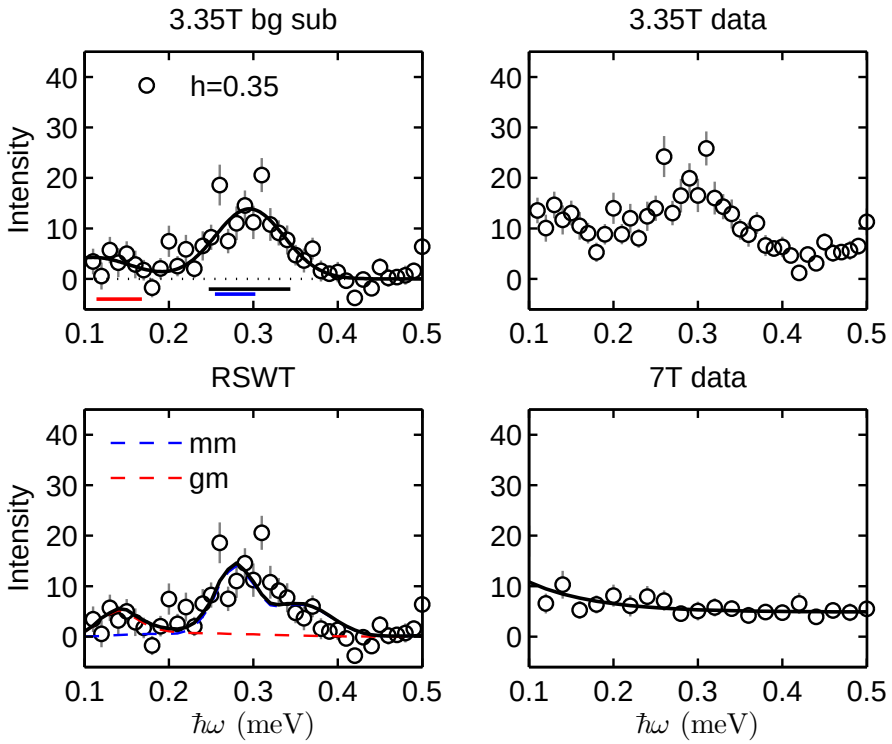

Figure A.11

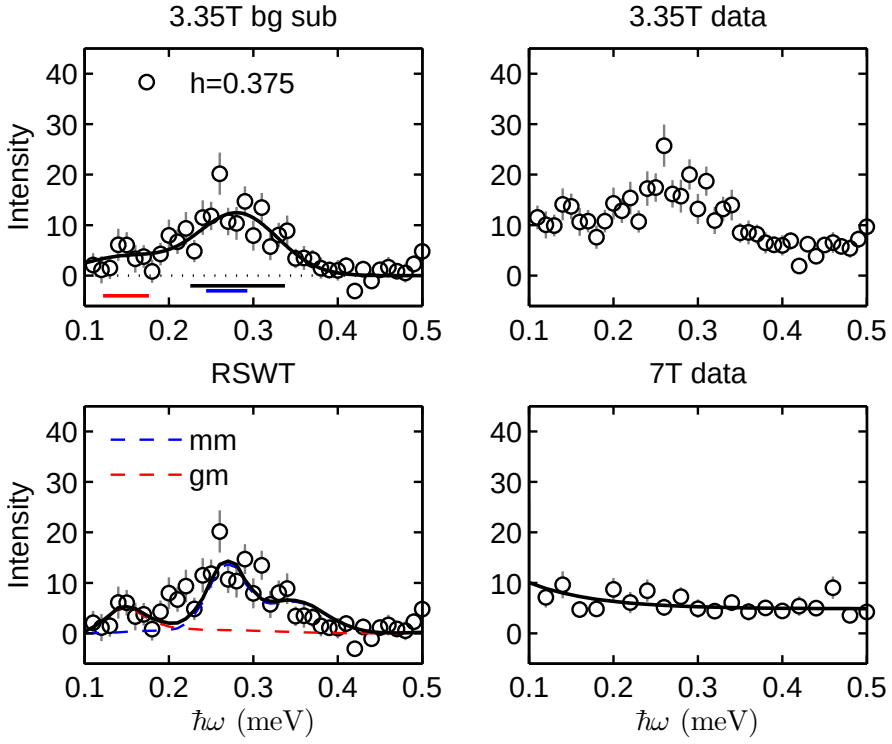

Figure A.12

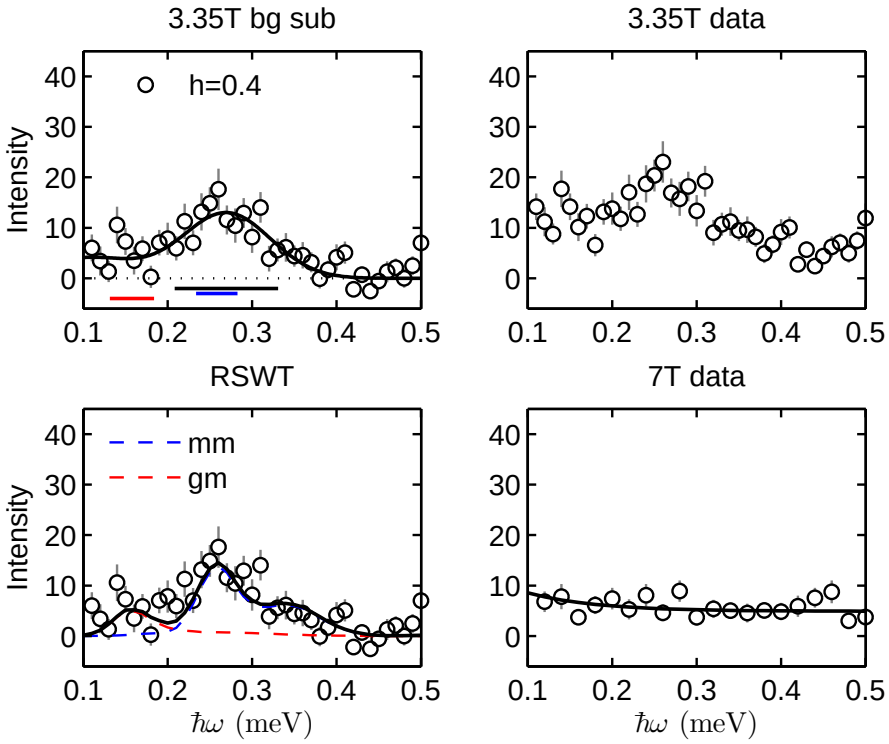

Figure A.13

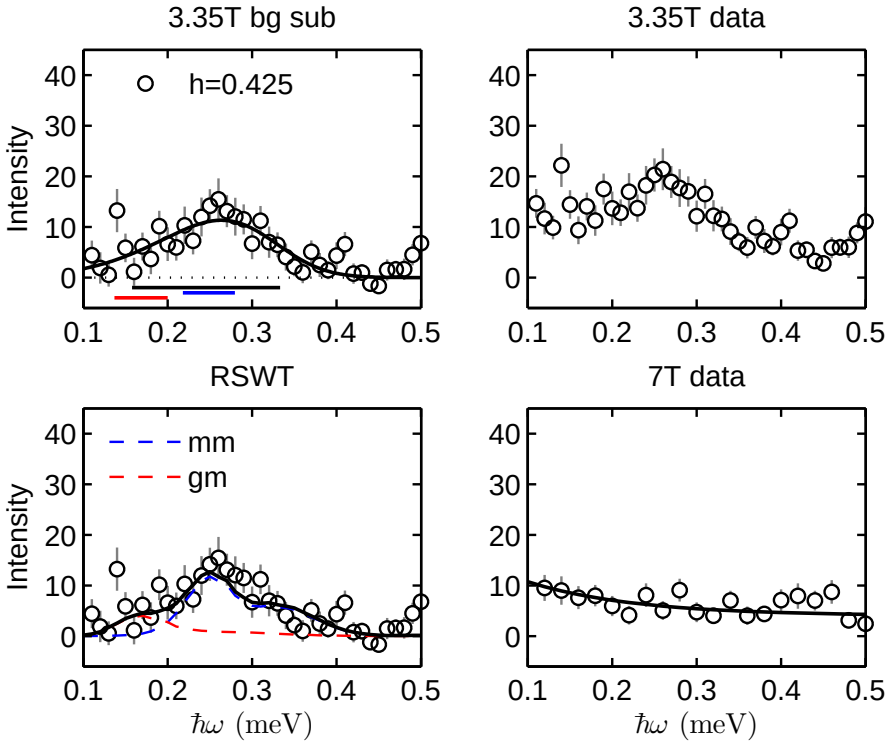

Figure A.14

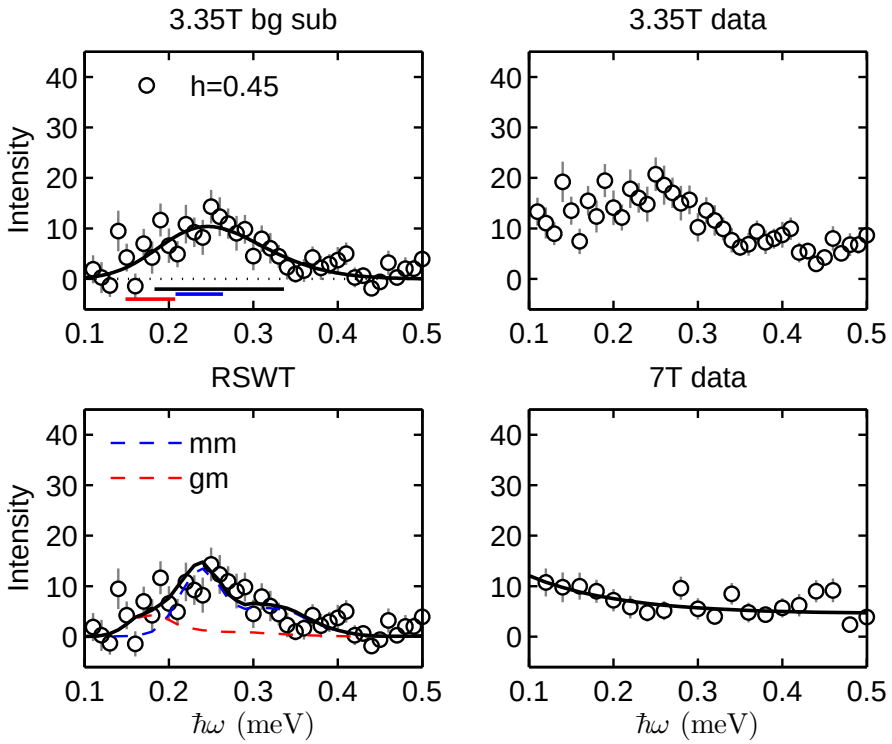

Figure A.15

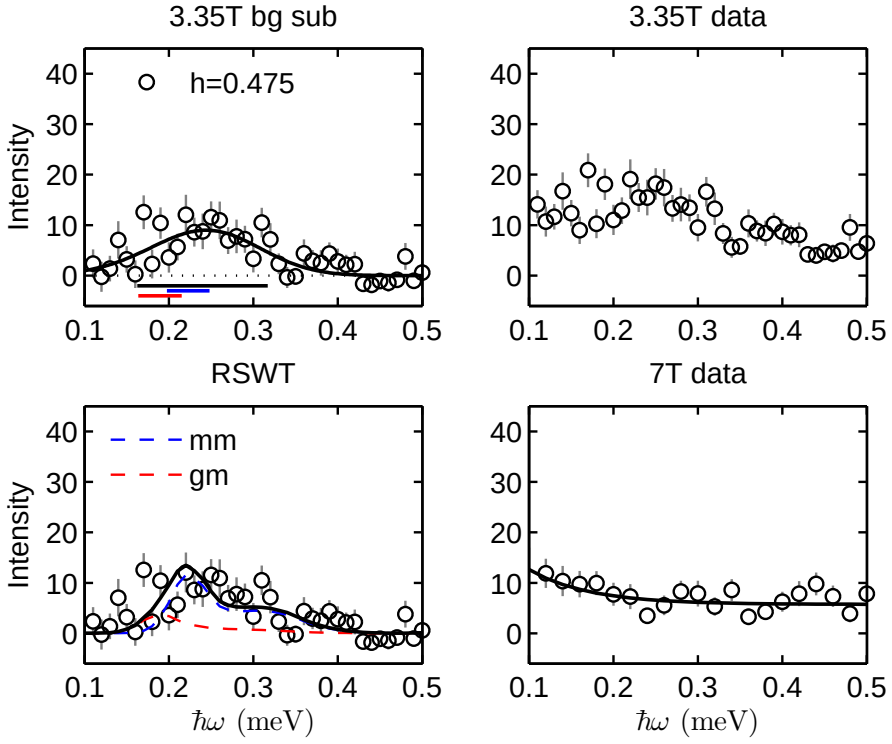

Figure A.16

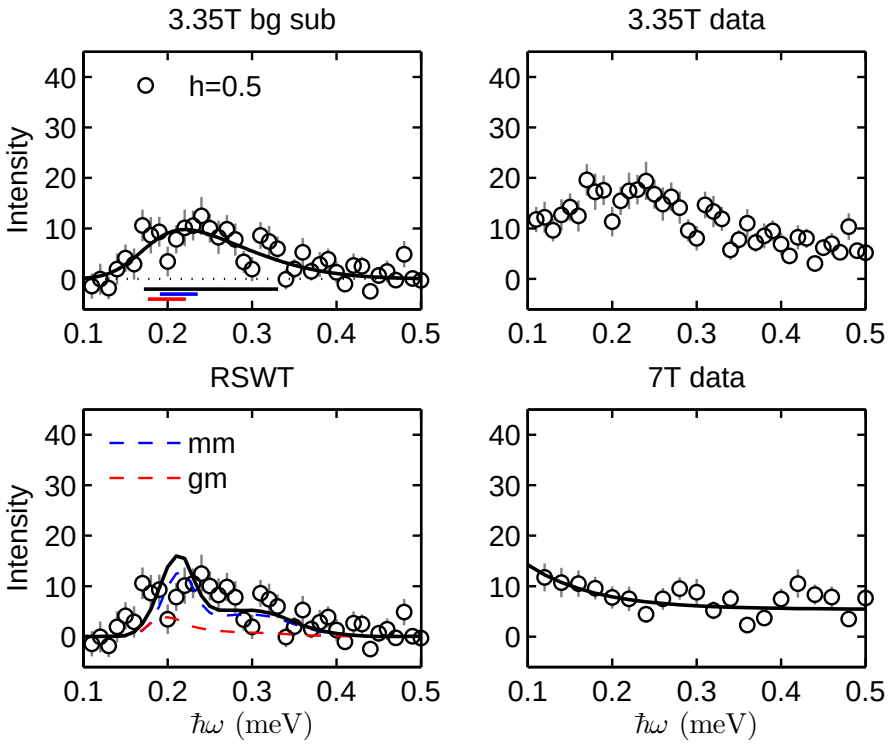

Figure A.17

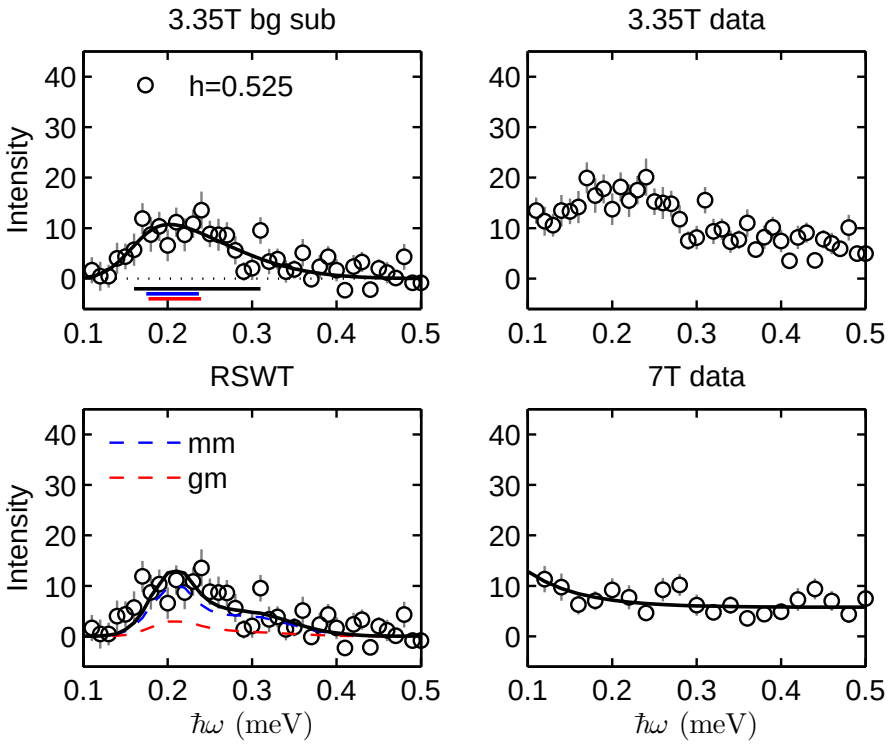

Figure A.18

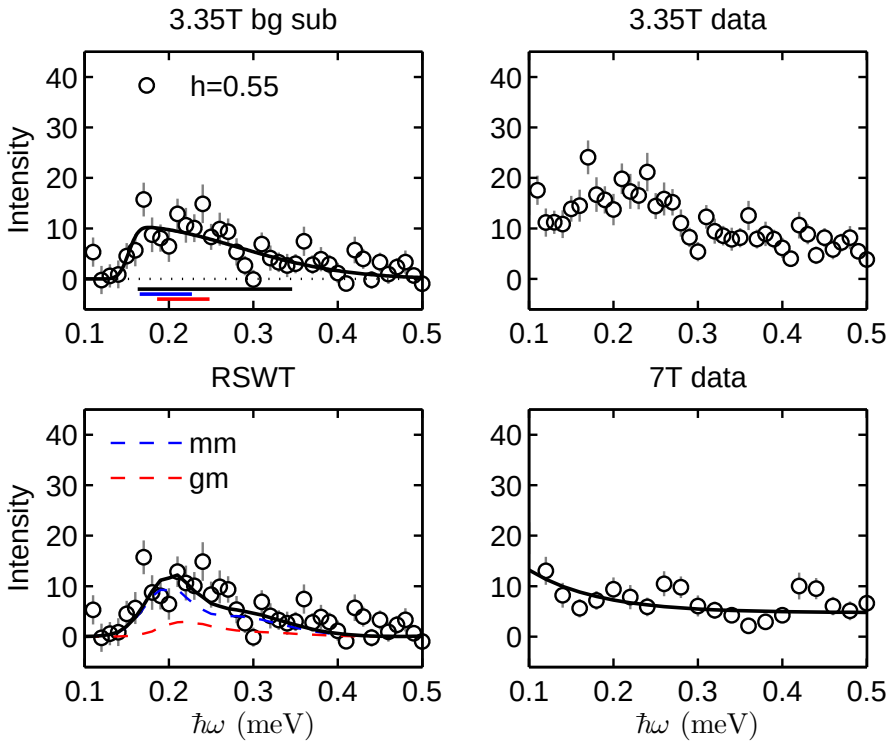

Figure A.19

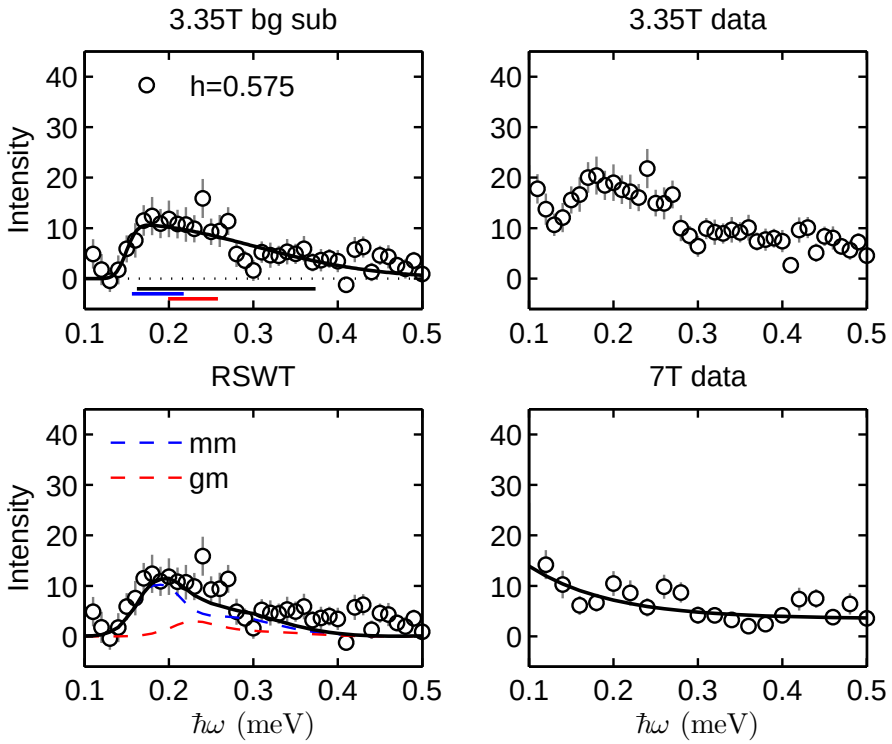

Figure A.20

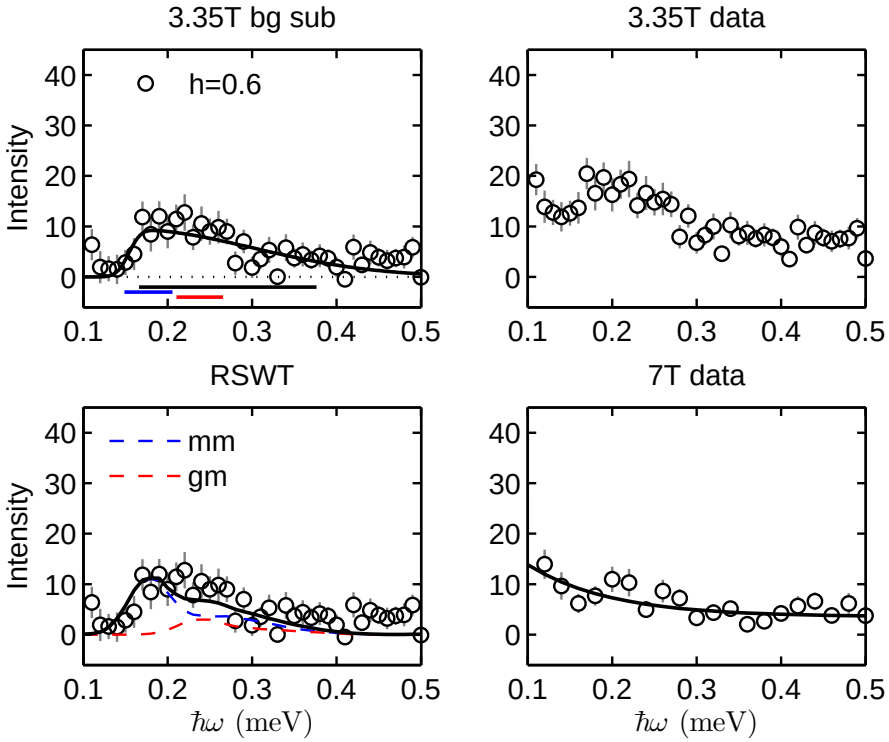

Figure A.21

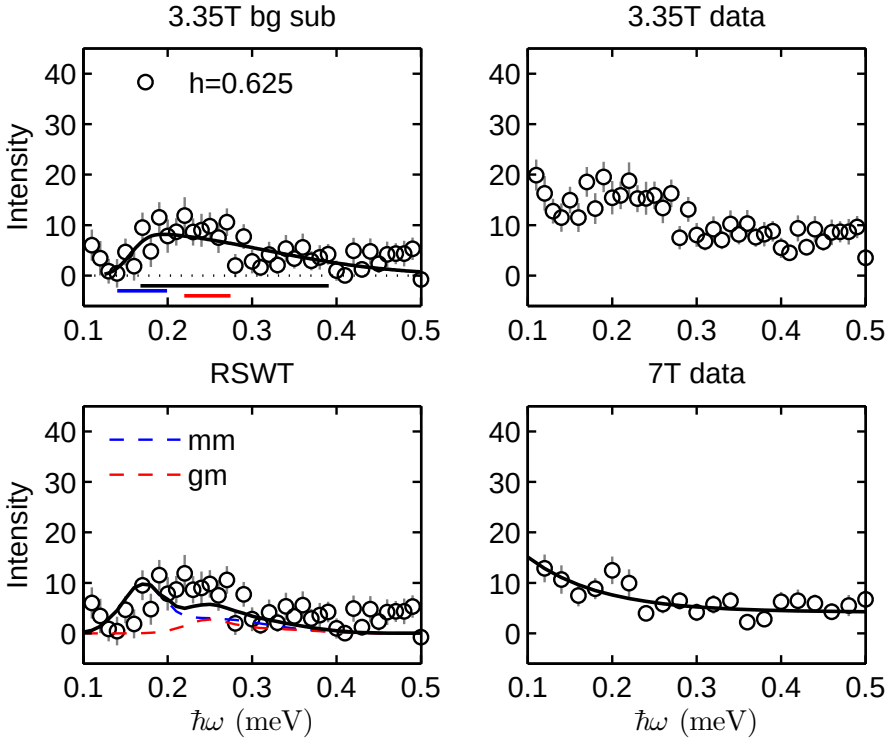

Figure A.22

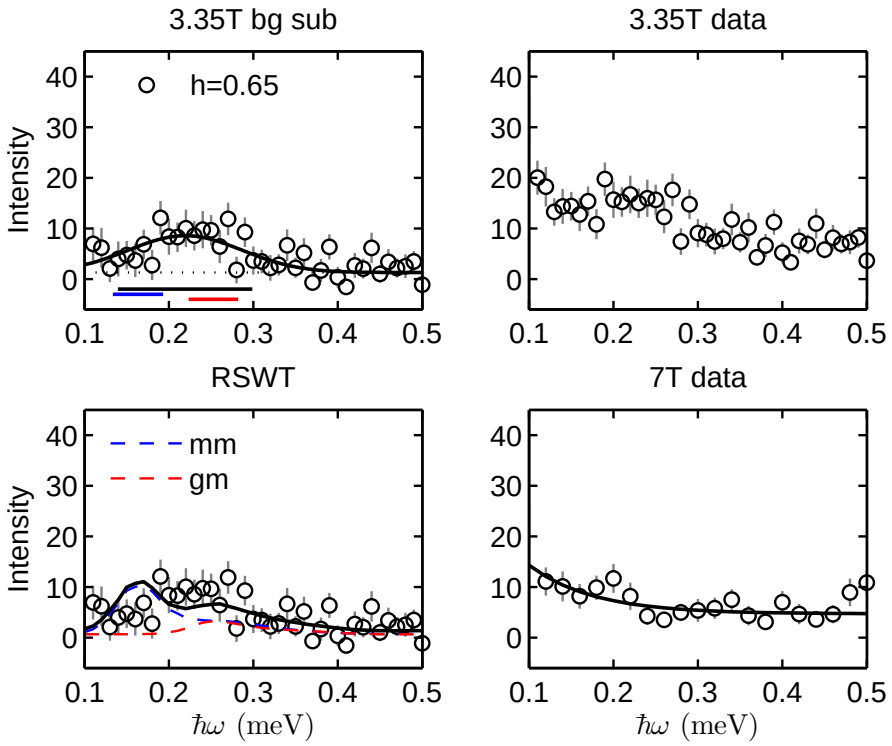

Figure A.23

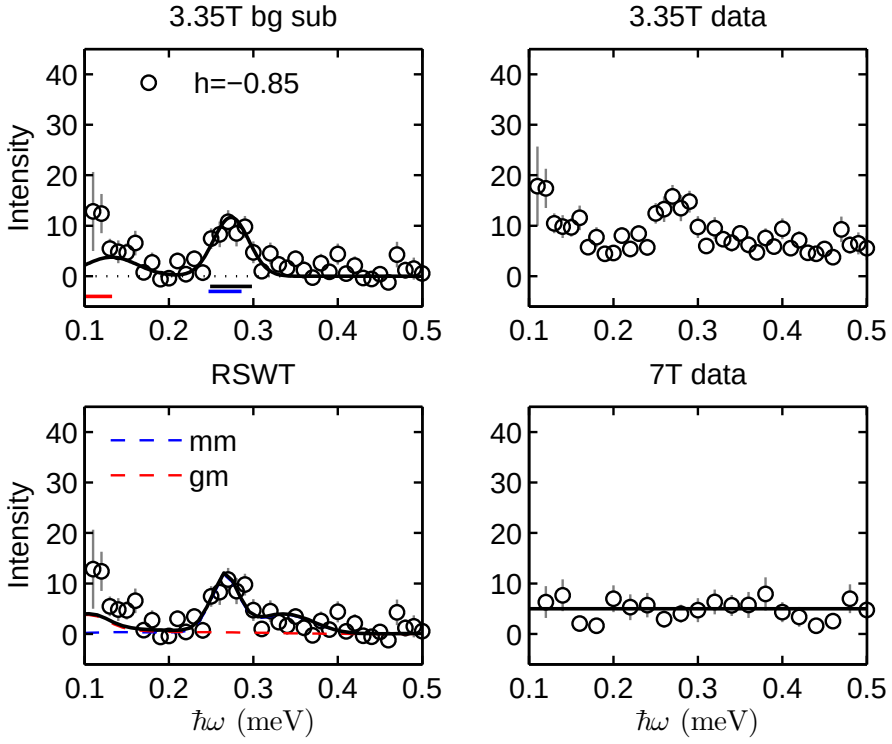

Figure A.24

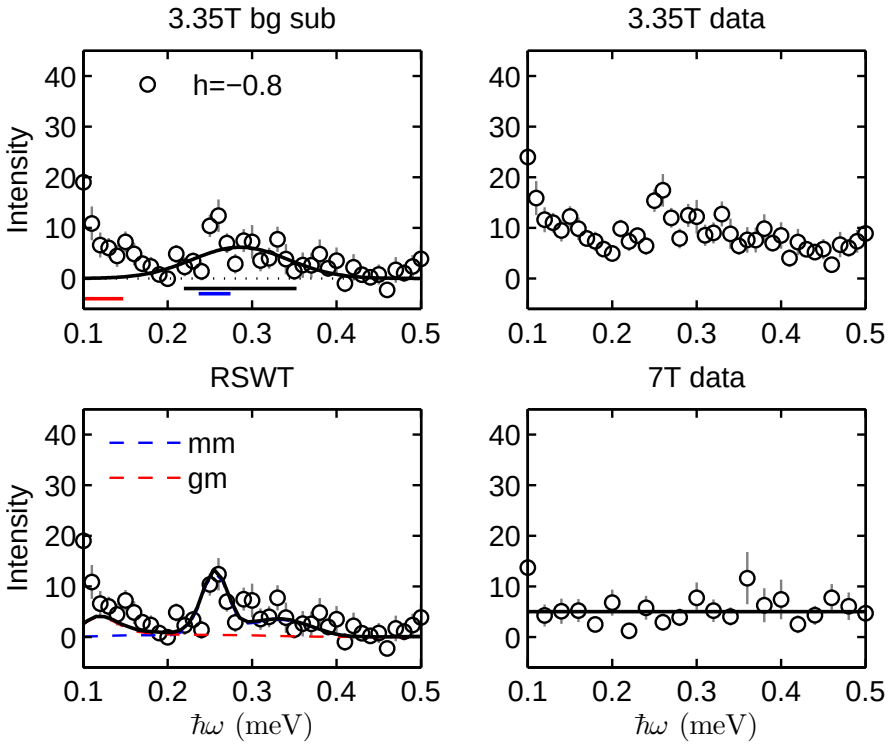

Figure A.25

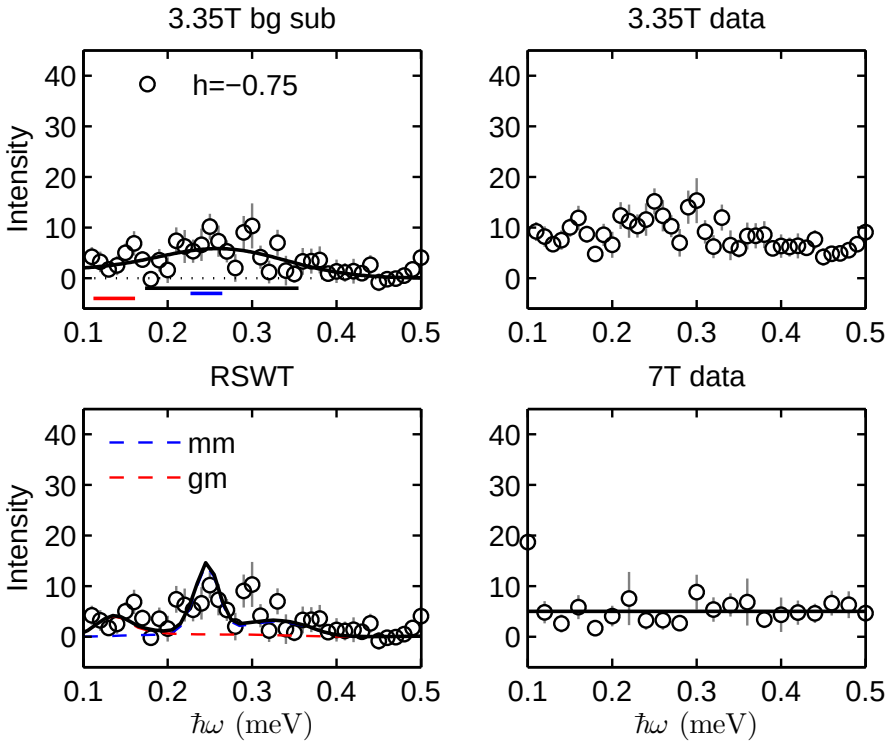

Figure A.26

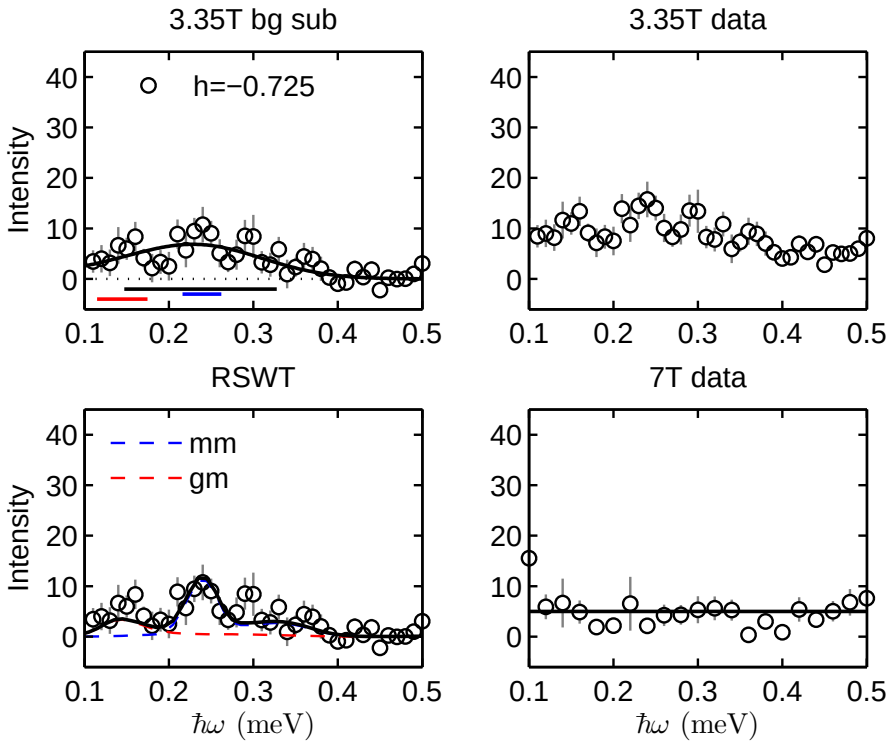

Figure A.27

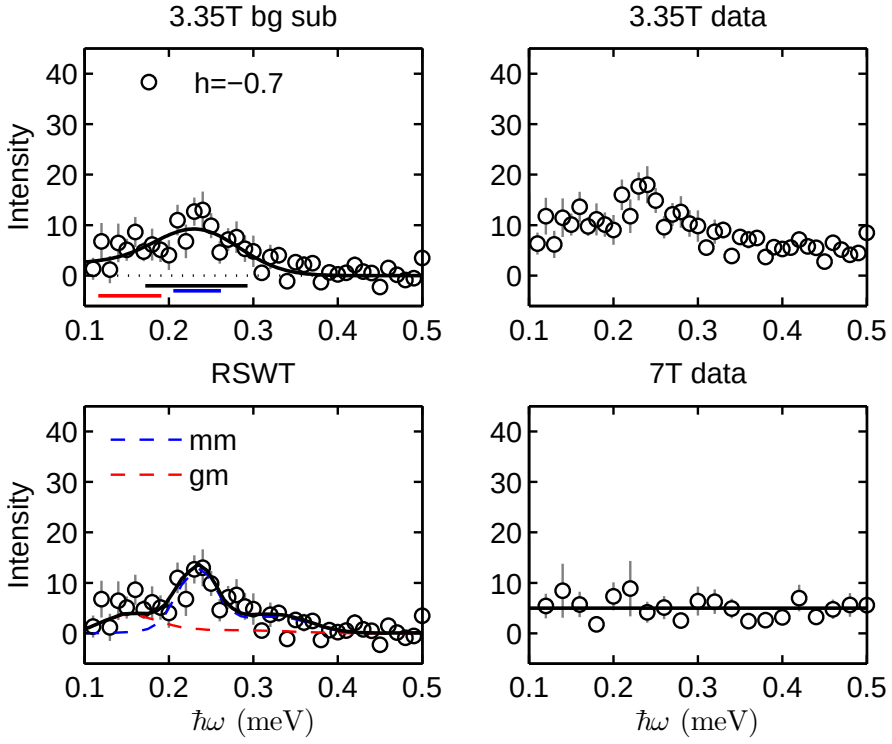

Figure A.28

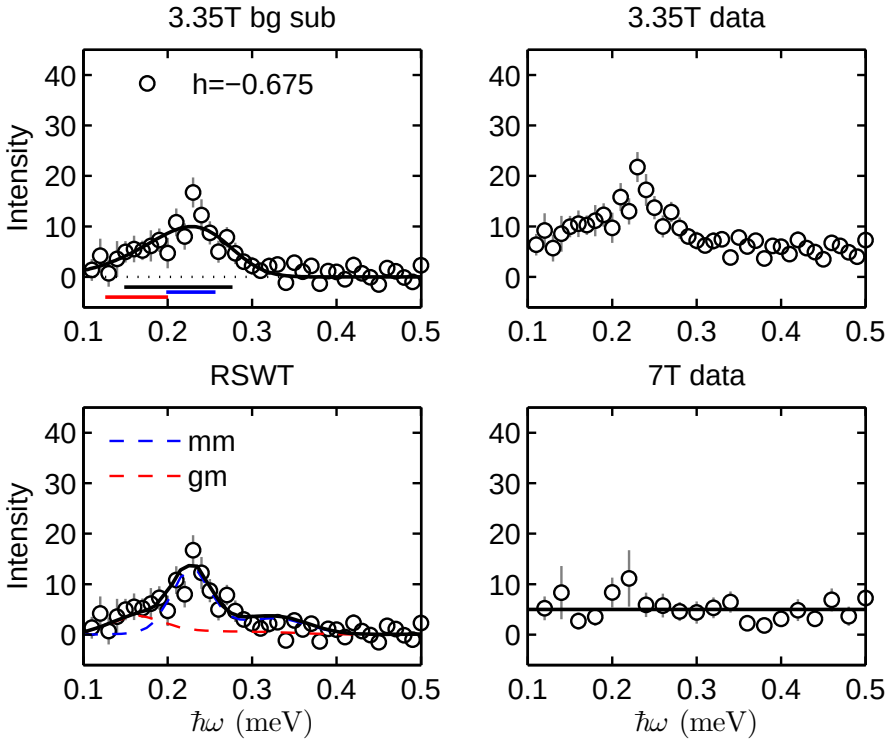

Figure A.29

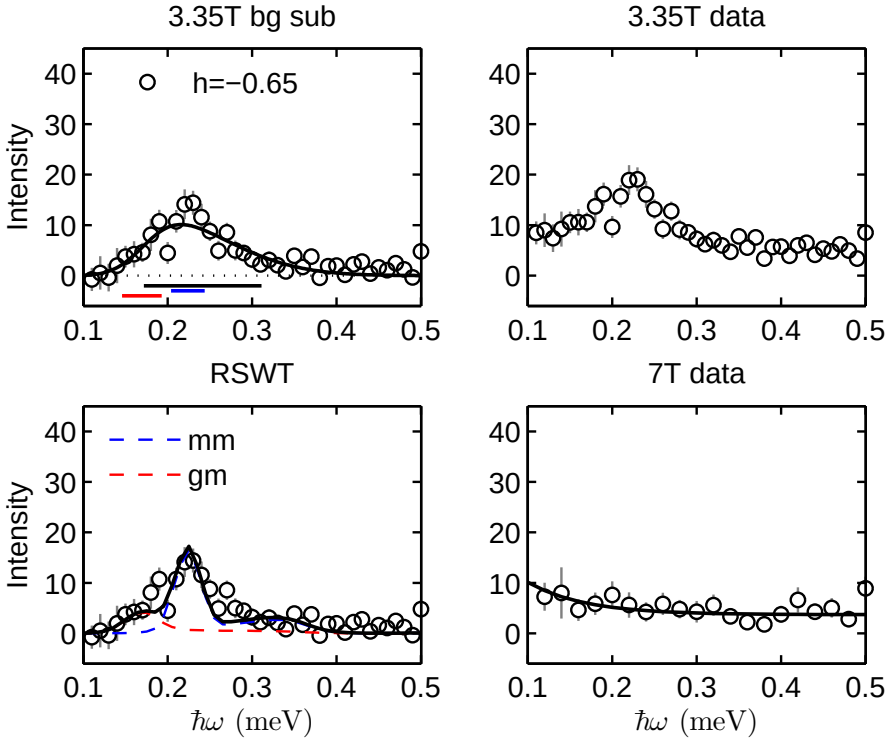

Figure A.30

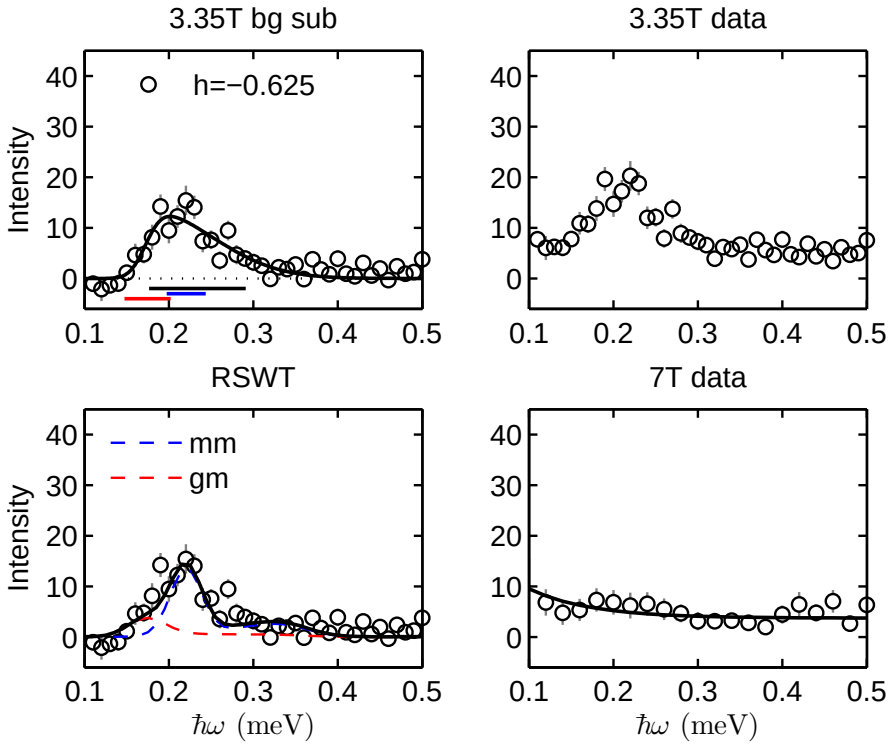

Figure A.31

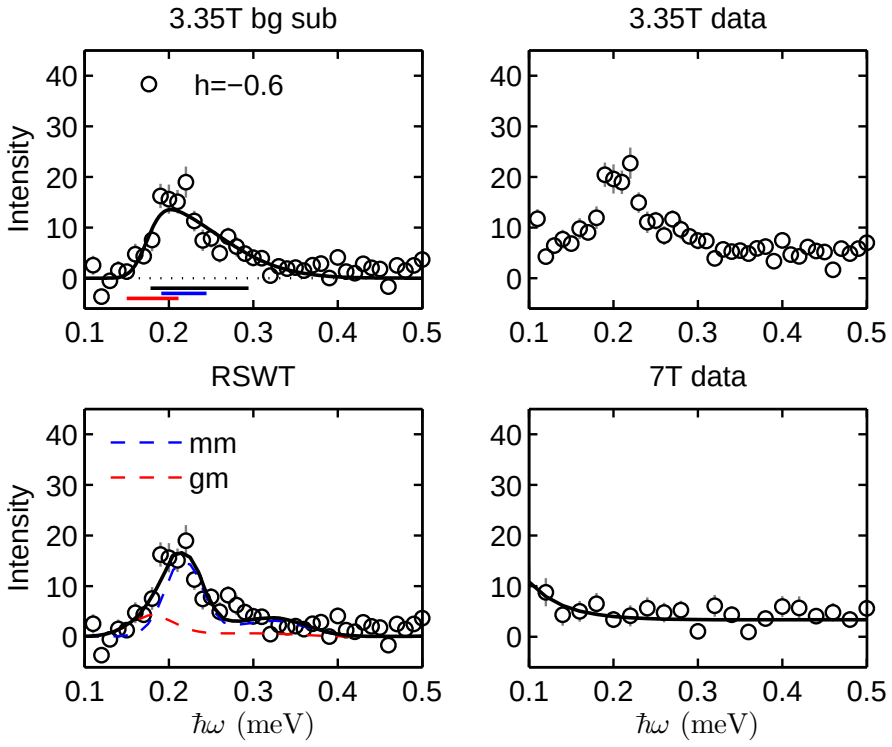

Figure A.32

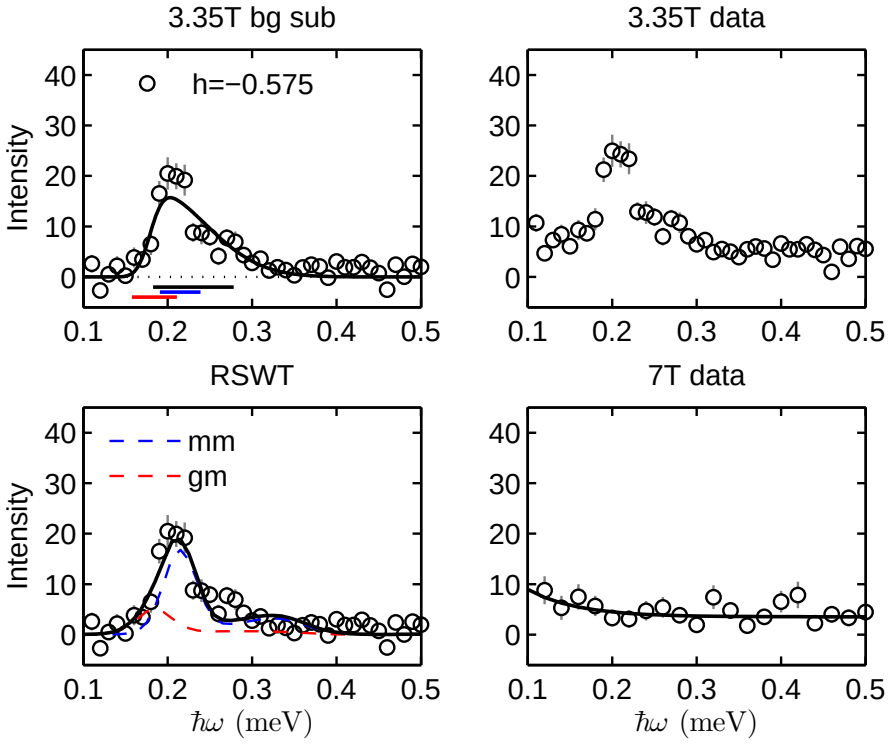

Figure A.33

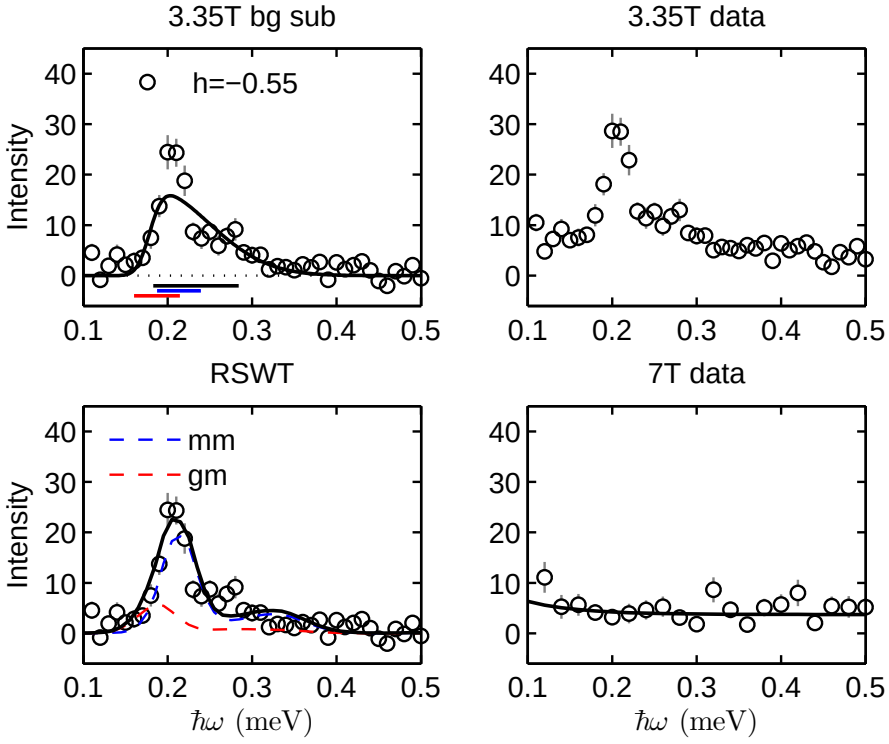

Figure A.34

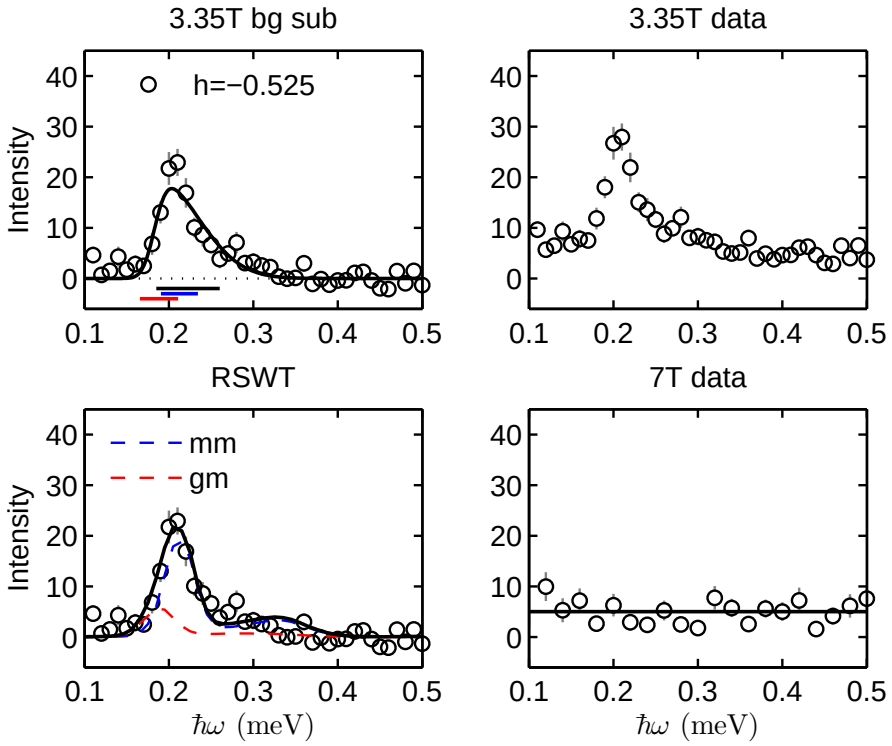

Figure A.35

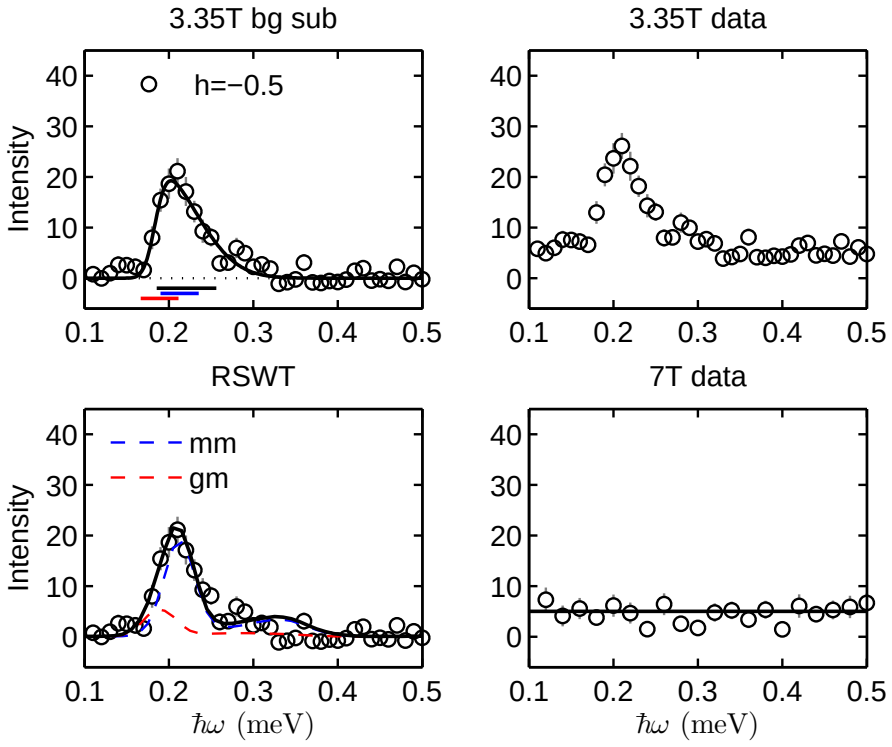

Figure A.36

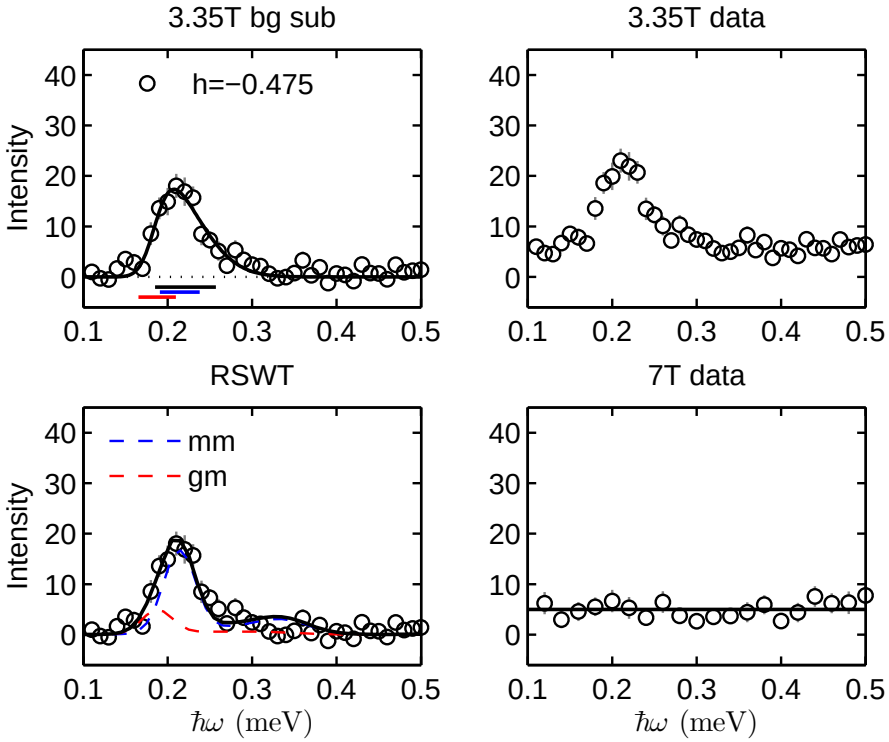

Figure A.37

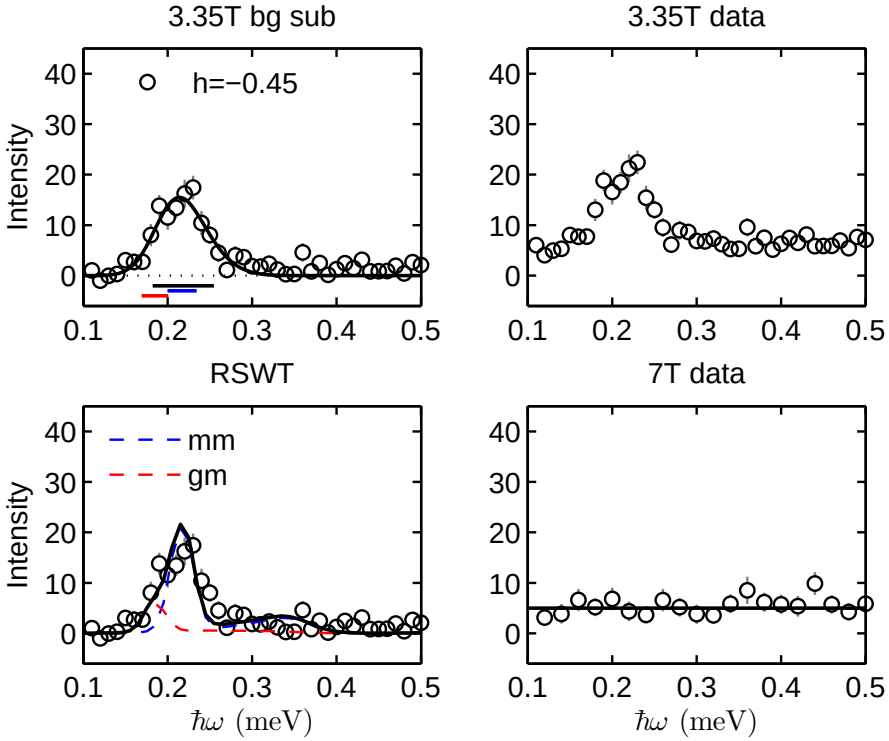

Figure A.38

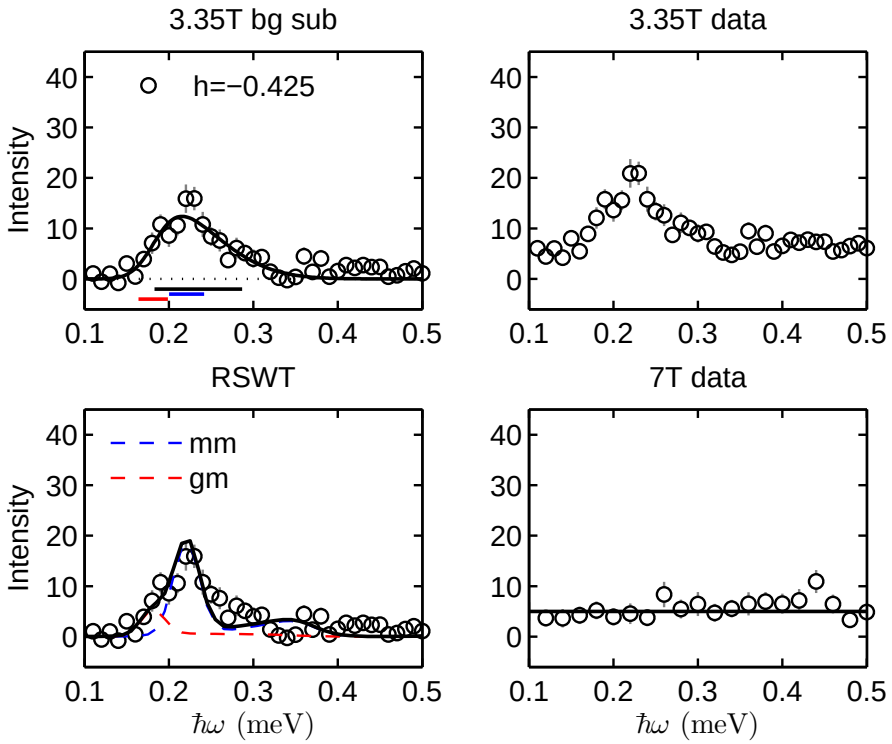

Figure A.39

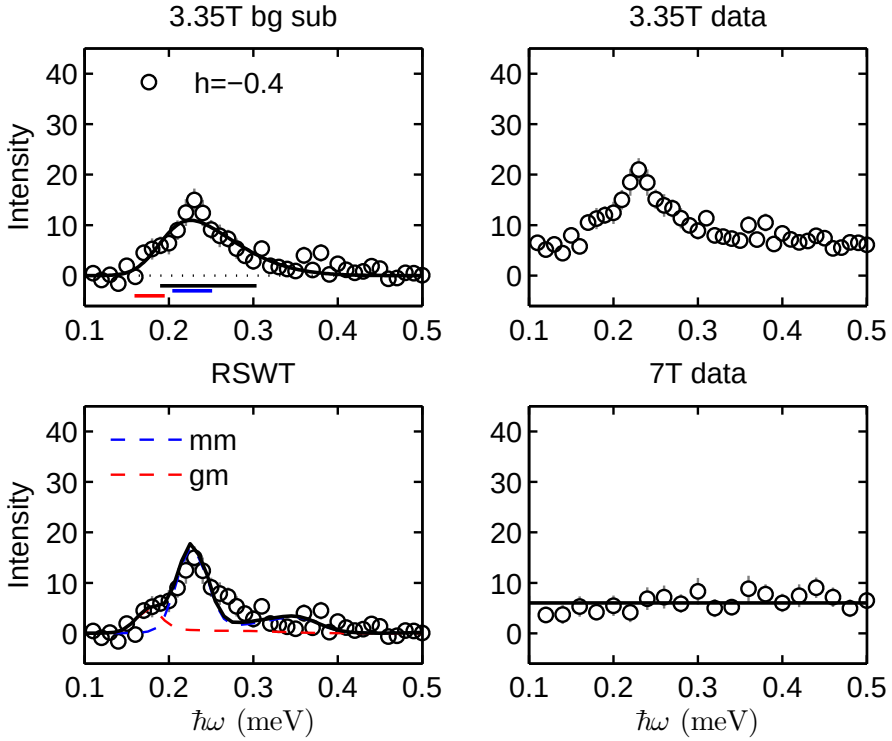

Figure A.40

Appendix B

Curvature of Triplet Dispersion in Y_2BaNiO_5

In this appendix we show how we derived the local curvature at the triplet dispersion minimum for Y_2BaNiO_5 considering the analytic form used by Xu et al. [117] to fit their inelastic neutron scattering data.

The one-magnon dispersion is given by

$$E^2 = \Delta^2 + v^2 sin^2 q + A cos^2(q/2) \tag{B.1}$$

where Δ is the value of the Haldane gap, q is the wave vector transfer along the chain direction, v is the spin-wave velocity and $A = 170$ meV^2 is a fixed constant. The local curvature of the dispersion at the triplet dispersion minimum energy $E_{min} = \Delta$, at $q = \pi$ is given by the second order derivative of the energy with respect to the wave vector transfer q. Given the above dispersion it follows that

$$\begin{aligned} 2E\frac{dE}{dq} &= v^2 \cdot 2sin(q) \cdot cos(q) - 2Acos(q/2)sin(q/2) \cdot \frac{1}{2} \\ &= v^2 sin(2q) - \frac{A}{2} sin(q) \end{aligned} \tag{B.2}$$

and

$$\begin{aligned}\frac{dE}{dq}\Big(2E\frac{dE}{dq}\Big) &= 2\Big(E\frac{d^2E}{dq^2}+\Big(\frac{dE}{dq}\Big)^2\Big)\\ &= v^2\cdot 2\cos(2q)-\frac{A}{2}\cos(q)\end{aligned} \tag{B.3}$$

At $q=\pi$, $dE/dq=0$ and $E=\Delta$ so it follows that

$$2\Delta\frac{d^2E}{dq^2}=2v^2+\frac{A}{2} \tag{B.4}$$

and

$$\frac{d^2E}{dq^2}\Big|_{q=\pi}=\frac{v^2+A/4}{\Delta} \tag{B.5}$$

To get the curvature in units of meVÅ^2, we multiply the curvature with the square of the lattice parameter in the chain direction a. The curvature is then given as

$$\frac{d^2E}{dq^2}=\frac{a^2(v^2+A/4)}{\Delta} \tag{B.6}$$

For the most accurate values know for Y_2BaNiO_5, a = 3.754 Å, Δ = 7.6 meV, v = 60.5 ± 1.5 meV and A = 170 meV^2, the curvature is given by

$$\frac{d^2E}{dq^2}=6866\pm 336.5\ \text{meVÅ}^2 \tag{B.7}$$

Bibliography

[1] T. H. Han, J. S. Helton, S. Chu, D. G. Nocera, J. A. Rodriguez-Rivera, C. L. Broholm, and Y. S. Lee. Fractionalized excitations in the spin-liquid state of a kagome-lattice antiferromagnet. *Nature*, 492:406–410, 2012.

[2] N. B. Christensen, H. M. Rønnow, D. F. McMorrow, A. Harrison, T. G. Perring, M. Enderle, R. Coldea, L. P. Regnault, and G. Aeppli. Quantum dynamics and entanglement of spins on a square lattice. *Proceedings of the National Academy of Sciences of the United States of America*, 104:15264–15269, 2007.

[3] I. A. Zaliznyak, H. Woo, T. G. Perring, C. L. Broholm, C. D. Frost, and H. Takagi. Spinons in the Strongly Correlated Copper Oxide Chains in $SrCuO_2$. *Phys. Rev. Lett.*, 93(8):087202, 2004.

[4] B. Lake, D. A. Tennant, C. D. Frost, and S. E. Nagler. Quantum criticality and universal scaling of a quantum antiferromagnet. *Nature Materials*, 4:329–334, 2005.

[5] B. Dalla Piazza, M. Mourigal, N. B. Christensen, G. J. Nilsen, P. Tregenna-Piggott, T. G. Perring, M. Enderle, D. F. McMorrow, D. A. Ivanov, and H. M. Rønnow. Fractional excitations in the square-lattice quantum antiferromagnet. *Nature Physics*, 11:62–68, 2014.

[6] S. T. Bramwell and M. J. P. Gingras. Spin Ice State in Frustrated Magnetic Pyrochlore Materials. *Science*, 294(5546):1495–1501, 2001.

[7] S. T. Bramwell, S. R. Giblin, S. Calder, R. Aldus, D. Prabhakaran, and T. Fennell. Measurement of the charge and current of magnetic monopoles in spin ice. *Nature*, 461:956–959, 2009.

[8] M. E. Zhitomirsky and A. L. Chernyshev. Instability of Antiferromagnetic Magnons in Strong Fields. *Phys. Rev. Lett.*, 82(22):4536–4539, 1999.

[9] O. Syljuåsen. Numerical evidence for unstable magnons at high felds in the Heisenberg antiferromagnet on the square lattice. *Phys. Rev. B*, 78:180413, 2008.

[10] A. Lüscher and A. M. Läuchli. Exact diagonalization study of the antiferromagnetic spin-1/2 Heisenberg model on the square lattice in a magnetic field. *Phys. Rev. B*, 79:195102, 2009.

[11] M. E. Zhitomirsky and A. L. Chernyshev. Colloquium: Spontaneous magnon decays. *Rev. Mod. Phys.*, 85:219–243, 2013.

[12] M. den Nijs and K. Rommelse. Preroughening transitions in crystal surfaces and valence-bond phase in quantum spin chains. *Phys. Rev. B*, 40(7):4709–4734, 1989.

[13] J. H. van Vleck. *The theory of electric and magnetic susceptibilities*. Clarendon Press, 1932.

[14] S. Blundell. *Magnetism in Condensed Matter*. Oxford University Press, 2001.

[15] J. M. D. Coey. *Magnetism and Magnetic Materials*. Cambridge University Press, 2010.

[16] C. Kittel. *Introduction to Solid State Physics*. John Wiley & Sons, 2005.

[17] L. Braicovich, L. Ament, V. Bisogni, F. Forte, C. Aruta, G. Balestrioni, N. Brookes, G. de Luca, P. Medaglia, F. Miletto Granozio, M. Radovic, M. Salluzzo, J. van den Brink, and G. Ghiringhelli. Dispersion of Magnetic Excitations in the Cuprate La_2CuO_4 and $CaCuO_2$ Compounds Measured Using Resonant X-Ray Scattering. *Phys. Rev. Lett.*, 102:167401, 2009.

[18] L. Ament, G. Ghiringhelli, M. Moretti Sala, L. Braicovich, and J. van den Brink. Theoretical demonstration of how magnetic excitations in cuprate compounds can be determined using resonant inelastic x-ray scattering. *Phys. Rev. Lett.*, 103:117003, 2009.

[19] C. Donnerer, M. C. Rahn, M. Moretti Sala, J. G. Vale, D. Pincini, J. Strempfer, M. Krisch, D. Prabhakaran, A. T. Boothroyd, and D. F. McMorrow. All-in-all-Out Magnetic Order and Propagating Spin Waves in $Sm_2Ir_2O_7$. *Phys. Rev. Lett.*, 117:037201, 2016.

[20] M. Vojta. Quantum phase transitions. *Rep. Prog. Phys.*, 66:2069–2110, 2003.

[21] T. Roscilde, P. Verrucchi, A. Fubini, S. Haas, and V. Tognetti. Studying Quantum Spin Systems through Entanglement Estimators. *Phys. Rev. Lett.*, 93:167203, 2004.

[22] S. M. Giampaolo, G. Adesso, and F. Illuminati. Theory of Ground State Factorization in Quantum Cooperative Systems. *Phys. Rev. Lett.*, 100:197201, 2008.

[23] J. Kurmann, H. Thomas, and G. Müller. Antiferromagnetic Long-Range Order in the Anisotropic Quantum Spin Chain. *Physica*, 112A:235–255, 1982.

[24] S. W. Lovesey. *The Theory of Neutron Scattering from Condensed Matter*. Oxford University Press, 1986.

[25] G. L. Squires. *Introduction to the Theory of Thermal Neutron Scattering*. Dover Publications, 1978.

[26] C. Rüegg. *Neutron Scattering Investigation of Quantum Phase Transitions in the Dimer Spin Systems* $TlCuCl_3$ *and* NH_4CuCl_3. PhD thesis, ETH Zürich, 2005.

[27] Institut Laue-Langevin, Grenoble, France. `http://www.ill.eu/sites/ccsl/ffacts/ffachtml.html`.

[28] ETH Zürich. `http://www.neutron.ethz.ch/research/resources/formafactor`.

[29] A. J. Freeman and J. P. Descalaux. Dirac-Fock studies of some electronic properties of rare-earth ions. *Journal of Magnetis*, 12:11–21, 1979.

[30] R. M. White. *Quantum Theory of Magnetism: Magnetic Properties of Materials*. Springer, 2010.

[31] M. J. Cooper and R. Nathans. The Resolution Function in Neutron Diffractometry I. The Resolution Function of a Neutron Diffractometer and its Application to Phonon Measurements. *Acta Crystallographica*, 23:357, 1967.

[32] N. J. Chesser and J. D. Axe. Derivation and Experimental Verification of the Normalized Resolution Function for Inelastic Neutron Scattering. *Acta Crystallographica*, A(29):160, 1972.

[33] M. Popovici. On the Resolution of Slow-Neutron Spectrometers. IV. The Triple-Axis Spectrometer Resolution Function, Spatial Effects Included. *Acta Crystallographica*, A(31):507, 1975.

[34] F. Mezei. Neutron Spin Echo: A New Concept in Polarised Thermal Neutron Techniques. *Zeitschrift für Physik*, (255):146–160, 1972.

[35] F. Mezei. *Lecture Notes in Physics : Neutron Spin Echo*. Springer-Verlag, 1980.

[36] R. Gähler and R. Golub. A High Resolution Neutron Spectrometer for Quasielastic Scattering on the Basis of Spin Echo and Magnetic Resonance. *Zeitschrift für Physik B Condensed Matter*, (65):269, 1987.

[37] P. W. Anderson. An approximate quantum theory of the antiferromagnetic ground state. *Phys. Rev.*, 86:694–701, Jun 1952.

[38] P. W. Anderson. Limits on the energy of the antiferromagnetic ground state. *Phys. Rev.*, 83:1260, 1951.

[39] H. Bethe. On the theory of metals. I. Eigenvalues and eigenfunctions of the linear atom chain. *Zeitschrift für Physik*, 71:205–226, 1931.

[40] F. J. Dyson, E. H. Lieb, and B. Simon. Phase Transitions in Quantum Spin Systems with Isotropic and Nonisotropic Interactions. *Journal of Statistical Physics*, 18(4):335–383, 1978.

[41] T. Kennedy, E. H. Lieb, and B. S. Shastry. Existence of Néel order in some spin-1/2 Heisenberg antiferromagnets. *Journal of Statistical Physics*, 53:1019–1030, 1988.

[42] E. Manousakis. The spin-1/2 Heisenberg antiferromagnet on a square lattice and its applications to the cuprous oxides. *Rev. Mod. Phys.*, 63(1):1–62, 1991.

[43] P. W. Anderson. Resonating valence bond: a new kind of insulator ? *Mat. Res. Bull.*, 8:153–160, 1973.

[44] N. D. Mermin and H. Wagner. Absence of Ferromagnetism or Antiferromangetism in One- or Two-Dimensional Isotropic Heisenberg Models. *Phys. Rev. Lett.*, 17:1133–1136, 1966.

[45] R. Kubo. The spin-wave theory of antiferromagnetics. *Phys. Rev.*, 87:568–580, Aug 1952.

[46] F. J. Dyson. General Theory of Spin-Wave Interactions. *Physical Review*, 102(5):1217–1230, 1956.

[47] T. Oguchi. Theory of spin-wave interactions in ferro- and antiferromagnetism. *Phys. Rev.*, 117(1):117–123, 1960.

[48] J. Igarashi. 1/S expansion for thermodynamic quantities in a two-dimensional Heisenberg antiferromagnet at zero temperature. *Phys. Rev. B*, 46(17):10763–10771, 1992.

[49] C.M. Canali, S.M. Girvin, and M. Wallin. Spin-wave velocity renormalization in the two-dimensional Heisenberg antiferromagnet at zero temperature. *Phys. Rev. B*, 45(17):10131–10134, 1992.

[50] C. M. Canali and M. Wallin. Spin-spin correlation functions for the square-lattice Heisenberg antiferromagnet at zero temperature. *Phys. Rev. B*, 48(5):3264–3280, 1993.

[51] A. Auerbach and D. P. Arovas. Spin Dynamics in the Square-Lattice Antiferromagnet. *Phys. Rev. Lett.*, 61(5):617–620, 1988.

[52] R. R. P. Singh. Thermodynamic parameters of the T=0, spin-1/2 square-lattice Heisenberg antiferromagnet. *Phys. Rev. B*, 39(13):9760–9763, 1989.

[53] R. R. P. Singh and M. P. Gelfand. Spin-wave excitation spectra and spectral weights in square lattice antiferromagnets. *Phys. Rev. B*, 52(22):R15695–R15698, 1995.

[54] J. D. Reger and A. P. Young. Monte Carlo simulations of the spin-1/2 Heisenberg antiferromagnet on a square lattice. *Phys. Rev. B*, 37(10):5978–5981, 1988.

[55] A. W. Sandvik and R. R. P. Singh. High-Energy Magnon Dispersion and Multimagnon Continuum in the Two-Dimensional Heisenberg Antiferromagnet. *Phys. Rev. Lett.*, 86(3):528–531, 2001.

[56] S. Chakravarty, B. I. Haperin, and D. R. Nelson. Two-dimensional quantum Heisenberg antiferromagnet at low temperatures. *Phys. Rev. B*, 39(4):2344–2371, 1989.

[57] W. Zheng, J. Oitmaa, and C. J. Hamer. Series studies of the spin-1/2 Heisenberg antiferromagnet at $T = 0$: Magnon dispersion and structure factors. *Phys. Rev. B*, 71:184440, 2005.

[58] A. V. Syromyatnikov. Spectrum of short-wavelenght magnons in a two-dimensional quantum Heisenberg antiferromagnet on a square lattice: third order expansion in 1/S. *J. Phys. Cond. Mat.*, 22(216003):1–7, 2010.

[59] O. F. Syljuåsen and H. M. Rønnow. Quantum renormalization of high-energy excitations in the 2D Heisenberg model. *Journal of Physics: Condensed Matter*, 12(25), 2000.

[60] N. B. Christensen. *Neutron scattering studies of two-dimensional antiferromagnetic spin fluctuations in insulating and superconducting S=1/2 systems.* PhD Thesis, Risø National Laboratory, January 2005.

[61] R. Coldea, S. M. Hayden, G. Aeppli, T. G. Perring, C. D. Frost, T. E. Mason, S. W. Cheong, and Z. Fisk. Spin Waves and Electronic Interactions in La_2CuO_4. *Phys. Rev. Lett.*, 86(23):5377–5380, 2001.

[62] Y.J. Kim, A. Aharony, R.J. Birgeneau, F.C. Chou, O. Entin-Wohlman, R.W. Erwin, M. Greven, A.B. Harris, M.A. Kastner, I. Y. Korenblit, Y.S. Lee, and G. Shirane. Ordering due to Quantum Fluctuations in $Sr_2Cu_3O_4Cl_2$. *Phys. Rev. Lett.*, 83(4):852–855, 1999.

[63] H. M. Rønnow, D. F. McMorrow, R. Coldea, A. Harrison, I. D. Youngson, T. G. Perring, G. Aeppli, O. Syljuåsen, K. Lefmann, and C. Rischel. Spin Dynamics of the 2D Spin-1/2 Quantum Antiferromagnet Copper Deuteroformate Tetradeuterate (CFTD). *Phys. Rev. Lett.*, 87(3):037202, 2001.

[64] N. Tsyrulin, T. Pardini, R. R. P. Singh, F. Xiao, P. Link, A. Schneidewind, A. Hiess, C. P. Landee, M. M. Turnbull, and M. Kenzelmann. Quantum Effects

in a Weakly Frustrated S=1/2 Two-Dimensional Heisenberg Antiferromagnet in an Applied Magnetic Field. *Phys. Rev. Lett.*, 102:197201, 2009.

[65] N. Tsyrulin, F. Xiao, A. Schneidewind, P. Link, H. M. Rønnow, J. Gavilano, C. P. Landee, M. M. Turnbull, and M. Kenzelmann. Two-dimensional square-lattice S=1/2 antiferromagnet $Cu(pz)_2(ClO_4)_2$. *Phys. Rev. B*, 81:134409, 2010.

[66] C. M. Ho, V. N. Muthukumar, M. Ogata, and P. W. Anderson. Nature of Spin Excitations in Two-Dimensional Mott Insulators: Undoped Cuprates and Other Materials. *Phys. Rev. Lett.*, 86(8):1626–1629, 2001.

[67] O. F. Syljuåsen and P. A. Lee. Anomalous Spin Excitation Spectrum of the Heisenberg Model in a Magnetic Field. *Phys. Rev. Lett.*, 88(20):207207, 2002.

[68] E. Dagotto and A. Moreo. Zero-temperature properties of the two-dimensional Heisenberg antiferromagnet: A numerical study. *Phys. Rev. B*, 38(7):5087–5090, 1988.

[69] T. Huberman, R. Coldea, R. A. Cowley, D. A. Tennant, R. L. Leheny, R. J. Christianson, and C. D. Frost. Two-magnon excitations observed by neutron scattering in the two-dimensional spin-5/2 Heisenberg antiferromagnet Rb_2MnF_4. *Phys. Rev. B*, 72:014413, 2005.

[70] N. S. Headings, S. M. Hayden, R. Coldea, and T. G. Perring. Anomalous High-Energy Spin Excitations in the High-Tc Superconductor-Parent Antiferromagnet La_2CuO_4. *Phys. Rev. Lett.*, 105:247001, 2010.

[71] D. A. Tennant, R. A. Cowley, S. Nagler, and A. M. Tsvelik. Measurement of the spin-excitation continuum on one-dimensional $KCuF_3$ using neutron scattering. *Phys. Rev. B*, 52(18):13368, 1995.

[72] M. Mourigal, M. Enderle, A. Klöpperpieper, J. S. Caux, A. Stunault, and H. M. Rønnow. Fractional spin excitations in the quantum Heisenberg antiferromagnetic chain . *Nature Physics*, 9:435, 2013.

[73] P. W. Anderson. The Resonating Valence Bond State in La_2CoO_4 and Superconductivity. *Science*, 235, 1987.

[74] P. R. Hammar, D. C. Dender, D. H. Riech, A. S. Albrecht, and C. P. Landee. Magnetic studies of the two-dimensional, S = 1/2 heisenberg antiferromagnets $(5CAP)_2CuCl_4$ and $(5MAP)_2CuCl_4$. *Journal of Applied Physics*, 81(8):4615–4617, 1997.

[75] T. Matsumoto, Y. Miyazaki, A. S. Albrecht, C. P. Landee, M. M. Turnbull, and M. Sorai. Heat Capacities of the S=1/2 Two-Dimensional Heisenberg Antiferromagnet Bis(2-amino-5-chloropyridinium) Tetrabromocuprate(II) $[(5CAP)_2CuBr_4]$ and Its Diamagnetic Analogue $[5CAP_2ZnBr_4]$. *J. Phys. Chem. B*, 104(43):9993–10000, 2000.

[76] F. M. Woodward, A. S. Albrecht, C. M. Wynn, C. P. Landee, and M. M. Turnbull. Two-dimensional S=1/2 Heisenberg antiferromagnets: Synthesis, structure and magnetic properties. *Phys. Rev. B*, 65:144412, 2002.

[77] F. C. Coomer, V. Bondah-Jagalu, K. J. Grant, A. Harrison, G. J. McIntyre, H. M. Rønnow, R. Feyerherm, T. Wand, M. Meisner, D. Visser, and D. F. McMorrow. Neutron diffraction studies of the nuclear and magnetic structures in the S = 1/2 square lattice Heisenberg antiferromagnets $(d_6 - 5CAP)_2CuX_4$ (X = Br and Cl). *Phys. Rev. B*, 75:094424, 2007.

[78] Y. J. Kim, R. J. Birgeneau, F. C. Chou, M. Greven, M. A. Kastner, Y. S. Lee, B. O. Wells, A. Aharony, O. Entin-Wohlman, I. Y. Korenblit, A. B. Harris, R. W. Erwin, and G. Shirane. Neutron scattering study of $Sr_2Cu_3O_4Cl_2$. *Phys. Rev. B*, 64:024435, 2001.

[79] S. S. Staniland, A. Harrison, N. Robertson, K. V. Kamenev, and S. Parsons. Structural and Magnetic Properties of $[BDTA]_2[MCl_4]$ [M = Cu (1), Co(2) and Mn(3)], Revealing an S=1/2 Square-Lattice Antiferromagnet with Weak Magnetic Exchange. *Inorg. Chem.*, 45:5767–5773, 2006.

[80] M. E. Zhitomirsky and T Nikuni. Magnetization curve of a square-lattice Heisenberg antiferromagnet. *Phys. Rev. B*, 57(9):5013–5016, 1998.

[81] M. Mourigal. *Order and Dynamics of Model Quantum Antiferromagnets*. PhD Thesis, Ecole Polytechnique Fédérale de Laussane, 2011.

[82] M. Mourigal, M. E. Zhitomirsky, and A. L. Chernyshev. Field-induced decay dynamics in square-lattice antiferromagnets. *Phys. Rev. B*, 82:144402, 2010.

[83] T. Masuda, S. Kitaoka, S. Takamizawa, N. Metoki, K. Kanedo, K. C. Rule, K. Kiefer, H. Manaka, and H. Nojiri. Instability of magnons in two-dimensional antiferromagnets at high magnetic fields. *Phys. Rev. B*, 81:100402, 2010.

[84] M. E. Zhitomirsky. Spontaneous magnon decays. *Habilitation Thesis, Grenoble University*, 2010.

[85] A. L. Chernyshev and M. E. Zhitomirsky. Hydrodynamic relation in a two-dimensional Heisenberg antiferromagnet in a field. *Phys. Rev. B*, 79:174402, 2009.

[86] A. V. Syromyatnikov. Collective excitations in a two-dimensional antiferromagnet in a strong magnetic field. *Phys. Rev. B*, 79:054413, 2009.

[87] W. T. Fuhrman, M. Mourigal, M. E. Zhitomirsky, and A. L. Chernyshev. Dynamical structure factor of quasi-two-dimensional antiferromagnets in high fields. *Phys. Rev. B*, 85:184405, 2012.

[88] O. Arnold, J. C. Bilheux, J. M. Borreguero, A. Buts, S. I. Campbell, L. Chapon, M. Doucet, N. Draper, R. Ferraz Leal, M. A. Gigg, V. E. Lynch, A. Markvardsen, D. J. Mikkelson, R. L. Mikkelson, R. Miller, K. Palmen, P. Parker, G. Passos, T. G. Perring, P. F. Peterson, S. Ren, M. A. Reuter, A. T. Savici, J. W. Taylor, R. J. Taylor, R. Tolchenov, W. Zhou, and J. Zikovsky. Mantid - Data analysis and visualization package for neutron sscattering and μSR experiments. *Nucl. Instrum. Methods Phys. Res., Sect. A*, 764:156–166, 2014.

[89] R. A. Ewings, A. Buts, M. D. Le, J. van Dujin, I. Bustinduy, and T. G. Perring. HORACE: Software for the analysis of data from single crystal spectoscopy experiments at time-of-flight neutron Instruments. *Nucl. Instrum. Methods Phys. Res. Sect. A*, 834:132–142, 2016.

[90] R. Coldea, D. A. Tennant, K. Habicht, P. Smeibidl, C. Wolters, and Z. Tylczynski. Direct Measurement of the Spin Hamiltonian and Observation of the Condensation of Magnons in the 2D Frustrated Quantum Magnet Cs_2CuCl_4. *Phys. Rev. Lett.*, 88(13):137203, 2002.

[91] T. Holstein and H. Primakoff. Field Dependence of the Intrinsic Domain Magnetization of a Ferromagnet. *Phys. Rev.*, 58:1098–1113, 1940.

[92] C. Yasuda, S. Todo, K. Hukushima, F. Alet, M. Keller, M. Troyer, and H. Takayama. Neel Temperature of Quasi-Low Dimensional Heisenberg Antiferromagnets. *Phys. Rev. Lett.*, 94:217201, 2005.

[93] J. Oh, M.D. Le, J. Jeong, J-H. Lee, H. Woo, W-Y. Song, T.G. Perring, W. J. L. Buyers, S. W. Cheong, and J-G. Park. Magnon Breakdown in a Two-Dimensional Triangular Lattice Heisenberg Antiferromagnet of Multiferroic $LuMnO_3$. *Phys. Rev. Lett.*, 111:257202, 2013.

[94] F. D. M. Haldane. Continuum Dynamics of the 1-D Heisenberg Antiferromagnet: Identification with the O(3) Nonlinear Sigma Model. *Phys. Lett.*, 93A(9):464, 1983.

[95] F. D. M. Haldane. Nonlinear Field Theory of Large-Spin Heisenberg Antiferromagnets: Semiclassically Quantized Solitons of the One-Dimensional Easy-Axis Neél State. *Phys. Rev. Lett.*, 50(15):1153, 1983.

[96] T. Kennedy and H. Tasaki. Hidden Z_2XZ_2 symmetry breaking in Haldane-gap antiferromagnets. *Phys. Rev. B*, 45(1):304–307, 1992.

[97] G. Xu, C. L. Broholm, Y. A. Soh, G. Aeppli, J. F. DiTusa, Y. Chen, M. Kenzelmann, C. D. Frost, T. Ito, K. Oka, and H. Takagi. Mesoscopic Phase Coherence in a Quantum Spin Fluid. *Science*, 317:1049, 2007.

[98] U. Schollwöck, J. Richter, D. J. J. Farnell, and R. F. Bishop. *Quantum Magnetism*. Lecture Notes on Physics. Springer, 2004.

[99] L. D. Faddeev and L. A. Takhtajan. What is the spin of a spin wave ? *Phys. Lett.*, 85A(6,7):375–377, 1981.

[100] J. des Cloizeaux and J. J. Pearson. Spin-Wave Spectrum of the Antiferromagnetic Linear Chain. *Phys. Rev.*, 128(5):2131, 1962.

[101] D. A. Tennant, T. G. Perring, R. A. Cowley, and S. E. Nagler. Unbound Spinons in the S=1/2 Antiferromagnetic Chain $KCuF_3$. *Phys. Rev. Lett.*, 70(25):4003, 1993.

[102] A. C. Walters, T. G. Perring, J. S. Caux, A. T. Savici, G. D. Gu, C. C. Lee, W. Ku, and I. A. Zaliznyak. Effect of covalent bonding on magnetism and the

missing neutron intensity in copper oxide compounds. *Nature Physics*, 5:867, 2009.

[103] S. R. White and I. Affleck. Spectral function for the S=1 Heisenberg antiferromagnetic chain. *Phys. Rev. B*, 77:134437, 2008.

[104] M. P. Nightingale and H. W. J. Blöte. Gap of the linear spin-1 Heisenberg antiferromagnet: A Monte Carlo calculation. *Phys. Rev. B*, 33(1):659–661, 1986.

[105] S. R. White and D. A. Huse. Numerical renormalization-group study of the low-lying eigenstates of the antiferromagnetic S=1 Heisenberg chain. *Phys. Rev. B*, 48(6):3844–3852, 1993.

[106] E. S. Sørensen and I. Affleck. Large-Scale Numerical Evidence for Bose Condensation in the S=1 Antiferromagnetic Chain in a Strong Field. *Phys. Rev. Lett.*, 71(10):1633–1636, 1993.

[107] O. Golinelli, T. Jolicoeur, and R. Lacaze. Finite-lattice extrapolations for a Haldane-gap antiferromagnet. *Phys. Rev. B*, 50(5):3037–3044, 1994.

[108] I. Affleck, T. Kennedy, E. H. Lieb, and H. Tasaki. Rigorous Results on Valence-Bond Ground State in Antiferromagnets. *Phys. Rev. Lett.*, 59(7):799–802, 1987.

[109] S. H. Glarum, S. Geschwind, K. M. Lee, M. L. Kaplan, and J. Michel. Observation of Fractional Spin S=1/2 on Open Ends of S=1 Linear Antiferromagnetic Chains: Nonmagnetic Doping. *Phys. Rev. Lett.*, 67(12):1614–1617, 1991.

[110] F. Tedoldi, R. Santachiara, and M. Horvatić. ^{89}Y NMR Imaging of the staggered magnetization in the doped Haldane chain $Y_2BaNi_{1-x}Mg_xO_5$. *Phys. Rev. Lett.*, 83(2):412–415, 1999.

[111] M. Kenzelmann, G. Xu, I. A. Zaliznyak, C. L. Broholm, J. F. DiTusa, G. Aeppli, T. Ito, K. Oka, and H. Takagi. Structure of End State for a Haldane Spin Chain. *Phys. Rev. Lett.*, 90(8):087202, 2003.

[112] U. Schollwöck, T. Jolicoeur, and T. Garel. Onset of incommensurability at the valence-bond-solid point in the S=1 quantum spin chain. *Phys. Rev. B*, 53(6):3304–3311, 1996.

[113] O. Golinelli, T. Jolicoeur, and R. Lacze. Haldane gaps in a spin-1 Heisenberg chain with easy-plane single-ion anisotropy. *Phys. Rev. B*, 45(17):9798–9805, 1992.

[114] O. Golinelli, T. Jolicoeur, and R. Lacaze. Dispersion of magnetic excitations in a spin-1 chain with easy-plane anisotropy. *Phys. Rev. B*, 46(17):10854–10857, 1992.

[115] O. Golinelli, T. Jolicoeur, and R. Lacaze. The magnetic field behaviour of a Haldane-gap antiferromagnet. *J. Phys. Cond. Mat.*, 5:7847–7858, 1993.

[116] S. Ma, C. L. Broholm, and D. H. Reich. Dominance of Long-Lived Excitations in the Antiferromagnetic Spin-1 Chain NENP. *Phys. Rev. Lett.*, 69(24):3571–3574, 1992.

[117] G. Xu, J. F. DiTusa, T. Ito, K. Oka, H. Takagi, C. L. Broholm, and G. Aeppli. Y_2BaNiO_5: A nearly ideal realization of the S=1 Heisenberg chain with antiferromagnetic interactions. *Phys. Rev. B*, 54(10):6827–6830, 1996.

[118] W. J. L. Buyers, R. M. Morra, R. L. Armstrong, M. J. Hogan, P. Gerlach, and K. Hirakawa. Experimental Evidence for the Haldane Gap in a Spin-1, Nearly Isotropic, Antiferromagnetic Chain. *Phys. Rev. Lett.*, 56(4):371–374, 1986.

[119] R. M. Morra, W. J. L. Buyers, R. L. Armstrong, and K. Hirakawa. Spin dynamics and the Haldane gap in the spin-1 quasi-one-dimensional antiferromagnet $CsNiCl_3$. *Phys. Rev. B*, 38(1):543–555, 1988.

[120] M. Kenzelmann, R. A. Cowley, W. J. L. Buyers, Z. Tun, R. Coldea, and M. Enderle. Properties of Haldane excitations and multiparticle states in the antiferromagnetic spin-1 chain compound $CsNiCl_3$. *Phys. Rev. B*, 66:024407, 2002.

[121] I. A. Zaliznyak, S. H. Lee, and S. V. Petrov. Continuum in the Spin-Excitation Spectrum of a Haldane Chain Observed by Neutron Scattering in $CsNiCl_3$. *Phys. Rev. Lett.*, 87(1):017202, 2001.

[122] L. P. Regnault, J. Rossat-Mignod, J. P. Renard, M. Verdauger, and C. Vettier. Magnetic excitations and fluctuations in quasi-Heisenberg antiferromagnetic chains. *Physica B: Condensed Matter (Amsterdam, Netherlands)*, (156 & 157):247–253, 1989.

[123] M. Date and K. Kindo. Elementary Excitation in the Haldane State. *Phys. Rev. Lett.*, 65(13):1659–1662, 1990.

[124] L. P. Regnault, I. Zaliznyak, J. P. Renard, and C. Vettier. Inelastic neutron scattering study of the spin dynamics in the Haldane-gap system $Ni(C_2H_8N_2)_2NO_2ClO_4$. *Phys. Rev. B*, 50(13):9174–9187, 1994.

[125] H. Mutka, J. L. Soubeyroux, G. Bourleaux, and P. Colombet. Support for the Haldane conjecture: Gap for magnetic excitations in the quasi-one-dimensional S=1 Heisenberg antiferromagnet $AgVP_2S_6$. *Phys. Rev. B*, 39(7):4820–4823, 1989.

[126] M. Takigawa, T. Asano, Y. Ajiro, M. Mekata, and Y. J. Uemura. Dynamics in the S=1 One-Dimensional Antiferromagnet $AgVP_2S_6$ via ^{31}P and ^{51}V NMR. *Phys. Rev. Lett.*, 76(12):2173–2176, 1996.

[127] H. Mutka, C. Payen, P. Molinié, J. L. Soubeyroux, P. Colombet, and A. D. Taylor. Magnetic correlation in the S=1 quasi-one-dimensional Heisenberg antiferromanget $AgVP_2S_6$. *Physica B*, 180 & 181:197–198, 1992.

[128] D. J. Buttrey, J. D. Sullivan, and A. L. Rheingold. Phase Equilibrium Study of the Y-Ba-Ni-O System and Structural Characterisation of the New Quasi-One-Dimensional Oxide Y_2BaNiO_5. *Journal of Solid State Chemistry*, 88:291–302, 1990.

[129] R. A. Cowley, M. Kenzelmann, W. J. L. Buyers, D. F. McMorrow, R. Coldea, and M. Enderle. New results on the excitations of an S=1 quantum chain. *Journal of Magnetism and Magnetic Materials*, (226-230):437–438, 2001.

[130] S. Ma, D. H. Reich, C. L. Broholm, B. J. Sternlieb, and R. W. Erwin. Spin correlation at finite temperature in an S=1 one-dimensional antiferromagnet. *Phys. Rev. B*, 51(5):3289–3292, 1995.

[131] J. Darriet and L. P. Regnault. The compound Y_2BaNiO_5: A new example of a Haldane gap in a S=1 magnetic chain. *Solid State Communications*, 86(7):409–412, 1993.

[132] P. E. Sulewski and S. W. Cheong. Raman study of one-dimensional spin fluctuations in the spin-1 Heisenberg chain compound Y_2BaNiO_5: Contrast to simple expectations. *Phys. Rev. B*, 51(5):3021–3026, 1995.

[133] T. Yokoo, T. Sakaguchi, K. Kakurai, and J. Akimitsu. Observation of the Haldane Gap in Y_2BaNiO_5 Single Crystal. *Journal of the Physical Society of Japan*, 64(10):3651–3655, 1995.

[134] T. Sakaguchi, K. Kakurai, T. Yokoo, and J. Akimitsu. Neutron Scattering Study of Magnetic Excitations in the Spin S=1 One-Dimensional Heisenberg Antiferromagnet Y_2BaNiO_5. *J. Phys. Soc. Japan*, 65(9):3025–3031, 1996.

[135] M. Kenzelmann, R. A. Cowley, W. J. L. Buyers, R. Coldea, M. Enderle, and D. F. McMorrow. Evolution of spin excitations in a gapped antiferromagnet from the quantum to the high-temperature limit. *Phys. Rev. B*, 66:174412, 2002.

[136] A. Zheludev, S. E. Nagler, S. M. Shapiro, L. K. Chou, D. R. Talham, and M. W. Meisel. Spin dynamics in the linear-chain S=1 antiferromagnet $Ni(C_3H_{10}N_2)_2N_3(ClO_4)$. *Phys. Rev. B*, 53(22):15004, 1996.

[137] A. Zheludev, T. Masuda, I. Tsukada, Y. Uchiyama, K. Uchinokura, P. Böni, and S. H. Lee. Magnetic excitations in coupled Haldane spin chains near the quantum critical point. *Phys. Rev. B*, 62(13):8921, 2000.

[138] K. Damle and S. Sachdev. Spin dynamics and transport in gapped one-dimensional Heisenberg antiferromagnets at nonzero temperatures. *Phys. Rev. B*, 57(14):8307–9339, 1998.

[139] T. Jolicoeur and O. Golinelli. σ model study of Haldane-gap antiferromagnets. *Phys. Rev. B*, 50(13):9265–9273, 1994.

[140] E. S. Sørensen and I. Affleck. S(k) for Haldane-gap antiferromagnets: Large-scale numerical results versus field theory and experiment. *Phys. Rev. B*, 49(18):13235–13238, 1994.

[141] F. H. L. Essler and R. M. Konik. Finite-temperature lineshapes in gapped quantum spin chains. *Phys. Rev. B*, 78:100403, 2008.

[142] S. Sachdev and K. Damle. Low Temperature Spin Diffusion in the One-Dimensional Quantum O(3) Nonlinear σ Model. *Phys. Rev. Lett.*, 78(5):943–946, 1997.

[143] J. Lou, S. Qin, T. K. Ng, Z. Su, and I. Affleck. Finite-size spectrum, magnon interactions, and magnetization of S=1 Heisenberg spin chains. *Phys. Rev. B*, 62(6):3786–3794, 2000.

[144] E. Garcia-Matres, J. L. Martinez, and J. Rodriguez-Carvajal. Structural Characterisation and Polymorphism of R_2BaNiO_5 (R=Nd, Gd, Dy, Y, Ho, Er, Tm, Yb) Studied by Neutron Diffraction. *Journal of Solid State Chemistry*, 103:322–333, 1993.

[145] B. Batlogg, S. W. Cheong, and L. W. Rupp. Haldane spin state in $Y_2Ba(Ni, Zn \text{ or } , Mg)O_5$. *Physica B: Condensed Matter (Amsterdam, Netherlands)*, (194-196):173–174, 1994.

[146] K. Habicht, R. Golub, F. Mezei, B. Keimer, and T. Keller. Temperature-dependent phonon lifetimes in lead investigated with neutron-resonance spin-echo spectroscopy. *Phys. Rev. B*, 69:104301, 2004.

[147] K. Habicht, T. Keller, and R. Golub. The resolution function in neutron spin-echo spectroscopy with three-axis spectrometers. *Journal of Applied Crystallography*, 36:1307–1318, 2003.

[148] A. L. Stancik and E. B. Brauns. A simple asymmetric lineshape for fitting infrared absorption spectra. *Vibrational Spectroscopy*, 47:66–69, 2008.

[149] F. Groitl. *High Resolution Spectroscopy with the Neutron Resonance Spin Echo Method*. PhD Thesis, Technical University Berlin, 2013.

[150] K. Habicht. SeRescal, NRSE-TAS resolution matrix calculations based on the Rescal code for Matlab by D.A. Tennant and D. F. Mcmorrow. Distributed by K. Habicht: habicht@hmi.de (2003).

[151] J. P. Renard, M. Verdauger, L. P. Regnault, W. Erkelens, J. Rossat-Mignod, J. Ribas, W. Stirling, and C. Vettier. Quantum energy gap in two quasi-one-dimensional S=1 Heisenberg antiferromagnets. *J. Appl. Phys.*, 63:3538, 1988.

[152] B. Náfrádi, T. Keller, H. Manaka, A. Zheludev, and B. Keimer. Low-Temperature Dynamics of Magnons in a Spin-1/2 Ladder Compound. *Phys. Rev. Lett.*, 106:177202, 2011.

[153] L. Amico, R. Fazio, A. Osterloh, and V. Vedral. Entanglement in many-body systems. *Rev. Mod. Phys.*, 80(2):517–576, 2008.

[154] L. Amico, A. Osterloh, F. Plastina, R. Fazio, and G. Massimo Palma. Dynamics of entanglement in one-dimensional spin systems. *Phys. Rev. A*, 69:022304, 2004.

[155] F. Baroni, A. Fubini, V. Tognetti, and P. Verruchi. Two-spin entanglement distribution near factorized states. *Journal of Physics A: Mathematical and Theoretical*, 49:9845–9857, 2007.

[156] M. A. Nielsen and I. Chuang. *Quantum Computation and Quantum Communication*. Cambridge University Press, 2000.

[157] W. K. Wootters. Entanglement of Formation of an Arbitrary State of Two Qubits. *Phys. Rev. Lett.*, 80(10):2245–2248, 1998.

[158] A. Aspect, P. Grangier, and G. Roger. Experimental Realization of Einstein-Podolski-Rosen-Bohm Gedankeneexperiment: A New Violation of Bell's Inequalities. *Phys. Rev. Lett.*, 49(2):91–94, 1982.

[159] B. Hensen, H Bernien, A. E. Dreau, A. Reiserer, N. Kalb, M. S. Blok, J. Ruitenberg, R. F. L. Vermeulen, R. N. Schouten, C. Abellan, W. Amaya, V. Pruneri, M. W. Mitchell, M. Markham, D. J. Twitchen, D. Elkouss, S. Wehner, T. H. Taminiau, and R. Hanson. Loophole-free Bell inequality violation using electron spins separated by 1.3 kilometres. *Nature*, 526(7575):682686, 2015.

[160] S. Gosh, T. F. Rosenbaum, G. Aeppli, and S. N. Coopersmith. Entangled quantum state of magnetic dipoles. *Nature*, 425:48–51, 2003.

[161] J. S. Caux, F. H. L. Essler, and U. Löw. Dynamical structure factor in the anisotropic Heisenberg chain in a transverse field. *Phys. Rev. B*, 68:134431, 2003.

[162] L. Amico, F. Baroni, A. Fubini, D. Patane, V. Tognetti, and P. Verrucchi. Divergence of the entanglement range in low-dimensional quantum systems. *Phys. Rev. A*, 74:022322, 2006.

[163] J. Quintanilla, L. Amico, and T. G. Perring. Quantifying entanglement through neutron scattering: detection of the entanglement transition. Private Notes, July 2010.

[164] J. Almeida, M. A. Martin-Delgado, L. Amico, and J. Quintanilla. Neutron scattering signature of the entanglement transition. Private Notes, February 2011.

[165] J. Quintanilla. Detection of the entanglement transition using neutron scattering: a finite-temperature study in the anisotropic XY model (quantum Ising model). Private Notes, February 2014.

[166] M. A. Porai-Koshits. *Kristallografiya*, 1:291, 1956.

[167] H. Yoshizawa, G. Shirane, H. Shiba, and K. Hirakawa. Neutron scattering study of a one-dimensional XY antiferromagnet Cs_2CoCl_4. *Phys. Rev. B*, 28(7):3904–3908, 1983.

[168] H. A. Algra, L. J. Jongh, H. W. J. Blöte, W. J. Huiskamp, and R. L. Carlin. Heat capacity of Cs_2CoCl_4 below 1 K, compared with the S = 1/2 linear chain XY model. *Physica*, 82B:239–246, 1976.

[169] P. M. Duxbury, J. Oitmaa, M. N. Barber, A. van der Bilt, K. O. Joung, and R. Carlin. Transverse susceptibility of the one-dimensional antiferromagnetic XY model. Application to Cs_2CoCl_4. *Phys. Rev. B*, 24(9):5149–515, 1981.

[170] S. Katsura. Statistical Mechanics of the Anisotropic Linear Heisenberg Model. *Phys. Rev.*, 127:1508–1518, 1962.

[171] O. Breunig, M. Garst, E. Sela, B. Buldmann, P. Becker, L. Bohatý, R. Müller, and T. Lorenz. Spin-1/2 XXZ Chain System Cs_2CoCl_4 in a Transverse Magnetic Field. *Phys. Rev. Lett.*, 111:187202, 2013.

[172] I. Chatterjee. Order-Disorder Transition in one-Dimensional Quantum Magnet. *Journal of Magnetism and Magnetic Materials*, 265, 2003.

[173] M. Kenzelmann, R. Coldea, D. A. Tennant, D. Visser, M. Hofmann, P. Smeibidl, and Z. Tylczynski. Order-to-disorder transition in the XY-like quantum magnet Cs_2CoCl_4 induced by noncommuting applied fields. *Phys. Rev. B*, 65:144432, 2002.

[174] J. N. McElearney, S. Merchant, G. E. Shankle, and R. L. Carlin. Low-temperature magnetic characteristics of the tetrahedrar $CoCl_4^{2-}$. III. Magnetic exchange in paramagnetic Cs_2CoCl_4. *Journal of Chemical Physics*, 66:450, 1977.

[175] C. J. Mukherjee, R. Coldea, D. A. Tennant, M. Koza, M. Enderle, K. Habicht, P. Smeibidl, and Z. Tylczynski. Field-induced quantum phase transition in the quasi 1D XY-like antiferromagnet Cs_2CoCl_4. *Journal of Magnetism and Magnetic Materials*, (272-276):921–921, 2004.

[176] G. L. Pascut. *Neutron and Resonant X-ray Scattering Studies of Low Dimensional Quantum Magnets*. PhD Thesis, School of Physics, Bristol University, 2010.

[177] O. Breunig, M. Garst, A. Rosch, E. Sela, B. Buldmann, P. Becker, L. Bohatý, R. Müller, and T. Lorenz. Low-temperature ordered phases of the spin-1/2 XXZ chain system Cs_2CoCl_4. *Phys. Rev. B*, 91:024423, 2015.

[178] O. Breunig. *Thermodynamics of the Spin-Chain Compunds* Cs_2CoCl_4 *and* $Cu(C_4H_4N_2)(NO_3)_2$. PhD Thesis, University of Cologne, 2015.

[179] R. Coldea, D. A. Tennant, E. M. Wheeler, E. Wawrzynska, D. Prabhakaran, M. Telling, K. Habicht, P. Smeibidl, and K. Kiefer. Quantum Criticality in an Ising Chain: Experimental Evidence for Emergent E_8 Symmetry. *Science*, 327(5962):177–180, 2010.

[180] I. Cabrera, J. D. Thompson, R. Coldea, D. Prabhakaran, R. I. Bewley, T. Guidi, J. A. Rodriguez-Rivera, and C. Stock. Excitations in the quantum paramagnetic phase of the quasi-one-dimensional Ising magnet $CoNb_2O_6$ in a transverse field: Geometric frustration and quantum renormalization effects. *Phys. Rev. B*, 90:014418, 2014.

[181] A. Bianchi, S. Carretta, P. Santini, G. Amoretti, T. Guidi, Y. Qiu, J. R. D. Copley, G. Timco, C. Muryn, and R. Winpenny. Rotational bands in open antiferromagnetic rings: A neutron spectroscopy study of the Cr_8Zn. *Phys. Rev. B*, 79:144422, 2009.

[182] M. L. Baker, T. Guidi, S. Carretta, J. Ollivier, H. Mutka, H. U. Gudel, G. A. Timco, E. J. L. McInnes, G. Amoretti, R. E. P. Winpenny, and P. Santini.

Spin dynamics of molecular nanomagnets unravelled at atomic scale by four-dimensional inelastic neutron scattering. *Nature Physics*, 8:906–911, 2012.

[183] M. S Reis, S. Soriano, A. M. dos Santos, B. C. Sales, D. O. Soare-Pinto, and P. Brandao. Evidence for entanglement at high temperatures in an engineered molecular magnet. *EPL*, 100:50001, 2012.

[184] S. Eggert and I. Affleck. Magnetic order and moment distribution in doped spin-chain systems. *Journal of Magnetism and Magnetic Materials*, 272-276:647–648, 2004.

[185] O. A. Starykh, H. Katsura, and L. Balents. Extreme sensitivity of a frustrated quantum magnet: Cs_2CuCl_4. *Phys. Rev. B*, 82:014421, 2010.

[186] C. J. Mukherjee. *Neutron Scattering Studies on Low-Dimensional Quantum Magnets*. PhD thesis, University of Oxford, 2005.